

A critical investigation of the use of infrared thermography
in determining the condition of composite materials

Sri Naga Pavan Addepalli

B.E (Mech), P.G. Dipl (Aero), M.Phil (Materials)

Submitted in partial fulfilment for the award of the degree of
Doctor of Philosophy

University of Wales Trinity Saint David

2017

A critical investigation of the use of infrared thermography in determining the
condition of composite materials

Sri Naga Pavan Addepalli
B.E (Mech), P.G. Dipl (Aero), M.Phil (Materials)

Supervised by:

Professor Kelvin Donne, Associate PVC (Corporate Strategy Development)
Dr Owen Williams, School of Automotive Engineering

and

Mr Ian Cooper, Consultant, TWI NDT Validation Centre Wales, Port Talbot

The research was undertaken under the auspices of The University of Wales –
Global Academy and TWI Ltd.

Submitted in partial fulfilment of award of the degree of
Doctor of Philosophy

University of Wales Trinity Saint David

2017

ABSTRACT

Since the introduction of synthetic composite materials as primary airframe structures in aircrafts, especially the Carbon Fibre Reinforced Polymers (CFRP) in the late 1990's, there has been increased use of these advanced materials that have completely replaced key metallic parts of the aircraft contributing to overall reduction in the weight of the aircraft. These innovative materials are increasingly preferred due to their material properties and better strength-to-weight ratio offering not just weight savings but increased resistance to issues such as abrasion and corrosion. As these composite materials are non-metallic in nature, their behaviour especially in the presence of defects and damage is less understood as they do not follow properties exhibited by metals and their alloy systems. This study thus focusses on establishing methods that could detect these defects and damage in a non-destructive manner such that the inspection systems do not cause further damage to the component. This study is primarily experimental in nature and has been presented in two parts. The first section looks at establishing pulsed thermography as a key technique capable of detecting sub-surface defects and its applicability to detect them. This has been presented by inspecting field representative samples and by introducing commonly occurring materials as inserts during the layup stage of the CFRP at controlled depths to determine the detection capability of the system. The second part of the work presented a parametric low-energy impact study where laminates were subject to modified Charpy and ballistic testing to create barely visible impact damage (BVID). The damaged parts were then subjected to inspection using techniques such as pulsed thermography, thermoelastic stress analysis (TSA), immersion ultrasonic testing, microscopy and laser doppler vibrometer (LDV). The aim was to establish TSA method as an alternative tool to detect surface breaking damage. It was found that pulsed thermography, though capable of detecting sub-surface damage, was less sensitive to near surface damage. Further, it was noticed that the TSA method showed a positive response when it came to detecting surface breaking damage created during ballistic impact, thus establishing the technique as an in-situ technique.

To my Father...

ACKNOWLEDGEMENTS

First of all I would like to express my profound gratitude and sincere thanks to my supervisor Professor Kelvin Donne for supporting my research for the last six years. I am greatly indebted to him for all his extensive help, support and patience without which this thesis would not have been possible. His academic knowledge, inspiration and enthusiasm have helped me accomplish this task. He has been my guide, mentor and above all a philosopher who has always supported me through thick and thin.

Sincere thanks to Mr. Ian Cooper who has helped me in completing this research by providing necessary training, supervision and the necessary guidance during my time at TWI Ltd. Thanks also to Mr. Philip Wallace, Associate Director, TWI Ltd, for his extensive support. Special thanks to Lorna and Maureen for their support.

I would like to thank my co-supervisor Dr. Owen Williams for his help supporting this research especially with the manufacture of the composite laminates. Thanks also to Dr. Peter Charlton for being my mentor and for all the numerous technical discussions that has helped improve my understanding of various associated research areas.

I would like to express my gratitude to Professor Roderick Thomas for introducing me to the concepts of active thermography and providing me with the necessary support both technical and personal during my time at TWI & SMU.

Special thanks to Mr. Gareth Staddon, Mr. Kevin Couling and Mr. John Kinsella for providing the necessary technical support for this research. I am grateful to Mrs. Louise Harris and all the Administrators at Swansea for assisting me in different ways to enable the smooth running of my research. Thanks to Ceri & Nigel for their support during my time at Swansea.

I would also like to express my sincere gratitude to Professor Rajkumar Roy, Cranfield University for his extensive support during my write-up period. Thanks to my good friends Luke Oakey and Lawrence Tinsley. Thanks also to my colleagues Yifan, John, Teresa, Charmaine, Sam, Paul, Ebi, Stefano, Jim, Jörn, Nic, and the entire team of TES Centre.

Special mention to my friends Arun, Shanta, Imtiaz, Warda, Suraj, Namratha, Rajaram, Mani, Anushka, Puneet and Kawal who continue to be my life-support. There are many other friends and family who have rendered help for the execution of this work; to them I express my gratefulness.

Lastly, I wish to dedicate this work to my parents and my sister. Their never ending love, support, encouragement, and advice during various stages of life have helped me grow up to what I am today.

Pavan Addepalli

TABLE OF CONTENTS

1	INTRODUCTION.....	1
1.1	Composite Materials.....	1
1.2	Infrared thermography	2
1.2.1	Advantages & disadvantages of infrared thermography	3
1.3	The research.....	4
1.4	Methodology.....	5
1.5	<i>Epilogue</i>	6
2	LITERATURE REVIEW.....	7
2.1	Composite Materials.....	7
2.1.1	History of Composite Materials	8
2.1.2	Why Composites?	9
2.1.3	Definitions & Classifications	9
2.1.4	Matrix & Reinforcement	11
2.1.5	Benefits of Composites	13
2.2	Defects occurring in Composite Materials	15
2.2.1	Fibres.....	15
2.2.2	Matrix.....	16
2.2.3	Manufacture	16
2.2.4	In-Service	16
2.2.5	Impact Damage	17
2.3	NDT of Composites.....	19
2.3.1	Ultrasonic Testing	20
2.3.2	X-Radiography.....	26
2.3.3	Vibrational Methods.....	28
2.4	Infrared Thermography.....	30
2.4.1	Science of Imaging.....	31
2.4.2	Infrared Radiation	32
2.4.3	Discovery of Infrared	33
2.4.4	Infrared Thermography – Principles	34
2.4.4.1	Infrared Waves	38

2.4.5	Pulsed Thermography – Principle	40
2.4.6	Lock-in Thermography – Principle	42
2.4.7	Recent advances in Thermography	44
2.5	Current study	51
2.5.1	Thermography for subsurface inspection	51
2.5.2	Impact damage – an overview	53
2.6	<i>Epilogue</i>	54
3	METHODS & MATERIALS.....	55
3.1	Research Methodology	55
3.2	Experimental Methods	57
3.2.1	Preliminary tests.....	57
3.2.2	Parametric Study	57
3.2.2.1	Computational Modelling.....	59
3.2.3	Impact Study	59
3.3	Composite laminate sample manufacture	61
3.3.1	The Stacking Sequence	63
3.3.2	Composite manufacture using hot press.....	63
3.4	Multiple inspection systems	65
3.4.1	Pulsed Thermography System – EchoTherm.....	65
3.4.2	FLIR Titanium Infrared Radiometer – Transient & TSA Mode	66
3.4.3	Pulse-echo immersion ultrasonic inspection system	67
3.4.4	Laser Doppler Vibrometer (LDV).....	68
3.5	<i>Epilogue</i>	70
4	RESULTS	71
4.1	Field reference samples investigation – Preliminary tests.....	72
4.1.1	Sample: ADAT 1	73
4.1.2	Sample: ADAT 3	80
4.1.3	Discussion	86
4.2	Parametric study.....	86
4.2.1	Experimental results.....	87
4.2.1.1	Sheet metal defect inserts	87
4.2.1.2	Teflon defect inserts	91

4.2.1.3	Bagging film defect inserts	101
4.2.2	Thermal Modelling.....	106
4.3	Impact Studies – Preliminary Experimental trials	115
4.3.1	Preliminary Charpy Trials.....	115
4.3.2	Preliminary TSA trials	125
4.4	Impact Studies – A parametric approach.....	129
4.4.1	Results.....	133
4.4.1.1	3mm Quasi-isotropic – Charpy.....	134
4.4.1.2	3mm TWI – Charpy.....	151
4.4.1.3	3mm Quasi-isotropic (QI) – Gas-gun	162
4.4.1.4	3mm TWI – Gas-gun.....	174
4.4.1.5	6mm Quasi-isotropic – Charpy.....	185
4.4.1.6	6mm Quasi-isotropic – Gas gun	187
4.4.1.7	6mm TWI – Gas gun	194
4.4.1.8	Epilogue.....	200
4.5	Impact Studies Comparison – vibrational analysis	201
4.5.1	Theoretical modelling – vibrational analysis	201
4.5.2	Random Error Estimation	204
4.5.3	Damage changes modal frequency – a hypothesis	211
4.6	<i>Epilogue</i>	213
5	REVIEW OF WORK	214
5.1	In-field samples.....	215
5.2	Manufacturing defects – a parametric study	215
5.3	Impact damage assessment – a parametric study.....	218
5.4	<i>Epilogue</i>	221
6	CONCLUSIONS & FUTURE WORK	222
6.1	Conclusions	222
6.2	Recommendations & Future Work.....	223
	BIBLIOGRAPHY	225

APPENDIX 1	231
APPENDIX 2	233
APPENDIX 3	234
APPENDIX 4	239
APPENDIX 5	241
APPENDIX 6	242
APPENDIX 7	248

LIST OF FIGURES

Figure 1 Classification of Fibres (Matthews and Rawlings 1999, Chawla 2001)	10
Figure 2 Material Selection Chart classifying various material systems based on Young's modulus and density. Source: Cambridge University (University)	14
Figure 3 Ground Equipment, Luggage Carts and Cargo Containers (Kim, DeFrancisci et al. 2009)	18
Figure 4 Set-up of Ultrasonic Testing (Kapadia 2013)	22
Figure 5 A-Scan from a typical Pulse-Echo UT test of CFRP Panel (Matthews and Rawlings 1999; Kapadia 2013)	23
Figure 6 B-Scan (above) & C Scan results representing defects present in CFRP Panel (Kapadia 2013)	23
Figure 7 Set up of Back-scatter technique using Pulse-Echo (Kapadia 2013)	24
Figure 8 Through-transmission testing using a water jet system (Kapadia 2013)	24
Figure 9 Ultrasonic Spectroscopy set up showing wavelength difference due to presence of defects (Kapadia 2013)	25
Figure 10 Set up of X-Radiography system (Kapadia 2013)	27
Figure 11 Force-time and force-frequency records illustrating the difference between sound and defective areas of adhesively bonded structure (Matthews and Rawlings 1999; Kapadia 2013)	29
Figure 12 The Electromagnetic Spectrum (Pratt 2013)	32
Figure 13 An experiment by Sir William Herschel leading to the discovery of "heating rays" (Ring 2000)	34
Figure 14 The first solar 'Thermogram' by Sir John Herschel (1840) (Ring 2000)	34
Figure 15 Heat transfer across a wall: Conduction (Vollmer and Möllmann 2010)	35
Figure 16 Heat transfer between a solid and a moving fluid: Convection. (Vollmer and Möllmann 2010)	37
Figure 17 Heat transfer between a solid and its environment: Radiation. (Vollmer and Möllmann 2010)	38
Figure 18 Illustration of IR waves in an EM spectrum (Vollmer and Möllmann 2010)	39
Figure 19 Basic arrangements for a pulsed thermography system (Maldague, Beaudoin et al. 2001)	42

Figure 20 Log time temperature plot showing pixel temperature decay profile of the parent material and damage (Shepard 2007).....	52
Figure 21 CAD drawing of the defects introduced at the lay-up stage (all dimensions in mm).....	58
Figure 22 Inserts of PTFE, metal shim and bagging film	59
Figure 23 The modified Charpy impact test setup with infrared and high speed camera	60
Figure 24 The ballistic gas gun	61
Figure 25 Sabot with stone that was introduced into the gas gun barrel for impact test	61
Figure 26 Carbon prepreg layer orientation	62
Figure 27 Representative parametric insert sample (120×120mm) (left) and impact sample (200×100mm) (right)	63
Figure 28 Hot Press	64
Figure 29 The hot plate (left) and the control unit (right).....	64
Figure 30 EchoTherm pulsed thermography system in use.....	65
Figure 31 FLIR Titanium infrared radiometer	66
Figure 32 Pulse echo immersion UT testing setup using USL Scanner	67
Figure 33 The Polytec PSV-400 laser doppler vibrometer	68
Figure 34 PSV LDV experimental setup	68
Figure 35 Tail plane wedge (a) top view; (b) side view	72
Figure 36 Tail plane wedge, side view.....	72
Figure 37 Radiograph image of ADAT 1 with red circular markers indicating the defect location	73
Figure 38 RAW image of ADAT 1 sampled at 5.973 seconds.....	74
Figure 39 Log plot representing the RAW image for ADAT 1; 1&5 – No defect, 2 – delamination, 3 – disbond and 4 – excess adhesive/water ingress.....	75
Figure 40 1st Derivative (1D) image of ADAT 1 at 5.973 seconds	77
Figure 41 Graph representing the 1D data of ADAT 1; 1&5 – No defect, 2 – delamination, 3 – disbond and 4 – excess adhesive/water ingress.....	78
Figure 42 2nd Derivative (2D) image of ADAT 1 at 5.973 seconds	78
Figure 43 Graph representing the 2D data of ADAT 1; 1&5 – No defect, 2 – delamination, 3 – disbond and 4 – excess adhesive/water ingress.....	79

Figure 44 Radiograph of ADAT 3 with red circular markers showing the defect location.....	81
Figure 45 RAW image of ADAT 3 sampled at 5.973 seconds	82
Figure 46 Log plot representing the RAW image for ADAT 3; 1&5 – No defect, 2 – delamination, 3 – disbond and 4 – excess adhesive/water ingress.....	82
Figure 47 1st Derivative (1D) image of ADAT 3 at 5.973 seconds	83
Figure 48 Graph representing the 1D data of ADAT 3; 1&5 – No defect, 2 – delamination, 3 – disbond and 4 – excess adhesive/water ingress.....	83
Figure 49 2nd Derivative (2D) image of ADAT 3 at 5.973.....	84
Figure 50 Graph representing the 2D data of ADAT 3; 1&5 – No defect, 2 – delamination, 3 – disbond and 4 – excess adhesive/water ingress.....	84
Figure 51 RAW Thermal image - Sample: 3SS2 (120×120mm); Sampling time: 0.7s	88
Figure 52 Log t-T plot for the RAW data; Sample: 3SS2; 1 – No defect; 2,3 – 0.5mm depth; 4,5 – 1.0mm; 6,7 – 1.5mm.	89
Figure 53 Time of flight (ToF) image for 3mm laminate (120×120mm) - Sample: 3SS2	90
Figure 54 RAW Thermal image - Sample: 3TF1 (120×120mm); Sampling time: 0.27s	92
Figure 55 Log t-T plot for the RAW data; Sample: 3TF1; 1 – No defect; 2,3 – 0.5mm depth; 4,5 – 1.0mm; 6,7 – 1.5mm	93
Figure 56 Time of flight (ToF) image for 3mm laminate (120×120mm) - Sample: 3TF1	94
Figure 57 RAW Thermal image - Sample: 6TF1 (120×120mm); Sampling time: 0.92s	96
Figure 58 Log t-T plot for the RAW data; Sample: 6TF1; 1 – No defect; 2,3 – 2.0mm depth; 4,5 – 2.5mm; 6,7 – 3.0mm	96
Figure 59 Time of flight (ToF) image for 6mm laminate (120×120mm) - Sample: 6TF1	97
Figure 60 RAW Thermal image - Sample: 9TF1 (120×120mm); Sampling time: 1.4s	99
Figure 61 Log t-T plot for the RAW data; Sample: 9TF1; 1 – No defect; 2,3 – 3.5mm depth; 4,5 – 4.0mm; 6,7 – 4.5mm	99

Figure 62 Time of flight (ToF) image for 9mm laminate (120×120mm) - Sample: 9TF1	100
Figure 63 RAW Thermal image - Sample: 3BGF1 (120×120mm); Sampling time: 1.47s	102
Figure 64 2 nd derivative (2D) Thermal image - Sample: 3BGF1 (120×120mm); Sampling time: 1.47s.....	103
Figure 65 Log t-T plot for the RAW data; Sample: 3BGF1; 1 – No defect; 2,3 – 0.5mm depth; 4,5 – 1.0mm; 6,7 – 1.5mm	103
Figure 66 Time of flight (ToF) image for 3mm laminate (120×120mm) - Sample: 3BGF1	104
Figure 67 The model with the slotted aperture insert - wire frame mode.....	106
Figure 68 Ideas model showing the laminate with the slotted aperture insert at 2mm from the top surface.	107
Figure 69 Laminate thermogram at sampling time 28ms	107
Figure 70 Laminate thermogram at sampling time 150ms	108
Figure 71 Laminate thermogram at sampling time 175ms	108
Figure 72 Log t-T plot for the laminate with PTFE; 1 – GFRP, 2 – Air Gap, 3 - PTFE	109
Figure 73 3mm laminate model with PTFE defects at different depths; top view ..	110
Figure 74 3mm laminate model with PTFE defects at different depths; side view ..	110
Figure 75 3mm laminate (120×120mm) with PFTE and air gap inserts; thermography sampling at 0.5s	111
Figure 76 Log t-T plot for the 3mm laminate model with 1 – CFRP (Red curve); 2 – Air gap (Green curve); 3 – PTFE (Blue curve); Defect depth: (a) 0.5mm, (b) 1.0mm and (c) 1.5mm below surface	112
Figure 77 6mm laminate with PTFE and Air gap inserts; computed thermogram at 3s	113
Figure 78 Log t-T plot for the 6mm laminate model with 1 – CFRP (Red curve); 2 – Air gap (Green curve) and 3 – PTFE (Blue curve); Defect depth – 2.0mm	113
Figure 79 Log t-T plot for the 6mm laminate model with 1 – CFRP (Red curve); 2 – Air gap (Green curve) and 3 – PTFE (Blue curve); Defect depth – 2.5mm	113
Figure 80 Log t-T plot for the 6mm laminate model with 1 – CFRP (Red curve); 2 – Air gap (Green curve) and 3 – PTFE (Blue curve); Defect depth – 3.0mm	114

Figure 81 Initial experimental setup – Charpy trial; Test schematic (left) and the test rig (right)	116
Figure 82 Indenter attached to the hammer on the left; and the infrared radiometer and test sample arrangement on the right.....	116
Figure 83 Digital image of CFRP Sample 1; Size 150×150mm.....	117
Figure 84 Settings of IR camera for transient thermography.....	119
Figure 85 Charpy initial trials - Thermogram at the time of impact; t=0ms.....	119
Figure 86 Charpy initial trials - Thermogram at the time of impact; t=1.09ms.....	120
Figure 87 Charpy initial trials - Thermogram at the time of impact; t=2.18ms.....	120
Figure 88 Charpy initial trials - Thermogram at the time of impact; t=9.824ms.....	120
Figure 89 Sample 2- UD Carbon OSL 90 - Transient Thermography at time t=0ms	122
Figure 90 Sample 2- UD Carbon OSL 90 - Transient Thermography at time t=1.08ms.....	122
Figure 91 Sample 2- UD Carbon OSL 90 - Transient Thermography at time t=6.5ms	123
Figure 92 Sample 2- UD Carbon OSL 90 - Transient Thermography at time t=8.656ms.....	123
Figure 93 Sample 2- UD Carbon OSL 90 - Transient Thermography at time t=12.98ms.....	123
Figure 94 TSA experimental setup	126
Figure 95 Cedip camera settings for TSA measurement	127
Figure 96 TSA image showing crush damage on the composite laminate at a synchronous excitation frequency of 9.998Hz.....	127
Figure 97 Modified Charpy Test Setup - now includes a high speed digital camera	130
Figure 98 The Gas Gun - ballistic testing	131
Figure 99 The gas-gun with sabot and stone.....	131
Figure 100 Experimental setup of gas-gun testing - view 1	132
Figure 101 Gas-gun experimental setup - view 2	132
Figure 102 Sample: 3QI20d12JC2 - microscopic image with damage dimension..	135
Figure 103 Settings for Sample 3QI20d12JC2	136
Figure 104 Sample: 3QI20d12JC2 at Frame - 0	136
Figure 105 Sample: 3QI20d12JC2 at Frame - 1	136

Figure 106 Sample: 3QI20d12JC2 at Frame - 2	137
Figure 107 Sample: 3QI20d12JC2 at Frame - 4	137
Figure 108 Sample: 3QI20d12JC2 at Frame – 8.....	137
Figure 109 Pulsed thermography result; Sample: 3QI20d12JC2; Size: 200×100mm; 2D Image; Sampling: 90fms	138
Figure 110 Pulsed thermography result; Sample: 3QI20d12JC2; RAW Thermal plot; 1&3 – sound area, 2 – damage area	139
Figure 111 Camera settings for the TSA analysis; Sample: 3QI20d12JC2.....	140
Figure 112 TSA map of Sample 3QI20d12JC2	140
Figure 113 Microscopy image of 3QI16d8JC2 with damage dimensions.....	142
Figure 114 Sample: 3QI16d8JC2 at Frame – 0.....	142
Figure 115 Sample: 3QI16d8JC2 at Frame – 1.....	143
Figure 116 Sample: 3QI16d8JC2 at Frame – 2.....	143
Figure 117 Sample: 3QI16d8JC2 at Frame – 3.....	143
Figure 118 Sample: 3QI16d8JC2 at Frame – 8.....	144
Figure 119 Pulsed thermography result; Sample: 3QI16d8JC2; Size: 200×100mm; 2D Image; Sampling: 90fms	145
Figure 120 Pulsed thermography result; Sample: 3QI16d8JC2; RAW thermal log t-T plot; 1&3 – sound area, 2 – damage area	145
Figure 121 TSA stress map of Sample 3QI16d8JC2	146
Figure 122 Microscopy image of 3QI12d4.5JC3 showing damage site – no visible damage	147
Figure 123 Sample: 3QI12d4.5JC3 at Frame – 0.....	148
Figure 124 Sample: 3QI12d4.5JC3 at Frame – 1.....	148
Figure 125 Sample: 3QI12d4.5JC3 at Frame – 2.....	148
Figure 126 Sample: 3QI12d4.5JC3 at Frame – 3.....	149
Figure 127 Sample: 3QI12d4.5JC3 at Frame – 4.....	149
Figure 128 Sample: 3QI12d4.5JC3 at Frame – 5.....	149
Figure 129 Sample: 3QI12d4.5JC3 at Frame – 6.....	150
Figure 130 Sample: 3QI12d4.5JC3 at Frame – 8.....	150
Figure 131 Microscopic image of 3TWI20d12JC3 with dimension of the damage	151
Figure 132 Sample: 3TWI20d12JC3 at Frame – 0	152
Figure 133 Sample: 3TWI20d12JC3 at Frame – 1	152
Figure 134 Sample: 3TWI20d12JC3 at Frame – 3	152

Figure 135 Sample: 3TWI20d12JC3 at Frame – 7	153
Figure 136 Sample: 3TWI20d12JC3 at Frame – 8	153
Figure 137 Sample: 3TWI20d12JC3 at Frame – 12	153
Figure 138 Sample: 3TWI20d12JC3 at Frame – 20	154
Figure 139 Pulsed thermography image; Sample: 3TWI20d12JC3; Size: 200×100mm; 2D image; Sampling: 90 frames	154
Figure 140 Pulsed thermography image; Sample: 3TWI20d12JC3; Log t-T plot; 1 – sound area, 2 – damage area	155
Figure 141 Microscopic image of 3TWI16d8JC2 with dimensions of damage	156
Figure 142 Sample: 3TWI16d8JC2 at Frame – 0	156
Figure 143 Sample: 3TWI16d8JC2 at Frame – 1	157
Figure 144 Sample: 3TWI16d8JC2 at Frame – 2	157
Figure 145 Sample: 3TWI16d8JC2 at Frame – 3	157
Figure 146 Sample: 3TWI16d8JC2 at Frame – 6	158
Figure 147 Sample: 3TWI16d8JC2 at Frame – 7	158
Figure 148 Sample: 3TWI16d8JC2 at Frame – 25	158
Figure 149 Microscopic image of 3TWI12d4.5JC3	159
Figure 150 Sample: 3TWI12d4.5JC3 at Frame – 0	159
Figure 151 Sample: 3TWI12d4.5JC3 at Frame – 1	160
Figure 152 Sample: 3TWI12d4.5JC3 at Frame – 2	160
Figure 153 Sample: 3TWI12d4.5JC3 at Frame – 3	160
Figure 154 Sample: 3TWI12d4.5JC3 at Frame – 4	161
Figure 155 Sample: 3TWI12d4.5JC3 at Frame – 6	161
Figure 156 Microscopic image of 3QI12JS2	162
Figure 157 Sample: 3QI12JS2 at Frame - 0.....	163
Figure 158 Sample: 3QI12JS2 at Frame - 1.....	163
Figure 159 Sample: 3QI12JS2 at Frame - 2.....	164
Figure 160 Sample: 3QI12JS2 at Frame - 3.....	164
Figure 161 Sample: 3QI12JS2 at Frame - 8.....	164
Figure 162 Pulsed thermography results: Sample: 3QI12JS2; Size: 200×100mm; 2D image; Sampling: 55fms	165
Figure 163 Pulsed thermography results: Sample: 3QI12JS2; Log t-T plot; 1 – sound area, 2 – damage area	165
Figure 164 TSA result for 3QI12JS2	166

Figure 165 Microscopic image of 3QI8JS1 with dimensions of damage	167
Figure 166 Sample: 3QI8JS1 at Frame – 0	167
Figure 167 Sample: 3QI8JS1 at Frame – 1	168
Figure 168 Sample: 3QI8JS1 at Frame – 8	168
Figure 169 Sample: 3QI8JS1 at Frame – 16	168
Figure 170 Pulsed thermographic image; Sample: 3QI8JS1; Size: 200×100mm; 2D image; Sampling: 55fms	169
Figure 171 Pulsed thermographic image; Sample: 3QI8JS1; Log t-T plot; 1 – sound area, 2 – damage area	169
Figure 172 TSA image with stress map plot on the right showing peaks for various damage areas	170
Figure 173 3QI4.5JS1 laminate's microscopic image with damage measurements	171
Figure 174 Sample: 3QI4.5JS1 at Frame – 0	171
Figure 175 Sample: 3QI4.5JS1 at Frame – 1	172
Figure 176 Sample: 3QI4.5JS1 at Frame – 8	172
Figure 177 Pulsed thermography image; Sample: 3QI4.5JS1; Size: 200×100mm; 2D image; Sampling: 55fms	172
Figure 178 Pulsed thermography results; Sample: 3QI4.5JS1; Log t-T plot; 1 – sound area, 2 – damage area	173
Figure 179 TSA stress map of 3QI4.5JS1 with a profile plot on the right	173
Figure 180 Microscopic image of 3TWI12JS3 laminate with damage measurements	174
Figure 181 Sample: 3TWI12JS3 at Frame – 0	174
Figure 182 Sample: 3TWI12JS3 at Frame – 1	175
Figure 183 Sample: 3TWI12JS3 at Frame – 8	175
Figure 184 Pulsed thermography results; Sample: 3TWI12JS3; Size: 200×100mm; 2D image; Sampling: 23 fms	175
Figure 185 Pulsed thermography results; Sample: 3TWI12JS3; Size: 200×100mm; 2D image; Sampling: 55 fms	176
Figure 186 Pulsed thermography results; Sample: 3TWI12JS3; Log t-T plot; 1 – sound area, 2 – damage area	176
Figure 187 TSA stress map for 3TWI12JS3 with profile plot on the right.....	177
Figure 188 Microscopic image of 3TWI8JST1 laminate with damage measurements	178

Figure 189 Sample: 3TWI8JST1 at Frame – 0	178
Figure 190 Sample: 3TWI8JST1 at Frame – 1	179
Figure 191 Sample: 3TWI8JST1 at Frame – 20	179
Figure 192 Pulsed thermography results; Sample: 3TWI8JST1; Size: 200×100mm; 2D image; Sampling: 39ms	179
Figure 193 Pulsed thermography results; Sample: 3TWI8JST1; Log t-T plot; 1 – damage area, 2&3 – sound area	180
Figure 194 TSA stress map for 3TWI8JST1 with profile plot on the right	180
Figure 195 Microscopic image of 3TWI4.5JS3 laminate with damage measurements	181
Figure 196 Sample: 3TWI4.5JS3 at Frame – 0.....	181
Figure 197 Sample: 3TWI4.5JS3 at Frame – 1.....	182
Figure 198 Sample: 3TWI4.5JS3 at Frame – 12 (Particles flying off)	182
Figure 199 Sample: 3TWI4.5JS3 at Frame – 15.....	182
Figure 200 Sample: 3TWI4.5JS3 at Frame – 304.....	183
Figure 201 Pulsed thermography results; Sample: 3TWI4.5JS3; Size: 200×100mm; 2D image; Sampling: 6 fms	183
Figure 202 Pulsed thermography results; Sample: 3TWI4.5JS3; Log t-T plot; 1 – damage area, 2 – sound area	184
Figure 203 TSA stress map for 3TWI4.5JS3 with profile plot on the right.....	184
Figure 204 Microscopic image of 6QI20d12JC3 laminate with damage measurements.....	185
Figure 205 Pulsed thermography results; Sample: 6QI20d12JC3; Size: 200×100mm; 2D image; Sampling: 55 fms	186
Figure 206 Pulsed thermography results; Sample: 6QI20d12JC3; Log t-T plot; 1 – damage area, 2&3 – sound area	186
Figure 207 Microscopic image of 6QI12JS1 laminate showing damage area 1.....	188
Figure 208 Microscopic image of 6QI12JS1 laminate showing damage area 2.....	188
Figure 209 Pulsed thermography results; Sample: 6QI12JS1; Size: 200×100mm; 2D image; Sampling: 17 fms	189
Figure 210 Pulsed thermography results; Sample: 6QI12JS1; Log t-T plot; 1 – damage area, 2&3 – sound area	189
Figure 211 TSA stress map for 6QI12JS1 with profile plot on the right.....	190
Figure 212 Microscope image of 6QI8JS1 with damage measurement	191

Figure 213 Pulsed thermography results; Sample: 6QI8JS1; Size: 200×100mm; 2D image; Sampling: 23 fms	191
Figure 214 Pulsed thermography results; Sample: 6QI8JS1; Log t-T plot 1 – damage area, 2&3 – sound area.....	192
Figure 215 TSA stress map for 6QI8JS1 with profile plot on the right.....	192
Figure 216 Microscope image of 6QI4.5JS3 with damage measurements.....	193
Figure 217 TSA stress map for 6QI4.5JS3 with profile plot on the right.....	193
Figure 218 Microscope image of 6TWI12JS1 with damage measurements.....	194
Figure 219 Pulsed thermography results; Sample: 6TWI12JS1; Size: 200×100mm; 2D image; Sampling: 44 fms	195
Figure 220 Pulsed thermography results; Sample: 6TWI12JS1; Log t-T plot; 1 – damage area, 2&3 – sound area	195
Figure 221 TSA stress map for 6TWI12JS1 with profile plot on the right.....	196
Figure 222 Microscope image of 6TWI8JS1 with damage measurements.....	197
Figure 223 Pulsed thermography results; Sample: 6TWI8JS1; Size: 200×100mm; 2D image; Sampling: 24 fms	197
Figure 224 Pulsed thermography results; Sample: 6TWI8JS1; Log t-T plot; 1 – damage area, 2&3 – sound area	198
Figure 225 TSA stress map for 6TWI8JS1 with profile plot on the right.....	198
Figure 226 Microscope image of 6TWI4.5JS2 with damage measurements.....	199
Figure 227 TSA stress map for 6TWI4.5JS2 with profile plot on the right.....	199
Figure 228 Mesh model of virgin CFRP laminate; Size: 200×100×3mm.....	202
Figure 229 Mesh model of CFRP laminate with centre cut-off; Size: 200×100×3mm; Cut-off size: 20×2.5×3mm.....	202
Figure 230 The Polytec PSV400 Laser Doppler Vibrometer	204
Figure 231 Test sample for the LDV measurement, clamped to a bench vice. This image also shows the laser spot on the sample together with the bench top shaker	205
Figure 232 Graph showing the averaged trials under each loading and analysing at 8 modal frequencies	206
Figure 233 The modal form with full spectrum at the bottom; Sample: 3TWI20d12JC1; Mode – 1	207
Figure 234 The modal form with full spectrum at the bottom; Sample: 3TWI20d12JC1; Mode – 2	207

Figure 235 The modal form with full spectrum at the bottom; Sample: 3TWI20d12JC1; Mode – 3	208
Figure 236 The modal form with full spectrum at the bottom; Sample: 3TWI20d12JC1; Mode – 4	208
Figure 237 The modal form with full spectrum at the bottom; Sample: 3TWI20d12JC1; Mode – 5	209
Figure 238 The modal form with full spectrum at the bottom; Sample: 3TWI20d12JC1; Mode – 6	209
Figure 239 The modal form with full spectrum at the bottom; Sample: 3TWI20d12JC1; Mode – 7	210
Figure 240 The modal form with full spectrum at the bottom; Sample: 3TWI20d12JC1; Mode – 8	210
Figure 241 Vibration Modes vs modal frequencies (average values) of the laminate before and after impact.....	212
Figure 242 Altair software interface	242
Figure 243 Altair software with camera live feed.....	242
Figure 244 Cirrus Control interface with digital temperature level window	243
Figure 245 Cirrus control window	243
Figure 246 Cirrus control window with annotations.....	244
Figure 247 Filter window to select for any filters.....	244
Figure 248 Cirrus control window	244
Figure 249 NUC Control window.....	245
Figure 250 NUC confirmation window for low temperature exposure	245
Figure 251 NUC confirmation window for high temperature exposure	246
Figure 252 Cirrus control window with NUC & BPR preferences control window.....	247
Figure 255 Defect materials meshed separately; Green - PTFE; Blue - Air gap.....	248
Figure 256 Model showing defect materials with mesh; orthogonal view	248

LIST OF TABLES

Table 1 Advantages and disadvantages of infrared thermography	4
Table 2 Mechanical properties of fibres and their monolithic counterparts (Matthews and Rawlings 1999; CMH-17 2012)	11
Table 3 Some applications of Polymer Matrix Composites (Matthews and Rawlings 1999; Baker, Dutton et al. 2004)	13
Table 4 Defects developing from in-service phenomenon	17
Table 5 FLIR Titanium infrared radiometer specifications	66
Table 6 USL Pulse Echo Scanner specifications	67
Table 7 Settings used for vibration testing using LDV	69
Table 8 Pulsed thermography experiment settings	73
Table 9 Defect classification markers	80
Table 10 Pulse thermography experimental settings for ADAT 3	81
Table 11 Defect classification markers	85
Table 12 3mm laminates with steel shim inserts; defect location and tests performed	87
Table 13 Pulsed thermography experimental settings. Sample: 3SS2	88
Table 14 Sample thickness measurement from PEUT - Sample: 3SS2	90
Table 15 3mm laminates with Teflon inserts; defect location and tests performed	91
Table 16 Pulsed thermography experimental settings. Sample: 3TF1	92
Table 17 Sample thickness measurement from PEUT - Sample: 3TF1	94
Table 18 6mm laminates with Teflon inserts; defect location and tests performed	95
Table 19 Pulsed thermography experimental settings. Sample: 6TF1	95
Table 20 Sample thickness measurement from PEUT - Sample: 6TF1	97
Table 21 9mm laminates with Teflon inserts; defect location and tests performed	98
Table 22 Pulsed thermography experimental settings. Sample: 9TF1	98
Table 23 Sample thickness measurement from PEUT - Sample: 9TF1	100
Table 24 3mm laminates with bagging film inserts; defect location and tests performed	101
Table 25 Pulsed thermography experimental settings. Sample: 3BGF1	102
Table 26 Sample thickness measurement from PEUT - Sample: 3BGF1	104
Table 27 Hot press cure settings for preliminary tests	115

Table 28 TSA capture settings	126
Table 29 Impact test parametric study parameters.....	129
Table 30 Modal frequencies of virgin and damage CFRP laminate as computed from NX-Ideas	202
Table 31 shows 8 modes identified during the LDV data analysis and their respective peaks. This data represents three sample loading conditions with three trials under each loading condition	206
Table 32 Modes and modal frequency comparison between the sample 3TWI12d20JC3T before and after impact	212
Table 33 Pulsed Thermography detection capability.....	216
Table 34 Impact damage detectability matrix.....	219
Table 35 A 3mm laminate stacking sequence.....	234
Table 36 A 6mm laminate stacking sequence.....	235
Table 37 A 9mm laminate stacking sequence.....	236
Table 38 Charpy impact test parameters.....	239
Table 39 Gas-gun experimental settings	240

LIST OF ABBREVIATIONS

1D	First Derivative
2d	Two Dimensional
2D	Second Derivative
3d	Three Dimensional
AO	Acousto-Optic
BGF	Bagging Film
BPR	Bad Pixel Replacement
BVID	Barely Visible Impact Damage
C	Celsius or Centigrade
CFRP	Carbon Fibre Reinforced Polymer
CMM	Co-ordinate Measuring Machine
COSHH	Control Of Substances Hazardous to Health
CT	Computed Tomography
DL	Digital Level (Temperature)
EM	Electromagnetic
FEA	Finite Element Analysis / Model
FFT	Fast Fourier Transform
fms	Frames
FMTWI	Frequency Modulated Thermal Wave Imaging
FVM	Finite Volume Method
fps	Frames Per Second
GFRP	Glass Fibre Reinforced Polymer
GRP	Glass Reinforced Plastics
GSM	Grams per Square Metre
HEALTHY	Heat Emitting Layer for Thermography
Hz	Hertz
InSb	Indium Antimonide
IR	Infrared
IRT	Infrared Thermography
IT	Integration Time
K	Kelvin

kHz	Kilo Hertz
kW	Kilo Watt
LDV	Laser Doppler Vibrometer
Log t-T	Logarithmic Time Temperature Plot
Mhz	Megahertz
mK	Milli Kelvin
mm	Millimetre
ms	Millisecond
NDT	Non Destructive Testing
nm	Nanometres
NUC	Non Uniformity Correction
PC	Personal Computer
PMC	Polymer fibre Matrix Composites
PEUT	Pulse Echo Ultrasonic Testing
PPT	Pulsed Phase Thermography
PT	Pulsed Thermography
PTFE	Polytetrafluoroethylene or Teflon®
PVT	Pulsed Video Thermography
QI	Quasi-Isotropic
s	Second
SNR	Signal-to-Noise Ratio
SS	Steel Shim
t	Time
T	Temperature
TF	Teflon®
ToF	Time of Flight
TSA	Thermoelastic Stress Analysis (or) Thermo-Stress Analysis
TSR	Thermographic Signal Reconstruction
UD	Uni-Directional
UT	Ultrasonic Testing
µm	Micrometre
µs	Microsecond

1 INTRODUCTION

Infrared Thermography has been increasingly used as an advanced Non-Destructive Testing (NDT) and a condition monitoring tool in commercial and industrial applications over the last fifty years. This study uses infrared radiometers to monitor the condition of Carbon Fibre Reinforced Polymer (CFRP) composite laminates using pulsed thermography and thermoelastic stress analysis (TSA) techniques. This project aims to establish the defect detection capabilities of thermography within the composite industry.

1.1 Composite Materials

Composite materials have been a part of human life for a long time. Different explanations exist as to define what a composite material is. Some define it as a combination of two or more different materials giving a new material with enhanced physical and mechanical properties to the new material formed and this new material is referred to as a composite material (Jones 1999; Kaw 2006; Vinson and Sierakowski 2008).

Carbon composites due to their physical, mechanical properties including better strength-to-weight ratio and corrosion performance, have found their way into the automotive and aerospace industry. These materials are robust, reliable and strong in comparison with their metallic counterparts. However, understanding the forces acting on such materials, their responses to those forces, overall performance, and strength are not fully understood and thus form a huge challenge to engineers. There is little evidence that helps understand the behaviour of such advanced materials in extreme environmental conditions. There is thus a constant need to detect and monitor those defects / anomalies using various destructive and non-destructive techniques as a preventive measure which might otherwise lead to catastrophic failure of the working environment where such advanced materials are used. Currently NDT techniques such as Ultrasonic testing (conventional & immersion) and x-radiography techniques are used within the aerospace industry to

detect in-service and manufacturing defects occurring in composites with Thermography being used mostly as a qualitative tool (Adams and Cawley 1988; Matthews and Rawlings 1999; Morgan 2005; Kapadia 2013).

Typically defects such as delaminations, disbonds, voids and impact occur in composite materials either on the surface or sub-surface. The ability to detect such sub-surface defects without destroying the sample is a challenge. Currently both contact and non-contact NDT techniques are used in the industry to evaluate the condition of the composite structure. Various contact based ultrasonic testing methods currently in use include manual, pulse-echo, through transmission, spectroscopy and acoustography (Kessler 2004; Kapadia 2013). X-Radiography and Thermography come under the non-contact NDT techniques.

1.2 Infrared thermography

Infrared thermography deals with studying the temperature gradient and making appropriate measurements of the flow of heat, thereby assessing the condition and working performance of the equipment and the structural integrity of the material under inspection. It has been noticed that anomalies and or defects present in the equipment alter their thermal pattern. In order to identify these anomalies, a complete understanding of the normal working environment of the equipment needs to be established. The thermal patterns change due to the presence of anomalies which can be interpreted from the variations in the associated heat flow patterns. Maldague, Jones et al. (2001) define this study of heat flow patterns through infrared images as *Thermography*.

Engineering science poses a range of challenges in a working industry especially in the maintenance of the equipment. There is a constant need to address maintenance issues and thermography, being a non-contact, non-destructive, non-intrusive thermal mapping technique is a perfect tool to analyse the performance characteristics of the machinery and thus aid in assessing its condition during preventive maintenance. The effective use of the technology mainly depends on the understanding of the material under inspection, the working environment and more importantly the technology itself.

In simple words, infrared imagers record the heat radiated by an object and analyse the objects characteristics and condition based on its temperature patterns. This technique is already being used as a diagnostic tool in the field of medicine to study blood flow and to detect the occurrence of tumours and other related problems of the human body (Vollmer and Möllmann 2010). The image thus acquired is referred to as a *Thermogram* (Ring 2000).

Thermography is completely dependent on temperature difference and hence the higher the difference the easier it is to identify defects. The simplest method is passive thermography where an infrared camera is pointed at an object and the temperature pattern is recorded at various time intervals. In the active thermography technique, an energy source provides the necessary temperature gradient and the camera records the cooling characteristics of the object. Thus Thermography is a highly innovative non-contact technology that has made its way through different industries including Medicine, Civil Construction, Energy, Aviation, Materials, Automotive and Transport in order to determine the condition of the object under operating conditions.

1.2.1 Advantages & disadvantages of infrared thermography

Thermography has advantages over other traditional testing techniques such as X-radiography and Ultrasonic testing (UT). In comparison with X-radiography, the biggest advantage of Thermography is the absence of both radiation health hazard and the need for skilled radiographic personnel to operate the equipment. Thermography is a non-contact technology and can inspect large areas whereas with UT contact is necessary. The UT probes are small and hence large area inspections can be time consuming in comparison with Thermography.

As with any technology there are advantages and disadvantages. The following table (Table 1) is the summary of advantages and disadvantages of thermography.

Table 1 Advantages and disadvantages of infrared thermography

Advantages	Disadvantages
Non-Contact	Can be expensive
Portable	Requires good batteries
Safe	Limited working temperature range of the instrument
Wide temperature measurement range	Wide temperature range is only possible with expensive cameras
High thermal sensitivity	Emissivity of the surface can be an issue
High spatial resolution	Surface temperature measurements only
Wide applications in the industry	Software compatibility with different platforms is limited
Immune to electromagnetic noise	Atmospheric influences / attenuations cause significant error in measurements

1.3 The research

The aim of this project was to explore the usage, robustness, adaptability and application of various infrared thermography techniques through various stages of testing to determine the condition of the CFRP laminate. Vibrational analysis, Pulse-echo immersion Ultrasonic testing and X-Radiography were also carried out to support detection using Thermography as no one technology can determine the establishment of a particular type of defect in the NDT world.

Therefore, the objectives of the research are

- To establish the effectiveness of Pulsed thermography technique to detect certain types of sub-surface defects in advanced composite materials.
- To explore Thermoelastic Stress Analysis (TSA) thermography technique as an alternate tool to detect certain defects that are hard to detect using pulsed thermography thereby establishing TSA as an effective NDT technique.

1.4 Methodology

This research was undertaken initially by reviewing the engineering challenges to carry out Non Destructive Testing (NDT) on advanced carbon composites. A literature search helped understanding the characteristics of CFRP composites and existing methodologies to carry out NDT on such materials. The literature search was particularly focused on thermography in order to establish the highly innovative, non-contact thermal technology as a qualitative tool.

Infrared thermography techniques such as online-monitoring, pulsed and TSA methods were used to determine the condition of CFRP laminates. Initially defects such as steel shims, Teflon and bagging film were introduced into the laminates during manufacturing (prepreg lay-up stage, refer to Chapter 3). These defects were of different geometries and were introduced at pre-determined depths to understand and establish the detection capabilities of the pulsed thermography equipment. A theoretical model was also introduced to validate the results obtained through various thermal non-destructive testing methods.

In the second part of the investigation, CFRP laminates of different thicknesses and layups were made from uni-direction (UD) carbon prepreg material using a hot press. The samples were then subjected to ballistic impact and Charpy test for different energy levels. Thermography in the transient mode was used to record the heat generated during impact. The impacted samples were then inspected using pulsed thermography and TSA techniques to determine the damage caused due to impact testing.

The methodological approach consisted of a literature review to identify the gap in knowledge, followed by an experimental and computational study of thermographic inspection techniques for the damaged CFRP laminates. The second chapter of this thesis undertakes a review of composites materials and non-destructive testing techniques with emphasis on pulsed thermography and TSA to detect inclusions and impact damage. Composite panel manufacture methodology, techniques used to carry out inspection, their working principle and the experimental setup are considered in Chapter 3. The results are compiled into three parts in Chapter 4. The first part of Chapter 4 includes initial thermographic inspection results of real-life aircraft parts using pulsed thermography and x-radiography. In the

second part of Chapter 4, a parametric study together with a computational model to establish the detection capabilities of pulsed thermography is presented. The third and final part of Chapter 4 presents the results obtained from pulsed thermography and TSA inspections carried out on impacted samples. Finally a brief discussion of all the results presented in the previous chapter (Chapter 4) is presented together with conclusions and recommendations for future work.

1.5 *Epilogue*

This chapter provided an introduction to the project and established the overall aim and the subsidiary objectives. The methodological approach is described and comprises a critical literature review, experimental investigation and computational model of pulsed thermography. Further, the CFRP laminate was subjected to a low speed Charpy and a high speed gas-gun ballistic impact test to create barely visible impact damage (BVID). These impact damaged laminates were subjected to transient, pulsed thermography and TSA methods. Thus multiple thermography techniques were studied to determine their suitability to detect near surface and sub-surface defects and damage occurring in CFRP laminates. The section will now be followed by a detailed review of basic concepts and associated research that supports this research.

2 LITERATURE REVIEW

This chapter presents the literature associated with the work undertaken as part of this research. In order to validate the hypothesis of this research, it is necessary to present the underlying principles of both materials and techniques that support this work. This literature review was undertaken to identify the gap in knowledge and support the current research. This chapter is divided into five sections where basic concepts ranging from composite materials through to current research techniques adapted for this research are presented. The prime focus of this chapter is mainly on the material and thermographic inspection systems.

2.1 Composite Materials

Extending on the definition presented in Chapter 1, it is noted that composite materials are advanced structural materials which are composed of two or more materials that remain separate, distinct, and insoluble in one another. Further when combined the resulting material exhibits material characteristics of both materials that are bonded together (Matthews and Rawlings 1999; Kaw 2006; Vinson and Sierakowski 2008; Miracle and Donaldson 2011). This definition holds true only when the constituent materials are present in greater proportions exhibiting distinct properties and is different from the composite material itself.

Composite materials act as a homogeneous material exhibiting the physical and chemical properties of all the constituent materials thereby improving the material characteristics such as strength, durability and resistance to corrosion of the material. Due to their performance to weight characteristics, better mechanical properties and their resistance to corrosion, composites are being increasingly used in the automotive and aerospace industry. Advanced materials such as graphite, Kevlar[®], boron, aluminium and magnesium are being increasingly used in aerospace and other commercial industries due to their better performance and increased strength-to-weight ratio in comparison with their monolithic metals. With the increasing use of composite materials and the development of new advanced

composite materials, their mechanical behaviour can be difficult to predict mainly due to their anisotropic material property.

2.1.1 History of Composite Materials

Literature suggests (Kaw 2006; Vinson and Sierakowski 2008) that the earliest form of composite materials were bricks made up of clay and straw reinforcement. Ancient Israeli people found that the used of straw together with clay improved the strength of the brick thereby preventing the development of cracks in the brick. History records show that there are many examples including bamboo reinforced mud walls, bonded laminated wood by Egyptians (1500 B.C.), forging swords using laminated metals by Japanese samurai warriors (1800 A.D.), proving the existence of composite materials for hundreds of years (Kaw 2006).

The modern 20th century developments in the field of composite materials started with the introduction of fibreglass and concrete around the 1930's. The world of civil engineering has been completely transformed with the introduction of steel bars in concrete marking the start of a new era in the construction industry. Research in the development of fibreglass has led to the development of a whole new range of composite materials with the introduction of fibres made up of carbon, boron and aramids (compounds made up of carbon, hydrogen, oxygen & nitrogen) (Kaw 2006).

The 21st century has seen the development and utilization of advanced composite matrix systems made up of fibres, metals and ceramics in a specialised system for specific applications. Thus composites have found their way into everyday life of ordinary man in the 21st century. Wood is by far the best example for naturally occurring composite. It is made up of fibres of cellulose in a matrix of lignin (Kaw 2006). Concrete is a perfect example for artificial composite and is the largest man-made structure.

2.1.2 Why Composites?

With the present day advancement in the field of science and technology, traditional materials such as steel, aluminium and magnesium are not preferred. Specific applications such as trusses used in space crafts and satellites need material that can operate at extreme temperatures of the order of -160°C to 100°C . The solution is typically in the form of composite materials such as epoxy graphite composites. These days, composites are preferred in the transport industry due to their improved strength and performance characteristics. Currently there is ever growing pressure on the aircraft manufacturers to look for alternative technologies to reduce the overall mass of the aircraft without compromising the stiffness and strength of its parts. The notion is that, reduction in weight contributes to a reduced fuel consumption leading to overall reduction in emissions into the atmosphere. This has led to the development of the current day advanced composite materials.

2.1.3 Definitions & Classifications

From the previous sub-sections in this chapter, it has been established that a composite is a material obtained as a result of the mixture of two or more materials having distinct constituents exhibiting different mechanical / chemical / structural properties and are present in proportions greater than 5%. The constituent that is present in a larger proportion appears to be present continuously in the microscopic level but not always present. Thus this constituent exhibits the desirable property which is enhanced by the addition of other constituents to form the composite material. Matthews and Rawlings (1999) define this primary constituent as the '*matrix*' and the secondary constituent as the '*reinforcing phase or reinforcement*'. Thus in a composite material, the matrix could be '*metallic, polymeric or ceramic*' and the reinforcement could be '*fibrous or particulate*' (Matthews and Rawlings 1999; Baker, Dutton et al. 2004; Kessler 2004; Kaw 2006; CMH-17 2012).

In this research, polymer matrix composites (PMCs) with continuous fibres were used for research and are of prime focus in this review. A positive and preferential attribute of the fibrous reinforcements is its variable aspect ratio which is derived from the ratio of the length of the fibre to its cross-sectional dimension. As a

preferred material, the fibre composite is termed as ‘*unidirectional*’ when all fibres run along the ply in one direction and the corresponding two directional random weave fibre composite is referred to as ‘*bidirectional woven*’ composite (Matthews and Rawlings 1999; Campbell 2004; Kessler 2004; CMH-17 2012; Hexcel 2013). Currently multi-layered polymer fibre matrix composites (PMC) are used at large due to the flexibility of stacking these layers of composite materials in a specified sequence. These multi-layered PMC’s are referred to as ‘*laminates*’ and the layers as ‘*plies or laminae*’ (Chawla 2001; Baker, Dutton et al. 2004; Kessler 2004; Morgan 2005; Kaw 2006; CMH-17 2012).

For the design of fibre composite material, it is important to understand the fibre characteristics such as elastic modulus, strength and density so that the fibres could be arranged in a sequence to produce the desirable material properties. The following is a flow chart explaining the different types of fibres which form the reinforcements in the composite material.

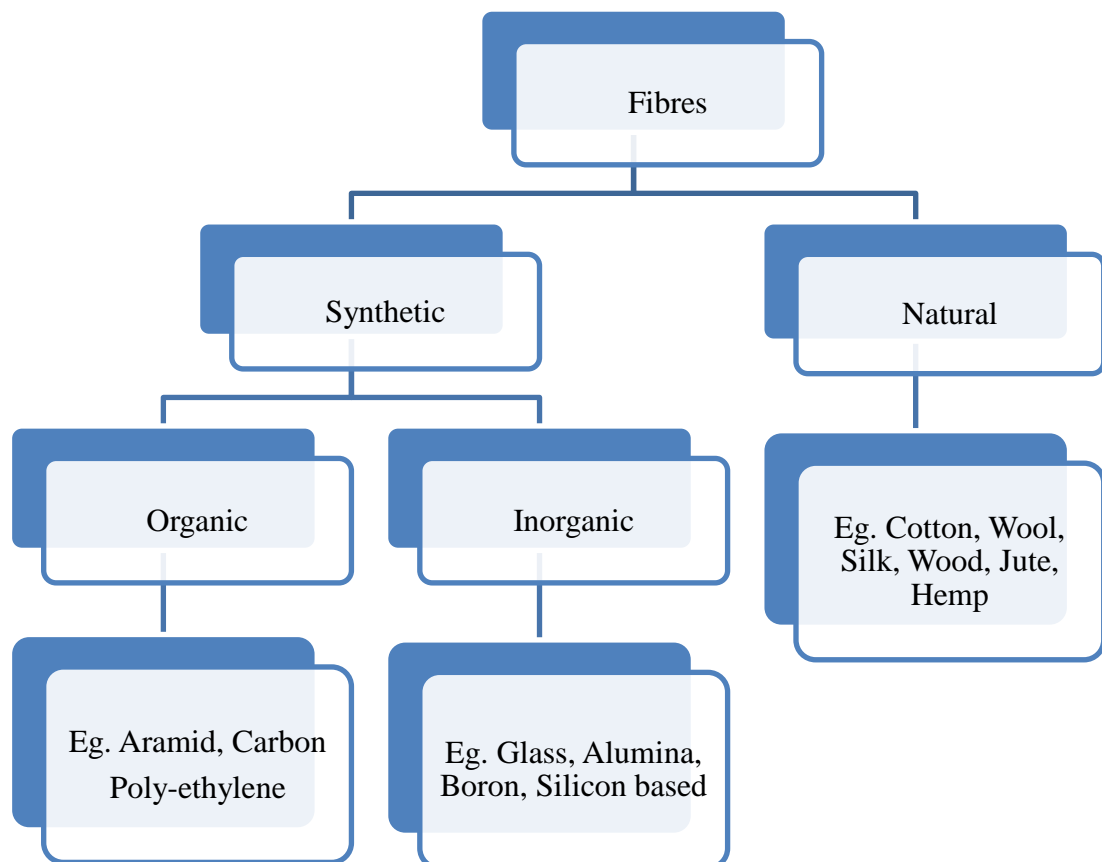


Figure 1 Classification of Fibres (Matthews and Rawlings 1999, Chawla 2001)

2.1.4 Matrix & Reinforcement

It has been established that the way the composites are designed and manufactured plays an important role in determining the engineering properties of the material. From literature it is understood that introduction of layered reinforcements either in the form of fibres or particulates produces strong materials with refined engineering properties. The following is a table comparing the mechanical properties of fibres and their monoliths.

Table 2 Mechanical properties of fibres and their monolithic counterparts
(Matthews and Rawlings 1999; CMH-17 2012)

Reinforcement	Young's modulus (GPa)	Tensile/Flexural Strength (MPa)
Alumina: fibre (Saffil RF)	300	2000
monolithic	382	332
Carbon: fibre (IM)	290	3100
monolithic	10	20
Glass: fibre (E)	76	1700
monolithic	76	100
Polyethylene: fibre (S1000)	172	2964
Monolithic (HD)	0.4	26
Silicon carbide: fibre (MF)	406	3920
monolithic	410	500

It can be inferred from the table (Table 1) that the fibres exhibit better strength in comparison with their monolithic counterparts. The major problem is their brittleness and susceptibility to surface damage. These materials can sustain high stress rates and when they fail, they are catastrophic. Research suggests that these failures are usually initiated from the initial damage and grow rapidly under certain loading conditions thereby suggesting that the failures are dependent on not just the type of damage, but their geometry, location and working environment as well.

When considering the design of the laminate, there are factors such as flexibility, weight fraction (w) and density (ρ) to be considered apart from the strength of the component. With fibre composites, flexibility is an important attribute and is dependent on the Young's modulus (E_f) and diameter (D) of the fibre. (Barbero 1998; Baker, Dutton et al. 2004)

Thus flexibility of the composite may be expressed as equation (1),

$$flexibility \propto \frac{1}{E_f D^4} \quad (1)$$

As a general guideline, the weight fractions can be estimated using equations (2) – (7)

$$W_f = \frac{W_f}{W_c} = \frac{\rho_f V_f}{\rho_c V_c} = \frac{\rho_f}{\rho_c} v_f \quad (2)$$

Where

$$v_f = \frac{V_f}{V_c} \quad (3)$$

And

$$W = \rho V \quad (4)$$

where W – Weight, V – Volume, ρ – Density, w – Weight fraction, v – Volume fraction and subscripts f and c represent fibre reinforcement and composite respectively.

$$W_m = \frac{W_m}{W_c} = \frac{\rho_m V_m}{\rho_c V_c} = \frac{\rho_m}{\rho_c} v_m \quad (5)$$

where

$$v_m = \frac{V_m}{V_c} \quad (6)$$

and subscript m represents the matrix.

Equation 6 can be further generalised into a single equation that determines the required composite property – X_c .

$$X_c = X_m v_m + X_f v_f \quad (7)$$

Thus it should be noted that most properties of the composite which need to be determined are complex in nature and work in synergy with its constituents and does not fully balance the above equation of the law of mixtures. It is important to have good bond strength for the composite to bear and transfer the load from the matrix to the fibres. The greater the interspatial bond strength; the better the load bearing capacity of the composite laminate. However, it should be noted that this greater bond strength does not always yield a strong component and will tend to develop failures such as debonding, fibre pull-out and or delamination.

2.1.5 Benefits of Composites

With their excellent engineering performance characteristics, composites have established themselves fully and are now a common sight in this modern world. The following is a table illustrating the applications of composites in the modern world (Table 3).

Table 3 Some applications of Polymer Matrix Composites
(Matthews and Rawlings 1999; Baker, Dutton et al. 2004)

Industrial Sector	Examples
Aerospace	Engine Nacelles, rudders, ailerons, wings, full fuselage and wing assemblies, antennae, tail-planes, helicopter blades, landing gears, front and rear landing gear doors, turbine blades, seats, floors, floor beams, interior panels, fuel tanks, rocket motor cases, nose cones, launch tubes.
Automobile	Body panels, cabs, spoilers, consoles, instrument panels, lamp-housings, bumpers, leaf springs, drive shafts, gears, bearings.
Boats	Hulls, decks, masts, engine shrouds, interior panels.
Chemical	Pipes, tanks, pressure vessels, hoppers, valves, pumps, impellers.
Domestic	Interior and exterior panels, chairs, tables, baths, shower units, ladders.
Electrical	Panels, housings, switchgear, insulators, connectors.
Leisure	Motor homes, caravans, trailers, golf clubs, racquets, protective helmets, skis, archery bows, surfboards, fishing rods, canoes, pools, diving boards, playground equipment.

The main reason for the success of composites is due to their low density which can be appreciated when Young's modulus (E/ρ) and tensile strength (σ_T/ρ) (both per unit mass) are considered (Barbero 1998; Baker, Dutton et al. 2004; Kessler 2004; Morgan 2005; Kaw 2006; CMH-17 2012). Thus higher Young's modulus and tensile strength would lead to the reduction in the weight of the

component without affecting the mechanical properties of the laminate. This reduction in weight is an important factor especially in industries where moving components are in use. Improved efficiency through reductions in energy and operating costs is found to be the norm.

Other reasons which have led to the continued and increased use of PMCs in various industries are

- The manufacture process (viz., thermosetting, thermoplastic)
- The ability to design a component with required engineering properties
- The choice of polymers, fibres and their lay-up sequence
- The ability to make complex geometry parts
- Durability & wear resistance
- Damping characteristics
- The non-interference of electrostatic noise & low electrical-conductivity
- Incredible corrosion performance due to chemically inert matrix components

The following is a chart illustrating the various materials currently in use based on their Young's modulus and density.

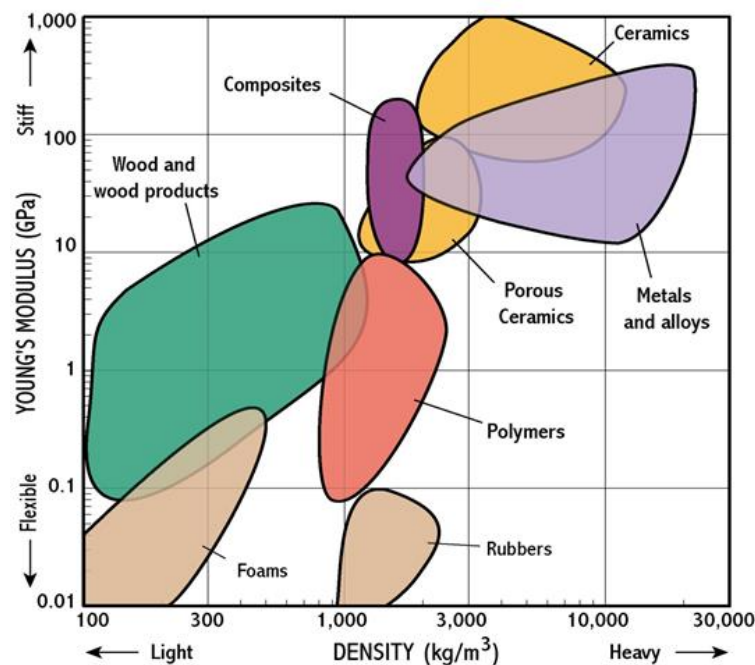


Figure 2 Material Selection Chart classifying various material systems based on Young's modulus and density. Source: Cambridge University (University)

2.2 Defects occurring in Composite Materials

A defect can be defined as a flaw or imperfection found in a homogenous and/or heterogeneous material with known constituents. An imperfection can be classified as a defect when the flaw affects the engineering performance of the material leading to failure of the component. As with any component, a majority of the defects occur in-service over a period of time while the others might have occurred during manufacturing process. In order to estimate the fitness level of the structure it is necessary to inspect the material first and then have an understanding of the defects. With composites, this is a huge challenge as the laminate tends to be non-homogenous and anisotropic in nature.

Typical defects found in composites are:

Delaminations, disbonds, impact damage, voids, porosity, barely visible impact damage (BVID), inclusions, fibre breakage, cracks, matrix cracking, core crushing, kissing bonds, ingress of moisture, fibre and ply misalignment, fibre waviness, erosion, incorrect cure, core splices, improper fibre splicing and incorrect stacking sequence (Adams and Cawley 1988; Baker, Dutton et al. 2004; Composites 2013; Kapadia 2013).

Defects occurring in composites are also classified under the following types

- Fibres
- Matrix
- Manufacture
- In-Service

2.2.1 Fibres

The most common type of fibre defects occur when the fibres are broken and or bundled up creating resin-rich or resin-starved areas in the finished composite laminate. This could result in wavy fibres which might result in the reduction of tensile and compressive strengths of the laminate being made. Thus defective fibres introduce stress concentration spots in the finished laminate (Adams and Cawley 1988; Kaw 2006; Composites 2013; Kapadia 2013).

2.2.2 Matrix

Storage and contamination are the two main reasons which cause problems to the PMCs. The issue with thermosetting materials is that prior to their manufacture they need to be stored at manufacturer specified temperature and humidity conditions as excess humidity will degrade the mechanical properties leading to the development of porosity. Storage at a higher temperature means that the resin will start curing and will become difficult to use for production which will lead to severe deterioration of mechanical properties of the finished laminate. In both cases, porosity develops during curing and might accumulate to form a void which becomes the internal stress concentration spot.

Contamination on the other hand will lead to a weak fibre-matrix adhesion affecting compression, tension, inter-laminar shear and fatigue performance of the material (Baker, Dutton et al. 2004; CMH-17 2012; Composites 2013; Kapadia 2013).

2.2.3 Manufacture

Fibre misalignment in the same layer or between layers, ply misalignment or missing plies, incorrect stacking sequence and ply-end discontinuities are the most common defects possible during laying up the composite before curing. Now these defects develop resin-rich or resin-starved areas deteriorating the strength of the material. Foreign body inclusions such as bagging film, dirt and debris also develop as stress concentration centres in the finished laminate. Care is also necessary to cure the sample at a particular temperature, pressure and time as mentioned by the manufacturer. A bad cure could be because of an over cured and/or under-cured material which develops cracks and or delaminations and disbonds (Composites 2013; Kapadia 2013).

2.2.4 In-Service

Forces such as impact, cyclic and or static degrade the engineering performance of these laminates. Exposure to high temperatures, humidity levels and chemicals also

affect the performance of the materials. The immediate damage formed is referred to as a barely visible impact damage (BVID) leading to matrix cracking, delamination, debonding and fibre breakage (Kapadia 2013). These defects affect the material properties in different ways. Cracks occurring in the fibre and the matrix can allow water to seep in; delamination reduces the compression strength leading to fibre buckling and breakage leading to failure of the component (Adams and Cawley 1988; Composites 2013; Kapadia 2013).

The following is a table (Table 4) describing the in-service phenomena and the damage caused due to those phenomena (Adapted from Net Composites Webpage (Composites)).

Table 4 Defects developing from in-service phenomenon

In-Service Phenomena	Damage Produced
Vibration / fatigue / creep	Fibre fracture
Impact / shock / high rate loading	Fibre disbond, delamination
Lightning strike	Matrix cracking
Environmental conditions (heat, humidity), loading history	Dents, scratches, punctures, crush damage, abrasions
Chemical / bacterial degradation	Delamination / disbond
Galvanic corrosion	Sandwich core crushing
Poor maintenance (tool drop) and repair	Sandwich skin delamination

2.2.5 Impact Damage

This research is partly focused on detecting surface and sub-surface defects occurring due to impact. With the increased use of PMCs, there is an urgent need to understand their behaviour in structural components especially in the Aerospace industry. As said previously, it is necessary to understand the performance of these advanced materials at extreme conditions, and with this comes the task of estimating damage without causing further damage to the structural component.

Impact damage in aircraft is a serious issue, whether it be caused by ground vehicles/service equipment or hail / bird strike which could cause significant structural damage, it is highly important that these defects be characterised before

they become catastrophic. This research primarily focuses on low speed impact and high speed impact and methods to detect damage.

Significant damage could be caused at high velocity. Debris being lifted up by aero-engines during take-off is a perfect example for high velocity impact especially with the fuselage and engine skins primarily made of composite materials (Matthews and Rawlings 1999; Baker, Dutton et al. 2004; Duell 2004; Kim, DeFrancisci et al. 2009). Sub-surface damage could also be developed over a period of time due to blunt impacts caused by ground vehicles / service equipment. This damage occurs on the aircraft skin panels when the impact from luggage belt loaders, walkway bumpers and or aero-bridges (Figure 3) exceed the failure threshold energy which then develops into a significant damage (Kim and Kedward 2000; Kim, Kedward et al. 2003; Kim, DeFrancisci et al. 2009). The current work is an effort to replicate these high and low velocity impact damage to replicate real-life scenarios. This is achieved with the help of ballistic and Charpy testing as suggested in the literature the details of which can be found in Chapter 3 (Duell 2004).



Ground Service Equipment Bumpers & Walkways

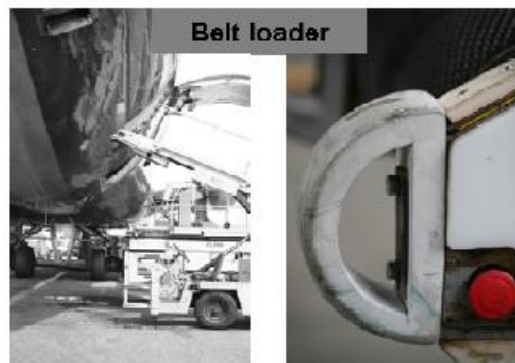


Figure 3 Ground Equipment, Luggage Carts and Cargo Containers (Kim, DeFrancisci et al. 2009)

2.3 NDT of Composites

In the real-world, it is an accepted fact that all materials in the field of engineering are susceptible to have flaws in them. The previous section in this chapter established that these flaws/defects are either introduced during manufacturing process or 'in-service'. The challenge is to develop suitable techniques to inspect and determine these defects without destroying or damaging the material. A flaw is characterised as a significant defect when the defect leads to the failure of the component. A lot of factors such as defect size, geometry, location, component operating environment and or loading conditions characterise a defect. Hence it is of utmost importance to identify innovative inspection routines that detect these defects before they become sizeable and lead to catastrophic failure of the system. NDT is currently being used to determine the defects on these advanced PMCs as these techniques do not affect the serviceability of the material.

Traditionally NDT was developed to inspect metallic components. With the increased use of PMCs, some of these traditional NDT methods are used on composites as well. The main inspections that dominate the NDT world are

- Visual Inspection
- Dye Penetrant Inspection
- Magnetic Particle Inspection
- Ultrasonic Testing
- X-Radiography
- Vibration Methods
- Eddy Current Testing

As these methods were developed primarily for metallic components, it is quite hard to fit these methods to detect defects in PMCs. Of these methods, dye penetrants are not desired as it is difficult to remove the penetrant. As PMCs are non-conducting in nature, magnetic particle inspection and eddy current testing have limited use especially in cases where the fibres are conducting in nature. Thus the most frequently used traditional NDT methods are Ultrasonic Testing and X-Radiography (Matthews and Rawlings 1999). Apart from traditional methods, Thermal testing (Thermography) is gaining importance as it is non-contact and non-

radioactive and can be fairly easy to use. In this section, the primary focus is on traditional NDT techniques currently in use to determine defects in PMCs. Thermography will be discussed in separate section (Section 2.4) as it is the prime focus of the thesis.

2.3.1 Ultrasonic Testing

Ultrasonic testing (UT) is an inspection technique in which sound / stress waves are used to assess the condition of the material. The wavelength (λ) of the stress wave / mechanical wave / vibration is the ratio of the velocity of the sound (c) wave travelling through the material to the frequency (f) of the stress wave / ultrasound.

Thus

$$\lambda = \frac{c}{f} \quad (8)$$

The frequency range in terms of traditional homogenous materials is between 20 kHz and 20 MHz. With PMCs the frequency of testing range drops down significantly due to signal attenuation and hence the testing frequency is limited to around 5MHz (Kapadia 2013). It is for this reason that the ability to detect defects of small sizes is difficult.

Ultrasound propagates in different modes in solids (Matthews and Rawlings 1999; Kaw 2006; Kapadia 2013).The following are the most important modes

- *compressional / longitudinal* waves – particle vibration is along the direction of propagation
- *shear / transverse* waves – the particles vibrate at right angles to the wave direction
- *surface* waves – the particle vibration is restricted to a certain depth from the surface of the object under inspection.

The working principle is simple; when the ultrasound travels through the material, the wave gets modified due to the change in material characteristics in the presence of defects and or boundaries of the surrounding area of the component. As the ultrasound wave hits the boundary of the defect part of the wave is reflected and

the remaining is transmitted through the defect boundary. The amount of reflected wave is dependent on the angle of incidence and acoustic impedance (Z) which is represented as

$$Z = \rho c \quad (9)$$

where ρ – density of the material, c – velocity of the wave.

During testing, the ultrasound is introduced into the component to be inspected and the transmitted and received/reflected signals are monitored. The ultrasound is transmitted using a probe which is usually made of piezoelectric transducers. The function of this piezoelectric material is to generate vibrations using an electrical pulse during transmission and to convert the vibrations back to electrical impulses on receiving the reflected sound waves

In case of composites, the common techniques used to detect flaws are manual ultrasonic testing, pulse-echo, through-transmission, ultrasonic spectroscopy and acoustography.

Manual Ultrasonic Testing:

A probe is manually moved by the operator on the surface of the component which is coated with a coupling fluid. The coupling fluid acts as a layer which prevents attenuation of the ultrasound signal. It should be noted that the amplitude of the signal transmitted and received by the probe is affected by the pressure applied by the operator causing inconsistency in the results obtained. Thus manual testing requires qualified inspection personnel and with the help of a set of operating procedures and recognised calibration, it should not pose a problem. The main advantage in this method of testing is that it is suitable for fieldwork as the kit is small and portable bearing in mind that only small area can be inspected. It should be noted that clearing the coupling fluid layer is difficult and hence advanced techniques are used to inspect the composite material.

Pulse-Echo Ultrasonic Testing (PEUT):

With the establishment of pulse-echo immersion ultrasonic testing (PEUT) as an NDT technique, PMC materials are being inspected by this method increasingly. In this method both the part and the transducer are immersed in water. The transducer is

positioned above the component to be inspected and an ultrasound pulse is applied to the sample. The direction of the ultrasound in this case is normal to the surface of the component.

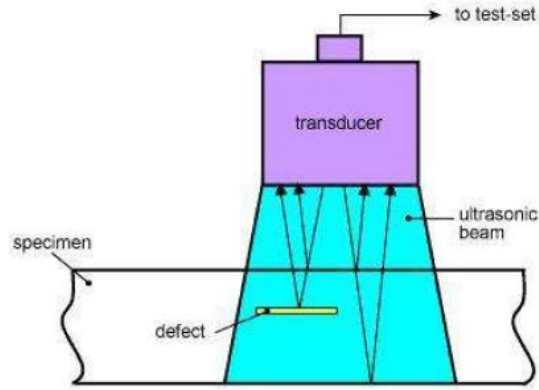


Figure 4 Set-up of Ultrasonic Testing (Kapadia 2013)

It can be seen from the above figure (Figure 4) that the ultrasound travels through the material until it hits the boundary and reflects back. Now it can be seen that the reflection could be from the back-wall of the component and also from the boundary of the defect whichever occurs first along the path of the ultrasound. Based on the time taken for the reflected wave to the probe, the defect is identified and then measured. The test takes into account the delay due to travel of ultrasound in water and the distanced travelled in water is referred to as *waterpath*.

As with any testing, it is important to present the result in an understandable format. The results from most ultrasonic methods are presented in the following scans

- A – Scan: represents echoes of different features along the path of the ultrasound at a point. (See Figure 5 which shows main ultrasound impulse (a), surface of the component (b), defect (c), and back-wall of the component (d))
- B – Scan: the A-Scan obtained at each point is combined together to form a 2D ‘slice’ section through the inspected component. (See Figure 6)
- C – Scan: can be interpreted as a ‘Plan’ view of the component. (See Figure 6)

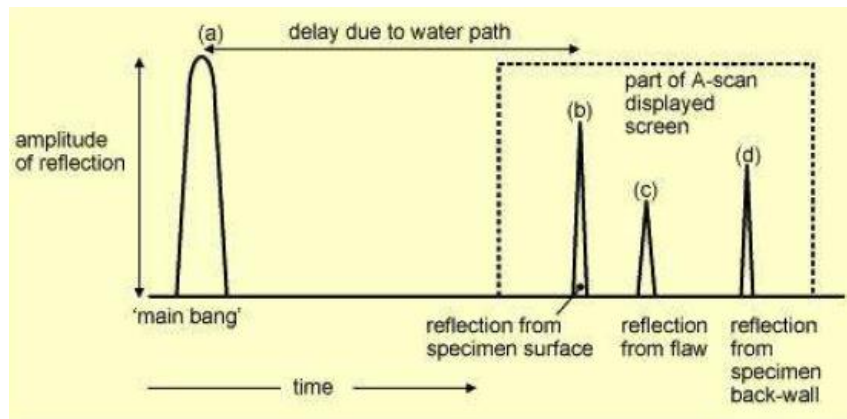


Figure 5 A-Scan from a typical Pulse-Echo UT test of CFRP Panel (Matthews and Rawlings 1999; Kapadia 2013)

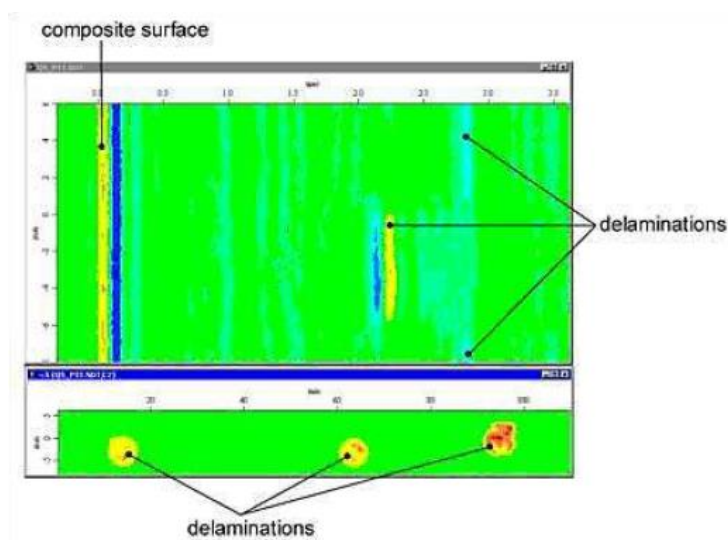


Figure 6 B-Scan (above) & C Scan results representing defects present in CFRP Panel (Kapadia 2013)

The main advantage of pulse-echo testing is the ability to detect sub-surface damage such as delamination, voids, porosity, foreign body inclusion and ingress of moisture. As long as the defects are present along the ultrasound path and are not deflected due to attenuation and or fibre orientation, good results can be obtained by this method. It should be noted that detection is only possible in samples the thickness of which is well known as the detection is dependent on the pulse length of the ultrasound and hence near surface defects could be easily missed (Adams and Cawley 1988; Matthews and Rawlings 1999; Morgan 2005; Kapadia 2013).

When inspecting composites, it is quite possible that defects such as cracks could be missed due to the stacking sequence of the composite. A variation to the pulse-echo can be achieved where the scanning probe instead of being normal to the surface is now inclined in this inspection type. Scanning is done by keeping the

probe in the calculated inclined angle (α) and either the component or the transducer is rotated along the axis β normal to the surface of the part being inspected (See Figure 7 below). This technique is referred to as *Back-Scatter* technique (Matthews and Rawlings 1999; Kapadia 2013).

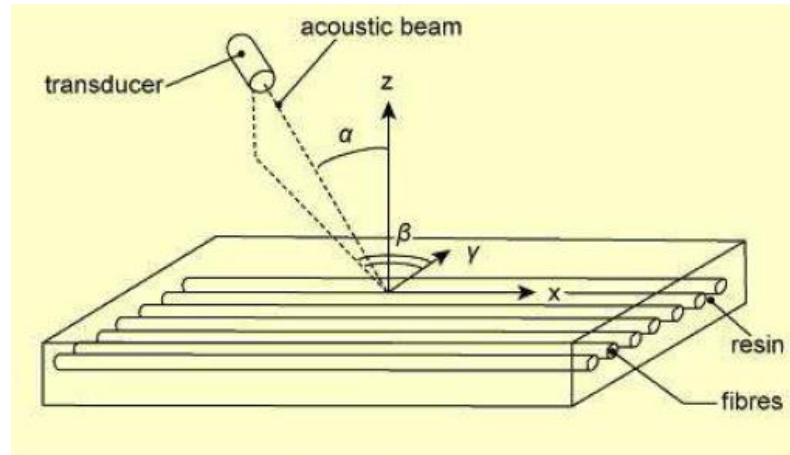


Figure 7 Set up of Back-scatter technique using Pulse-Echo (Kapadia 2013)

The back-scatter techniques can be used to inspect for defects such as porosity, fibre waviness and laminar cracks. This technique also helps to check the stacking sequence of the component.

Through Transmission Ultrasonic Testing:

As the name suggests, two probes are used on opposite surfaces of the component where one probe transmits the ultrasound and the other receives the signal. This technique uses a water jet system where the water jet forms the coupling fluid for transmitting and receiving the ultrasound.

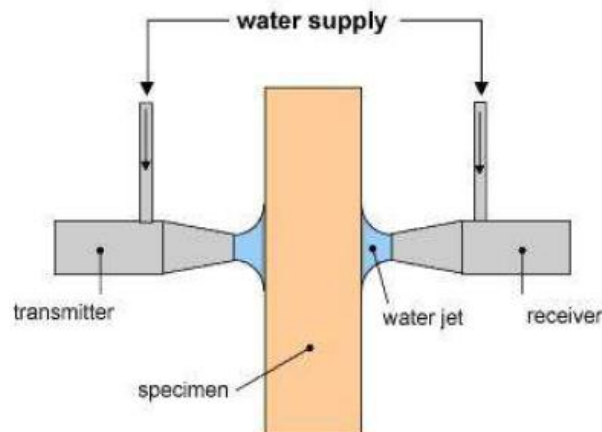


Figure 8 Through-transmission testing using a water jet system (Kapadia 2013)

Typically, C-Scan results obtained from through-transmission technique are used to detect flaws including delamination, inclusions, fibre volume fraction and cracks (as long as they are along the path of the ultrasound). The biggest disadvantage with this technique is that it does not provide information on the defect depth. Care should be taken when aligning the probes as both surfaces of the component need access.

Ultrasonic Spectroscopy:

This technique can be better understood based on the through-transmission technique. In this case the probes are in direct contact and frequency of the transmitted wave is compared with the received wave. Whenever a defect is present along the path of the ultrasound, the frequency of the transmitted wave is altered especially in the harmonic mode which is dependent on the change in vibrations of the fibre-matrix.

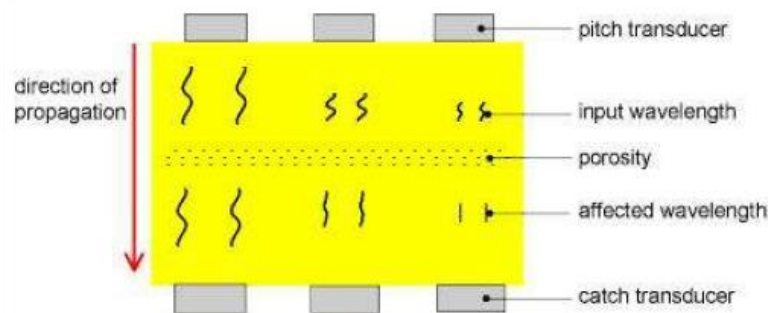


Figure 9 Ultrasonic Spectroscopy set up showing wavelength difference due to presence of defects (Kapadia 2013)

This technique helps detecting defects when the pulse length is smaller than the thickness of the specimen. Based on a calibration scale, each independent frequency can be isolated and compared to determine the change in amplitude due to the presence of a defect. However, for thin samples, the pulse length is bigger causing interference which needs to be assessed carefully. This technique is helpful in detecting delaminations, under cured matrix and porosity. However it should be noted that the results could only be interpreted from a large database of similar inspections as the received signal is easily attenuated due to the structure of the composite (Adams and Cawley 1988; Matthews and Rawlings 1999; Kapadia 2013).

Acoustography:

Acoustography is a recent development in the field of NDT which combines acoustic emission technique together with ultrasound with the help of an acousto-optic (AO) sensor. Thus ultrasound is generated by the probe and is allowed to transmit through the sensor using a system of lenses after the component is tested. In other words, the ultrasound is passed through the material first and then the resulting wave is detected and measured by the sensor system for the acoustic emission system. The acoustic emission system works on the principle that when a stress wave passes through a defective material, the amplitude and frequency of the wave changes in the presence of the defect. With high frequencies, it is possible that the stress wave cannot be heard and hence a suitable amplification system is needed to identify the defects. It should be noted that this acousto-ultrasonic technique only provides information of the condition of the tested component to a mere average and the location of the defect is only possible with simultaneous movement of the probe and the sensor (Adams and Cawley 1988; Matthews and Rawlings 1999; Morgan 2005; Kapadia 2013).

Typical defects detected by acoustography include voids, delaminations, cracks, impact damage and inclusion. The advantage of this technique over ultrasonic testing is the speed of inspection. However, the image obtained by UT has a better resolution when compared to acoustography where the image is slightly grainy (Kapadia 2013).

2.3.2 X-Radiography

X-Radiography is the measurement of the absorbed and unabsorbed electromagnetic radiation which is obtained when a beam of X-rays are bombarded on to a test sample. The measurement is usually in the form of film which is placed behind the part. The radiation after passing through the part to be inspected is exposed to the film which is then developed to obtain a shadow image.

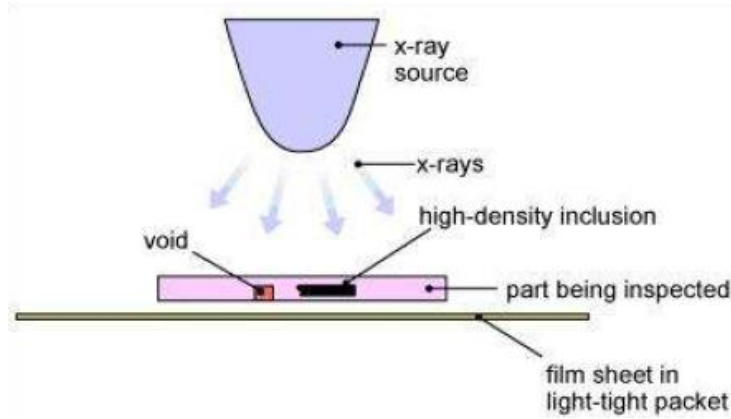


Figure 10 Set up of X-Radiography system (Kapadia 2013)

The radiation intensity (I) is dependent on the incident radiation (I_o), thickness (x), density (ρ) and coefficient of linear absorption (μ) of the material to be inspected as per the following relationship, (Matthews and Rawlings 1999)

$$I = I_o \exp(-\mu x) \quad (10)$$

In practice, as X-rays pass through the test sample the radiation becomes attenuated in presence of defect along the path of the x-rays. The evaluation of the results is by comparing a sound defect free sample with that of a sample with defect. The limitation of this traditional method is that it produces a 2D image and does not provide details of the depth of the defect. Again it should be noted that only defects with volume and occurring perpendicular to the x-ray beam are detectable.

An alternate method is the micro-focus system where the x-rays are emitted close to the focal spot of about $100\mu\text{m}$ or less which produces sharp images thus detecting small defects (Matthews and Rawlings 1999). Radio-opaque penetrants are used to enhance the contrast of the x-ray image when conventional radiography does not produce a useful result.

One of the recent developments in the field of radiography is computed tomography (CT) where multiple images are taken by rotating the test sample around an axis at calculated angles and reconstructed to form a 3D image. This 3D image could be assessed from the information provided in any image plane thereby characterising the defects in the test sample (Adams and Cawley 1988; Matthews and Rawlings 1999; Kapadia 2013).

Radiography though used to detect defects such as delaminations, cracks and fibre alignment, cannot detect delaminations caused due to impact and can only do so in the presence of a penetrant. The major drawback is the hazardous nature of the ionising radiation on the health of the personnel. Proper personal protective gear is needed to shield the technician from harmful radiations as specified by the 'national regulatory body on radiation protection'. Further, the chemical penetrants used to enhance the image contrast are hazardous and have to be adhered to COSHH (Control of Substances Hazardous to Health) (Matthews and Rawlings 1999; Kapadia 2013).

2.3.3 Vibrational Methods

Vibrational methods have found use in PMCs as alternate testing methods as it does not need any coupling fluid and or is not classified as a radiation hazard. Typically low frequency methods of vibration are used to excite structures. Now these vibration methods could be

- Global – involves measuring natural, damping frequencies monitoring the condition of the structural integrity of the entire test sample from a single point.
- Local – involves exciting the component and measuring the vibrational response of the test sample around the region of excitation.

Global Methods:

The properties of natural / damping frequencies entirely depend on the material properties including structure, size and shape. When a test sample is vibrated using an actuator, the sample resonates at specific frequencies which are natural to the sample. These frequencies are termed as modal frequencies. On comparison of these resultant frequencies, samples with defects can be easily distinguished. Thus from a single point excitation, the condition of the entire sample can be determined. A simple example is the 'railway wheel-tap test' (Matthews and Rawlings 1999; Morgan 2005). These modal frequencies can be effectively measured with analysers using a time based Fast Fourier Transform (FFT). The main limitation with such

testing method is that the influence of the defect is spread across the entire test sample making the test less sensitive in detecting the exact location of the defects.

Local Methods:

The simplest version of local test method is a traditional tap test where a coin or a hammer is used to strike the test sample at a predetermined point and the sound resonating from the sample is monitored. The difference in sound indicates the difference in local stiffness of the test sample indicating the presence of flaws.

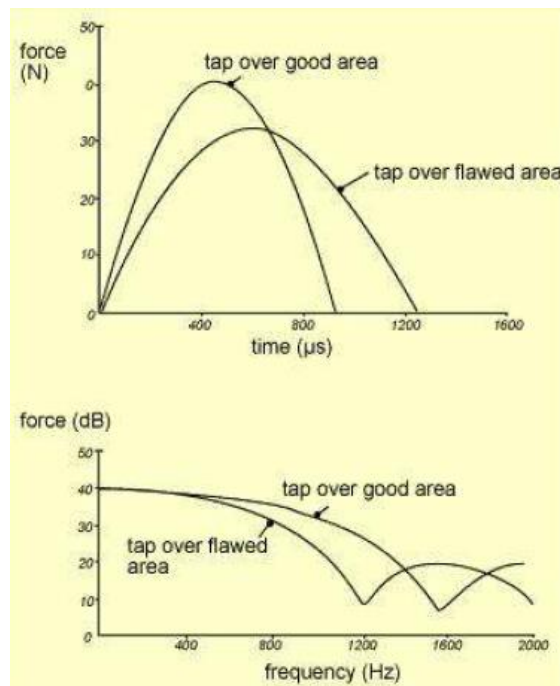


Figure 11 Force-time and force-frequency records illustrating the difference between sound and defective areas of adhesively bonded structure (Matthews and Rawlings 1999; Kapadia 2013)

The local method can be grouped into the following groups based on the type of excitation.

Mechanical Impedance Method:

A continuous harmonic tap test is a good example for the mechanical impedance method. A piezoelectric actuator with a contact tip slightly resting on the test sample is excited at a pre-determined frequency by supplying a sinusoidal voltage to the actuator. Changes in the amplitude and phase of the vibration indicate the presence

of a defect. Again, as in previous methods, a set of results indicating sound material are needed to identify defective samples (Matthews and Rawlings 1999; Kapadia 2013).

Membrane Resonance Method:

This method is similar to the mechanical impedance method. However, this is a non-contact method and monitors local vibrations in the test sample. The layers of delamination collectively constitute the membrane which is constrained along the edge of the delamination. Thus when stress wave is applied on to the sample surface using a probe, the resonant frequencies differ thereby differentiating the response between the sound and the delaminated regions of the test sample (Matthews and Rawlings 1999; Kapadia 2013).

In all these low frequency vibration methods, the sensitivity of these tests is low especially for deeply buried defects. On the contrary, for the defects occurring in thin samples, the local stiffness values vary making this test method unreliable. This is mainly due to the fact that with the reduction in laminate thickness increases its flexibility. Thus the difference in contact pressure and boundary conditions of the test sample will increase measurement errors.

2.4 Infrared Thermography

Infrared thermography deals with studying the temperature gradient and making appropriate measurements of the flow of heat thereby assessing the condition and working performance of the equipment and the structural integrity of the material under inspection. It has been noticed that anomalies and or defects present in the equipment alters the thermal pattern of the equipment. In order to identify these anomalies, a complete understanding of the normal working environment of the equipment needs to be established. The thermal patterns change due to the presence of anomalies which can be interpreted from the difference in the associated heat flow patterns. Maldague, Jones et al. (2001) define this study of heat flow patterns through infrared images as *Thermography*.

2.4.1 Science of Imaging

Blount (1707) interprets Image as “an artificial resemblance either in Painting or Sculpture”. From Blount’s interpretation, we can define an image as a two dimensional (photograph) or a three dimensional (model / object / prototype) visual representation of an object. An image reproduces a person or an object in the form of a photograph or a virtual / graphical / actual model (rendered by computer softwares’). These images help in assessing the nature and characteristics of the object and form a reference for future work modifications. Recent advancements in science and technology have paved way to the development of a whole new area of imaging coining the term ‘Imaging Science’. Imaging science is a technologically advanced discipline concerned with generating, collecting, duplicating, analysing, modifying, evaluating and visualising various characteristics of the image (Hornak 2002). This branch of science attracts research and researchers across various fields including Science, Mathematics, Engineering, Computer Science and Psychology.

The discipline of imaging science includes various factors which depends upon

- The human visual system
- The image details
- The capturing device
- The processing of the image
- The image – reproduction and display

As the factors suggest, the person responsible for producing the image should be experienced in order to provide an image of high quality. The visual system, the objects needed in the image alongside the subject under study (could be emitted / reflected energy of various forms), the capability of the image capturing device (including technologies relating to optics, electronic detectors and sensors), the format of the image (film / electronic data), and finally the reproduction of the object in a suitable format (physical / digital image) is what forms the process cycle of imaging. 3d imaging, animations, optics, astronomical imaging, digital imaging – conversion – restoration, photography (analogue and digital), holography, infrared imaging and ultrasonic imaging are some of the various subfields of imaging science which are constantly in development for acquiring high quality images.

2.4.2 Infrared Radiation

Infrared radiation is a part of the electromagnetic spectrum with wavelengths between 0.7 micrometre (μm) and 1 millimetre (mm). In general, the electromagnetic spectrum is defined as the range of all possible frequencies of electromagnetic radiation. Visible spectrum (*Latin* for “appearance” or “apparition”) with wavelengths between 390 and 750 nanometres (nm) is also a part of the electromagnetic spectrum.

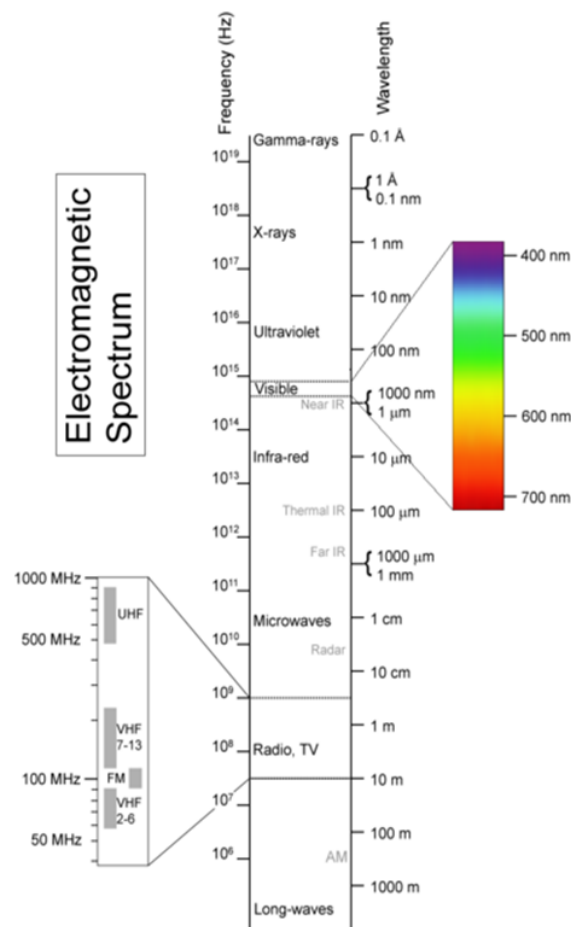


Figure 12 The Electromagnetic Spectrum (Pratt 2013)

Figure 12 illustrates various frequencies of the electromagnetic spectrum. Though the image shows an accurate classification scheme, it should be noted that in reality the electromagnetic energy zones of the spectrum overlap neighbouring zones. It can be seen that the Infrared zone starts at 700 nm ($0.7 \mu\text{m}$) just below the red end of the visible spectrum. Thus the literal meaning of the term Infrared and

was derived from *Latin* meaning below red (*Latin* meaning of “Infra”) ¹. It can be noticed that the human visible spectrum is only between 380 nm and 760 nm. Thus all other frequencies associated with gamma rays, X-rays, Ultraviolet, infrared, microwaves, radio – waves and or long waves are invisible to naked eye.

2.4.3 Discovery of Infrared

It was observed that when a thermometer was left under sunlight, the temperature increased. This explains that a part of the visible radiation is absorbed by the surface of the thermometer, thereby increasing the temperature of the thermometer causing the mercury to rise in the glass bulb. However, this phenomenon was unexplained in the 18th century. In 1800, Sir William Herschel (1738 – 1822) accidentally discovered “heating rays”¹ (Ring 2000).

Being a British astronomer, and having interests in constructing telescopes, Herschel discovered that, though he used filters to look at the sky, the use of certain filters increased the temperature on his eye. This made him demonstrate a simple experiment using a prism. Herschel passed visible sunlight through a glass prism to measure the temperature across the various colours of the visible spectrum (a phenomenon discovered and published by Sir Isaac Newton in *Opticks* 1704)². He noticed that the temperature rose as he measured temperatures from the violet end to the red end. When he measured the temperature beyond the red end, he saw that the temperature continued to rise and as he moved further down, the temperature went to zero.

In 1800 William Herschel published his results in his series of papers describing the experiments he used to find the invisible heat radiation which led to the discovery of infrared radiation. In 1840, John Herschel coined the term ‘*thermogram*’ for the first time. With keen interests in photography, the first known solar thermogram was produced by John Herschel, son of the inventor William Herschel.

¹ Ring, E. F. J. (2000). "The discovery of infrared radiation in 1800." *The Imaging Science Journal* **48**(1): 1-8.

² *Opticks* : or, A treatise of the reflections, refractions, inflections and colours of light. Retrieved 11 September 2016. <https://archive.org/details/opticksortreatis1730newt>

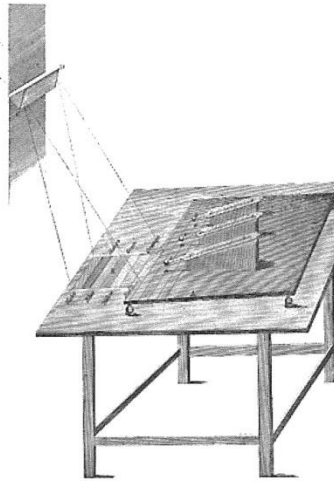


Figure 13 An experiment by Sir William Herschel leading to the discovery of "heating rays"
(Ring 2000)

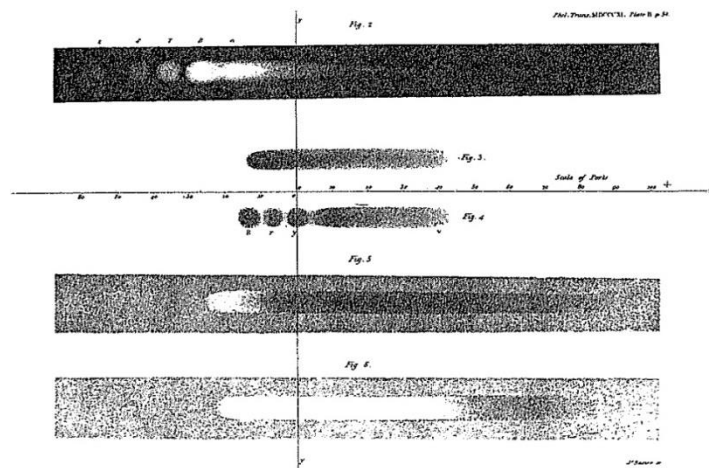


Figure 14 The first solar 'Thermogram' by Sir John Herschel (1840) (Ring 2000)

2.4.4 Infrared Thermography – Principles

Engineering science poses a range of challenges in a working industry especially in the maintenance of the equipment. There is a constant need to address maintenance issues and thermography, being a non-contact, non-destructive, non-intrusive thermal mapping is a perfect tool to analyse the performance characteristics of the machinery and aid in assessing its condition during preventive maintenance. The effective use of the technology mainly depends on the understanding of the material under inspection, the working environment and more importantly the technology itself.

Thermography or *Thermal Imaging* may be defined as a technique used to record the heat radiated by an object and analyse the objects characteristics and condition with reference to its temperature patterns. For example, this technique is currently used as a diagnostic tool in the field of medicine to study blood flow and detect the occurrence of tumours and other related problems of the human body. Thermography is a highly innovative non-contact technology that has made its way through different industries including Medicine, Civil Construction, Energy, Aviation, Materials, Automotive and Transport in order to determine the condition of the object under operating conditions.

There are three primary ways of heat transfer in isotropic (materials with similar material properties in all orientations): *Conduction*, *Convection* and *Radiation*.

Conduction:

Heat transfer in a material with closely packed molecules through direct contact can be referred to as conduction. Conduction predominantly occurs in solids and or fluids (liquids & gases). Let us consider a one dimensional heat transfer across a wall with thickness ‘s’ and surface area ‘A’, with temperatures on either sides of the wall to be T_1 & T_2 (Figure 15)(Carslaw and Jaeger 1959; Vollmer and Möllmann 2010). Then the heat transfer due to conduction \dot{Q}_{cond} can be defined as

$$\dot{Q}_{cond} = -\kappa \cdot A \cdot \frac{dT}{ds} \approx \frac{\kappa}{s} \cdot A \cdot (T_1 - T_2) = \alpha_{cond} \cdot A \cdot (T_1 - T_2) \quad (11)$$

where the heat transfer coefficient is,

$$\alpha_{cond} = \frac{\kappa}{s} \quad (12)$$

and κ is thermal conductivity of the wall.

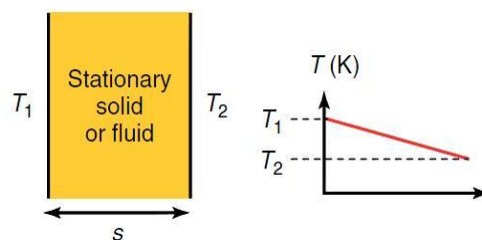


Figure 15 Heat transfer across a wall: Conduction (Vollmer and Möllmann 2010)

Thus heat transfer across a wall can be measured in terms of heat flux when the surface area A , and the temperature difference is known. This condition is true in the case of solids and liquids, though the rate of conduction would be much lower in terms of liquids.

In general, for a three dimensional heat flow in a solid, the temperature T at a point $P(x,y,z)$ will be a continuous function of x,y,z and time t (Carslaw and Jaeger 1959). This can be represented as

$$\nabla^2 T - \frac{1}{\kappa} \frac{\partial T}{\partial t} = 0 \quad (13)$$

where

$$\nabla^2 T \equiv \frac{\partial^2 T}{\partial x^2} + \frac{\partial^2 T}{\partial y^2} + \frac{\partial^2 T}{\partial z^2} \quad (14)$$

and κ , the thermal conductivity of the material which is dependent on the material properties; α – diffusivity, ρ – density and C – the specific heat capacity

$$\kappa = \frac{\alpha}{\rho C} \quad (15)$$

In solids and most liquids, the inter-atomic forces are much higher than in gases restricting the movement of molecules. Due to their internal structure, the movement of free electron and lattice waves enable the transfer of heat from higher temperature to a lower temperature as in metals. This transfer of energy vibrates and or excites the molecules changing the kinetic energy of the molecules.

In the case of gases, there is a huge movement of molecules as their inter-atomic forces are weak thereby allowing the gas molecules to vibrate. This movement of molecules in turn transfers the kinetic energy acquired from the higher energy region and passes them on to the neighbouring molecules. Since there are multiple collisions occurring randomly, the kinetic energy transferred to the molecules is much lower. Thus conduction in gases occurs through the collision of gas molecules. However, in case of solids, these molecular movements are restricted and it can be understood that only atoms vibrate in the crystal lattice of the molecule. This phenomenon of atomic vibrations in solid-state physics leads to the concept of

phonons (Janna 2000; Vollmer and Möllmann 2010). This concept holds true for non-metals where the movement of valence electrons is restricted.

Convection:

Convection may be referred to as the process of heat transfer by a fluid in motion (Carslaw and Jaeger 1959; Janna 2000; Vollmer and Möllmann 2010). Consider a heat radiator in the house. Hot water from the boiler enters the radiator. As the water circulates, the heat from the radiator is transferred to the room due to natural air circulation in the room. This transfer of heat from radiator to the room due to flow of fluids is referred to as natural convection. Let us consider a fan blowing wind over a heat exchanger. The air gets heated up as it passes through the heat exchanger due to collision of the air molecules with a body at higher temperature. This type of heat transfer is referred to as forced convection. Vollmer and Möllmann (2010) describes convection as a process of transfer of heat between a solid and a moving fluid (Figure 16). If \dot{Q}_{conv} is the heat transfer due to convection between a solid at temperature T_1 and the fluid in motion T_2 can be assumed to follow the following relationship,

$$\dot{Q}_{conv} = \alpha_{conv} \cdot A \cdot (T_1 - T_2) \tag{16}$$

where, α_{conv} is the heat transfer coefficient for convective heat transfer (Carslaw and Jaeger 1959; Vollmer and Möllmann 2010).

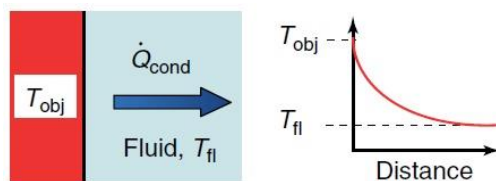


Figure 16 Heat transfer between a solid and a moving fluid: Convection. (Vollmer and Möllmann 2010)

Radiation:

The transfer of heat through electromagnetic radiation of various wavelengths is referred to as radiation (Carslaw and Jaeger 1959; Vollmer and Möllmann 2010). A system is always surrounded by its working environment. Let us assume that the surrounding temperature is uniform and constant. Assuming, an object with

temperature T_o be in a surrounding with temperature T_s , (Figure 17) the heat transferred due to radiation can be computed using the formula

$$\dot{Q}_{rad} = \varepsilon \cdot \sigma \cdot A \cdot (T_o^4 - T_s^4) \quad (17)$$

where ε – is the emissivity of the object (will be described in the following section), σ – is the Stephen – Boltzmann’s constant and is equal to $5.67 \times 10^{-8} \text{ W (m}^2\text{K}^4\text{)}^{-1}$ (Carslaw and Jaeger 1959; Vollmer and Möllmann 2010).

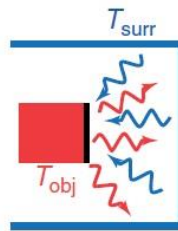


Figure 17 Heat transfer between a solid and its environment: Radiation. (Vollmer and Möllmann 2010)

Theoretically the heat radiates from an object at higher temperature and is absorbed by the environment at a lower temperature. It is to be noticed that the radiated heat is derived from a different set of equations and is dependent on the emissivity of the object. Further the Stephen – Boltzmann’s constant has to be introduced due to the non-linearity in heat transfer in solid medium. In other words a linear temperature is difficult to establish in the process of radiation.

2.4.4.1 Infrared Waves

In order to understand the concept of radiation, it is necessary to understand the facts governing the electromagnetic (EM) spectrum. As we know, the EM spectrum is made up of gamma rays, X-rays, Ultraviolet rays, Visible light, Infrared rays, Microwaves and radio frequency waves (in the increasing order of wavelength. Periodic changes or disturbances which occur continuously during a time period is referred to as “wave” (Vollmer and Möllmann 2010). The time taken to complete one full cycle or oscillation is the “period of oscillation (t)” and the distance covered depicts the “wavelength (λ)” of the wave. Thus the speed of the wave (c) can be determined using the formula

$$c = \frac{\lambda}{t} = \nu \cdot \lambda \quad (18)$$

where $\nu = 1/t$ (s^{-1} or Hertz)

The propagation speed of the wave depends on the material it passes. For example, sound waves can only propagate in the presence of matter. The speed of light through vacuum is approximately 300,000 km/s.

Infrared (IR) waves are a part of the EM spectrum which occur at the red end of the visible light. Typically, in the EM spectrum, the waves propagate due to magnetic and electrical disturbances and travel perpendicularly with each other along the direction of propagation (Figure 18). The amplitude of the wave is determined from the maximum disturbance of the wave (Janna 2000; Vollmer and Möllmann 2010).

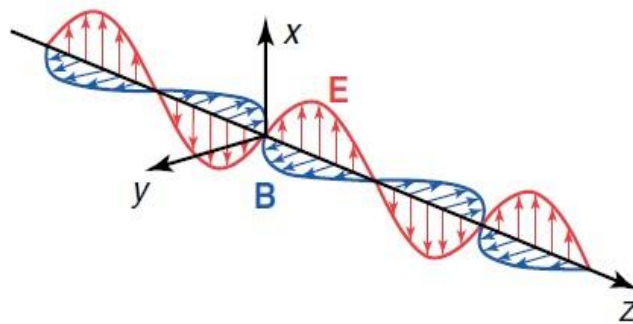


Figure 18 Illustration of IR waves in an EM spectrum (Vollmer and Möllmann 2010)

Blackbody Radiation:

A blackbody is defined as an instrument that is capable of absorbing the entire energy incident on it at different wavelengths and directions and emits all the energy absorbed until it reaches thermodynamic equilibrium. The blackbody follows Kirchhoff's laws and acts as a perfect radiator of energy. The following holds true for a perfect blackbody (Maldague, Jones et al. 2001; Vollmer and Möllmann 2010)

- “A blackbody absorbs every incident radiation, regardless of wavelength and direction.”
- “For given temperature and wavelength, no surface can emit more energy than a blackbody.”
- “Radiation emitted by a blackbody depends on wavelength, however, its radiance does not depend on direction, and that is, it behaves like a Lambertian radiator.”

Though precise experimental blackbodies existed, it was Max Planck who introduced the famous Planck's constant 'h' in 1900 to explain the measurement of radiation with the help of a blackbody. Max Planck described that the distribution of radiance (L) of the spectra is determined by rate at which energy was emitted at a stated temperature (T) by the blackbody as a function of its wavelength (λ) and can be represented by

$$L_{\lambda}(T) = \frac{2hc^2}{\lambda^5 (e^{\frac{hc}{\lambda kT}} - 1)} \quad (19)$$

where $h = 6.626076 \times 10^{-34}$ J. s – Planck's constant

$c = 2.998 \times 10^8$ ms⁻¹ – speed of light

$K = 1.381 \times 10^{-23}$ J. K⁻¹ – Boltzmann's constant

The above equation holds true for a perfect blackbody. However for energy emitters other than the blackbody, the equation becomes

$$L_{\lambda}(T) = \varepsilon \cdot L_{\lambda}(T) \quad (20)$$

where ε is the emissivity of the material (Maldague, Jones et al. 2001; Vollmer and Möllmann 2010).

Emissivity:

Emissivity of a material is the ratio of the amount of energy emitted by the surface of a material to that of the energy emitted by a perfect blackbody under the same temperature and energy exposure conditions. It has been universally accepted that only a blackbody can emit the entire absorbed radiation incident on it, has a value of 1 and all other materials have emissivities between 0.1 and 1. Emissivity is a dimensionless quantity and hence has no units.

2.4.5 Pulsed Thermography – Principle

Over the years Pulsed thermography (PT) has become a popular thermal evaluation tool in the NDT industry. A short thermal excitation or pulse between 3ms to about 4s made it robust enough to carry out inspection in the engineering industry

(Maldague, Beaudoin et al. 2001; Shepard 2007). The process involved heating up the part to be inspected with the help of a pulse and recording the surface temperature decay of the part. It has been seen that the pulse energy generated the necessary thermal gradient which then due to diffusion passed through the surface of the material being inspected. Any discontinuity present on the path of diffusion changed the rate of diffusion. Thus on the thermal image, the areas with discontinuities appeared with a different temperature. It was also noticed that deeper discontinuities appeared later with a lower contrast. Maldague, Beaudoin et al. (2001) say that the propagation time (t) and contrast (C) are a function of the depth of the defect (z) and can be approximated from the following equations

$$t = \frac{z^2}{\alpha} \quad (21)$$

α being thermal diffusivity and is equated to $\alpha = \frac{\kappa}{\rho c}$, κ being thermal conductivity, ρ being density of material, and c being specific heat

and

$$C \cong \frac{1}{z^3} \quad (22)$$

It can be seen that time is directly proportional to the square of the depth and contrast is inversely proportional to the cube of the depth of the discontinuity. The authors say that this phenomenon is due to the diffusion of the pulse heat in all directions in the material. In order to find a defect the rule of thumb is that for a homogeneous isotropic material “the radius of the smallest detectable discontinuity should be at least one to two times larger than its depth under the surface” (Maldague, Beaudoin et al. 2001; Shepard 2007; Vollmer and Möllmann 2010).

There are two primary arrangements used in pulse techniques, (Maldague, Beaudoin et al. 2001)

- (a) Reflection mode – where the pulse thermal source and the infrared camera are on the same side of the inspection sample when the anomaly is close to the heat surface

(b) Transmission mode – where the pulse thermal source is on the front side and the infrared camera on the rear side when the anomaly is close to the rear surface

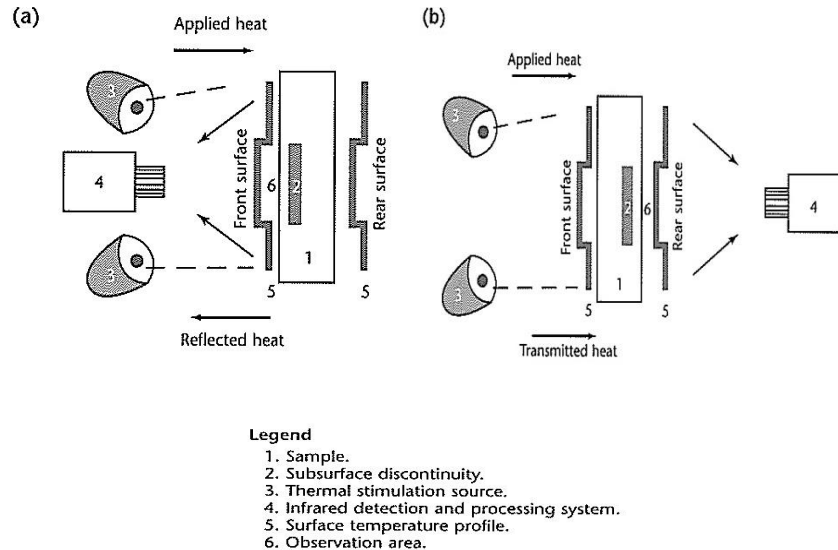


Figure 19 Basic arrangements for a pulsed thermography system (Maldague, Beaudoin et al. 2001)

The reflection mode is more preferred as access to the rear side of the material under inspection may not be accessible. It was also noticed that the depth of the discontinuity could not be established using the transmission mode as the time taken by the thermal wave to reach the back surface was always the same.

2.4.6 Lock-in Thermography – Principle

The typical arrangement of a lock-in thermography system is similar to that of a pulsed thermography system. However, in case of a lock-in system, instead of single pulse, multiple pulses (or a modulated lamp) at calculated time intervals is fired and the camera captures images on a continuous basis (Giorleo, Meola et al. 2000; Maldague, Beaudoin et al. 2001; Breitenstein, Warta et al. 2010). This periodic exposure of heat is harmonic in nature and develops a harmonic excitation in the test piece. This harmonic excitation inside the test material increases the temperature at the surface of the material on a constant basis. In this research, Lock-in is set-up where the harmonic excitation is achieved through sinusoidal vibrations from a mechanical actuator.

Let us consider the material to be homogeneous and the harmonic progression of heat passes through the material at a set frequency and amplitude over a period of time. As the material is homogeneous, the shift in phase angle due to the simultaneous heating of the surface appears to be the same. When a defect / anomaly is present in the path of the heat wave, the phase change occurs thereby increasing or decreasing the rate of heat flow. The infrared camera then records the surface temperature over a time period and the images are analysed as a function of time for each pixel (x,y) . Several modulation cycles are run and several images are acquired using the thermographic camera. With the help of Fourier transform function, each pixel is analysed to determine the phase and amplitude of the pixel finally producing a pair of images. One image is the amplitude image which is dependent on the intensity of illumination of the lamp, absorption and emission of the surface of the material. The other image gives the phase angle based on change in temperature. Let us consider four modulations $S_1(x,y) - S_4(x,y)$ where (x,y) defines the pixel where the modulation can be obtained from the temperature signal and can be represented as

$$T(t) = T_{av} + S(t) \quad (23)$$

where T_{av} is the average temperature (Maldague, Beaudoin et al. 2001; Vollmer and Möllmann 2010).

The amplitude image $A(x)$ and phase image $\phi(x)$ can be constructed using the following relations

$$A(x, y) = \sqrt{[S_1(x, y) - S_3(x, y)]^2 + [S_2(x, y) - S_4(x, y)]^2} \quad (24)$$

$$\phi(x, y) = \arctan \left[\frac{S_1(x, y) - S_3(x, y)}{S_2(x, y) - S_4(x, y)} \right] \quad (25)$$

It can be inferred from the above equations that the phase image is independent of the illumination intensity on the surface of the sample (Maldague, Beaudoin et al. 2001; Vollmer and Möllmann 2010). Typically, lock-in thermography requires a signal to be accumulated over many cycles in order to obtain an acceptable signal-to-noise ratio (SNR). Thus the thermoelastic stresses generated in the sample due to cyclic excitation can be estimated using the equation

$$\Delta T = -\frac{T}{\rho C_\varepsilon} \frac{\partial \sigma}{\partial T} \varepsilon + \frac{Q}{\rho C_\varepsilon} \quad (26)$$

where T – absolute temperature, ρ – density, C_ε – specific heat capacity at constant strain, σ – stress, ε – strain and Q – the heat input.

Partially differentiating eq 26 gives,

$$\Delta T = -\kappa T \Delta(\sigma_x + \sigma_y) \quad (27)$$

and

$$\kappa = \frac{\alpha}{\rho C} \quad (28)$$

which is similar to eq 15 above and κ – the thermal conductivity of the material, α – diffusivity, ρ – density and C – the specific heat capacity (Breitenstein, Warta et al. 2010; Addepalli and Tinsley 2015).

2.4.7 Recent advances in Thermography

Chatterjee, Tuli et al. (2011) compared pulsed, lock-in and frequency modulated thermal wave imaging (FMTWI) techniques on a CFRP laminate. It was shown that the pulsed images showed better SNR in comparison to other methods. It was also shown that the FMTWI technique overcame the “blind frequencies” issue faced by lock-in technique. All the tests were performed at a similar energy level and were time dependent. It was shown that shallow defects of the composite sample were detected more easily due to the higher SNR. It was also noted that the noise found in the thermal images was governed by the composite material’s non-uniform structure.

There is research establishing the fundamentals of pulsed phase thermography (PPT) which is a combination of pulsed and lock-in thermography techniques (Maldague, Beaudoin et al. 2001; Maldague, Galmiche et al. 2002). They discuss the use of Fourier transformation to invert data obtained from PPT. It was reported that the inversion of PPT data resulted in the early detection of the defect. However, the data obtained resulted in an increase in noise in the thermal image thereby becoming sensitive to defect size. Calibrations and comparisons were made on samples with flat bottom holes at different depths. Improvement in the signal was obtained using pulsed thermal “shaping”. The research suggested that advancements

to improve the signal could be performed using direct polynomial fitting function in MATLAB.

Subsurface defects on sample made up of Plexiglas were assessed quantitatively by Montanini (2010) using Lock-in and PPT. Based on preliminary investigations to evaluate the distance of the camera, heat source and heating cycles required, measurements on the Plexiglas sample with drilled in flat bottom holes at different depths were made for specific frequency amplitude response (Lock-in method), pulse duration and sampling rate (PPT). The data from PPT was found to be more effective as it was found to be independent of localised heating and surface emissivity issues thereby affecting only the surface topography and not the phase. Post-processing of the data obtained from the tests demonstrated that the thermal diffusivity measurements yielded better results addressing the problems faced by both Lock-in and PPT. The limitation of the Lock-in method is that low frequency heat flux is required to detect deeper defects and multiple tests are needed to detect all the defects. In the case of PPT, the surface needs to be heated to a much higher temperature in order to locate deeper defects. This increase in temperature may damage the test sample and also affect the data obtained from the test. Effort has been made to estimate the size of the defect and found that shallower defects were off by 2% and deeper defects to about 28%. It was concluded that defect size estimation for artificial defects (flat bottomed holes) would be different to that of natural defects (delaminations, disbonds and inclusions) and are dependent on variables such as thickness of the defect and orientation of the fibres in the material.

Research has been carried out by Dudzik (2009) to enhance the detection of defects found in the sub-surface of plexiglass material. An algorithm based on the standard deviation obtained from the thermal image has been tested to improve the sub-surface area detection for a material which has a low thermal diffusivity. It was found that the use of algorithm to determine the statistical detectivity ratio detected control defects even when the plexiglass sample was non-uniformly heated. There were limitations reported during this research which included selection of defect area, the size of the defect, selection of a suitable thermogram with proper thermal contrast, the SNR associated with the detector of the camera and the associated uncertainties. Despite these limitations the author claims that defect detection over an area under different heating conditions was fairly easy and suggested that this

method could be adapted to portable systems enhancing the NDT applications in the industry.

Giorleo, Meola et al. (2000) in their publication on the defect detection techniques using lock-in thermography describe inspection methodology on carbon-epoxy samples with all possible kinds of defects that occur either during manufacturing process or during their service. The analysis of different defects produced by varying the weave and orientation of the laminates of the composite material, introducing inclusions, excess or lack of resin and or adhesives at certain areas and delaminations was performed to mimic most defects occurring in composites materials. It was found that the lock-in method successfully detected a range of defects. However the limitations lie with the depth of the defect and the diameter of the defect in addition to the thermal diffusivity of the material. The only other benefit from the method is the capability of detection of the depth of the defect faster as it does not involve much post-processing techniques.

Research has been carried out on the comparison of an analytical model with that of actual experimental data obtained by subjecting carbon – epoxy composite material to fatigue testing (Toubal, Karama et al. 2006). It was seen that the model output and the experimental data obtained from the tension load testing were similar to each other. A thermographic system was used to detect external surface temperature of the sample subjected to cyclic loading thereby predicting the extent of damage and its evolution. Fatigue growth modes were studied and it was reported that at the first stage, multiple modes of damage occur leading to rapid growth in damage. The damage growth is slow and steady forming the second stage of failure. The composite material damage now grows rapidly leading to the fracture of independent fibres of the material. Thus the characteristics of the formation, evolution, accumulation and failure of the material have been studied on carbon – epoxy composite materials.

Brady and Kulkarni (1996) in their research used pulsed video thermography (PVT) to determine the distribution of thermal diffusivity (two dimensional) over the surface of three types of materials. The results obtained were compared with those obtained using laser flash diffusivity testing. Variables which were unavailable or difficult to obtain were found using numerical, experimental and other methods such

as parameter normalization. The tests were carried out on low carbon steel, plastics and carbon-carbon composites and the results when compared with that obtained from laser flash testing differed by 15%. It was suggested that the difference in results obtained could be because of the fact that the resolution of the PVT is finer than that of the laser technique. Moreover the benefit of PVT was its ability to obtain contour plotting data from a single test.

A new method termed HEALTHY was introduced by Nino, Ahmed et al. (2009). HEALTHY stands for “Heat Emitting Layer for THERmographY”. As the name suggests, heating elements were introduced in the welding process which acted as a heat source to carry out thermographic inspection. Aerospace grade samples made up of glass and carbon fibre with variable thickness were studied from the surface temperature maps (direct temperature measurement) and phase images acquired from Lock-in mode. Defects were introduced during the welding process to investigate the detection of defects using a C-Scan, surface temperature measurement and Lock-in mode. Better results were obtained from thermographic inspection in comparison to ultrasonic testing methods as the process obtained well defined thermal images with details of defect shapes and dimensions.

Effort was taken to use thermography in the active mode to detect most defects occurring in composite materials with sandwich structures by Dattoma, Marucuccio et al. (2001). Defects caused by infiltration of the glue, water ingress and disbonds were introduced in glass reinforced plastics (GRP). Further thermography was also applied for a GRP wind-turbine blade. Cooling rates of reference materials and samples with defects were monitored. Defects were then identified from the intersection point of the cooling curves of both reference samples and samples with defects and conclusions were made accordingly. Satisfactory results were obtained from the tests even when there was a fine layer of powder on the surface of the wind-turbine blade.

Thermography has been successfully implemented to detect sub-surface defects of simple geometries. However, defects with complex geometries have always been a concern. Krishnapillai, Jones et al. (2005) focussed on setting up a finite element analysis (FEA) model to address the problem of ‘complex non-axisymmetric geometries’. A thermographic experiment was conducted on a carbon

composite laminate with flat bottom holes drilled at various depths. The data obtained from the thermogram was analysed and a mathematical model was set up using MATLAB. The data thus obtained was used to model samples on NE-NASTRAN. A calibration model was also modelled which helped in comparing the data obtained from the actual model. With the relevant thermal properties of the materials known, the authors (Krishnapillai, Jones et al. 2005) demonstrated defects such as delaminations and or disbonds can be simulated accurately.

In another independent study authors Krishnapillai, Jones et al. (2006) came up with a 2d numerical finite element model to look at sub-surface defects such as delaminations. Assumptions that there is no real lateral flow of heat and non-conservation of heat flux have been made to the finite element model. Only plate structures that are flat have been considered for modelling which constitute sub-surface defects that lie parallel to the surface. The finite element models were built on samples modelled by Maillet, Houlbert et al. (1993) in this investigation. A comparison of 2d approximation modelling and 3d finite element modelling was carried out. It was noticed that the size of the defect with respect to the area does not change in the 2d numerical model whereas in the 3d finite element model, the defect size increases. This probably is due to the effect of diffusion of heat laterally in the sample. Thus the authors prove that the 2d model does not accurately model the true surface of the defect. They suggest that precise experimental data needs to be incorporated into to finite element model in order to simulate the exact the defect prediction there by helping improve the SNR to achieve thermal images with superior contrast. It was noted that the use of Teflon and other inserts to create artificial defects (delaminations and other sub-surface defects) might not be suitable for use in the thermal model due to disparity that exists between the actual and theoretical thermal property values of the material itself.

Sakagami and Kubo (2002) carried out experimental investigations of pulse and lock-in thermography. Pulse thermography was carried out on various samples ranging from steel to ceramic with artificial defects (flat bottom drilled holes) at different depths. They noticed that the thermal conductivity had a huge impact on the ability to detect the defects of each independent material they tested. The technique was also applied to determine corrosion protection of oil storage tanks and to identify cavities and demineralisation of human tooth. Lock-in thermography was

used to detect cracks by a technique termed as ‘singular method’, where in the temperature rise near the cracks was detected as the sample was introduced into an electrothermal field. Results obtained from a steel plate with flat bottom drilled holes using lock-in thermography were also presented.

In another study, a carbon fibre composite plate with flat bottom holes drilled to its back surface was tested by both lock-in and pulse transient thermography with identical excitation energies. Pickering and Almond (2008) found that the pulse thermography images of shallow defects had a better signal to noise ratio (SNR) in comparison to the lock-in method. However, the SNR for deeper defects were found to be approximately the same for both the techniques. It was also seen that increasing the energy of excitation would improve the SNR of the thermal image obtained by both the techniques. They noted that lower excitation energy levels would mean lower SNR. This would mean that some frequencies at that level might be completely masked in a lock-in system which will cause the defect to disappear from the image. This issue of defect disappearance at lower frequencies is due to the phase change that occurs due to the lock-in method and is referred to as “blind frequency effect” (Bai and Wong 2001; Pickering and Almond 2008). The authors suggested that by using magnitude data obtained during the inspection this issue of “blind frequencies” could be avoided.

There is research suggesting the application of pulse thermography to detect defects in composite joints that were adhesively bonded. The authors, Schroeder, Ahmed et al. (2002) used pulsed thermography to investigate the performance of the bonds in a pick-up truck box made up of composite materials that were adhesively bonded. Continuous bonds were identified using thermal imaging in most parts of the box except for the headboard due to additional fixtures that were found in the assembly line. This issue with the fixture attachments limited the amount of force applied to the headboard bonds during testing and was effectively highlighted by pulsed thermal images. This study was undertaken primarily in the production line and hence no in-service defects were addressed. The authors claimed that pulse thermography gave an exact insight to the ‘correctness’ of the manufacturing process giving supporting data as to where the defect zones were and how the process could be improved. Further, pulse thermography could be used to locate anomalies such as disbands in the production line if they were to occur. The authors suggested that

there was a possibility of using this technology to assess the quality of the part produced by introducing it in an actual, live production line.

Defects such as delaminations, impact damage and fatigue failure were introduced into different aircraft materials including composites, sandwiches and metals and was tested using Lock-in thermography (Meola, Carlomagno et al. 2006). Various conclusions were discussed in the paper and the key points are as follows,

- Sub-surface defects close to the inspecting surface were identified at low lock-in frequencies.
- Real defect shape could be obtained for deeper defects at higher exposure frequencies.
- Fibre rupture in case of impact damage can only be found if the part to be inspected has had a strong impact.
- Light colour pattern (magnifying the image around the pattern using close-up lenses) from the image indicated the presence of adhesive layer and probably the possibility of the adhesive to run into the cut edges and or honeycomb structure of the sample.
- The effect of hole elongation with and without lateral constraints was clearly visible in the thermal image.
- Laser weld beads obtained at different weld speeds were subjected to lock-in analysis. It was seen that the welds which were processed at high speeds were completely visible whereas the ones with low speed parts of the weld vanished over the top surface of the weld. This effect was noticed because of the strong influence of heat transfer in the melted zone of the material.

Meola, Carlomagno et al. (2006) thus suggest that lock-in thermography is useful in detecting defects, their geometry and impact damage. Further, this technique could identify damage associated with the performance of the material with respect to the defects in the internal structure such as the presence of excess resin, behaviour of composite fibres and choice of welding speeds.

2.5 Current study

The previous sections presented a detailed overview of basic concepts of composites, their susceptibility to damage and related thermal and other NDT methods to detect them. This section mainly focusses on identifying the supporting literature for the experimental work undertaken as part of this thesis. To detect and characterise the condition of composite laminate, it is necessary to understand and expand knowledge on the techniques that are being applied through existing literature. This overview is limited to the establishment of not just thermography as a tool, but also to understand the creation of damage due to impact.

2.5.1 Thermography for subsurface inspection

The motivation for the initial part of this work and to support the hypothesis that pulsed thermography is suitable for certain type of sub-surface defects; a literature search to determine the applicability of the technique for composite defect and damage characterisation was undertaken. In order to present various applications of pulsed thermography, it is essential to present the technique used for this work. Pulsed thermography in the reflection mode with post processing using thermographic reconstruction (TSR) technique has been used for the work presented in Chapter 4 (Maldague 2001; Shepard 2007; Omar and Zhou 2008; Genest, Martinez et al. 2009; Addepalli and Tinsley 2015; Zhao, Tinsley et al. 2016)(See Appendix 1).

Shepard (2007) in his paper titled “Flash Thermography of Aerospace Composites” presented the results obtained using pulsed thermography, where the results were post-processed using the Thermographic Signal Reconstruction method or TSR (Addepalli and Tinsley 2015; Zhao, Tinsley et al. 2016). The working principle is as follows; the component for inspection is flashed instantaneously over a short pulse using two xenon flash lamps and the surface temperature decay profile is simultaneously recorded by an infrared camera. For a homogeneous material, the surface temperature decay is found to be even and is directly dependent on the materials heat diffusion characteristics. As soon as the heat wave is interrupted due to a sub-surface anomaly, the diffusion characteristics change which is then observed

on the surface temperature map of the component as a hot spot or a cold spot. The heat equation for a semi-infinite homogeneous plate can be represented as (Shepard 2007)

$$T(t) - T(0) = \frac{Q}{\kappa\rho C\sqrt{\pi t}} \quad (29)$$

where T – Surface temperature, t – time, Q – energy per unit area, κ – thermal conductivity, ρ – density of the material and C – the materials specific heat capacity.

When a natural logarithmic plot for a pixel representing a sound area is obtained using the above equation (Eq. 26), a linear profile with a slope of -0.5 is obtained. It was noticed that when another plot from the surface pixel from a defective area was plotted, the logarithmic temperature profile now deviates from the one plotted before thus confirming the presence of a subsurface anomaly as seen in Figure 20 below.

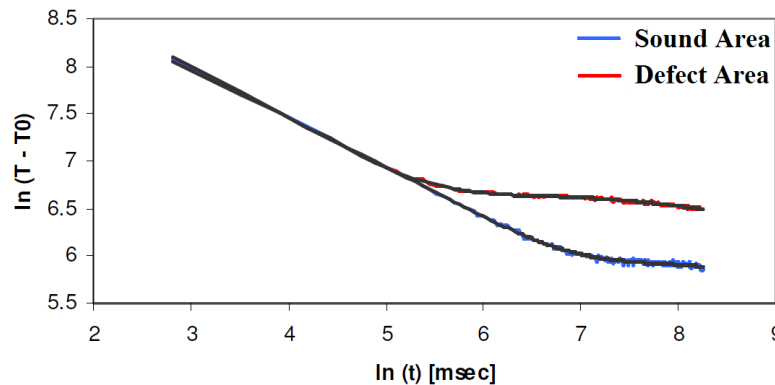


Figure 20 Log time temperature plot showing pixel temperature decay profile of the parent material and damage (Shepard 2007)

The plot in Figure 20 shows two temperature decay profiles; the blue curve indicating the characteristics of a sound area. Once the part was flash heated, there is instantaneous temperature rise followed by a linear temperature decay in the logarithmic domain. After a set time ‘t’, the temperature deviates from linearity which is confirmed with the change in slope of the curve. This change is mainly due to the fact that the heat has diffused through the material thickness and has now reached the back wall. This time is referred to as t^* throughout this work and in line with the findings of Shepard (2007) and Zhao, Tinsley et al. (2016). When the same is applied to the defect area, the deviation occurs much earlier due to the fact that the

defect in this case holds more heat indicating change in heat diffusion characteristics as represented by the red curve in Figure 20.

2.5.2 Impact damage – an overview

There is a continuing concern in the composite industry with regards to damage caused due to impact and methods to maintain them as repairing composites is a difficult process when compared with that of metallic parts. Impact damage to composite materials has been widely studied, especially to understand its mechanics (Ball and Almond 1998; Shyr and Pan 2003; Craven, Sztefek et al. 2008; Kim, DeFrancisci et al. 2009; Azouaoui, Azari et al. 2010). It has been found in the literature that even low energy impact in the order of a few joules of energy causes damage at a macroscopic scale. Several researchers' have investigated this issue with low energy impact and have established the mechanics of impact damage itself. One of the prime areas that have been identified in case of impact damage is the occurrence of barely visible impact damage or BVID (Li, Hu et al. 2002; Corum, Battiste et al. 2003; de Morais, Monteiro et al. 2005). Further, studies have shown that the type of impact especially in the case of a controlled event, the damage created varies with the indenter's geometry (Mitrevski, Marshall et al. 2005). The research further suggested that the greater the contact area of the indenter; smaller the damage caused. In other words, a sharp pointed indenter pierced through the laminate where as a hemispherical indenter created a surface crush damage and did not pierce through the laminate. To understand the impact event, several studies exist. Further, to compliment physical damage creation numerical modelling has also been taken up (Pavier and Clarke 1995; Kim and Kedward 2000; Sohn, Hu et al. 2000; Li, Hu et al. 2002; Kim, Kedward et al. 2003; Duell 2004).

Though multiple studies exist that perform controlled impact damage, the assessment methods vary. The primary need to characterise impact damage is to understand the performance of such damaged parts when subjected to normal operation. This has been monitored through mechanical tests such as compression after impact and fatigue test to capture damage growth (Schubel, Luo et al. 2007; Craven, Sztefek et al. 2008; Azouaoui, Azari et al. 2010; Gunasekera 2010; Schmutzler, Alder et al. 2014). All of these mechanical tests destroy the laminate and thus are not directly suitable for in-situ inspection scenarios. However, with the

advent of NDT techniques, it is now possible to characterise impact damage using traditional and advanced NDT methods (Adams and Cawley 1988; Marty, Desai et al. 2004; Yan, Drinkwater et al. 2009; Garnier, Pastor et al. 2011; Kapadia 2013).

For the purpose of this research, impact damage assessment using multiple thermography methods has been considered. The suitability of composite laminate damage detection using thermography is well established (Schroeder, Ahmed et al. 2002; Avdelidis and Almond 2004; Gleiter, Spiessberger et al. 2008; Ibarra-Castanedo, Susa et al. 2008; Feuillet, Ibos et al. 2012; Grys 2012). Further there is evidence of techniques such as lock-in, transient and PPT methods that are being used to detect damage occurring in composites (Brady and Kulkarni 1996; Bai and Wong 2001; Giorleo and Meola 2002; Avdelidis, Hawtin et al. 2003; Choi, Kang et al. 2008; Burrows, Dixon et al. 2010). However, the ability to detect near surface and certain types of barely visible damage is a challenge in itself.

2.6 Epilogue

This chapter presented the basic concepts of the material together with a review of literature identifying the gap in knowledge especially when it comes to establishing the applicability and suitability of thermographic techniques. Further, the review identified that there is a huge disparity between various techniques where full damage characterisation is required. Though the limitations of traditional and advanced NDT techniques are understood, there is lack of understanding of suitable methods that could identify barely visible damage. There is significant evidence of thermography as a suitable tool to evaluate the condition of composite laminate when subjected to damage. However, the limitations with respect to the type of damage have not been fully established. Further, this work attempts to further our understanding of the impact event itself similar to the studies presented by authors such as Giorleo, Meola et al. (2000); Meola, Carlomagno et al. (2006); Meola and Carlomagno (2009); Meola and Carlomagno (2010). This chapter identifies impact damage, particularly in the aerospace context, where advanced techniques like the thermography methods explored in this thesis could lead to improved diagnostic procedures.

3 METHODS & MATERIALS

This chapter presents the methodologies that were used to determine the condition of the composite material and includes creation of both manufacturing defects and controlled damage creation methods, sample manufacturing process and various techniques used to evaluate the apparent defects and damage that were introduced in a controlled way. It should be understood that most of these defects and damage were created to test the limitation of the existing techniques and to demonstrate the strength of each of those NDT methods.

3.1 Research Methodology

With the ever increasing use of composites in primary aircraft structures, it is important to understand their behaviour especially when ‘in-service’. This work presents those approaches that are able to determine damage occurring during service and their potential detection ‘in-situ’ that could become part of preventive maintenance schedule of the system.

Initially, a literature review was carried out to understand various NDT techniques and their ability to detect a range of defects and damage. The aim was to identify non-contact techniques that were capable of performing large area inspections with reduced inspection and analysis downtimes. Infrared thermography was chosen as an overall technique that showed promising results especially in defect and damage detection in the case of advanced composite materials. The literature presented evidence of both the working principle where the rate of decay of temperature was dependent upon the laminates material properties such as diffusivity, density and specific heat capacity and their suitability to detect sub-surface anomalies. Techniques such as pulsed thermography, TSA and transient thermography were used for defect and damage detection. To illustrate the suitability of these techniques, various preliminary tests were designed and performed to address both the strength and limitations of those systems. The data was then compared with traditional and advanced NDT techniques such as x-ray, UT and LDV tests to fully characterise the defects and damage occurring in CFRP laminates.

The initial preliminary tests were carried out on field derived samples with artificial sub-surface defects and other scrap samples. Later, a full parametric study was taken up to look at the sub-surface defect's occurrence during manufacturing with an interest to mimic representative defect materials that could be introduced and their detectability using pulsed thermography.

The next study was used to determine a range of barely visible impact damage (BVID) occurring due to impact. To determine representative in-field damage scenarios the following impact tests were undertaken:

- A fully controlled impact tests using a modified Charpy tests; representing a low speed impact using with a controlled surface
- A ballistic gas-gun ballistic impact test using stones; representing a high speed impact event with irregular surface impact.

The laminates were then subjected to pulsed thermography, TSA and vibrational analysis. It should be noted that the entire impact event was captured using the transient thermography technique where the infrared radiometer measured the temperature difference caused during impact from the non-impact side of the laminate.

As part of the damage detection methods, LDV measurements were carried out as a case study for a set of laminates before and after impact testing to observe and record any changes that may have occurred due to the impact itself. Further the suitability of both pulsed and TSA methods for specific damage types were investigated to help propose those methods that could determine the condition of the laminate.

For the entirety of the experimental investigation, at least 3 laminates with similar defect and damage levels were produced to ensure repeatability.

3.2 Experimental Methods

This section describes various experimental methods that were adapted as part of this study. The following are the methods that were used as part of the current study

- Preliminary tests
 - Pulsed Thermography
 - X-Radiography
- Parametric Study – Composite laminate with defect inserts
 - Pulsed Thermography
 - Pulse-Echo Ultrasonic testing (PEUT)
 - 3D modelling using Ideas10
- Impact Study – Composite laminate (as manufactured)
 - Transient Thermography
 - Pulsed Thermography
 - Thermo-Stress Analysis (TSA)
 - Vibrational Analysis – using LDV

3.2.1 Preliminary tests

The preliminary tests involved the use of EchoTherm pulsed thermography system to understand the working principle of the technique itself. These tests were used as a base line to establish detection capabilities and analysis parameters. This established the procedure to optimise the data acquisition settings and the related analytical tools to characterise defects. Once the working parameters were established, the technique was implemented on field samples representing the tail plane section, the details including problem description and results are described in Chapter 4, Section 4.1 below. In order to confirm the damage occurring in field samples, x-ray inspection data was used as a validation tool.

3.2.2 Parametric Study

The preliminary tests established the testing method, but still required further analysis to establish the limitations of the system, especially with the depth and type

of defects occurring through the material thickness. Hence defects that were more likely to occur during the manufacturing stage were selected. Three types of materials in two geometrical shapes were selected for this study. The analogy is to select different thicknesses and insert these defects at the lay-up stage at set layers and set locations before cure. The type of materials used were

- Steel Shims
- Teflon
- Bagging film

The geometrical shapes chosen were

- Circular dots – having two diameters 6mm and 8mm
- A 25mm square part – with a 6mm and 8mm rectangular material taken off from the square part.

See Figure 21 below for the CAD model of the geometric shape and location of the defects.

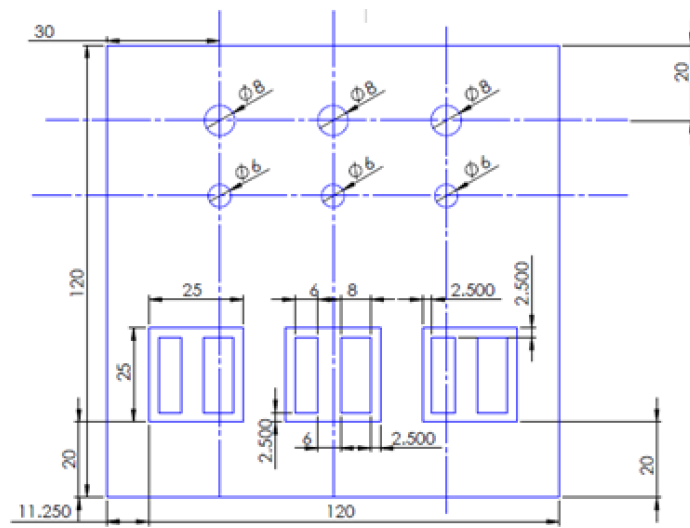


Figure 21 CAD drawing of the defects introduced at the lay-up stage (all dimensions in mm)

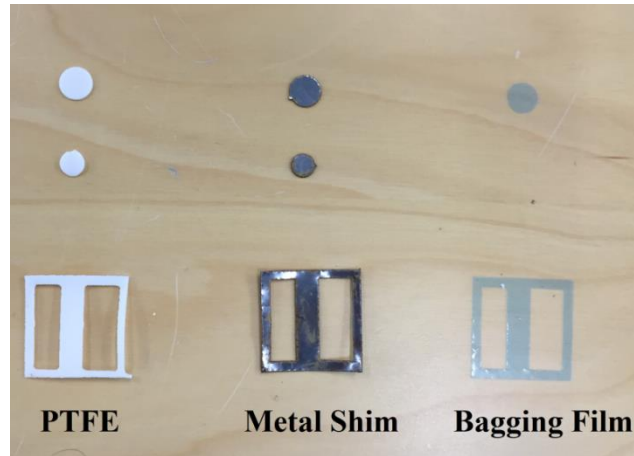


Figure 22 Inserts of PTFE, metal shim and bagging film

Three different laminate thicknesses, 3mm, 6mm and 9mm were chosen and the defects were introduced at various thickness intervals during the manufacturing process, the details of which can be found in the results section. The laminates were then cured in a hot press to make the final sample.

As part of the parametric study, the samples post-manufacture were subjected to inspection using the pulsed thermography system and the PEUT system to detect the previously introduced artificial defects. This parametric study was designed to capture the capability of the thermography system and validate the data obtained from the inspection with the data from the pulse-echo UT system. At the same time, this method was used to demonstrate the limitations of the system in the area of detection of deeply buried sub-surface defects.

3.2.2.1 Computational Modelling

A separate study was undertaken to reconstruct the actual inspection into a theoretical model. Section 4.2.2 presents the study which helped to clarify the limitations of the pulsed thermographic inspection technique.

3.2.3 Impact Study

From the review that identified gap in knowledge, it was understood that a representative in-field sample with damage during operation was needed. It was also established that the most difficult form of damage that cannot be easily identified is

the BVID. Hence to understand the response of CFRP laminates to impact the following methodology was proposed,

- A controlled definite impact using a modified Charpy with a hemispherical indenter of 24mm diameter; as suggested in the literature, was setup to create damage for three low energies; 4.5J, 8J and 12J.
- A controlled in-definite impact using a ballistic gas-gun to replicate real life scenario was setup to perform high speed impact for low energies; 4.5J, 8J and 12J
- Two sample thicknesses, 3mm and 6mm were selected for the impact test. Three impact trials for each type of impact (Charpy and gas gun), two different layup sequences and each energy level (3 levels as above) were chosen for the parametric study.
- All samples were subjected to microscopy for visual damage detection, pulsed thermography and TSA for surface and sub-surface damage measurement.
- A set of samples were selected, where the sample's modal frequencies were measured using a LDV. These selected set of samples' resonant frequencies were measured in the "as manufactured" condition in the first instance. Once the impact was carried out, the sample's modal frequencies were measured again using the LDV to monitor any shift in frequencies due to the creation of the damage. This shift in modal frequencies has been explained through the use of a theoretical model as seen in section 4.5.



Figure 23 The modified Charpy impact test setup with infrared and high speed camera

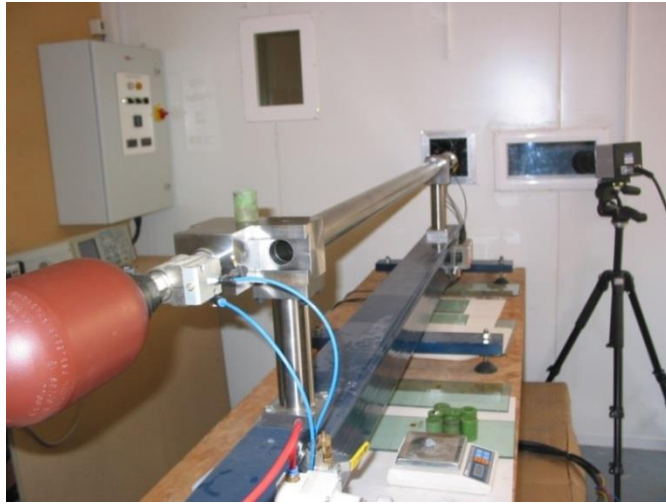


Figure 24 The ballistic gas gun



Figure 25 Sabot with stone that was introduced into the gas gun barrel for impact test

3.3 Composite laminate sample manufacture

This section describes the manufacturing process of Carbon Fibre Reinforced Polymer (CFRP) composite laminates including the choice of lay-up / stacking sequence and the equipment used to make them. Further on, the method of introduction of different defects into the laminate panels and various NDT methods used to detect and characterise the defects has been presented.

The composite laminates for this research were manufactured using 600mm wide uni-directional 120GSM (grams per square metre) carbon fibre prepreg with an epoxy resin content of 35% manufactured by Advanced Composites Group Ltd.

Please refer to Appendix 2 for carbon prepreg material properties as supplied by Advanced Composites Group Ltd.

As described in the previous chapter (Chapter 2) multiple layers of continuous single layer fibres are laid to a predetermined stacking sequence. The orientations in which the prepreg layers were laid consists

- 0° - Consider this as the direction along which the continuous UD fibres occur in an X-Y coordinate system. (See Figure 26)
- 45° - This layer all the fibres are at 45° (anti-clockwise) to the 0° layer
- 90° - All fibres in this layer are perpendicular to the 0° layer.
- 135° - All fibres in this layer are at 135° (anti-clockwise) to the 0° layer

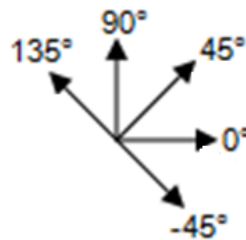


Figure 26 Carbon prepreg layer orientation

For this research, two different stacking sequences were taken into consideration to understand the behaviour of the laminate panel. This research was split into two parts and the stacking sequences remained the same.

1. Parametric study – where steel shims, Teflon and bagging film offcuts of defined geometries were introduced at different depths in the composite laminate during the lay-up process. The details of the exact location and the layers where they were introduced can be found in the results section (Chapter 4) and Appendix 3 below.
2. Impact study – where virgin samples without defects were subjected to impact and then inspected for the damage caused during impact. Two thickness, 3mm and 6mm were made for the impact study. Both low speed Charpy impact and high speed ballistic stone impact experiments were undertaken as part of this thesis. Appendix 4 presents the measured charpy angle and velocity of gas-gun for the actual impact tests.



Figure 27 Representative parametric insert sample (120×120mm) (left) and impact sample (200×100mm) (right)

3.3.1 The Stacking Sequence

Two major types of sequences were used to look at the variation in strengths of the laminates. The following are the sequences,

- a. A quasi-isotropic layup (QI) – This was primarily chosen based on the existing literature so that the work could be comparative in nature. The sequence was $[45^\circ, 135^\circ, 0^\circ, 90^\circ]_s$. Based on the thickness requirements the layup was set to be symmetric around the centre of the stacking sequence. The detailed stacking sequence to make up 3mm and 6mm samples can be found in Appendix 3 below. It should be noted that this stacking sequence was only considered for the impact tests.
- b. A case-specific layup (TWI) – This layup was chosen based on consultation with experts from industry. Though it was a fairly regular layup, a majority of the sequence was laid in such a way that at least two thirds of the layers were in the 0° & 90° , the remainder being 45° & 135° . The sequence was symmetric around the centre of the sample. The detailed sequence can be found in Appendix 3 below. It should be noted that all parametric samples which had inserts, representing manufacturing discrepancies and those for impact testing were made from this sequence.

3.3.2 Composite manufacture using hot press

The prepreg stacked up samples were manufactured using the in-house hot press as seen in Figure 28 below. Two metal plates were first coated with a mould release agent, Frekote supplied by Henkel. At least three coats of the release agent were applied before the prepreg material was laid up on one of the metal plate with the

release agent. The second plate was then closed carefully so that the layers were not disturbed.

The prepreg material was then introduced into the hot press for the curing process. The cure pressure was set to 2 tonnes and cure temperature to 120°C. The cure time was 60 minutes for the samples. These settings were based on the prepreg material supplier information. The hot press cooling function was set to 30°C and was water cooled. Care was taken especially during the sample introduction as the hot plate was allowed to heat up to 120°C.



Figure 28 Hot Press



Figure 29 The hot plate (left) and the control unit (right)

3.4 Multiple inspection systems

This section presents the various methods that were employed to detect and characterise defects and damage that were introduced into the samples.

3.4.1 Pulsed Thermography System – EchoTherm

The pulsed thermography system used was a commercially available unit by the trademark EchoTherm® manufactured and supplied by Thermal Wave Imaging Inc., USA. The system consists of an integrated computer control unit and houses the capacitor banks that power 2 xenon flash lamps. These flash lamps are enclosed in a hood system on which sits an advanced, cooled, quantum detector based, infrared radiometer and goes by the commercial name Phoenix manufactured by Cedip – FLIR Systems. The radiometer is a 640×512 pixel, indium antimonide (InSb) detector based; Stirling cooled system with ability to acquire data at 100Hz at a full frame size of 640×512 pixels. The detailed specification sheet can be found in Appendix 5 below.



Figure 30 EchoTherm pulsed thermography system in use.

The pulsed thermography working principle is as described in sub-sections 2.4.5 & 2.5.1 presented in Chapter 2 and is setup to acquire data in the reflection mode.

3.4.2 FLIR Titanium Infrared Radiometer – Transient & TSA Mode

A FLIR Titanium mid-wave cooled, InSb infrared radiometer was used to make stress measurements, as part of the transient and thermos-elastic stress analysis (TSA). The following is the specification of the radiometer (Table 5).

Table 5 FLIR Titanium infrared radiometer specifications

Name & model	FLIR - Titanium
Detector Name & Type	InSb, Quantum
Equipment Type	Cooled
Operating wavelength	3-5 μm
Operating Temperature	5°C - 300°C
Frame rate	100 Hz – 1.4kHz (based on windowing)
Pixel pitch	15 μm
Sensitivity	15-20 mK
Software controller	Altair, Altair LI, Cirrus

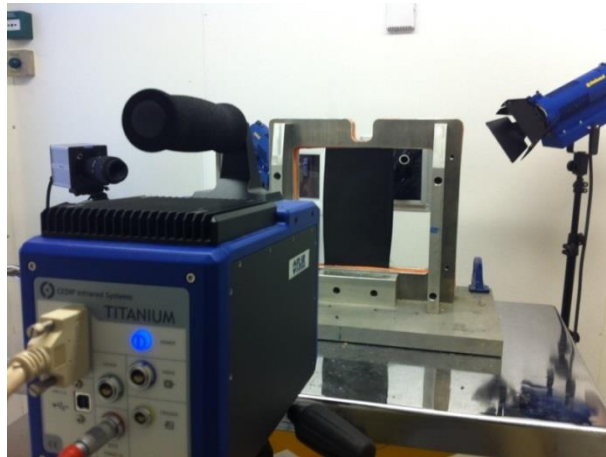


Figure 31 FLIR Titanium infrared radiometer

The same camera system was used in the transient mode where the impact event was recorded on the back surface of the laminate. To achieve a high frame rate acquisition, windowing option was selected. Standard procedure of using a two point black body calibration procedure was followed to perform the non-uniformity correction for a specific window size and acquisition frame rate. The details of the calibration process can be found in the appendix (Appendix 6).

3.4.3 Pulse-echo immersion ultrasonic inspection system

The pulse echo immersion UT method employs a single transducer that does both transmission and reception of the sound signal. The working principle is as described in section 2.3.1. The equipment used for this research is a commercial system with the name USL Scanner manufactured by Ultrasonic Sciences Ltd and the test setup can be seen in the image below (Figure 32).

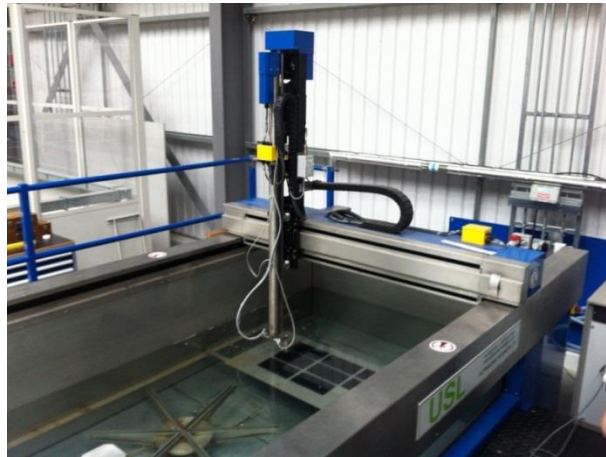


Figure 32 Pulse echo immersion UT testing setup using USL Scanner

As seen in the image above, an ultrasonic probe controlled by a robotic coordinate measuring machine (CMM) arm scans the laminates that are fully immersed in deionised water. The entire scan is controlled by the in-house software, which includes the positioning of the system, and scan settings. The specifications of the scanner can be found in Table 6.

Table 6 USL Pulse Echo Scanner specifications

Name, model & Serial Number	USL Scanner; 3381
Certification Number & Date	6154; 22/05/2013
Scan Procedure	ASTM 317-11
Probe Frequency	5Mhz
Probe Serial Number	056772
Probe Size	0.75" ϕ (dia)
Beam Focus	6" Spherical
Ultrasound Velocity	2880m/s
Scan Step	1mm
Preamp Gain; Gain	10dB; 7dB

3.4.4 Laser Doppler Vibrometer (LDV)

A Polytec PSV-400 laser doppler vibrometer (as seen in Figure 33) was used for the vibrational analysis. The system consisted of a laser scanning head, a computer controller, junction box and a signal generator unit.



Figure 33 The Polytec PSV-400 laser doppler vibrometer

A typical LDV measurement setup is as shown in Figure 34 below.

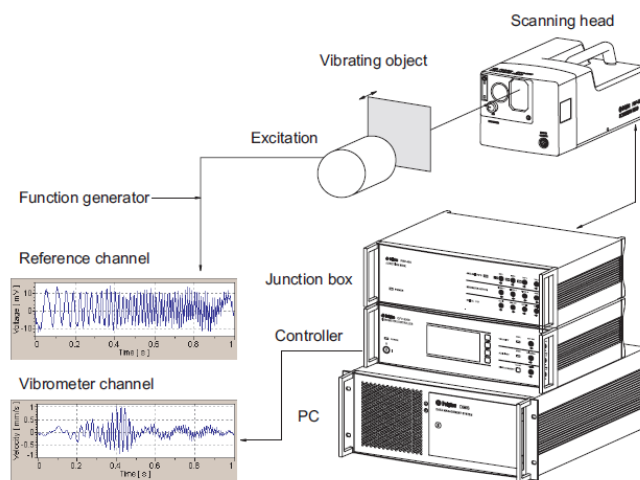


Figure 34 PSV LDV experimental setup

The working principle of the LDV can be summarised as below;

- A shaker is used to vibrate the sample. A periodic signal from the generator is fed to the shaker. As the signal is small, an amplifier unit is used to amplify the signal to enable periodic vibration.

- Using the software interface, scan points are defined on the sample. This is possible through the inbuilt digital camera on the scanner head.
- A measurement beam from the interferometer is positioned on the predefined scan point using on board mirrors. The beam is thus scattered back to the scan head.
- Now the laser beam which is backscattered from the object surface interferes with the reference beam in the scanning head.
- The interference is now recorded by a photodetector that superimposes the data onto the digital image.
- Additionally, a decoder provides a voltage which is directly proportional to the velocity of vibration of the sample and is then digitized.
- This data is now presented as modal frequency maps using the Fast Fourier Transformation of the time signal to the frequency spectrum, thus reconstructing the natural modes of vibration of the sample being vibrated.

The following are the settings used for the vibrational analysis;

Table 7 Settings used for vibration testing using LDV

Channels	Vibrometer + Ref 1
Filters	High Pass -100Hz
Frequency (bandwidth)	10Hz
Sample Frequency	25.6KHz
FFT	6400 lines
Trigger	Analogue – Ref 1
Trigger Level	1% (rising)
Pre-trigger	-20%
Vibrometer Range	VD-03 100mm/s/v
Maximum Frequency (Vibrometer)	1.5MHz
Generator (Active)	Sine Waveform
Frequency (Generator)	5Hz
Amplitude (Generator)	5v
Steady State Time	5s

3.5 Epilogue

This chapter presented the research methodology together with various experimental methods that were used as part of this study. This chapter included the description, specifications and settings of the actual test equipment that were used for this study. Only common test settings were presented, with specific setting being introduced in the next chapter (Chapter 4). It should also be noted that some of the preliminary test setups and results acquired from the tests are presented in Chapter 4 for better readability.

4 RESULTS

This chapter deals with the main body of work undertaken as part of this thesis. It consists of preliminary experimental work, confirming the working principle of pulsed thermography followed by a parametric study on composite laminates confirming the working limitations of the system. As part of the parametric study, the laminates were manufactured by introducing inserts made of steel shims, Teflon and bagging film into the layup. The last part of this chapter presents the results obtained from parametric impact testing on composite laminates with low energy impacts using a modified Charpy and a gas gun ballistic testing.

For the entire work presented in this chapter, thermography remains the main inspection technique to evaluate the condition of the test samples. However, other conventional techniques such as x-radiography, PEUT and LDV have been used to validate the results obtained from the thermography system.

The main aim of this work is to understand and determine the applicability of pulsed thermography in the area of field maintenance. With the increased use of composite materials in the aerospace industry, it is of utmost importance to understand their maintenance requirements by identifying damage as it occurs in the most efficient way and carry out necessary repair thereby increasing the service-life of such advanced components. It is also the notion that pulsed thermography can be an ideal solution for ‘in-situ’ defect and damage characterisation in composite laminates.

As part of this work, other thermography techniques such as passive and thermo-elastic stress (TSA) measurement have been used to characterise the defects and or damage both during their creation (high-speed live monitoring) and post damage creation stages.

4.1 Field reference samples investigation – Preliminary tests

In order to represent field sample, samples ADAT1 and ADAT3 were sourced from a commercial airline company. The samples were inspected using X-Ray and Pulsed Thermography methods. The objective of the inspection was to establish the ability of pulsed thermography to detect artificially introduced sub-surface defects in the sample. This thermal investigation was then validated against conventional X-Radiography to confirm the results obtained from the pulsed thermography system.

Sample Description:

The samples were a cut section of a tail plane wedge of a commercial airliner (300×320mm). The sample was made up of glass fibre reinforced polymer (GFRP) composite outer skin and wood/paper honeycomb material (Nomex®). Figure 35 and Figure 36 show a representative image of the tail plane wedge with the cut edge revealing the internal honey comb structure. The sample was sealed to prevent any additional damage to its internal structure.

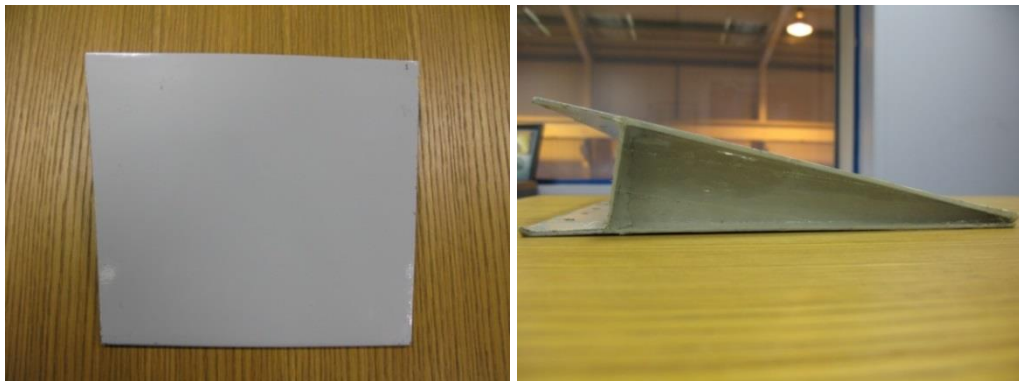


Figure 35 Tail plane wedge (a) top view; (b) side view



Figure 36 Tail plane wedge, side view

4.1.1 Sample: ADAT 1

Problem Description:

- a) To detect sub-surface defects present in the artificially manufactured samples using pulse thermography.
 - i. Figure 35 & Figure 36 show a representative sample to be tested
 - ii. Radiograph of the sample (Figure 37) with the location of the defects indicated by arrows.
- b) The test was conducted on an EchoTherm system. (Please refer to Section 3.4.1 for construction and working principle of the pulse thermography system)

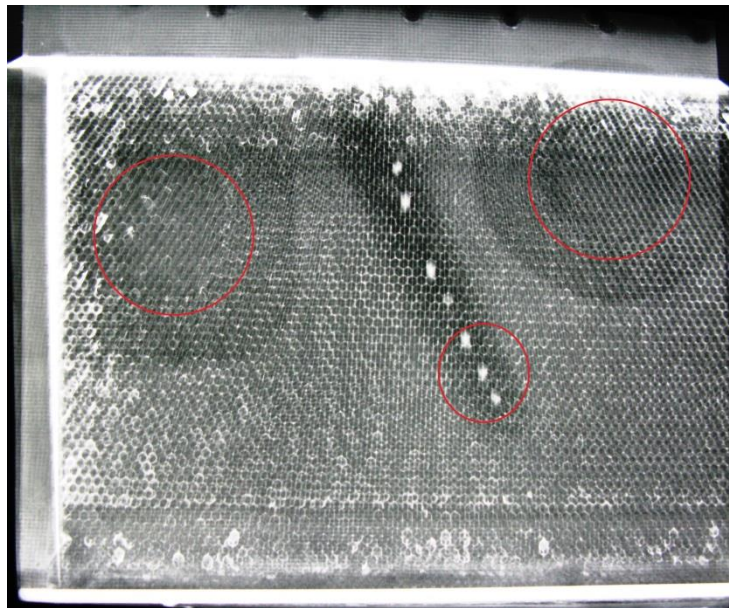


Figure 37 Radiograph image of ADAT 1 with red circular markers indicating the defect location

Pulse Thermography Experimental Settings:

The following are the details of the experimental settings and images acquired from the inspection.

Table 8 Pulsed thermography experiment settings

Sample Number	ADAT 1
Pulse length	25 ms
Frame rate	60 Hz

No. of frames captured	1179
Capture time	19.67 s
Image Sampling – Frame no.	358
Image Sampling – Time	5.97 s

The sample surface was flashed instantaneously using the flash lamps for a pulse length of 25ms and the infrared radiometer recorded the changes in surface temperature just before the flash to the set time of 19.67 s (post flash) acquiring 1179 frames at an acquisition rate of 60Hz. The regions of interest have been represented by red circular markers in the X-ray image (Figure 37). The data obtained from the pulse thermography system was represented in terms of thermograms and time-temperature log plots which were evaluated using the Mosaiq software. The following thermogram was obtained for the time at which the temperature gradient deviated from the linear decay profile for a sound area on the parent material which is referred to as t^* . The frame at which the sampling was done can be inferred from the RAW graphical data. (Represented by a red vertical dotted line. See Figure 39).

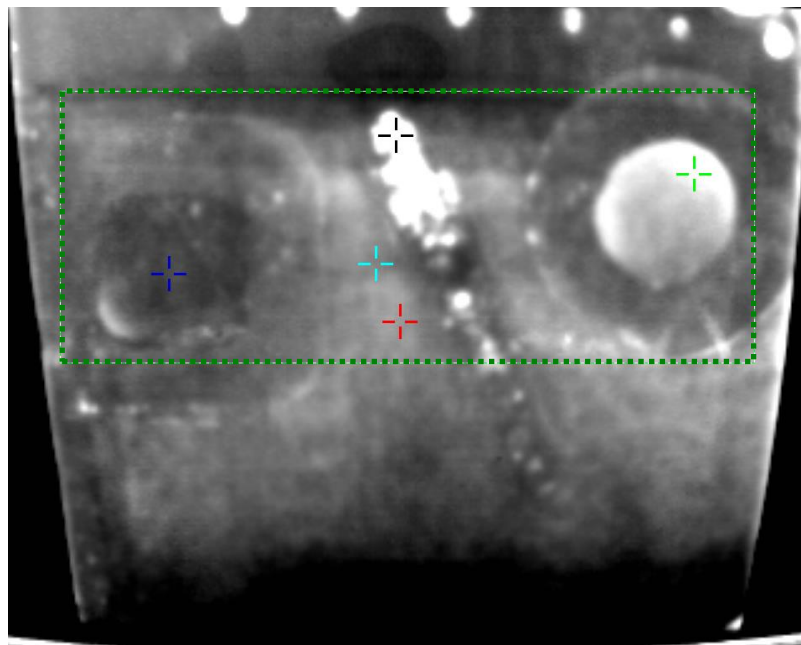


Figure 38 RAW image of ADAT 1 sampled at 5.973 seconds

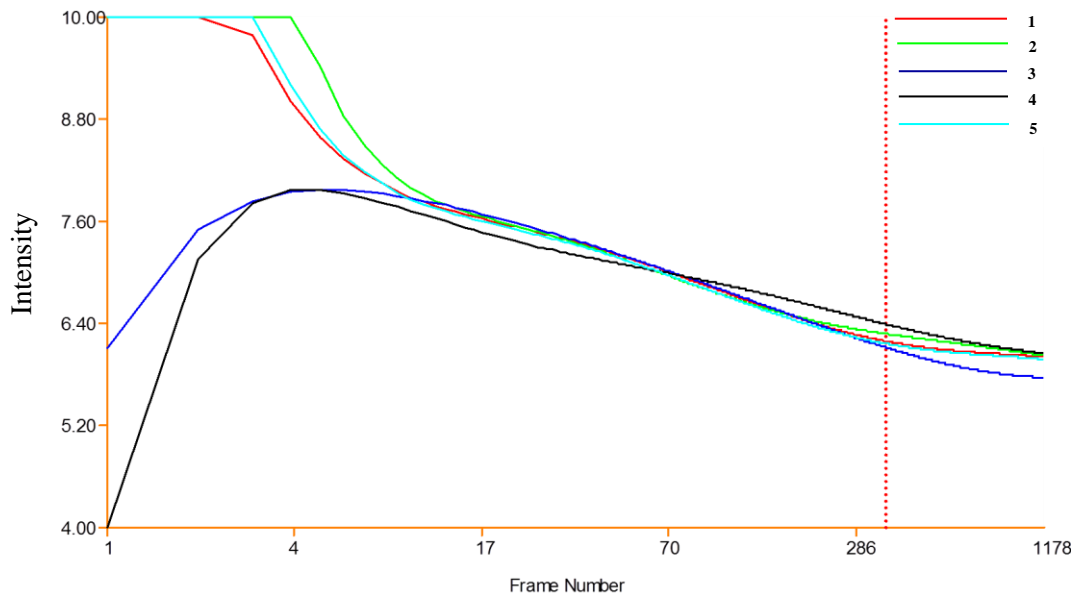


Figure 39 Log plot representing the RAW image for ADAT 1; 1&5 – No defect, 2 – delamination, 3 – disbond and 4 – excess adhesive/water ingress

Result description:

The green box in Figure 38 focuses on the region of interest in the sample. The colour markers on the image represent the position of the defect and defect free areas and correspond to respective curves in the log plot. Figure 38 shows the infrared image obtained at a sampling time of 5.973s (t^*) (Shepard 2007) for an acquisition rate of 60Hz.

It can be inferred from the log plot (Figure 39) that the pulse energy was targeted on the sample and there was a rapid rise in the surface temperature due to the heat dissipated from the flash lamps. The mode of heat transfer by which the energy heated up the surface of the sample was radiative in nature. It was noticed that after about 83ms, the surface temperature of the sample started to cool down as the heat diffused through the upper skin of the sample. The Red & Cyan curves, represented by respective markers from the thermogram, represent the surface temperature decay profile over time and are dependent on the material characteristics of the upper skin of the sample. Further the log plot (Figure 39) revealed that temperature decay characteristics changed indicating that the heat has now diffused through the upper skin, which is referred to as t^* .

As the heat diffused through the defect area, the temperature pattern on the surface of the sample changed thereby changing the profile of the curve. This is due

to the fact that the heat wave either conducts quickly or gets trapped causing localised hot or cold spots over a period of time. In this case, it was noticed that three different defects could be identified in the thermogram corresponding with the defects highlighted in the X-ray image (Figure 37). Though the X-ray image showed the defect locations, it failed to identify and characterise the defects. The thermogram on the other hand gave additional information helping characterise the defects. It was noticed that one of the defects was at a higher temperature and the other at a lower temperature than the overall temperature of the sample.

Analysis:

Literature suggests that the zone where there is localised heating on the surface of the sample represents an area having different heat diffusion characteristics (Green marker) (Schroeder, Ahmed et al. 2002; Shepard 2007). This is because of the fact that localised heating seems to occur at the very beginning of the acquisition suggesting that the defect occurs early on and that the location is in-between the laminate layers of the skin of the sample. The gaps in the skin act as heat barriers preventing the flow of heat through that region causing a localised increase in temperature. Thus this defect was classified as a delamination defect as it appeared in-between the laminate layers of the composite skin.

The second defect represented by the Dark Blue marker acted as a heat sink dissipating the heat quickly through the material. This is represented by the darker patch in the thermogram and continues to cool with an extended t^* than the parent material indicating that the defect occurs at the boundary of the top skin. This defect can thus be classified as a disbond. It should be noted that disbond and delamination are quite similar in the x-ray image whereas the thermogram gives two different temperature prints clearly distinguishing the difference between the two defects. Thus the delamination temperature curve (Green curve) is higher than the defect free zone curve (Red curve) and the disbond temperature curve (Blue curve) is lower than the defect free zone (Red curve).

The third defect represented by the Black curve (Figure 38) could be because of the presence of a different material in the honey comb structure. This may be either a problem of water ingress in the material or excess adhesive in those cells of the honeycomb structure. The RAW image clearly highlights all the subsurface defects

as indicated by the radiograph and with additional details of the possible type of defects occurring in the sample. Additionally, if the material's thermal conductivity was known, the depth of the defects could be established thus improving the inspections data.

The first derivative image (1D) (rate of change of time and temperature) also detects the defects. This 1D image and data are acquired at the same sampling time (5.973s) as the RAW image. The colour markers are representative of the position and characteristics of the defects identified previously from the RAW image. The following is the data obtained for the 1D condition (Figure 40-Figure 41).

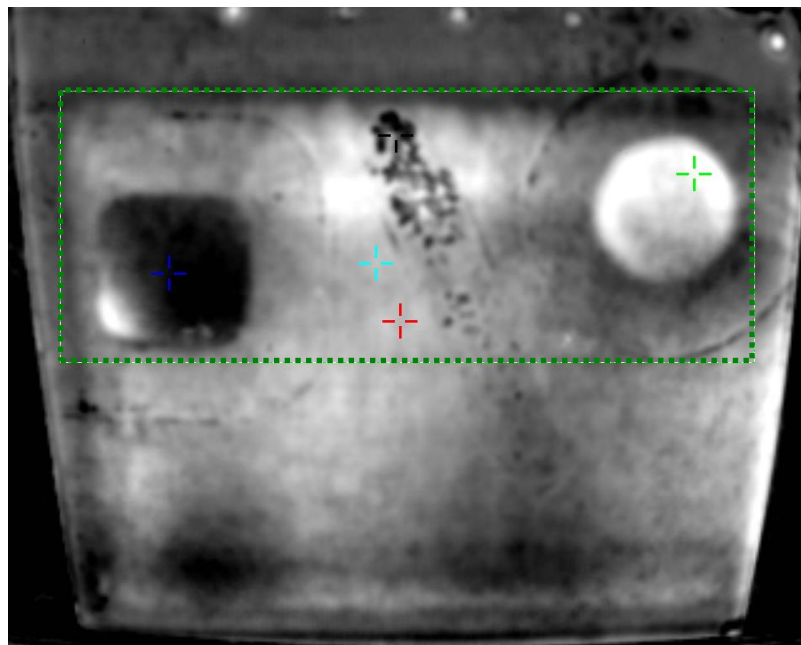


Figure 40 1st Derivative (1D) image of ADAT 1 at 5.973 seconds

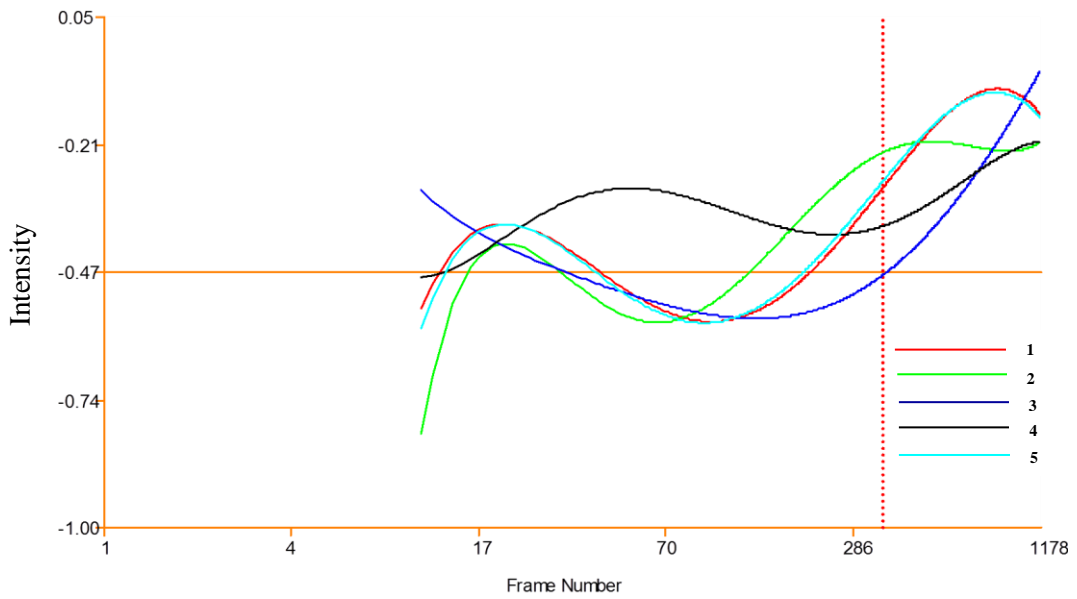


Figure 41 Graph representing the 1D data of ADAT 1; 1&5 – No defect, 2 – delamination, 3 – disbond and 4 – excess adhesive/water ingress

It can be inferred from the above graph that the characteristics of the parent material are superimposed on each other. However, the defects show a different pattern when compared with the parent material confirming them as defects.

The following is the second derivative (2D) image and graphical data obtained at 5.973 seconds as before (Figure 42-Figure 43).

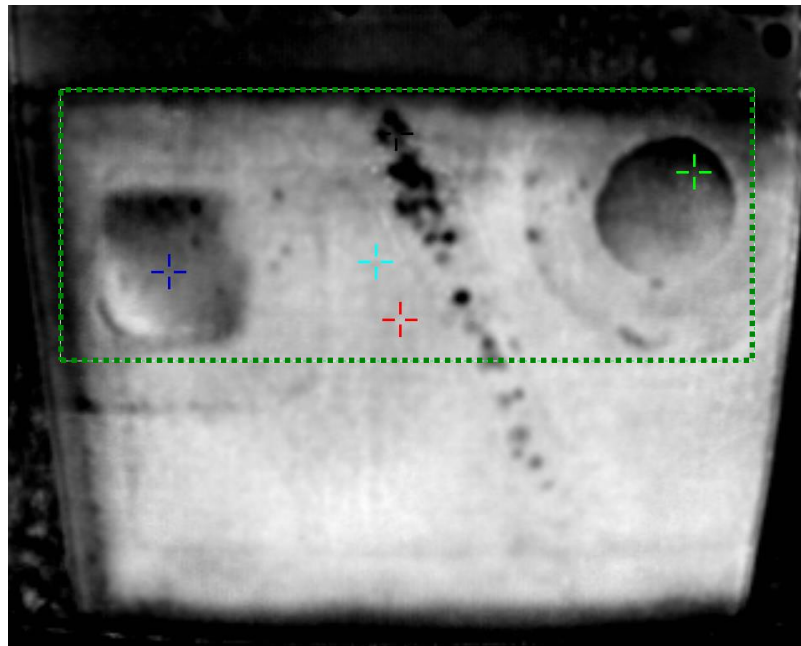


Figure 42 2nd Derivative (2D) image of ADAT 1 at 5.973 seconds

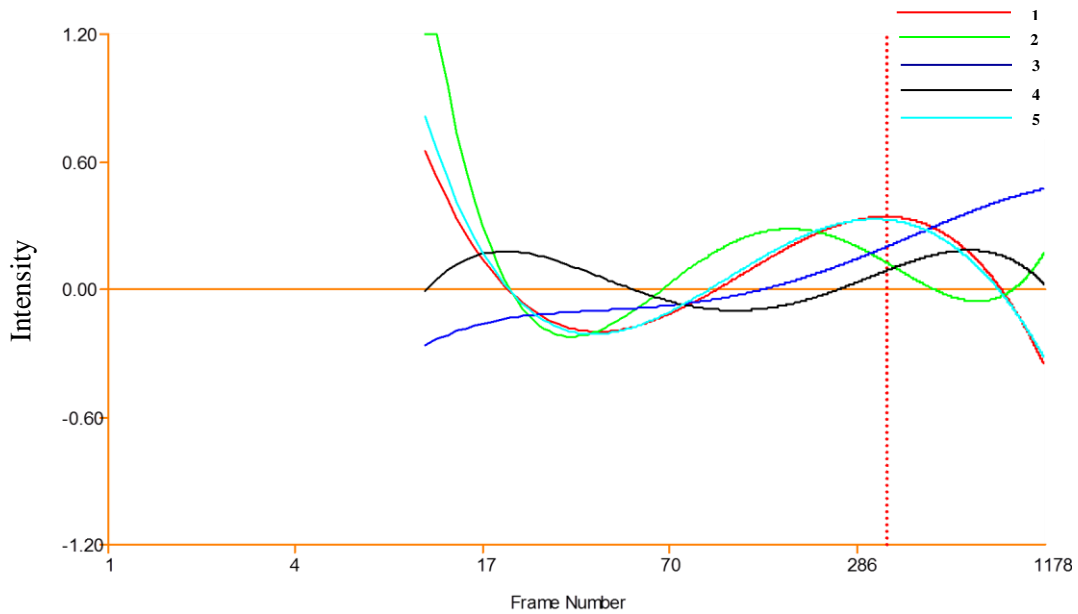







Figure 43 Graph representing the 2D data of ADAT 1; 1&5 – No defect, 2 – delamination, 3 – disbond and 4 – excess adhesive/water ingress

As before, it can be noticed from the 2D graphical plot that the parent material represented by the Red and Cyan curve show a decline in temperature, whereas the defect curves show a different pattern and is representative of the samples damage characteristics. The 2D plot for the parent material show a complete peak directly corresponding with the t^* confirming that the heat has completely diffused through the upper skin. Now the delamination curve (Green curve) peaks significantly ahead of the 2D peak of the parent material, confirming its occurrence through thickness of the upper skin whereas the disbond peak does not yet occur indicating that the peak would be much later than the parent material. This indicated the need for an extended data capture to investigate the disbond further. However, taking in view the qualitative nature of the data, the results were found to be sufficient to yield conclusive results where all defects were identified by the inspection.

Conclusion:

Thus it can be seen from the above data that more information on the defect characterisation has been obtained from pulse thermography in comparison with the x-ray image. There is a clear distinction in the type of the defects introduced in the sample. The following is a table summarising the types of defects found in ADAT1 sample.

Table 9 Defect classification markers

Colour markers	Defect classification
Red 	Defect free area
Green 	Delamination
Dark Blue 	Disbond
Black 	Excess adhesive / water ingress
Cyan 	Defect free area

4.1.2 Sample: ADAT 3

In order to validate the results obtained from ADAT1, ADAT 3 another tail plane wedge similar to ADAT1 and had defects manually introduced at different locations, was used to repeat the pulsed thermography inspection. The following are the inspection results obtained from ADAT3.

Problem Description:

- a) To detect sub-surface defects present in the artificially made samples using pulse thermography and confirm if they are in line with the findings of ADAT1.
 - i. Figure 35& Figure 36 show a representative sample to be tested
 - ii. Radiograph of the sample (Figure 44) with the location of the defects indicated by arrows.
- b) The test is conducted on an EchoTherm system. (Please refer to Section 3.4.1 for construction and working principle of the pulse thermography system)

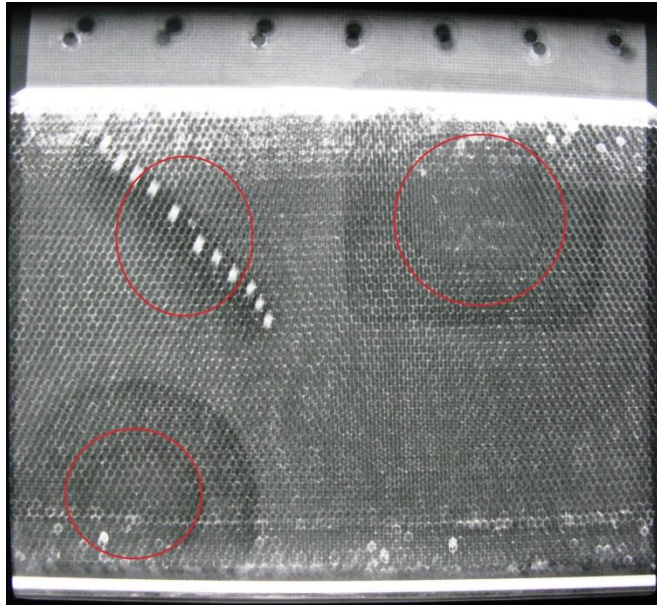


Figure 44 Radiograph of ADAT 3 with red circular markers showing the defect location

Pulse thermography experimental settings:

The following are the details of the experimental settings and images acquired from the inspection.

Table 10 Pulse thermography experimental settings for ADAT 3

Sample Number	ADAT 3
Pulse length	25ms
Frame rate	60 Hz
No. of frames captured	1179
Capture time	19.67s
Image Sampling – Frame no.	358
Image Sampling – Time of capture	5.97s

As before, the setting used to acquire data for ADAT 1 was used to acquire data for ADAT 3. The sample surface was instantaneously heated with a 25ms flash and the infrared radiometer recorded the surface temperature profile of the sample. The data was acquired at 60Hz for a time of 19.67s accumulating a total of 1179 frames (post flash). As before, the time t^* at which the change in slope of the parent material occurred in case of ADAT 3 was found to be at 5.973 seconds matching

with the data time for ADAT 1. The following are the RAW, 1D and 2D data acquired for ADAT 3 from the thermographic inspection (Figure 45-Figure 50).

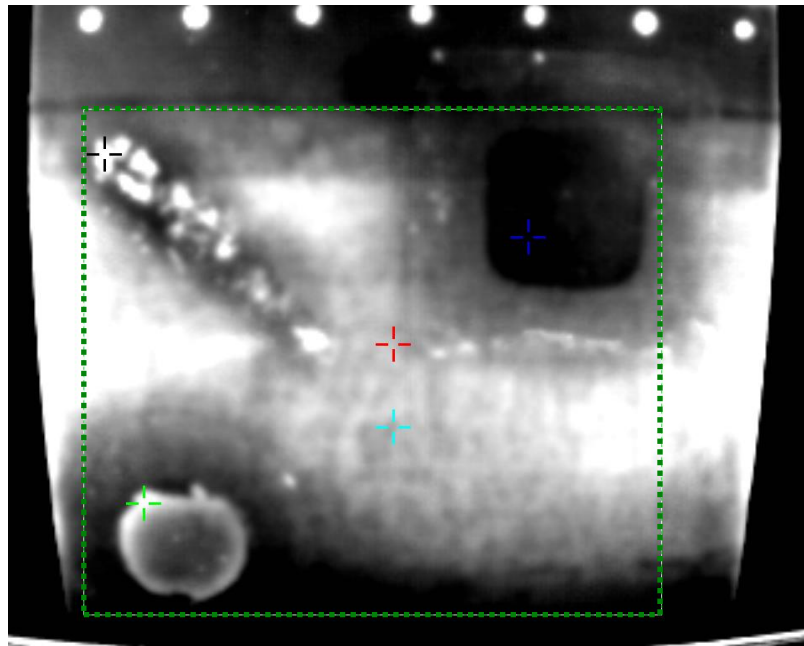


Figure 45 RAW image of ADAT 3 sampled at 5.973 seconds

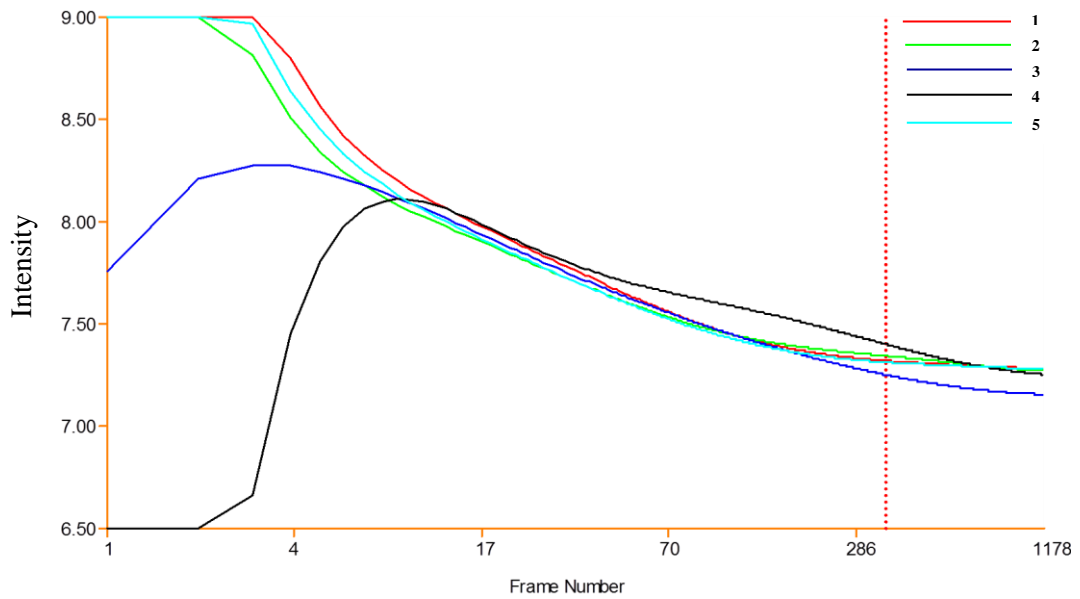


Figure 46 Log plot representing the RAW image for ADAT 3; 1&5 – No defect, 2 – delamination, 3 – disbond and 4 – excess adhesive/water ingress

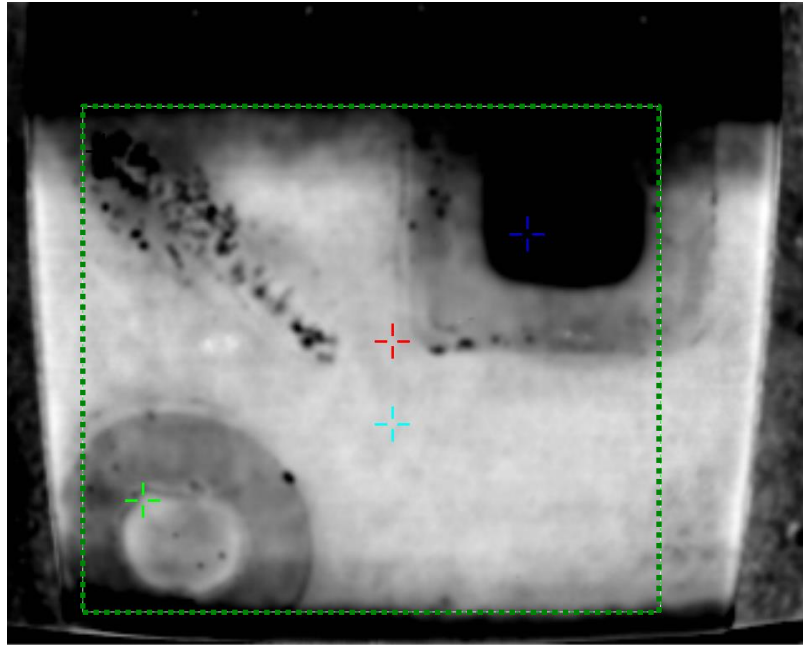


Figure 47 1st Derivative (1D) image of ADAT 3 at 5.973 seconds

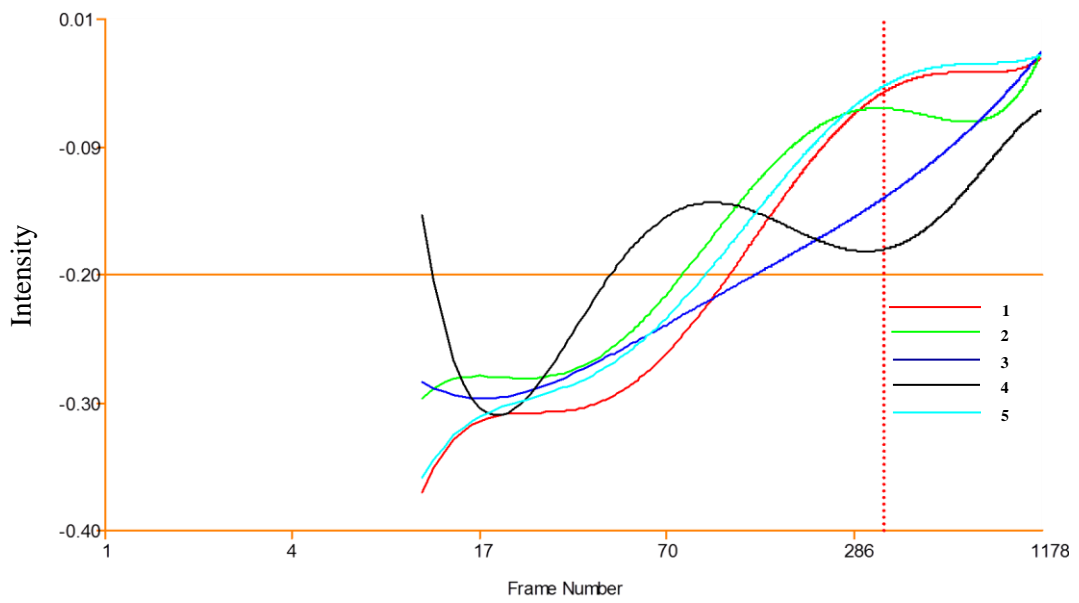


Figure 48 Graph representing the 1D data of ADAT 3; 1&5 – No defect, 2 – delamination, 3 – disbond and 4 – excess adhesive/water ingress

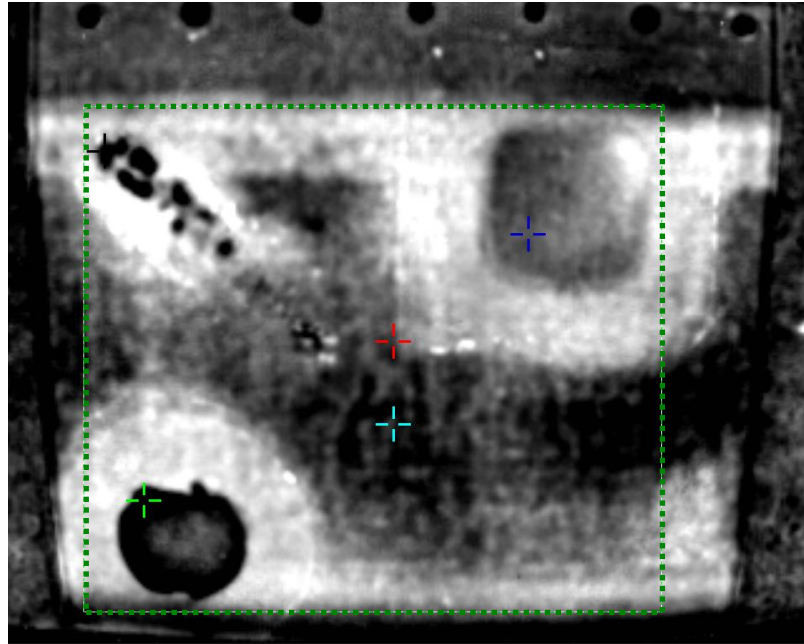


Figure 49 2nd Derivative (2D) image of ADAT 3 at 5.973

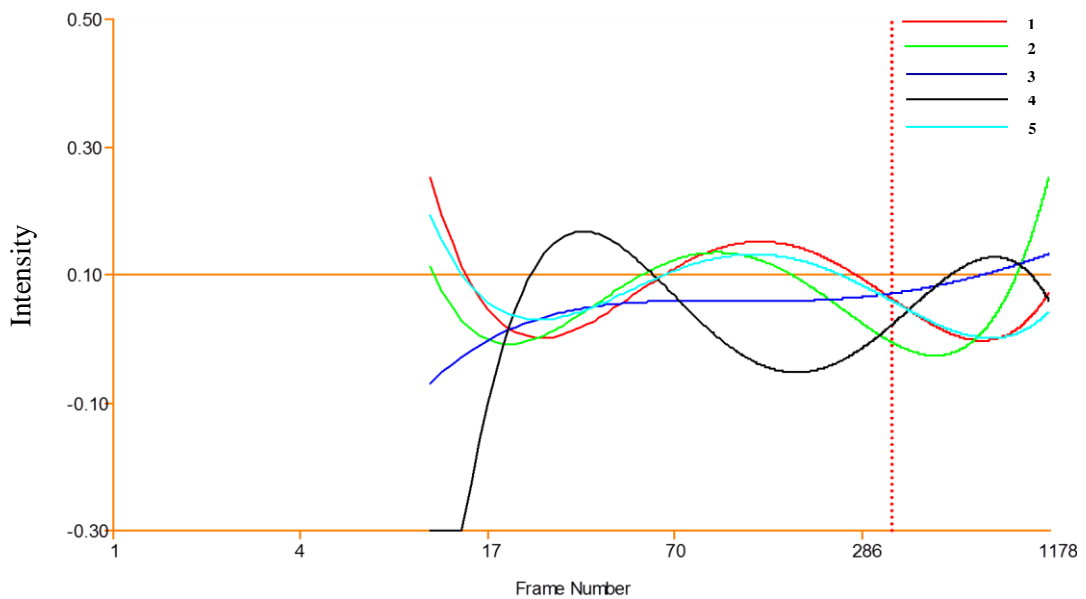


Figure 50 Graph representing the 2D data of ADAT 3; 1&5 – No defect, 2 – delamination, 3 – disbond and 4 – excess adhesive/water ingress

Result description:






This experiment has been conducted with the same settings as in the case of ADAT 1. Hence a similar colour marking system has been adapted. As before, the green box (Figure 45) focuses on the region of interest in the sample. The different colour markers on the image represent the position of the defect and defect free areas and correspond to respective curves in the log plot.

Again, it can be noticed that three different defects were identified in the thermographic image corresponding with the defects highlighted in the X-ray image. As before, the X-ray image only showed the defect locations and did not provide any additional information. The major differences in the case of ADAT 3 were due to the location of the defects. In other words, the parent material's temperature decay was found to be similar to that of ADAT 1. Additionally, the delamination (Green marker & curve) and the disbond (Blue marker & curve) exhibit similar characteristics. The 1D and 2D data show that the delamination is almost close to the back wall and hence the change in slope isn't that prominent. However, the thermogram shows a sharp distinction between the parent material and defect. Thus the inspection data clearly highlighted all the subsurface defects with clear distinction of the defects than that acquired from the X-ray data.

Conclusion:

Thus it can be seen from the above data that more information on the defect characterisation has been obtained from pulse thermography. The data was found to be in close agreement with the data obtained for ADAT 1. It was also noted that the intensity levels varied from the previous inspection and is a combination of the factors such as, the nature of sample, the location of the defects and the variations in the flash heating of the samples. These changes are fully observed in the 1D and 2D plot above. The following is a table summarising the types of defects found in ADAT3 sample.

Table 11 Defect classification markers

Colour markers	Defect classification
Red 	Defect free area
Green 	Delamination
Dark Blue 	Disbond
Black 	Excess adhesive / water ingress
Cyan 	Defect free area

4.1.3 Discussion

The field maintenance study carried out on samples obtained from a commercial airline establishes the working principle of pulsed thermography even though the defects were artificially introduced into the sample. As per the results presented above, the samples ADAT 1 and ADAT 3 reveal similar type of defects. They also follow similar heat diffusion patterns. It can be noted that the RAW thermal image of both the samples ADAT1 and ADAT3 reveal the most prominent defects. The heat diffusion characteristics when plotted in a log time – temperature ($\log t-T$) curve show the change in slope of the defect from the sound area much ahead of the t^* of the samples. From the above samples, after repeated trials, a time of 20 sec seems to be an optimum inspection setting. The analysed data detects the damage at t^* sampled for maximum contrast. This was confirmed from the 1D and 2D data as presented in the results above. This preliminary testing also established a methodology for determining the optimum test setting the pulsed system needs to be configured to.

4.2 Parametric study

The parametric study to understand the defect detection capability of EchoTherm Pulsed Thermography system was carried out as described in Section 3.1. The results presented in the preliminary tests (Section 4.1) were based on field maintenance samples. Those samples were artificially manufactured externally and complete information on the manufacture of those samples is unknown. It is thus necessary to perform tests that are systematic in nature to understand the detection capability of the pulsed thermography system and to establish its limitations.

This section will primarily focus on a systematic parametric approach to determine the working limitations of the system together with its strength which aids the system to confirm the defects. For this a set of samples with various inserts made of different materials were designed. These inserts were introduced at the lay-up stage into the prepreg material at specific locations and pre-determined depths. These samples were then press cured using a hot press to manufacture the samples. A range

of samples having different thicknesses having different material inserts were thus designed to perform this parametric test.

The following are the materials inserted into 120GSM UD carbon fibre to make up samples of 120 × 120mm

- Sheet shim inserts
- Teflon inserts
- Bagging film inserts

It should be noted that the selection of these three materials was based on literature that identified the most common defects that occur during manufacture as explained in Section 2.5.1 above. The following are the results obtained from the study.

4.2.1 Experimental results

This section deals with the experimental results obtained by inspecting the laminates with inserts using pulsed thermography and pulse echo immersion ultrasonic testing.

4.2.1.1 Sheet metal defect inserts

As described in the previous chapter mild steel shim defects of 20µm thickness were introduced into 120 × 120mm UD carbon fibre composites. Refer section 3.3 for lay-up procedure, Figure 21-Figure 22 for defect morphology and Appendix 3 for the stacking sequence. Only TWI layup was used for this study.

Table 12 3mm laminates with steel shim inserts; defect location and tests performed

Sample Thickness in mm	Defect Material	Defect Dimensions in mm	Defect Location from surface in mm	NDT tests carried out
3	Mild steel shim, Thickness: 20 µm	∅6 - circular defect	0.5	PT ³ Immersion UT ⁴
			1.0	
			1.5	
3	Mild steel shim, Thickness: 20 µm	∅8 - circular defect	0.5	PT Immersion UT
			1.0	
			1.5	

³ PT – Pulsed thermography

⁴ UT – Ultrasonic testing

3	Mild steel shim, Thickness: 20 μm	6 & 8 cutoffs – slotted aperture	0.5	PT Immersion UT
			1.0	
			1.5	

Table 13 Pulsed thermography experimental settings. Sample: 3SS2

Sample Number	3SS2
Pulse length	25ms
Frame rate	30Hz
No. of frames captured	450
Capture time	14.68s
Image Sampling – Frame no.	21
Image Sampling – Time of capture	0.7s

The settings for the inspection can be referred from Table 13. The test was carried out at 30Hz acquisition frame rate for 14.7s (450 fms). The following results were obtained from the thermographic inspection.

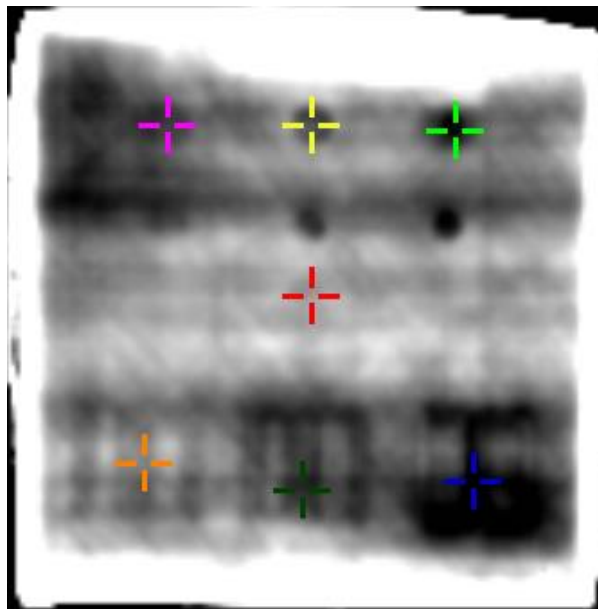


Figure 51 RAW Thermal image - Sample: 3SS2 (120×120mm); Sampling time: 0.7s

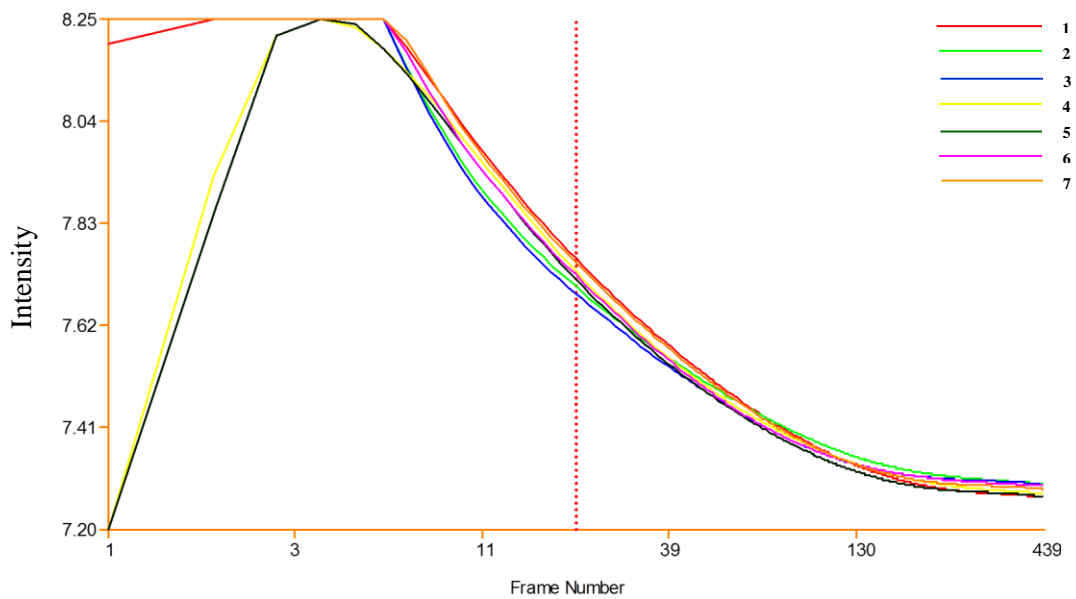


Figure 52 Log t-T plot for the RAW data; Sample: 3SS2; 1 – No defect; 2,3 – 0.5mm depth; 4,5 – 1.0mm; 6,7 – 1.5mm.

Analysis:

From the log t-T plot (Figure 52) the t^* for the 3mm thick laminate was estimated at 3.97s. The thermogram above (Figure 51) shows the defects at depths 0.5mm and 1mm which relate to the defects on the right and centre of the laminate respectively. The third set of defects were barely visible on the left hand side which were at a depth of 1.5mm from the surface of the laminate.

The following observations can be made from this result:

- It was observed that the thermogram at t^* did not show the defects and hence the sampling time of 0.7s was used to get the best contrast for the defects.
- It can be seen from the temperature decay characteristics that there is a different profile between the sound and defect areas; for defects occurring at 0.5mm depth (represented by Green & Navy Blue curves).
- As the heat wave hits the 1st set of defects (Green & Navy Blue marker), them being metallic in nature; tend to conduct the heat much faster than the sound area pixel. Thus the temperature profile was found to be cooler than the parent material.
- There is also distinction of the 2nd set of defects represented by the Yellow and Dark Green markers and thus are clearly visible on the thermogram.

- The 3rd set of defects are found to be much deeper and hence the temperature profile for the defects on the left side appear to follow the parent material indicating that the thermal wave has lost its intensity mainly due to the depth location of the defects.

Thus the inspection of the laminate with mild steel shim insert of thickness 20 μ m, though showed three set of defects, the signal to noise ratio (SNR) was only ideal to clearly distinguish two sets of defects. Further, it should be understood that the defect thickness and depth of occurrence play a vital role in improving the SNR. Hence the third set of defects showed a profile similar to that of the parent material.

UT Results:

Immersion pulse echo UT was performed on the above laminate using the USL scanner with a 5Mhz probe as per the settings mentioned in section 3.4.3. The following time of flight image was obtained.

Table 14 Sample thickness measurement from PEUT - Sample: 3SS2

Sample Number	3SS2
Measured Sample Thickness	2.52mm
Waterpath	149.4mm

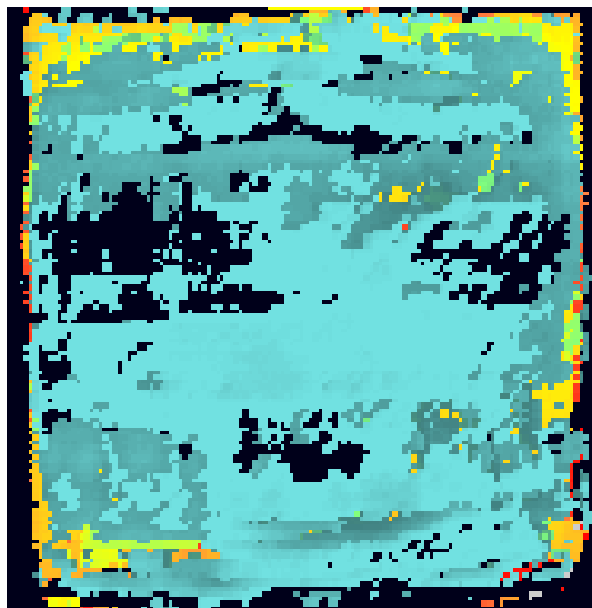


Figure 53 Time of flight (ToF) image for 3mm laminate (120x120mm) - Sample: 3SS2

The results from the PEUT technique measured the laminate thickness to be 2.52mm. However the time of flight or ToF image did not detect the defects and thus the results were found to be inconclusive. Further this laminate in particular was found to be quite noisy indicating that the manufactured quality was not optimum.

Conclusion:

The 3mm laminate with sheet metal insert results indicate that pulsed thermography detected all defects. However, the temperature profiles of the 3rd set of defects occurring at about 1.5mm depth were not fully detectable. This helped reach the detection limits of the system and hence a 6mm laminate was not manufactured.

4.2.1.2 Teflon defect inserts

Teflon inserts (500µm thick) were introduced into 120 × 120mm UD carbon fibre composites. 3mm, 6mm and 9mm thick samples were made in the hot press. Refer to section 3.3 for lay-up procedure, Figure 21-Figure 22 for defect morphology and Appendix 3 for lay-up sequence. Only TWI layup was used for this study.

3mm laminates with Teflon inserts:

The following are the details of the defect type and locations for the 3mm laminate.

Table 15 3mm laminates with Teflon inserts; defect location and tests performed

Sample Thickness in mm	Defect Material	Defect Dimensions in mm	Defect Location from surface in mm	NDT tests carried out
3	Teflon Thickness: 500 µm	∅6 - circular defect	0.5	PT Immersion UT
			1.0	
			1.5	
3	Teflon Thickness: 500 µm	∅8 - circular defect	0.5	PT Immersion UT
			1.0	
			1.5	
3	Teflon Thickness: 500 µm	6 & 8 cutoffs – slotted aperture	0.5	PT Immersion UT
			1.0	
			1.5	

Pulsed Thermography Results:

The settings for the inspection can be referred from Table 16. The test was carried out at 30Hz frame rate for the acquisition time of 14.7 sec (450 fms). The following is the thermographic data from the inspection.

Table 16 Pulsed thermography experimental settings. Sample: 3TF1

Sample reference no.	3TF1
Frame rate	30 Hz
No. of frames captured	450
Capture time	14.68s
Image Sampling – Frame no.	8
Image Sampling – Time of capture	0.27s

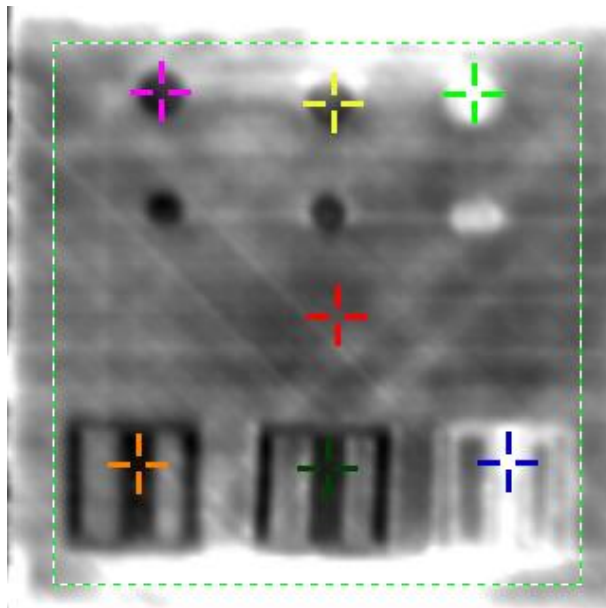


Figure 54 RAW Thermal image - Sample: 3TF1 (120×120mm); Sampling time: 0.27s

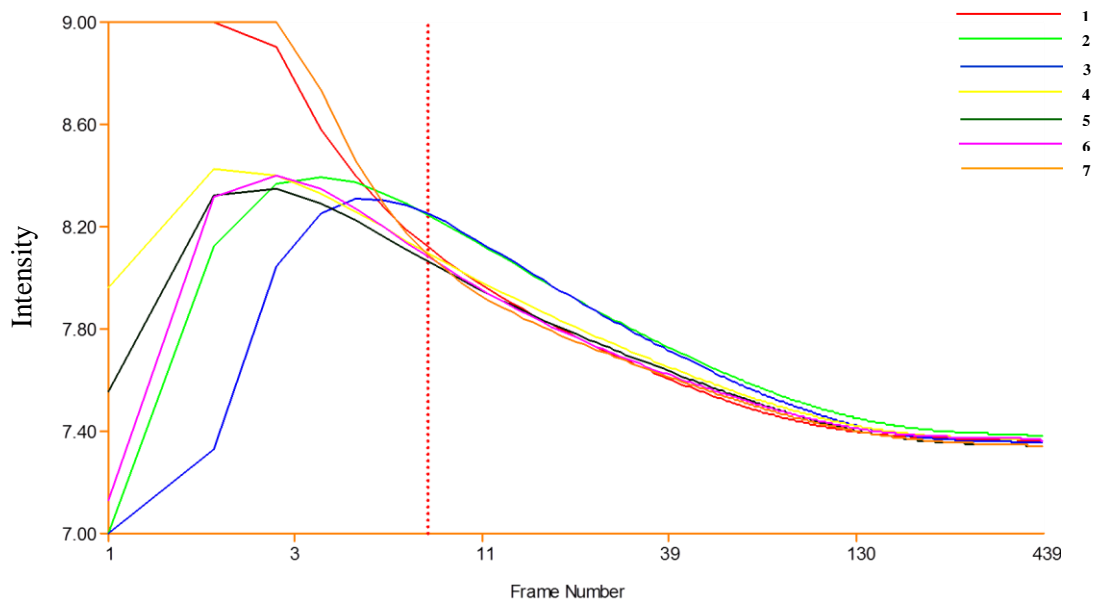


Figure 55 Log t-T plot for the RAW data; Sample: 3TF1; 1 – No defect; 2,3 – 0.5mm depth; 4,5 – 1.0mm; 6,7 – 1.5mm

Analysis:

From the log t-T plot the t^* was estimated at 3.97s which is exactly the same as seen in the case of 3mm laminate with steel shim insert. Based on the above results presented in Figure 54, the following observations were made;

- As before, the thermogram was obtained for best contrast and not at t^* .
- The set of defects closest to the surface at a depth of 0.5mm is on the right side of the sample and represented by Green and Navy Blue markers.
- It was noticed that the 1st set of defects were closest to the laminate surface. Further, Teflon is non-conducting in nature and hence showed higher temperature decay profile in comparison with the parent material which is represented by the Red marker on the thermogram and Red curve on the log thermal plot.
- The 2nd set of defects (represented by Yellow and Dark Green markers) occur at a depth of 1mm from the laminate surface and located around the middle section showed a good contrast on the thermogram. It was observed that the temperature decay curve was found to be quite close with the sound areas of the laminate and did not show a huge difference.

- For the 3rd set of defects (represented by Pink and Orange markers) occurring on the left hand side were located at a depth of 1.5mm. These defects are clearly identified in the thermal image through a good contrast difference, but did not show a huge difference in the thermal profile when compared with sound areas of the laminate.

UT Results:

The following is the ToF image obtained from the PEUT immersion test.



Figure 56 Time of flight (ToF) image for 3mm laminate (120×120mm) - Sample: 3TF1

Table 17 Sample thickness measurement from PEUT - Sample: 3TF1

Sample Number	3TF1
Measured Sample Thickness	2.56mm
Waterpath	147.4mm

The UT results in this case clearly picked up all the defects. The ToF image showed the three sets of defects with a slight colour gradient suggesting that the defects occur at different depths.

Conclusion – 3mm laminate with Teflon inserts:

Thus all three sets of defects occurring at 0.5mm, 1mm and 1.5mm were easily detected using both pulsed thermography and immersion ultrasonic testing. Further the UT results validated the pulsed thermography results.

6mm laminate with Teflon inserts:

The following are details of the defect and their depth locations.

Table 18 6mm laminates with Teflon inserts; defect location and tests performed

Sample Thickness in mm	Defect Material	Defect Dimensions in mm	Defect Location from surface in mm	NDT tests carried out
6	Teflon Thickness: 500 µm	∅6 - circular defect	2.0	PT Immersion UT
			2.5	
			3.0	
6	Teflon Thickness: 500 µm	∅8 - circular defect	2.0	PT Immersion UT
			2.5	
			3.0	
6	Teflon Thickness: 500 µm	6 & 8 cutoffs – slotted aperture	2.0	PT Immersion UT
			2.5	
			3.0	

Pulsed Thermography Results:

The following are the pulsed thermography experimental settings:

Table 19 Pulsed thermography experimental settings. Sample: 6TF1

Sample reference no.	6TF1
Frame rate	12 Hz
No. of frames captured	310
Capture time	25s
Image Sampling – Frame no.	11
Image Sampling – Time of capture	0.92s

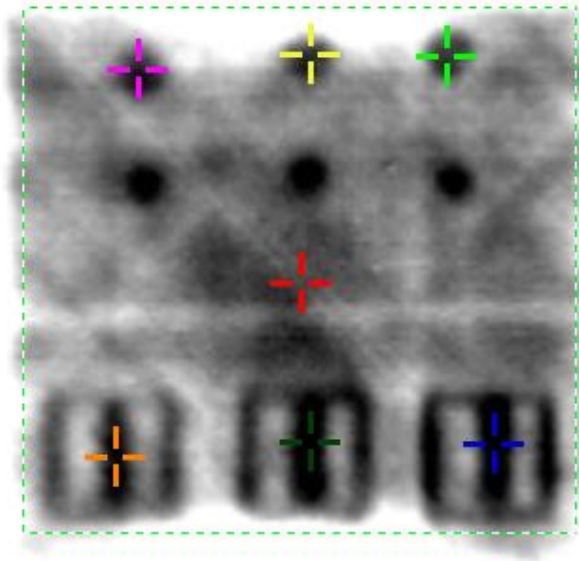


Figure 57 RAW Thermal image - Sample: 6TF1 (120×120mm); Sampling time: 0.92s

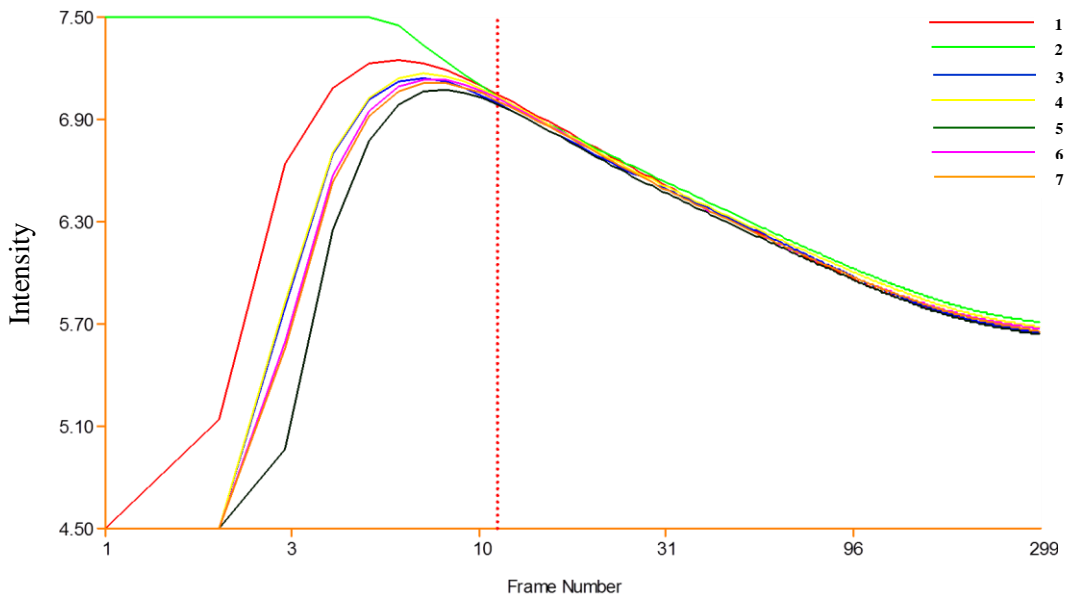


Figure 58 Log t-T plot for the RAW data; Sample: 6TF1; 1 – No defect; 2,3 – 2.0mm depth; 4,5 – 2.5mm; 6,7 – 3.0mm

Analysis:

For the inspection of 6mm thick Teflon insert sample (6TF1), the inspection was carried out at 30Hz initially. It was noticed that not all control defects were visible in the thermal image. This is due to the fact that the diffusion of heat through the composite material is much slower than in the metals as they are non-conducting in nature. In order to achieve complete penetration of the heat through the sample and

the surface temperature data to be captured, the acquisition frame rate for this sample was reduced to 12Hz.

As before, from the above figures, (Figure 57-Figure 58) all the control defects, both dots and the slotted aperture inserts are visible in the thermal image. These defects follow a similar cooling pattern to that of the 3mm thick Teflon sample, 3TF1 mentioned in the sub-section above. Though the thermogram in Figure 58 clearly indicated all the control defects, it was noticed from the log plot that the temperature decay pattern is very close to the sound area of the sample and the t^* in this case was at 16.68s. As before, the thermogram was acquired for a sampling time of 0.92s which achieved the maximum thermal contrast that clearly identified all embedded defects.

UT results:

The following results were acquired using the PEUT system.

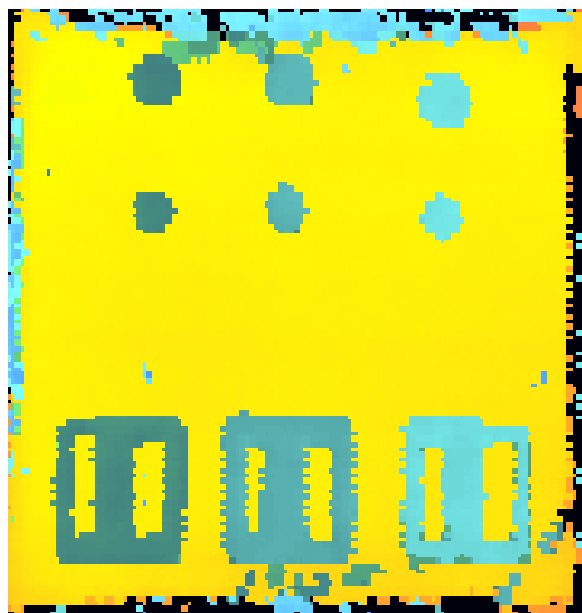


Figure 59 Time of flight (ToF) image for 6mm laminate (120x120mm) - Sample: 6TF1

Table 20 Sample thickness measurement from PEUT - Sample: 6TF1

Sample Number	6TF1
Measured Sample Thickness	5.12mm
Waterpath	147.5mm

As before, the UT ToF image detected all Teflon defects introduced into the laminate validating the pulsed thermography data. There is also difference in amplitude measurements between different sets of defects confirming their variation in depth of the laminate.

Conclusion – 6mm laminate with Teflon inserts:

Thus all Teflon inserts at depths 2mm, 2.5mm and 3mm were detected by both the pulsed thermography and immersion UT testing.

9mm laminate with Teflon inserts:

The following are the details of the Teflon inserts and their locations:

Table 21 9mm laminates with Teflon inserts; defect location and tests performed

Sample Thickness in mm	Defect Material	Defect Dimensions in mm	Defect Location from surface in mm	NDT tests carried out
9	Teflon Thickness: 500 µm	∅6 - circular defect	3.5	PT Immersion UT
			4.0	
			4.5	
9	Teflon Thickness: 500 µm	∅8 - circular defect	3.5	PT Immersion UT
			4.0	
			4.5	
9	Teflon Thickness: 500 µm	6 & 8 cutoffs – slotted aperture	3.5	PT Immersion UT
			4.0	
			4.5	

Pulsed thermography results:

The following are the setting used for the inspection of 9mm thick laminates with Teflon inserts at locations as specified in Table 21.

Table 22 Pulsed thermography experimental settings. Sample: 9TF1

Sample reference no.	9TF1
Frame rate	8.56Hz
No. of frames captured	240
Capture time	28s

Image Sampling – Frame no.	12
Image Sampling – Time of capture	1.4s

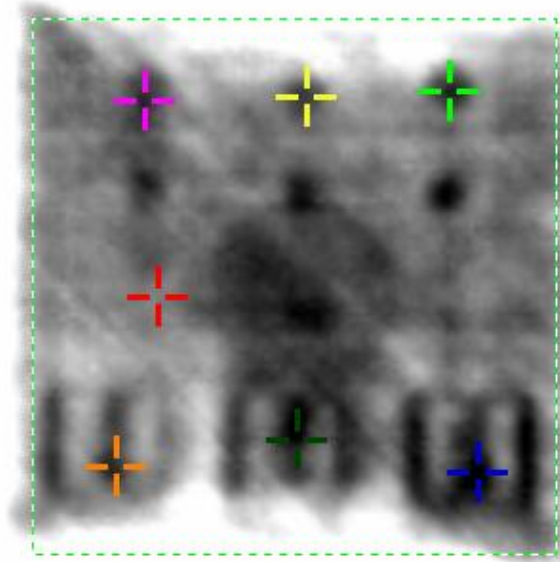


Figure 60 RAW Thermal image - Sample: 9TF1 (120×120mm); Sampling time: 1.4s

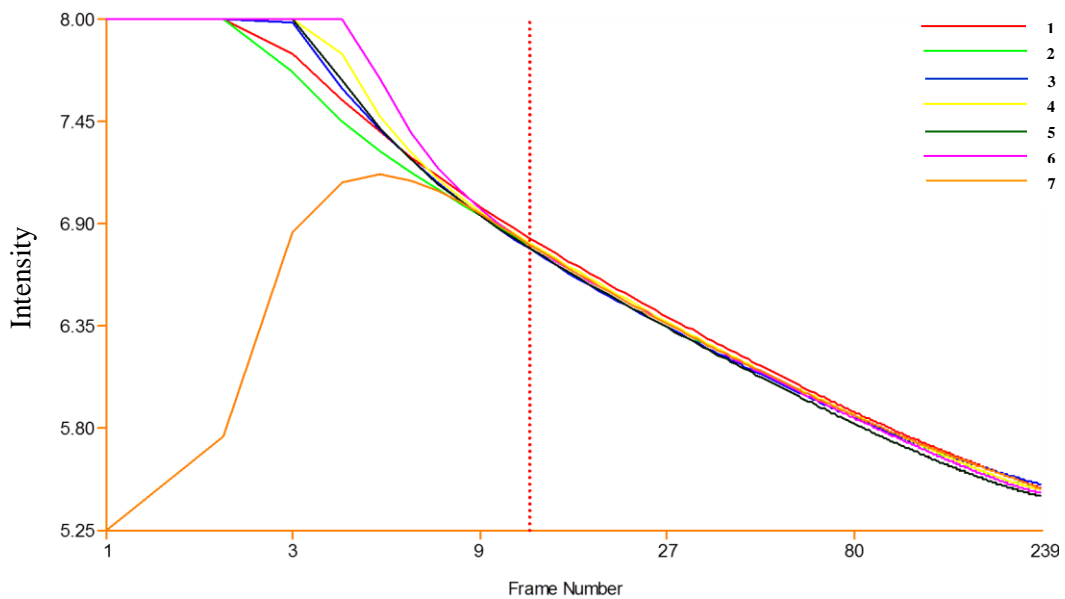


Figure 61 Log t-T plot for the RAW data; Sample: 9TF1; 1 – No defect; 2,3 – 3.5mm depth; 4,5 – 4.0mm; 6,7 – 4.5mm

Analysis:

Due to the thickness of the laminate, the acquisition frame rate was reduced to 8.56Hz for a maximum time of 28s. The t^* in this case was estimated around 19.85s. It should be noted that the accuracy of this back wall time measurement is reduced

due to the reduced frame rate. Further extended data capture beyond 30s meant that the heat wave is completely dissipated and thus there is reduction in the surface temperature. This also meant that the data beyond this point was not physically possible for the current system establishing the limitation of the system.

All buried defects were identified by the inspection. However, the set of defects occurring at a depth of 4.5mm are just faintly visible on the thermogram and have the same pattern as the sound area.

UT results:

The following are the results obtained by the immersion UT system:



Figure 62 Time of flight (ToF) image for 9mm laminate (120×120mm) - Sample: 9TF1

Table 23 Sample thickness measurement from PEUT - Sample: 9TF1

Sample Number	9TF1
Measured Sample Thickness	7.5mm
Waterpath	143.6mm

The UT results picked up all the Teflon inserts in the 9mm thick laminates. It was observed that there was a loss in thickness measurement based on the waterpath suggesting that there was attenuation of the ultrasound in the material. However, all

defects were detected by the UT system, confirming the findings of the pulsed system.

Conclusion:

The Teflon inserts at different depths in 3mm, 6mm and 9mm samples were successfully detected by both pulsed thermography and immersion pulse echo ultrasonic testing techniques. This test further looked at the system limitations, where defects beyond the depth of 4.5mm will now be difficult to detect. Further, a reduced capture rate and increased capture time meant the accuracy of the results is reduced. In a real life scenario, this would also mean that some deeper defects might be missed and hence where possible higher capture rate needs to be employed. The limitations of the system to detect defects made of Teflon are restricted to a depth of 4.5mm.

4.2.1.3 Bagging film defect inserts

Bagging film inserts (20µm thick) were introduced into 120 × 120mm UD carbon fibre composites as before. 3mm & 6mm thick samples were made in the hot press. Refer section 3.3 for lay-up procedure, Figure 21-Figure 22 for defect morphology and Appendix 3 for lay-up sequence.

3mm laminate with bagging film inserts:

The following are the details of the bagging film defects that were introduced into the 3mm laminate.

Table 24 3mm laminates with bagging film inserts; defect location and tests performed

Sample Thickness in mm	Defect Material	Defect Dimensions in mm	Defect Location from surface in mm	NDT tests carried out
3	Bagging film Thickness: 20 µm	∅6 - circular defect	0.5	PT Immersion UT
			1.0	
			1.5	
3	Bagging film Thickness: 20 µm	∅8 - circular defect	0.5	PT Immersion UT
			1.0	
			1.5	

3	Bagging film	6 & 8 cutoffs – slotted aperture	0.5	PT Immersion UT
	Thickness: 20 μm		1.0	
			1.5	

Pulsed thermography results:

The inspection settings and results for the 3mm laminate with bagging film at set locations is as follows:

Table 25 Pulsed thermography experimental settings. Sample: 3BGF1

Sample reference no.	3BGF1
Frame rate	30 Hz
No. of frames captured	450
Capture time	14.68s
Image Sampling – Frame no.	44
Image Sampling – Time of capture	1.47s

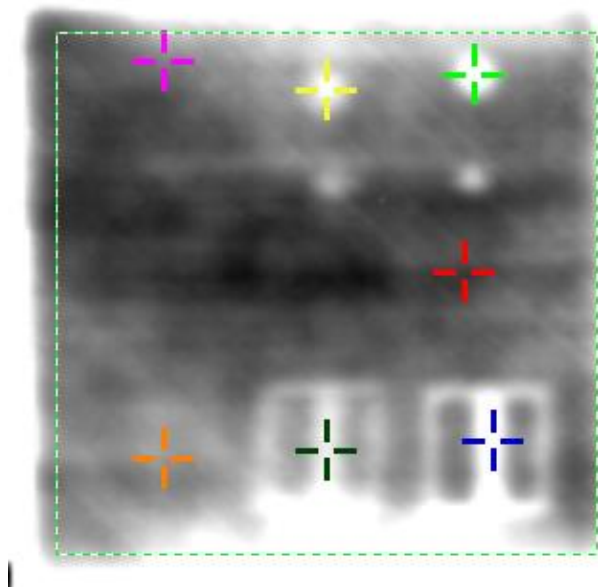


Figure 63 RAW Thermal image - Sample: 3BGF1 (120×120mm); Sampling time: 1.47s

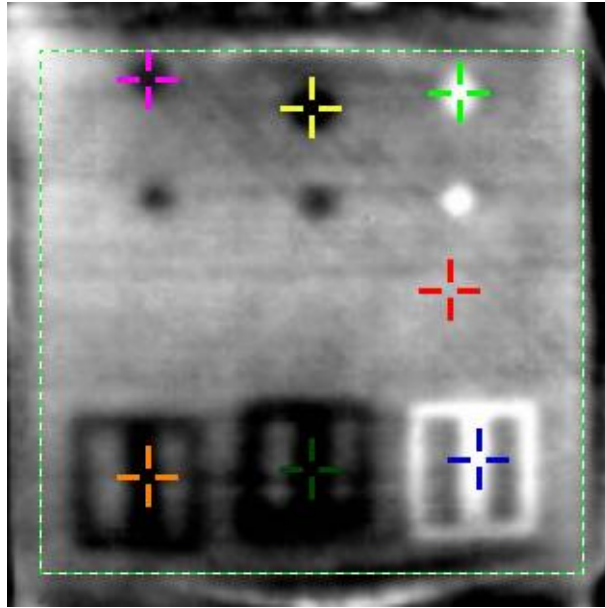


Figure 64 2nd derivative (2D) Thermal image - Sample: 3BGF1 (120×120mm); Sampling time: 1.47s

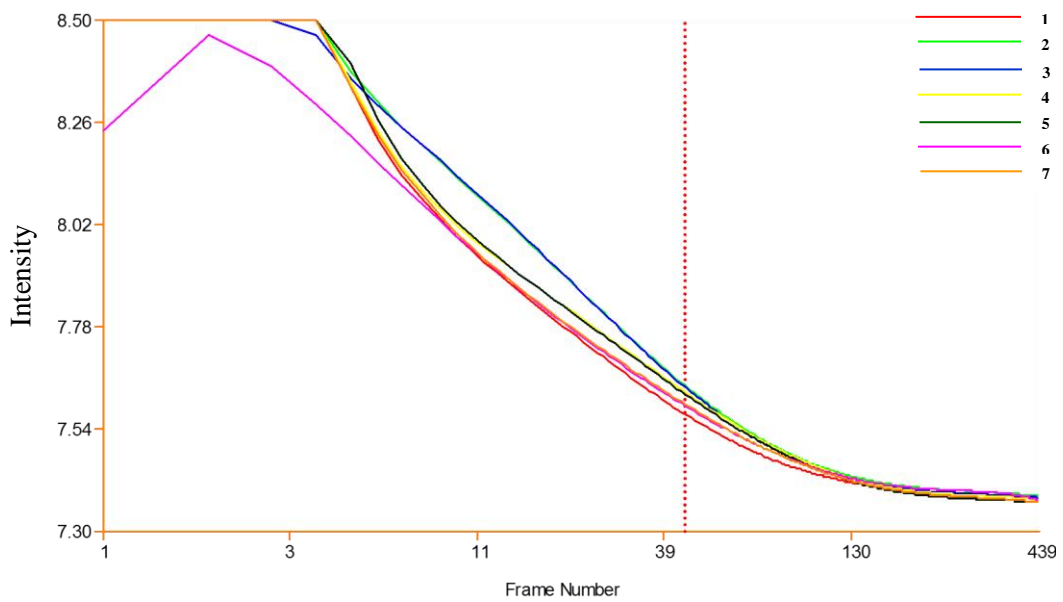


Figure 65 Log t-T plot for the RAW data; Sample: 3BGF1; 1 – No defect; 2,3 – 0.5mm depth; 4,5 – 1.0mm; 6,7 – 1.5mm

Analysis:

Figure 63-Figure 65 present the pulsed thermography inspections results of the 3mm laminate with bagging film defects inserted at locations as per Table 24. For this sample, the t^* was estimated as 3.97s as seen with other 3mm thick laminates. The following observations were made from the results:

- The inserts close to the surface at 0.5mm are on the right hand side of the thermogram and are clearly visible on the thermogram. As expected, these set of defects exhibit a higher temperature profile (represented by Green and Navy Blue markers) than the parent material (Red marker).
- Even the 2nd set of defects occurring in the middle section of the laminate are visible showing a slightly higher temperature decay profile (represented by Yellow & Dark Green markers) than the sound areas of the parent material.
- However, the RAW thermal image fails to identify the 3rd set of defects occurring at 1.5mm depth. A further investigation revealed that a 2nd derivative image (Figure 64) showed this defect clearly. This feature was found to be only appearing in this type of defect.
- There was no indication of defect in the log t-T plot as the RAW data failed to identify the 3rd set of defects, although a 2D image clearly identified it.

UT results:

The following results were acquired from the UT inspection of 3mm laminate.



Figure 66 Time of flight (ToF) image for 3mm laminate (120×120mm) - Sample: 3BGF1

Table 26 Sample thickness measurement from PEUT - Sample: 3BGF1

Sample Number	3BGF1
Measured Sample Thickness	2.62mm
Waterpath	147.4mm

As before, the UT results picked up all the defect inserts validating the pulsed thermography results. The ToF image (Figure 66) show the depth variation in terms of colour map.

Conclusion:

The 3mm laminated with bagging film inserts were detected by the pulsed thermography and UT inspection results. Although the RAW thermal image did not identify the 3rd set of defects occurring at 1.5mm depth, the 2nd derivative analysis did identify the defect. Further a 6mm laminate with defects at depths 2mm, 2.5mm and 3mm was manufactured. The laminate RAW thermal and 2nd derivative data did not detect any of the defects. However, the presence of the defects was confirmed from the UT data, suggesting that the limitations of the system to detect bagging film type defects is restricted to depths of 1.5mm. This is primarily due to the heat diffusion characteristics of the bagging film. It should also be noted that the thickness of the film was under 20µm suggesting that their inclusion in deeper laminates will go undetected.

Conclusion – Parametric study:

This section, as defined in the methodology in Chapter 3 introduced steel shims, Teflon and bagging film defects. The results showed that while, the limitations for the steel shims and bagging film was at 1.5mm depth, Teflon showed good results with a detectability of 4.5mm from the surface thereby establishing the limitations of the pulsed system. Further the UT results validated the findings of the parametric study. A detailed set of findings is presented in Chapter 5.

4.2.2 Thermal Modelling

A Finite Volume Method (FVM) solver was used to simulate the pulsed thermography experiment. A geometric model was designed in Siemens NX-Ideas and a mesh density of 10 elements per smallest defect (rule of thumb) was used to resolve the smallest geometric detail. Thermal material properties were used for the CFRP, PTFE and Air (Appendix 7). It was assumed that the CFRP laminate material was homogeneous. In order to understand and validate the thermal results obtained from the parametric defect study (Section 4.2.1), thermal modelling approach using Ideas TMG was used. A preliminary test using a GFRP laminate with PTFE and representative air gap was modelled. The laminate was designed to be 4mm thick and had the PTFE with airgap at about 2mm, and as part of the model, a 1kW heat flux was applied onto the top surface of the model as seen in Figure 67 below.

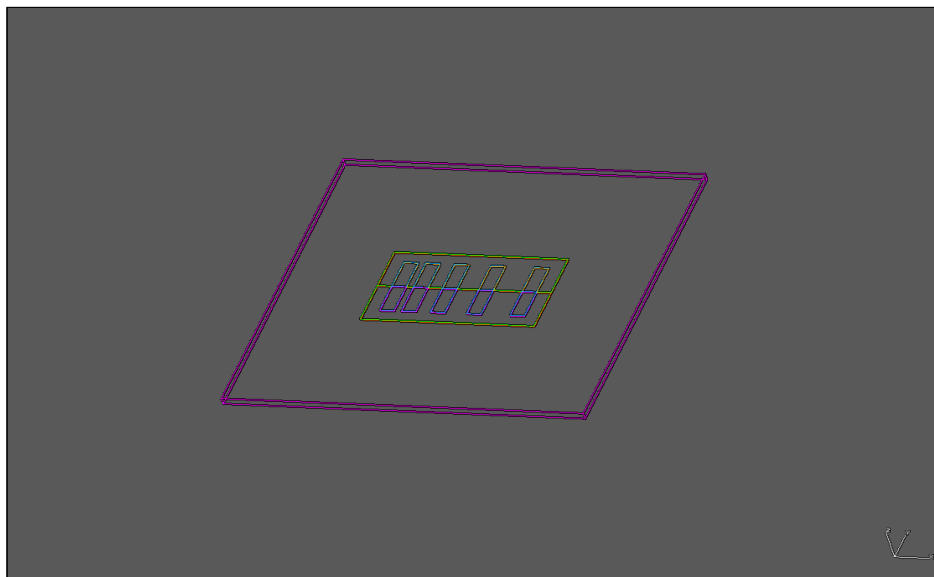


Figure 67 The model with the slotted aperture insert - wire frame mode

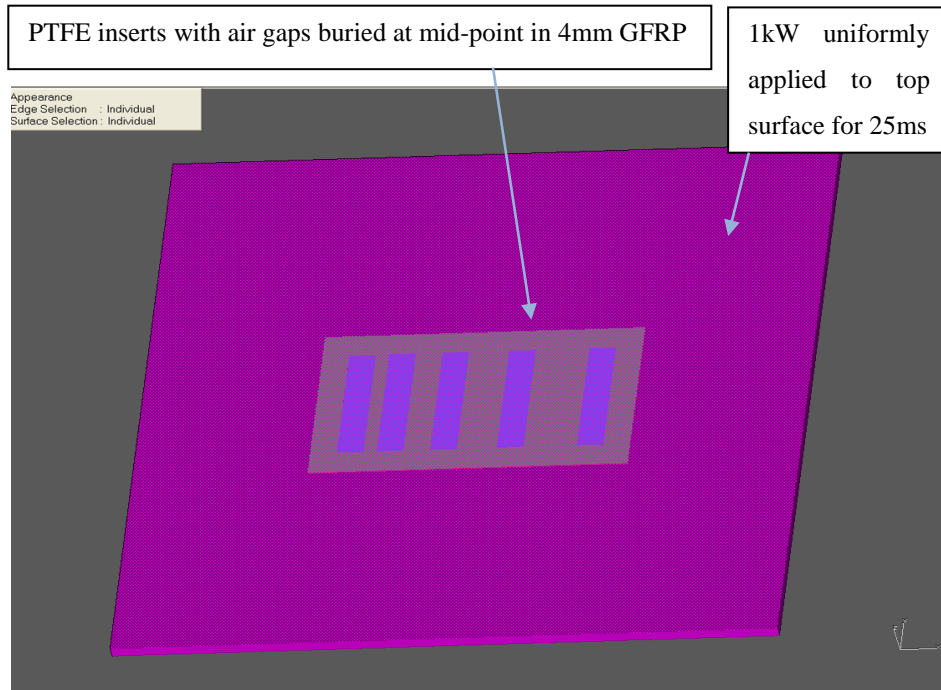


Figure 68 Ideas model showing the laminate with the slotted aperture insert at 2mm from the top surface.

The model was run for the above specifications and the following are the results obtained from the model.

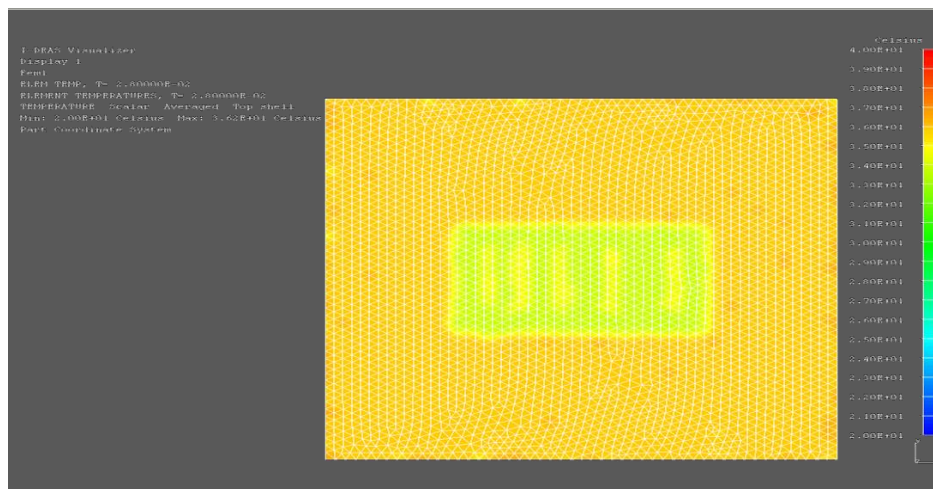


Figure 69 Laminate thermogram at sampling time 28ms

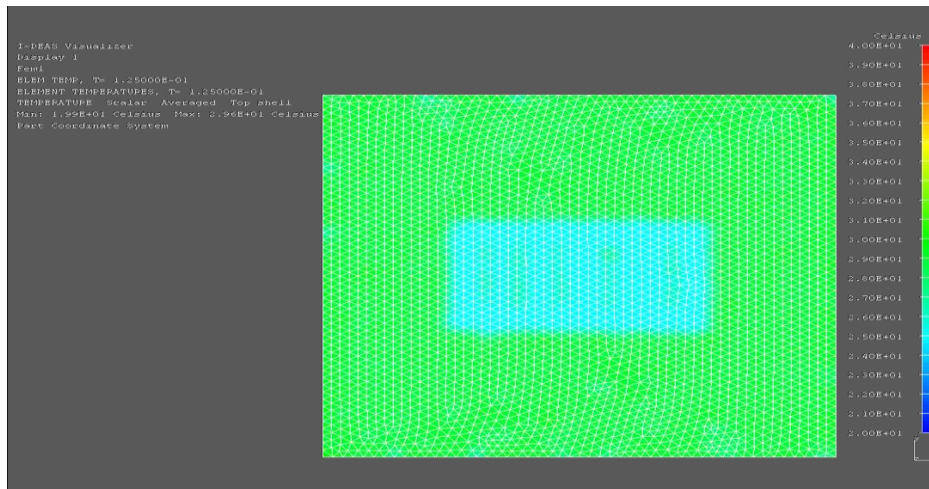


Figure 70 Laminate thermogram at sampling time 150ms

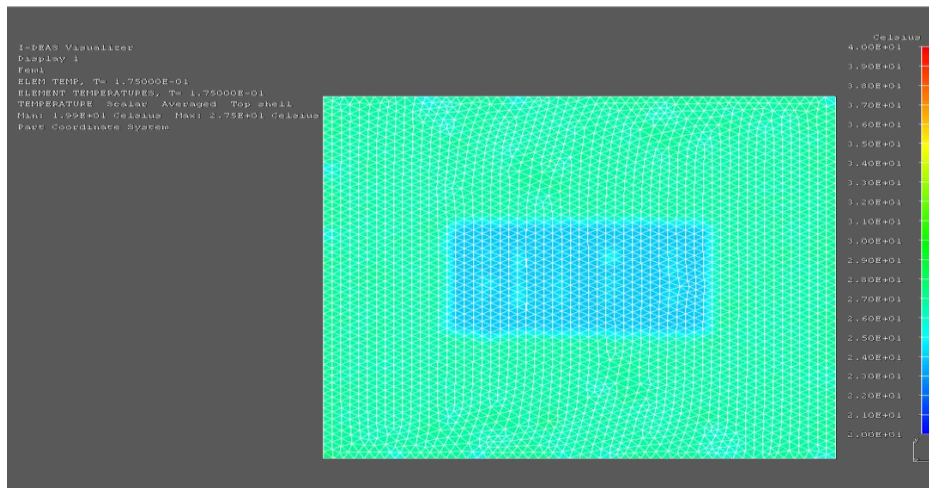


Figure 71 Laminate thermogram at sampling time 175ms

Figure 69-Figure 71 show snapshots of the surface temperature at various times after the application of the pulse. This proof of principle clearly shows that, for a 4mm sample, good contrast is obtained between the sound and defect area. It was observed that the thermal model detected the sub-surface defect as early as 28ms. The decay profile continued to show the defect on the surface temperature model.

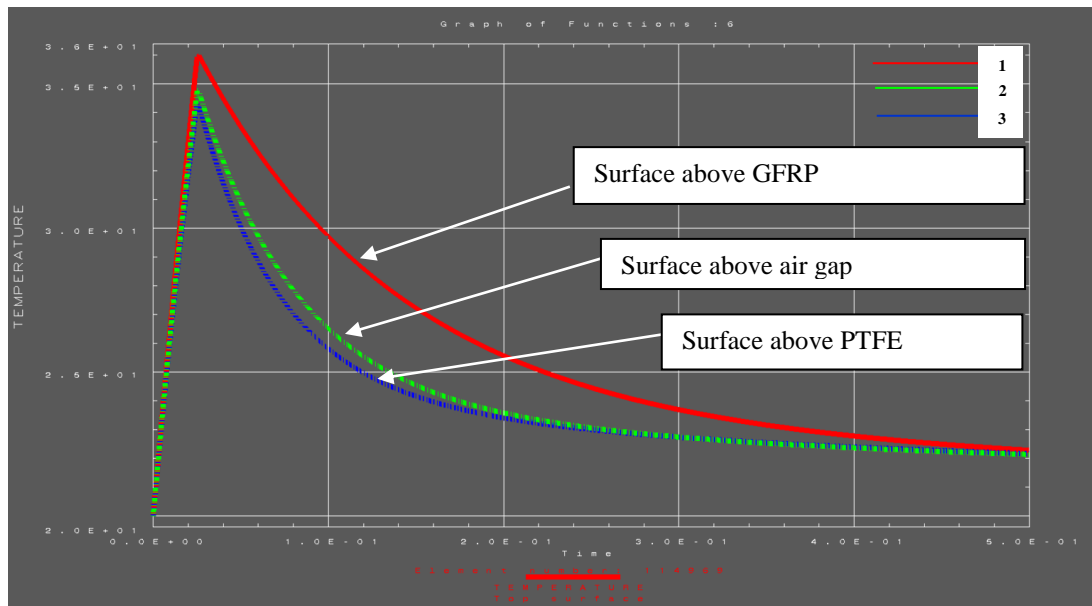


Figure 72 Log t-T plot for the laminate with PTFE; 1 – GFRP, 2 – Air Gap, 3 - PTFE

Figure 72 shows the log t-T plots for three selected points on the irradiated surface, directly above the defect-free GFRP, above the PTFE and above the air gaps. Again, these curves indicate good discrimination between the sound and defect area. The initial observation showed that the GFRP surface temperature for a sound area node showed a higher temperature than the air gap and PTFE. This model was obtained from a basic model with relevant boundary conditions as required. This clearly showed not only the ability of the software to reproduce a pulsed thermography model but also confirmed the experimental approach as a viable technique for detecting defects in composite samples of 4mm thickness.

This initial trial provided confidence in building further simulations of CFRP samples used in the parametric study, namely, 3mm and 6mm thick laminate.

Figure 73-Figure 74 show the geometric model of the laminate with defects.

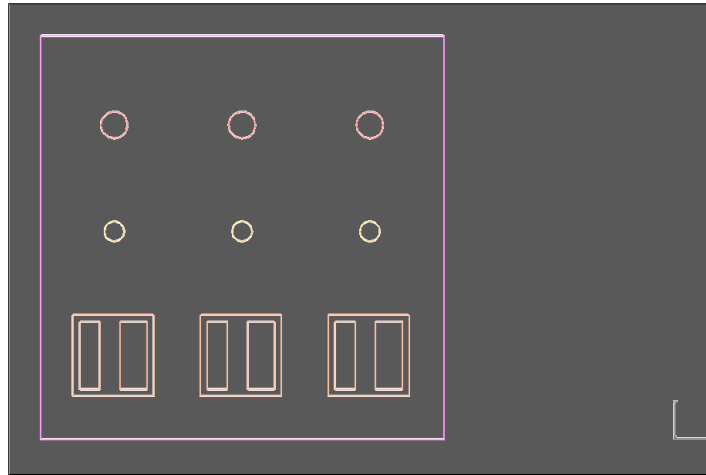


Figure 73 3mm laminate model with PTFE defects at different depths; top view

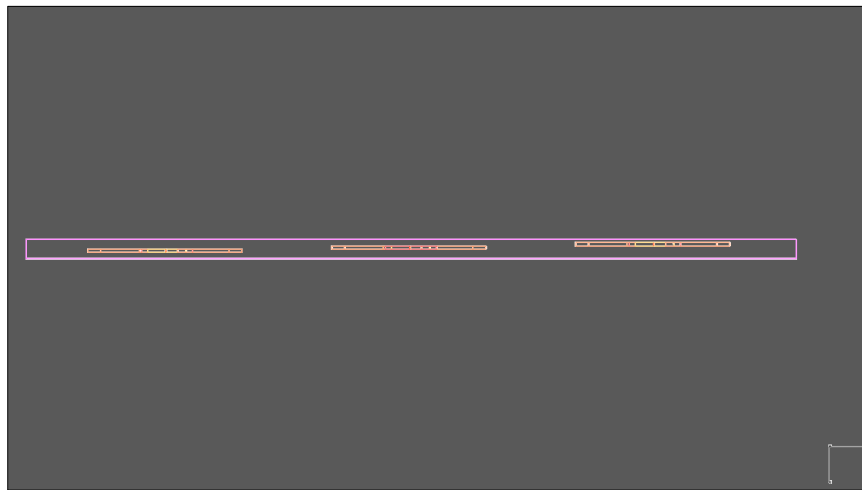


Figure 74 3mm laminate model with PTFE defects at different depths; side view

3mm laminate – computational model:

The following are the results obtained for the 3mm laminate with PTFE and air gap type defects at depths 0.5mm, 1.0mm and 1.5mm.

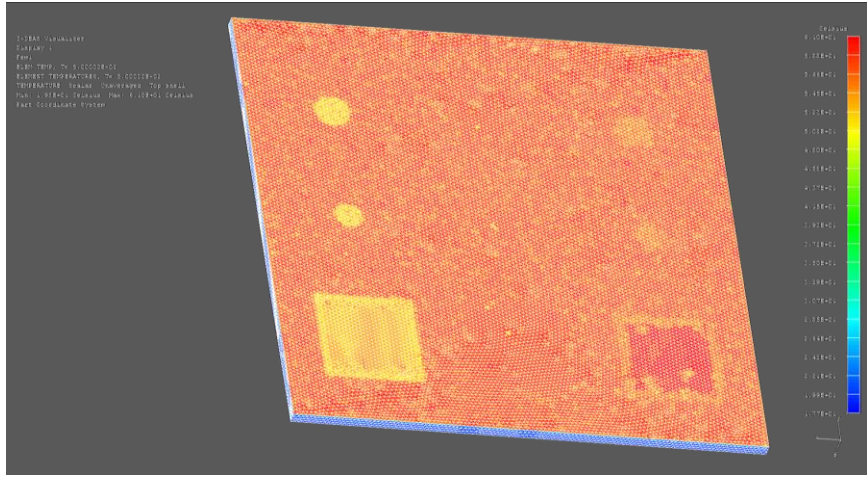
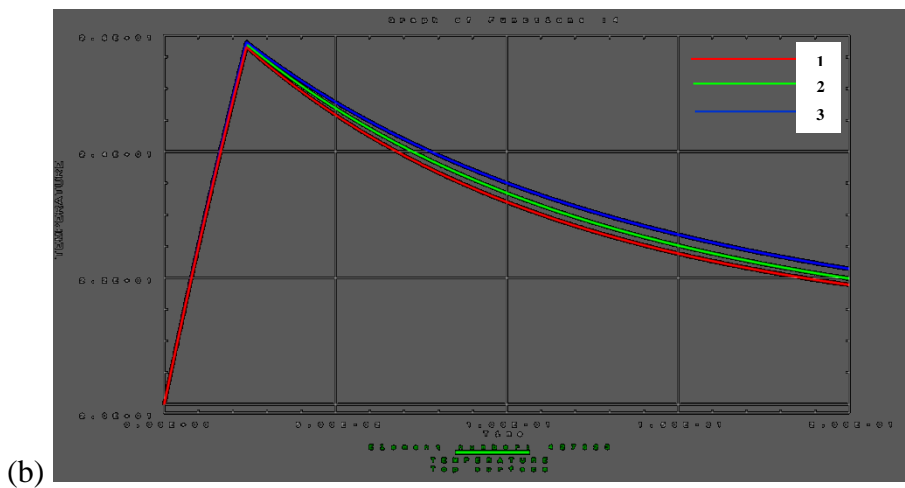
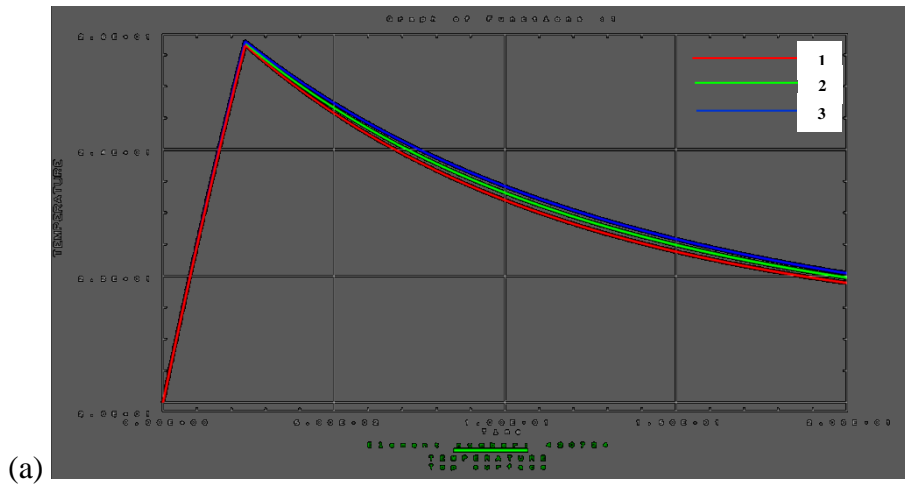


Figure 75 3mm laminate (120×120mm) with PFTE and air gap inserts; thermography sampling at 0.5s



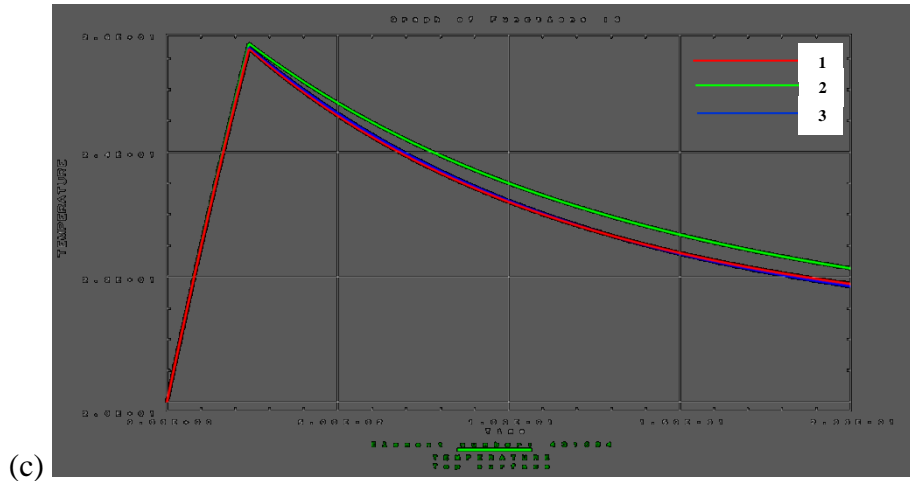


Figure 76 Log t-T plot for the 3mm laminate model with 1 – CFRP (Red curve); 2 – Air gap (Green curve); 3 – PTFE (Blue curve); Defect depth: (a) 0.5mm, (b) 1.0mm and (c) 1.5mm below surface

Figure 75 illustrates good contrast between the laminate and defects obtained at 0.5 sec. Figure 76 (a)-(c) show the resultant log t-T plots for a 25ms pulse on the upper surface for defects at 0.5, 1.0 and 1.5mm below surface. Three points were selected: above the defect-free CFRP, above the PTFE and above the air gaps. The results indicate that defects in a 3mm sample are easily detectable by the thermography system with a sensitivity of $\pm 0.2^{\circ}\text{C}$.

6mm laminate – computational model:

A further simulation was undertaken for a 6 mm CFRP sample, with PTFE/air defects buried at three levels; 2.0mm, 2.5mm and 3.0mm. Figure 78 shows the log t-T plot for the sampled points above the defects located at 2mm below the surface. Though we see the slotted aperture defect, we now observe the lack of discrimination relative to the defect free point, suggesting that pulsed thermography would struggle to detect defects at this depth.

The following are the results obtained for the 6mm laminate with PTFE and air gap type defects at depths 2.0mm, 2.5mm and 3.0mm (Figure 77-Figure 80).

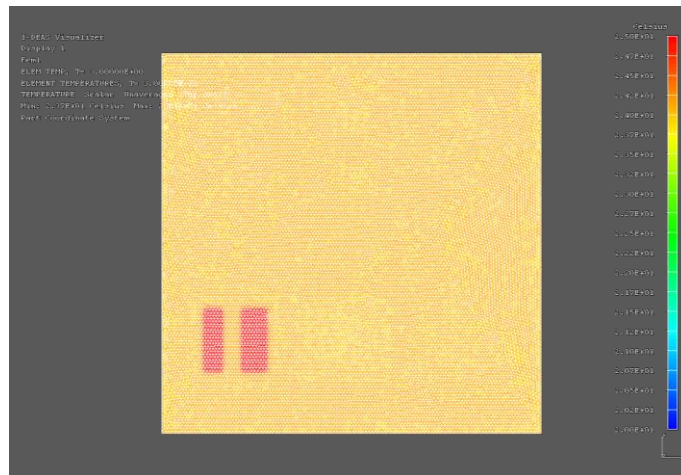


Figure 77 6mm laminate with PTFE and Air gap inserts; computed thermogram at 3s

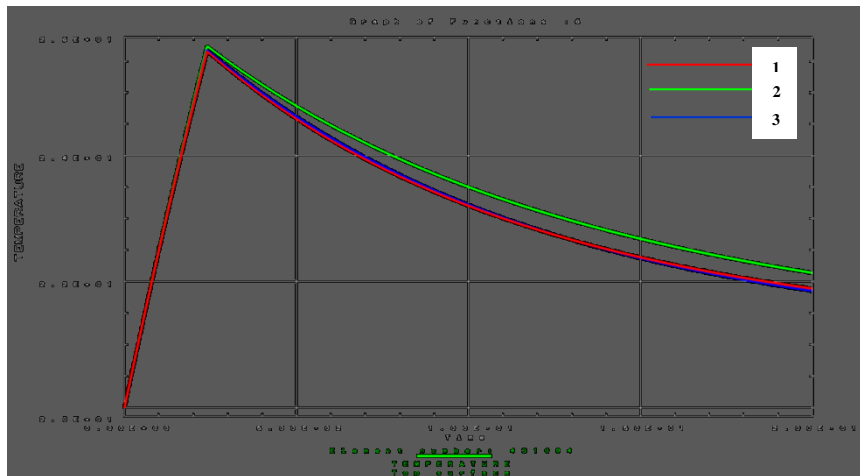


Figure 78 Log t-T plot for the 6mm laminate model with 1 – CFRP (Red curve); 2 – Air gap (Green curve) and 3 – PTFE (Blue curve); Defect depth – 2.0mm

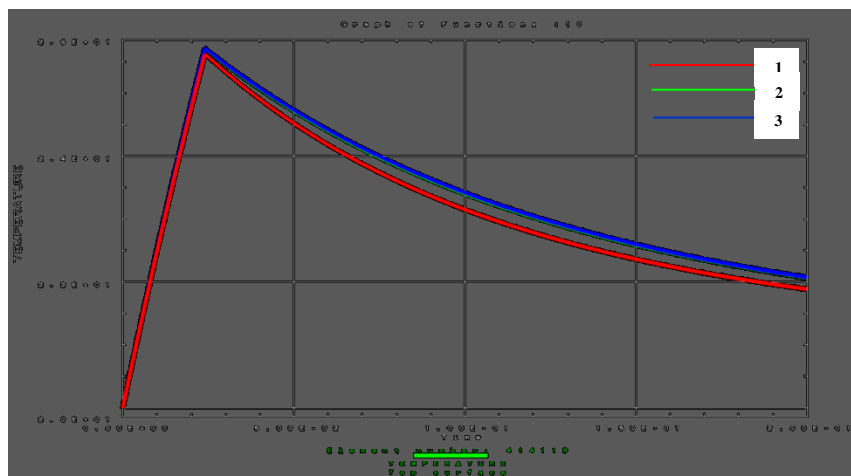


Figure 79 Log t-T plot for the 6mm laminate model with 1 – CFRP (Red curve); 2 – Air gap (Green curve) and 3 – PTFE (Blue curve); Defect depth – 2.5mm

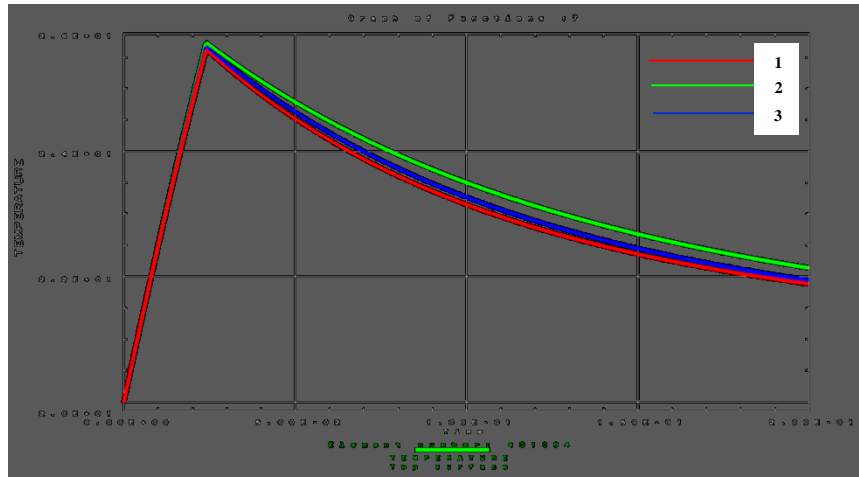


Figure 80 Log t-T plot for the 6mm laminate model with 1 – CFRP (Red curve); 2 – Air gap (Green curve) and 3 – PTFE (Blue curve); Defect depth – 3.0mm

Figure 78 – Figure 80 are the log t-T plot for the 6mm laminate with the individual defects occurring at depths 2.0mm, 2.5mm and 3.0mm. As before the CFRP is represented by the Red curve and the PTFE and air gap by Blue and Green curves respectively. It was observed that there was slight change in their thermal profile which is associated with their depth location. However, the trend line follows the sound areas curve represented by the Red curve. It was observed that the air gap defect appearing closest to the surface had an overall higher decay profile in comparison with the laminate profile. However, the computed thermogram does not identify all the buried defects as indicated by the time temperature plots.

Thus these straightforward computations illustrate the challenge with pulsed thermography and clearly explain the limits of the results that are experimentally obtained from the parametric study in section 4.2.

4.3 Impact Studies – Preliminary Experimental trials

This section primarily presents the results obtained from the impact study. As mentioned in chapter 3, this section reports the approach used for the main study. This section establishes the test setup and the data obtained, together with preliminary analysis confirming the detectability of damage through the use of thermography based systems. It should be noted that in most cases, scrap samples and offcuts were used to perform these tests.

4.3.1 Preliminary Charpy Trials

Introduction:

Impact studies are carried out on UD carbon fibre composites to understand the behaviour and fracture mechanics of the material. The samples are monitored during impact and the following report is a summary of the findings.

Sample Description:

The sample is made from a 300GSM UD Carbon fibre provided by Amber Composites. The sample is out of shelf life and is currently used as trial samples to set-up the Charpy impact test. The samples were fabricated using the hot press. The following are the curing process settings

Table 27 Hot press cure settings for preliminary tests

Cure cycle time	45 mins
Cure temperature	120°C
Cure pressure	2 tonnes

Experimental Set-up:

The impact experiment was carried out on Sample 1 using a modified Charpy impact tester. Figure 81 shows the initial experimental setup. A hemispherical indenter of 14mm diameter was attached to the conventional Charpy impact tester (Figure 82). A custom fixture as seen in Figure 82 was fabricated to hold the test sample in place. The fixture was designed based on British Standard –BS ISO

18352:2009 (Uncontrolled) with the title ‘Carbon-fibre – reinforced plastics – Determination of compression after impact properties at a specified impact energy level’. The sample was held by elastic bands tied vertically on both the edges.

The Cedip Titanium 560M infrared camera was placed behind the fixture directly in line with the indenter position at the centre (Free standing position, 0°). A computer then drives the infrared camera through camlink.

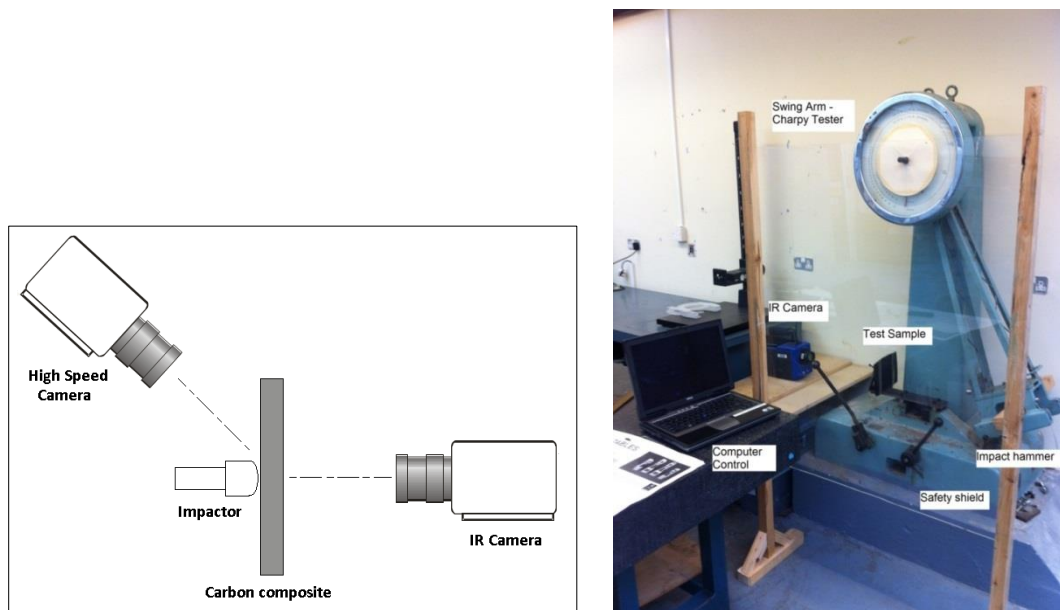


Figure 81 Initial experimental setup – Charpy trial; Test schematic (left) and the test rig (right)



Figure 82 Indenter attached to the hammer on the left; and the infrared radiometer and test sample arrangement on the right

Sample 1:

The sample (as seen in Figure 83) was manually laid up. The stacking sequence is $[0^\circ, 90^\circ, 0^\circ]_{2S}$. The sample was fabricated in the hot press as described previously. The cured thickness of the sample was 3mm and the overall dimensions of the sample were 150mm \times 150mm.

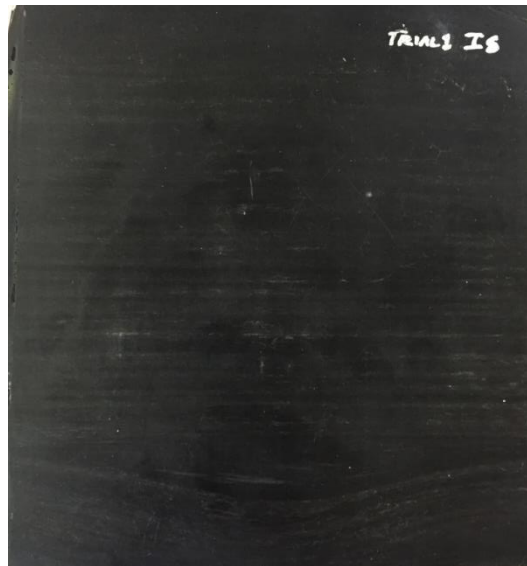


Figure 83 Digital image of CFRP Sample 1; Size 150 \times 150mm

The Impact Test:

The sample was subjected to impact test. The swing arm of the Charpy was raised by an angle of 20° and allowed to impact the sample. Care was taken not to allow the indenter to bounce for a second time.

The impact energy that was given to the sample was calculated to be 12.7J. (See Energy calculation below)

Energy Calculation:

Mass of hammer, $m = 23.53\text{kgs}$

Acceleration due to gravity, $g = 9.81 \text{ m/s}^2$

Length of the arm, $r = 0.91\text{m}$

Angle of inclination, $\alpha = 20^\circ$

Energy, $E = m \times g \times r \times (1 - \cos \alpha) = 23.53 \times 9.81 \times 0.91 \times (1 - \cos 20) = 12.67\text{J}$

Research showed that when a material is subjected to dynamic loading, there are structural changes occurring as a response to the load acting on the sample. This response is both physical and usually associated with change in temperature. The advancement in the field of infrared thermography (IRT) has made it possible to capture this change in temperature. Thus IRT can be used at every stage of manufacturing monitoring the processes critically thereby assessing the condition of the equipment as well as the material / product being made. Thus IRT has established itself as an effective condition monitoring method to prevent failure.

During impact, many physical and mechanical changes occur simultaneously. The potential energy stored in the Charpy hammer translates into kinetic energy when the hammer is released from the previously calculated angle. As the indenter attached to the hammer head impacts the sample, the kinetic energy is then transferred to the sample. In response to the energy acquired from impact, the composite material tries to flex. This flexing causes the stress to build up thereby causing the fibres to move. This movement in fibres causes friction which generates heat. Advancement in camera technologies has made it possible to capture such small changes in temperature. Initially there is a localised cooling followed by increase in heat due to flexing of the sample. This is described as the thermos-elastic effect. As the energy level increases, there is a large flexing of the sample causing the shock wave to develop stresses of higher order. This physical dislocation causes the fibres to bend beyond the elastic limit and as a result causes fracture. This has been described by various researchers as the thermoplastic effect. As a result of thermoplastic effect, microcracks appear in the sample and mostly occur along the back surface where the flexing is found to be maximum.

The Cedip Infrared camera was set to operate at a capture frequency of 916.1Hz with an integration time of 901 μ s for a reduced window size of 256 \times 88 pixels.

Note: The camera integration time is set in microseconds (μ s) as prescribed by the manufacturer. Whereas the sampling time as seen for images below is represented in milliseconds (ms) due to disparity in sampling time.

The following settings (Figure 84) were incorporated to the camera to capture the change in temperature caused due to the flexing of the sample.

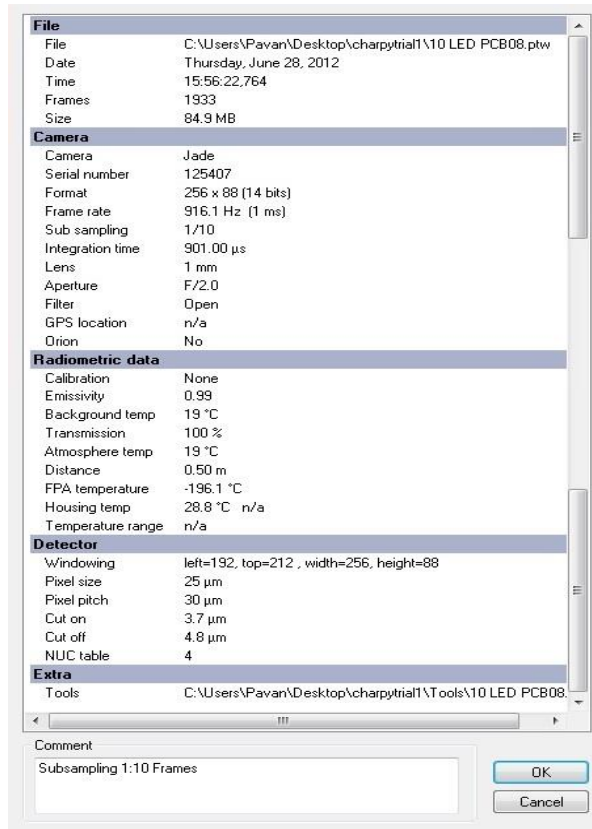


Figure 84 Settings of IR camera for transient thermography

The experiment was carried out and the sample was impacted with a hemispherical indenter. The impact energy was calculated to be about 12.67J (approx.). The camera was activated to record the data before the impact took place until the rate of cooling of the sample was steady. Figure 85 to Figure 88 show the results obtained from the test.

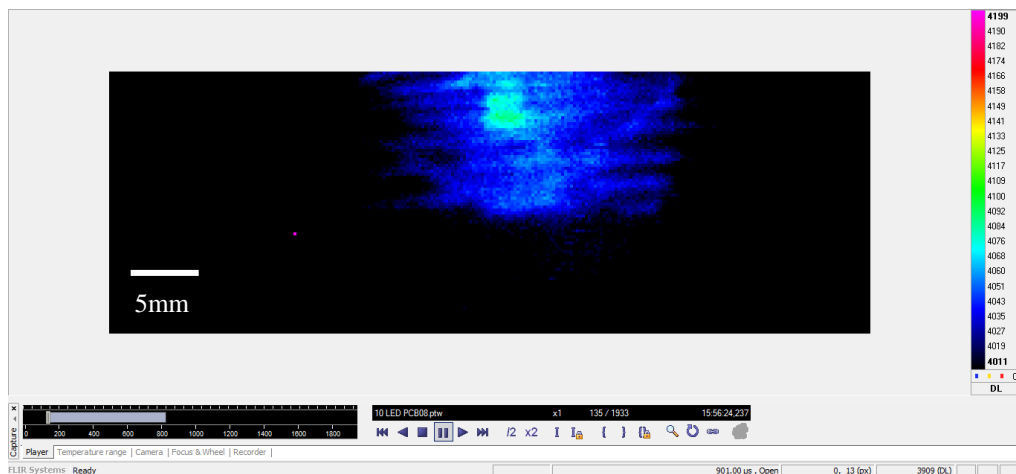


Figure 85 Charpy initial trials - Thermogram at the time of impact; t=0ms

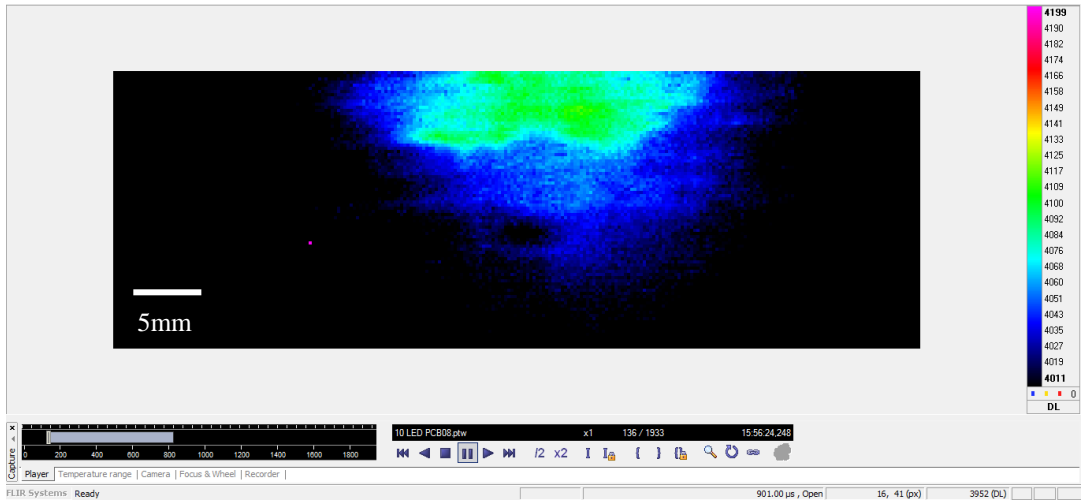


Figure 86 Charpy initial trials - Thermogram at the time of impact; $t=1.09\text{ms}$

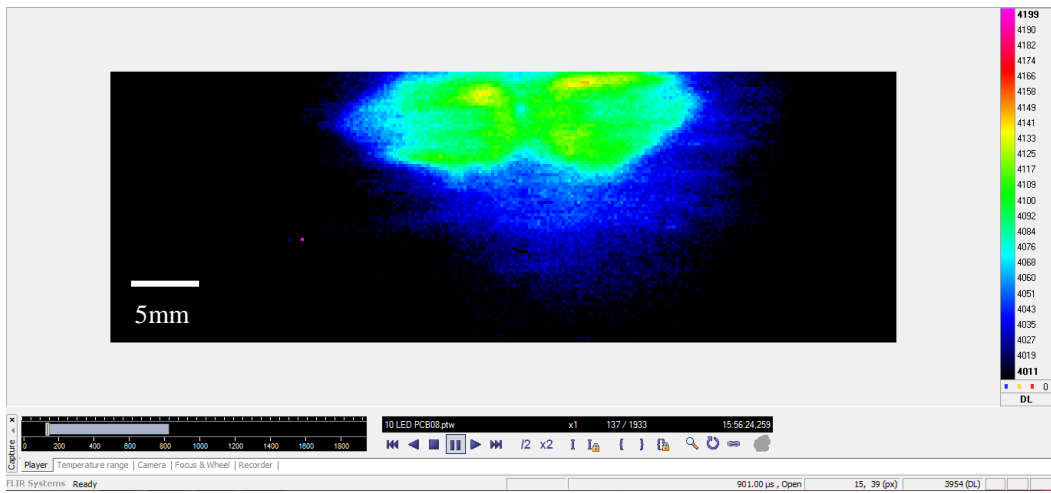


Figure 87 Charpy initial trials - Thermogram at the time of impact; $t=2.18\text{ms}$

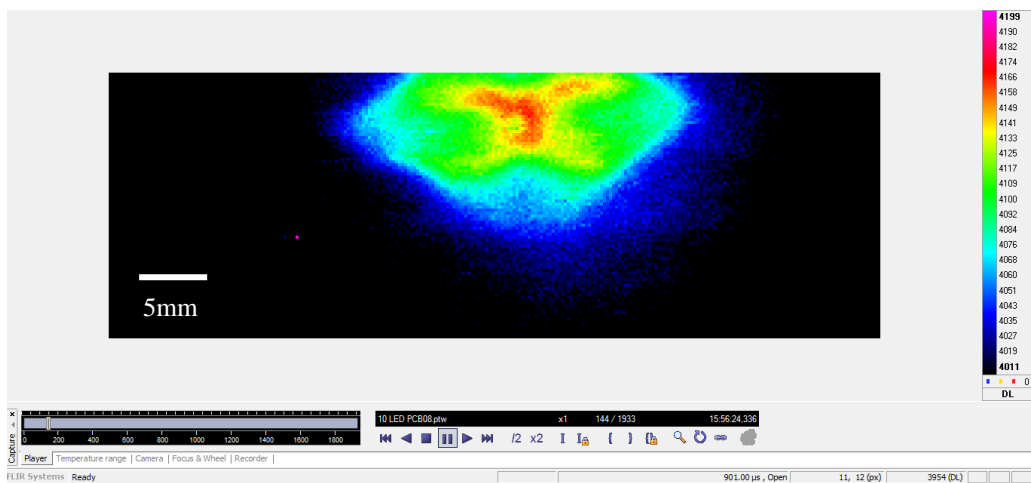


Figure 88 Charpy initial trials - Thermogram at the time of impact; $t=9.824\text{ms}$

It was observed from the above set of images (Figure 85-Figure 88) that the impact produced a change in the surface temperature of the sample. It should be noted that the image is acquired from the back surface of the laminate and not the actual impact side. Hence there is no immediate rise in back wall temperature. From the Figure 85 and Figure 86, a band of heat in the horizontal direction was observed. The sample constituted of two third layers in the 0° direction (horizontal along the surface of the sample). It was speculated that this pattern was due to a majority of plies occur in the 0° direction.

However, from Figure 87 and Figure 88, it is not clear if the orientation of the ply has caused such a pattern to develop. More over a significant amount of heat starts developing sometime after 2ms.

From the above results, it was concluded that understanding the thermal behaviour especially from the back wall is a challenge in itself. Hence it was decided to fabricate a sample with all the plies in 0° orientation to help understand the behaviour of the sample under impact.

Note:

The temperature scale is a digital temperature level scale.

Sample 2: UD Carbon OSL 90

The sample 2 was made with all plies in the 0° orientation. The fabrication of the sample was in hot press similar to Sample 1. The stacking sequence was $[0^\circ]_{6S}$ and the thickness of the sample was 2.7mm. This reduction in thickness of the sample was due to the spreading of the fibres during fabrication under pressure. Two different samples were made to a size of 150mm \times 150mm.

For the impact test, the sample was placed with the fibres running vertical to the plane of impact and held to the fixture by elastic bands on either side as before. It was agreed to reduce the impact energy as there were chips & cracks seen on the impact side. The idea of low energy impact is to prevent damage on the impact side and maximise damage occurrence on the back side due to flexing of the sample. The following changes were made to the impact test:

1. The diameter of the hemispherical indenter was increased from 14mm to 24mm (based on suggestions by Meola and Carlomagno (2010))
2. The impact energy was reduced to about 10.28J (inclination angle = 17°)

The Cedip camera was set to 924.2Hz with a viewing window of 288 × 80 pixels and integration time of 1000μs. The remaining settings for the Cedip camera were as similar to the previous acquisition settings used for Sample 1. The live monitoring of the impact test using the Cedip camera produced the following results.

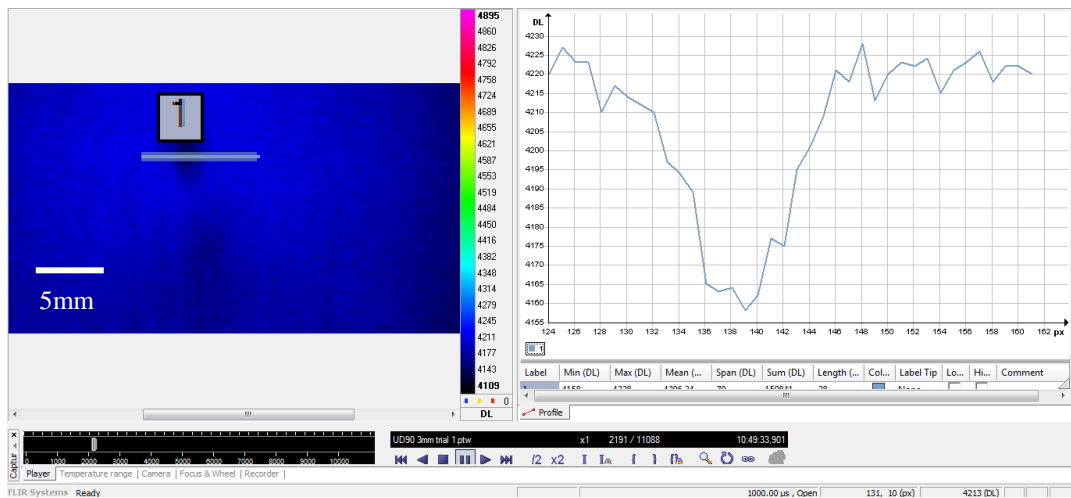


Figure 89 Sample 2- UD Carbon OSL 90 - Transient Thermography at time t=0ms

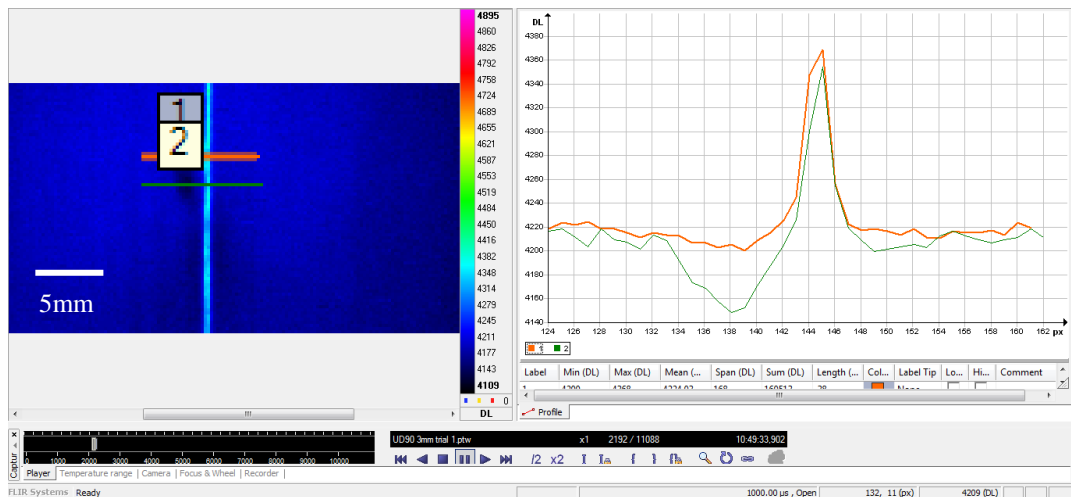


Figure 90 Sample 2- UD Carbon OSL 90 - Transient Thermography at time t=1.08ms

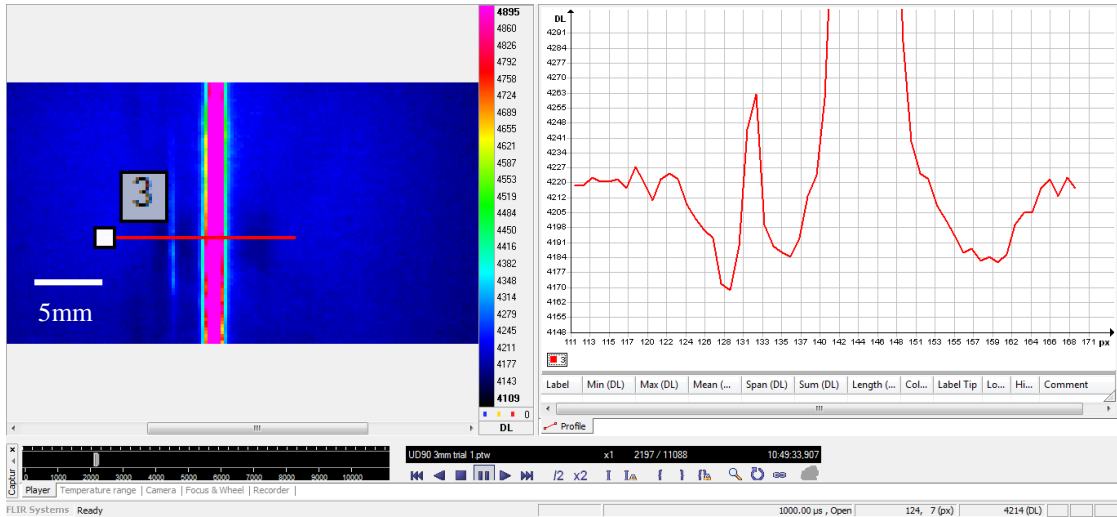


Figure 91 Sample 2- UD Carbon OSL 90 - Transient Thermography at time $t=6.5\text{ms}$

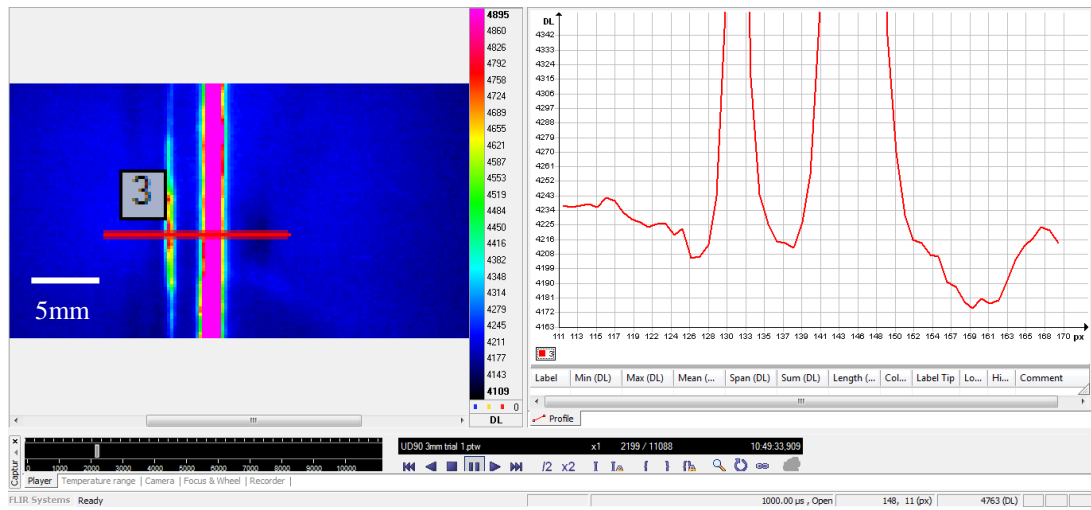


Figure 92 Sample 2- UD Carbon OSL 90 - Transient Thermography at time $t=8.656\text{ms}$

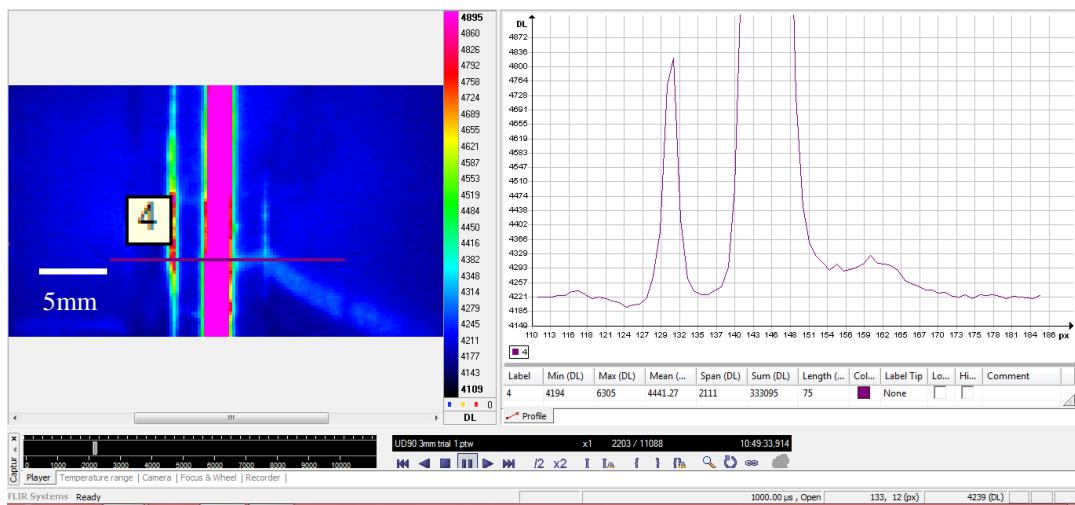


Figure 93 Sample 2- UD Carbon OSL 90 - Transient Thermography at time $t=12.98\text{ms}$

Figure 89 showed the development of a cold spot and registered a drop in temperature. This was illustrated using the thermogram on the left and the graph on the right. The graph is a plot of the digital temperature level plotted against each pixel on the line obtained using the line profile tool. It was observed seen from the graph that the drop in digital temperature level is about 60 units.

As soon as the shock wave hit the sample a narrow band with huge temperature gradient developed together with alternating cooling (Figure 90). This can be described as the thermoelastic effect due to the flexing of the sample. The green line (2) in the graph clearly indicates the cooling effect surrounding the impact area. It should also be noted that the rise in temperature is along the length of the fibre instead of just the impact site as seen previously (Sample 1).

Figure 91 clearly shows that the sample is now under the thermoplastic region characterised by rise in digital temperature within 6ms. This indicated that the sample has fractured and developed a gap that has caused the temperature to rise and conduct to the back surface of the sample. It should also be noted that this hot zone is parallel to the orientation of the fibre and is significant at the area where impact occurred. We also notice a second hot zone to the left of the impact site starting to evolve after 6ms. This can be confirmed by both the thermogram and the graphical plot presented in Figure 91 and Figure 92. This gives rise to two possible explanations

- a. This rise in temperature in the second zone could be due to the induced stress trying to move in the sample
- b. This could also be due to a secondary impact which occurred within 6 milliseconds before the hammer retracted.

In Figure 93 we can see a third set of heat tracks appearing to the right of the impact site. This could be the heat generated as a result of the crack developed due to impact. The visual inspection of the front surface showed that a crack was formed in the front surface along the orientation of the fibre. Even after about 13ms, localised heating and cooling spots / tracks can be found confirming that the stress wave moves parallel to the orientation of the fibres in the sample.

Similar results have been seen by Meola and Carlomagno (2010). It can be inferred from the above results that the development of initial cracks to the actual fibre breakage is quite fast and is directly related to the amount of heat generated during impact. Secondly, it can be said that the movement of the shockwave has also resulted in the formation of delamination. The speculation would however be the size and location of the delamination.

The possible way to check for the exact response of the composite due to impact is to incorporate the following additions to the experiment:

1. Capture the impact data from the impact side using a high speed camera – this will answer the previous question of whether the sample bounces on to the hammer to develop a secondary damage.
2. Calibrate the resolution of the camera and derive a pixel to actual spot temperature relation thereby approximating the exact location of impact.
3. Carry out microscopy & Pulse thermal inspection to check for indications of cracks, microcracks, fibre breakages and chips.
4. Carry out a TSA test to compare the results obtained with pulsed thermography.

4.3.2 Preliminary TSA trials

In order to establish various testing techniques that help characterise impact damage, TSA inspection was identified. To establish the suitability of the technique for the impact testing methods, a carbon fibre sample with impact damage was used as an initial trial specimen to illustrate the strength of the technique. The laminate was of the size of 200mm × 150mm with a thickness of 6mm. The impact was created using a drop test machine; the details of the impact test were unknown. The damage created showed clear signs of crush damage and it is estimated that the impact energy could be between 20J and 30J.

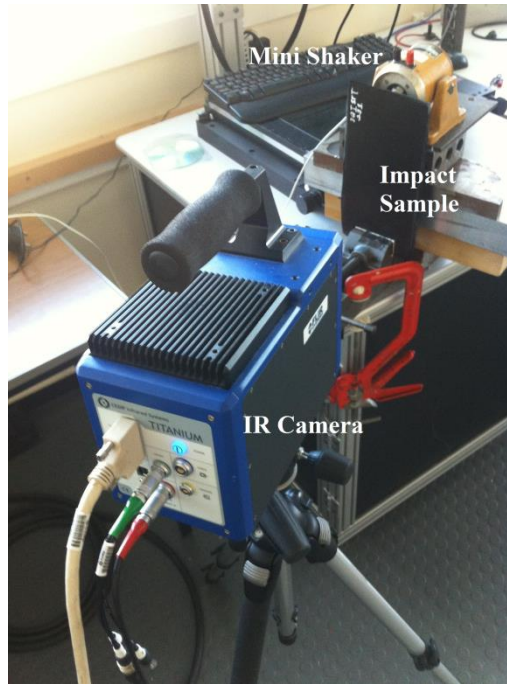


Figure 94 TSA experimental setup

The following are the settings used to setup the TSA test.

Table 28 TSA capture settings

Description	Settings
Synchronisation frequency	9.998Hz
Acquisition frequency	25Hz
Acquisition length	500 frames

Figure 94 shows the experimental setup for the TSA technique where the sample was excited using a mini electrical shaker at a synchronous frequency of ~10Hz. The IR camera looked directly at the impact side of the composite laminate from a distance of 500mm (note the image in Figure 94 is a representative image and not an exact measure of the distance). The mini shaker was controlled by a function generator and the frequency was set to 10Hz (sine wave). The sample was clamped to the table using a bench-top vice on one end and the other end rests against the shaker that has a rubber tip which excites the sample.

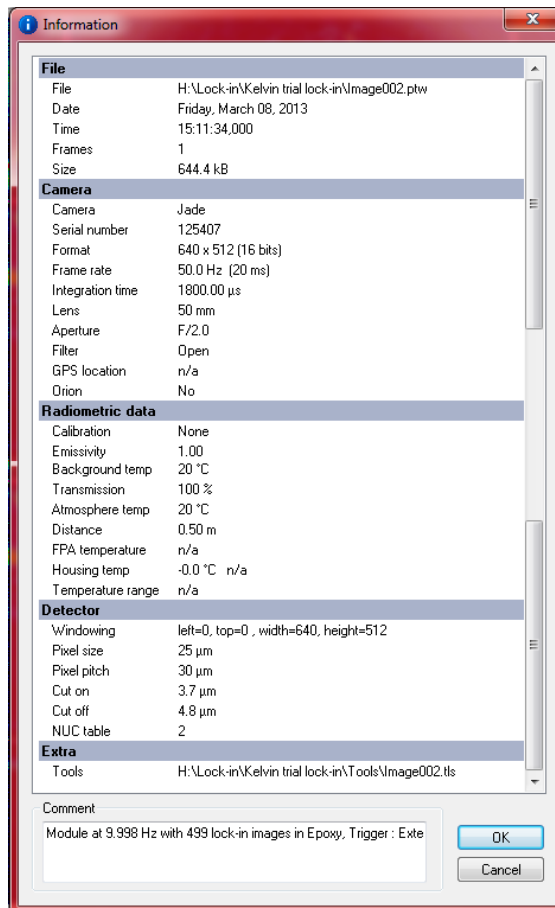


Figure 95 Cedip camera settings for TSA measurement

The following is the result obtained on testing the impacted carbon fibre laminate.

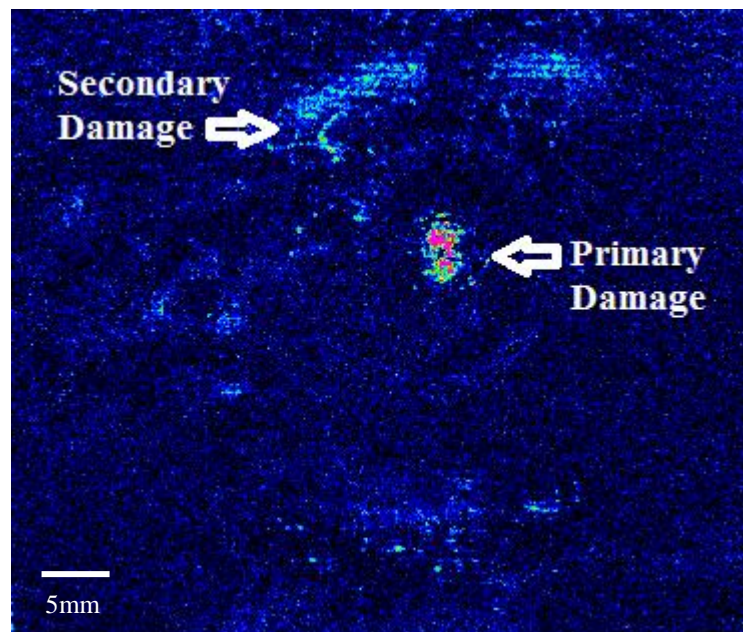


Figure 96 TSA image showing crush damage on the composite laminate at a synchronous excitation frequency of 9.998Hz

Figure 96 shows the module image obtained as a result of combination of the phase image and the amplitude image. Though the image is noisy, it clearly shows the primary impact damage in the centre of the image together with peripheral features which could be interpreted as secondary damage. The typical impact damage centre is characterised by a higher temperature pixel value indicated by the pink scale, whereas the surrounding areas on the sample show a darker image in the black to blue scale. As explained in the literature, this characteristic image is obtained as a result of heat developed due to the friction between damaged fibres at the crush area caused due to the sinusoidal vibration of the shaker. It should be noted that a significant change in temperature stress value does confirm the presence of primary damage.

It can be seen from the image (Figure 96) that there are areas where the temperature stress is higher than the sound area of the sample, especially at the periphery of the primary damage. This could be interpreted as secondary damage that was created as a result of the impact event. A better understanding of the impact event can only be understood from the live capture of the entire impact event.

Conclusion:

Though this preliminary trial clearly showed the impact damage, it is an understanding that the damage, in terms of thermal stress intensity, can only be noticed above a certain degree of damage. This trial though highlights the damage clearly, shows the strength of the TSA technique for damage occurring at higher impact energy levels and hence the damage due to lower impact energy could be a challenge in itself. The suitability of the technique can only be understood from the following parametric impact test presented in Section 4.4 below.

4.4 Impact Studies – A parametric approach

Based on the preliminary tests, a range of impact tests were designed to understand the mechanics of impact and the materials resistance to such impact. It was decided that only low energy impact will be taken up for this research to understand the boundary when a measurable damage is created and then identified by transient, pulsed thermography and TSA methods, together with pulse echo ultrasonic testing, vibrational methods and microscopic images. This study is aimed to work at the boundary at which there is confirmation of the damage creation and the ability of various techniques to detect and characterise them.

This section presents the results obtained when 3mm and 6mm laminates were subjected to impact testing. The laminates were made up of two different lay-up sequences (Appendix 3) and impacted with 3 low energy impact energy levels using a modified Charpy test and a ballistic gas gun testing.

Table 29 Impact test parametric study parameters

Impact Method	Laminate Thickness in mm	Lay-up	Impact Energy in J
Charpy	3	Quasi-Isotropic	12
Charpy	3	Quasi-Isotropic	8
Charpy	3	Quasi-Isotropic	4.5
Charpy	3	TWI	12
Charpy	3	TWI	8
Charpy	3	TWI	4.5
Charpy	6	Quasi-Isotropic	12
Charpy	6	Quasi-Isotropic	8
Charpy	6	Quasi-Isotropic	4.5
Charpy	6	TWI	12
Charpy	6	TWI	8
Charpy	6	TWI	4.5
Gas-Gun	3	Quasi-Isotropic	12
Gas-Gun	3	Quasi-Isotropic	8
Gas-Gun	3	Quasi-Isotropic	4.5

Gas-Gun	3	TWI	12
Gas-Gun	3	TWI	8
Gas-Gun	3	TWI	4.5
Gas-Gun	6	Quasi-Isotropic	12
Gas-Gun	6	Quasi-Isotropic	8
Gas-Gun	6	Quasi-Isotropic	4.5
Gas-Gun	6	TWI	12
Gas-Gun	6	TWI	8
Gas-Gun	6	TWI	4.5

Charpy Set-up – A recap:

Based on the preliminary testing, minor modifications were made to the test setup. This included the use of a high-speed digital camera capable of recording the entire impact even on the visual spectrum at a resolution of 1024×128 pixels and an acquisition speed of about 9000fps (frames per second – maximum) . At the same time, the IR camera was used at a reduced window size of 280×156 pixels to acquire data at 524Hz (maximum). The following is the modified Charpy experimental setup.

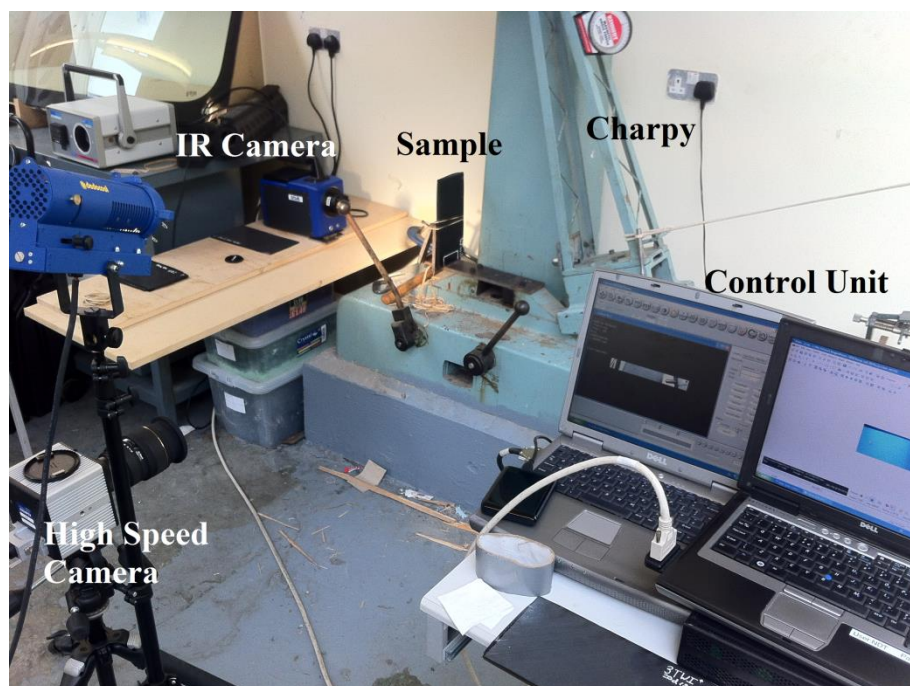


Figure 97 Modified Charpy Test Setup - now includes a high speed digital camera

Figure 97 above shows the typical experimental setup of the Charpy testing which now includes the high speed digital camera.

Gas-gun ballistic testing setup:

The gas-gun testing was set up in the ballistics chamber as illustrated in the images below.



Figure 98 The Gas Gun - ballistic testing



Figure 99 The gas-gun with sabot and stone

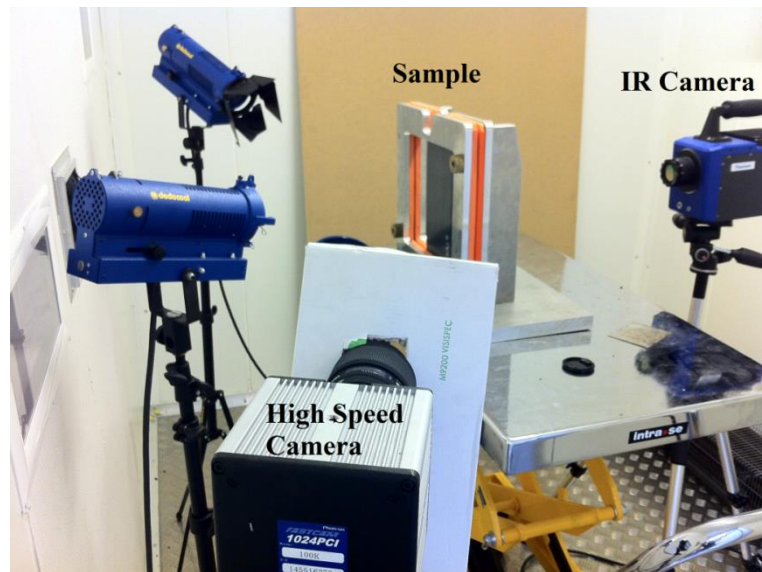


Figure 100 Experimental setup of gas-gun testing - view 1



Figure 101 Gas-gun experimental setup - view 2

Figure 98 to Figure 101 show the typical ballistic testing setup. Figure 98 shows the gas-gun housed in the operators room. This testing unit is separated by a climate controlled chamber that contains the gun firing end. The sabot with the stone is loaded into the gas gun as illustrated in Figure 99. The gas-gun has a barrel which carries the sabot to the impact chamber where the sample is housed at the exit of the gas-gun. A high speed camera and an IR camera are used to capture the events occurring in the impact side and non-impact side respectively (Figure 100-Figure 101).

Note: As part of health & safety regulations, care was taken during the experimental setup in the chamber and in-between test samples changes. During the actual gas-gun firing, the chamber was sealed and no one was allowed to enter the chamber and the researchers were directed to remain in the operator's area. Due to regulations covering the use of firearms, only a licenced user was allowed to operate the gas-gun with the assistance of the laboratory technician. No lone working was permitted and proper signs were displayed together with restricted entrance to the testing area during the impact test.

4.4.1 Results

This section presents the results of the parametric impact testing. It consists of the following results.

1. Enlarged image of the damage area obtained from Leica microscope (with damage size)
2. Series of images obtained during the impact event using the IR Camera in the transient mode operating at reduced window size and high speed acquisition showing the damage creation and heat imprint that remains for a few seconds post impact. This should confirm the creation of the damage.
3. Pulsed thermography inspection of the impacted composite laminate.
4. TSA inspection of the impacted composite laminate.

The results presented below are for the parameters described in Table 29 above and include the results of both 3mm and 6mm laminates when subjected to both Charpy and gas-gun testing at three distinct energy levels as established previously.

All laminates manufactured were of the size of 200 × 100mm and were laid up as per stacking sequences mentioned in Appendix 3. The following is the sample naming nomenclature.

If the sample name is 3QI20d12JC2, then it can be identified as

- 3 – denotes the thickness of the sample, in this case 3mm

- QI – denotes the type of layup sequence, in this case Quasi-Isotropic
- 20d – Will denote the angle of impact, meaning this was a Charpy test
- 12J – denotes the impact energy, in this case 12 J
- C – denotes that the impact system was using a swing-arm Charpy device
- 2 – denotes the trial number, in this case trial 2

Thus if the sample name is 6TWI12JS1 will indicate that the laminate is a 6mm laminate having a TWI layup and was impacted with an energy of 12 J. The S indicates a stone impact using gas-gun and the laminate is the 1st trial in the series. For each of the sample variations, three samples were used. Due to the large datasets, only the best images with maximum contrast were used in this section. However, for the actual conclusion of the results, all three trials were considered and averaged to arrive at the final test result.

4.4.1.1 3mm Quasi-isotropic – Charpy

The following are the set of results obtained from the 3mm quasi-isotropic CFRP laminate during and post impact for energy levels 12J, 8J, 4.5J using the modified Charpy impact tester.

Impact energy 12J; Sample: 3QI20d12JC2

As described above, this is a 3mm quasi-isotropic sample and was impacted using Charpy setup for an impacted energy of 12J obtained when the Charpy head was released at an angle of 20°.

Microscope image:

The following is the image obtained from the microscope post impact.



Figure 102 Sample: 3QI20d12JC2 - microscopic image with damage dimension

The microscopic image of the sample shows areas of deformation, indicated by the depression in the centre of the sample together with the actual size of the damage. It shows that the damage about 3mm has been created when the Charpy indenter impacted the sample at the estimated impact energy of 12J. The damage, though visible, had been well rounded and no severe crush damage has been found. In other words, though the sample surface has undergone a plastic deformation due to the impact energy, no fibre breakage or crush damage has been found on the sample surface.

Transient thermography results:

As described in the preliminary tests (Figure 97), the infrared camera was setup in the transient mode and the entire impact event was recorded. It should be noted that the infrared camera only recorded the back surface of the laminate and following are the results obtained.

Camera	
Camera	Jade
Serial number	125407
Format	288 x 156 (14 bits)
Frame rate	542.1 Hz (2 ms)
Integration time	1000.00 μ s
Lens	1 mm
Aperture	F/2.0
Filter	Open
GPS location	n/a
Orion	No
Radiometric data	
Calibration	None
Emissivity	0.95
Background temp	21 $^{\circ}$ C
Transmission	100 %
Atmosphere temp	20 $^{\circ}$ C
Distance	1.00 m
FPA temperature	-195.9 $^{\circ}$ C
Housing temp	32.4 $^{\circ}$ C n/a

Figure 103 Settings for Sample 3QI20d12JC2

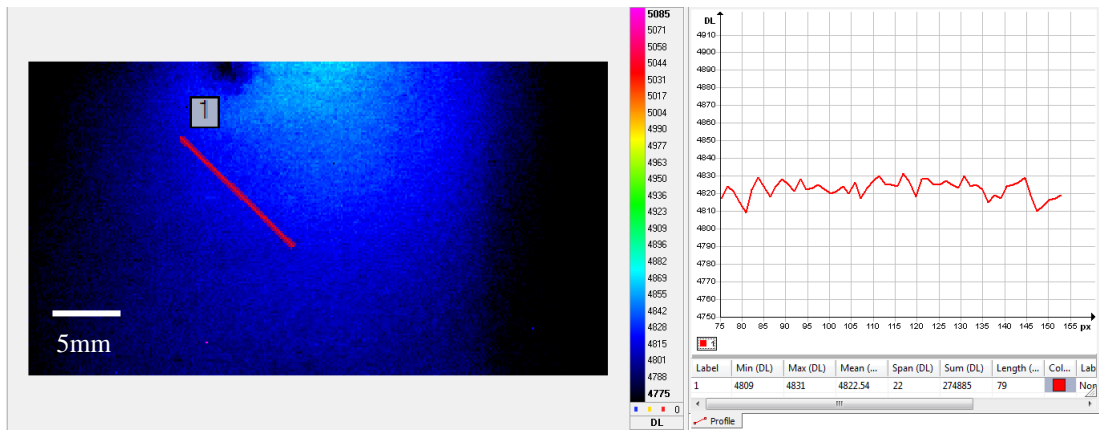


Figure 104 Sample: 3QI20d12JC2 at Frame - 0

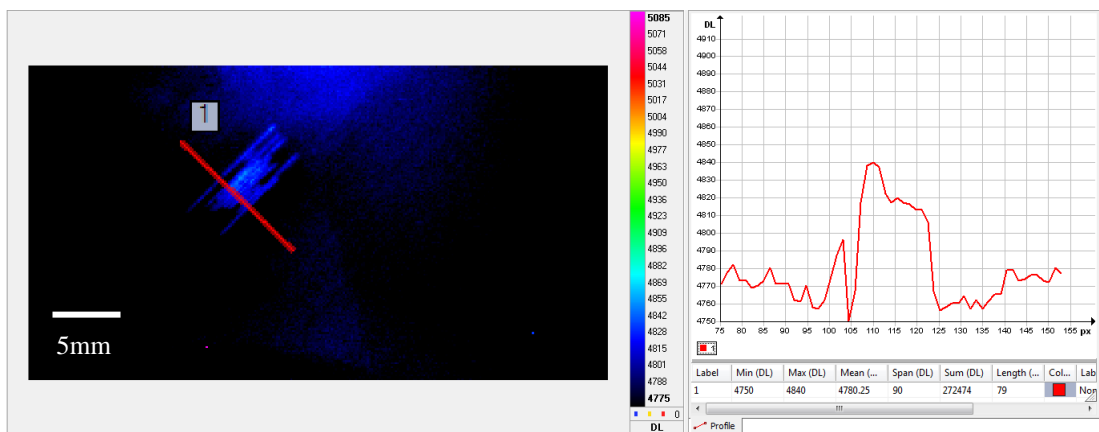


Figure 105 Sample: 3QI20d12JC2 at Frame - 1

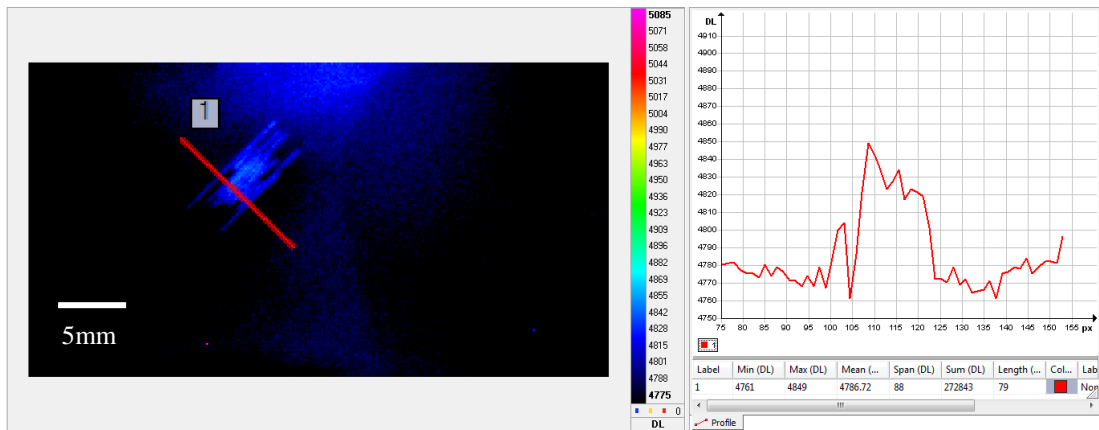


Figure 106 Sample: 3QI20d12JC2 at Frame - 2

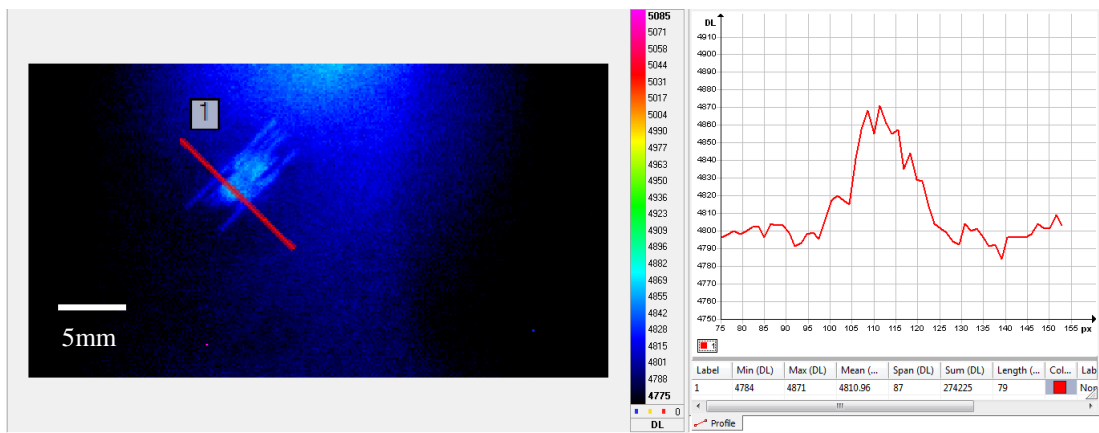


Figure 107 Sample: 3QI20d12JC2 at Frame - 4

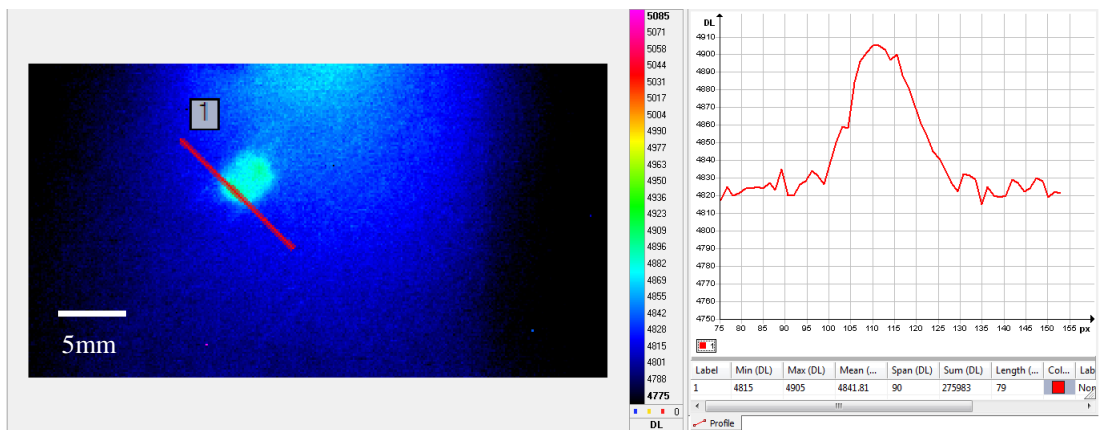


Figure 108 Sample: 3QI20d12JC2 at Frame - 8

The images above (Figure 104 to Figure 108) were acquired at an acquisition frame rate of 542.1Hz for a window size of 288×156 at a camera integration time of 1ms. It can be seen from the above set of images that just after the impact event, there is a stress concentration around the fibres, which had direct contact with the indenter head. The initial impact stress beyond the strength of the fibre has led to the

plastic deformation stage with a possible fibre breakage as observed in the preliminary trials in section 4.3. Thus the resultant of the impact led to the deformation of the sample. It should be understood that the various features that constitute the impact event in CFRP are, the initial impact noise, the shock wave propagation through the material including the flexing of the laminate, creation of damage itself, and heat generated as a result of this complex process. Though the impact event can be suspected to have been completed at the first frame, the heat generated from the front surface has not completely been transmitted to the back surface and is dependent on the thermal conductivity of the material. Hence the heat continues to rise on the back surface until it becomes a circular area with a higher temperature. It can be seen that Frame 1 shows the temperature rise along the fibre orientation as seen in the preliminary tests in section 4.3.1. This temperature rise along the fibre orientation continues to rise until the heat generated due to contact between the indenter and the laminate reaches the back surface of the laminate.

Pulsed thermography results:

The sample 3QI20d12JC2 post impact was subjected to pulsed thermography inspection as per settings established in the parametric study section 4.2. The following is the result obtained from the inspection.

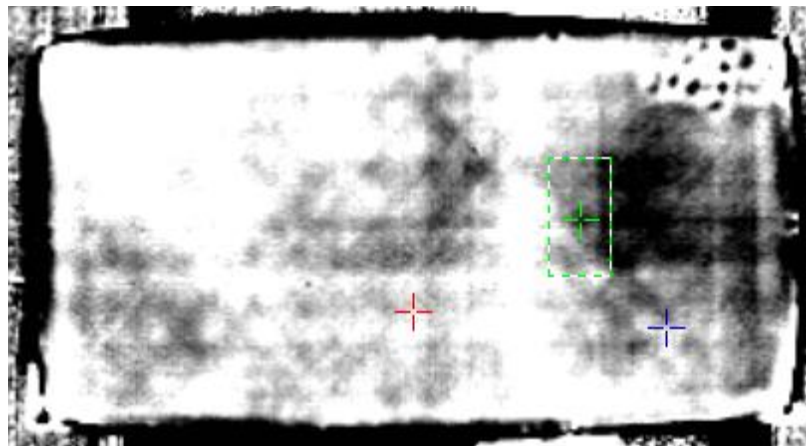


Figure 109 Pulsed thermography result; Sample: 3QI20d12JC2; Size: 200×100mm; 2D Image; Sampling: 90fms

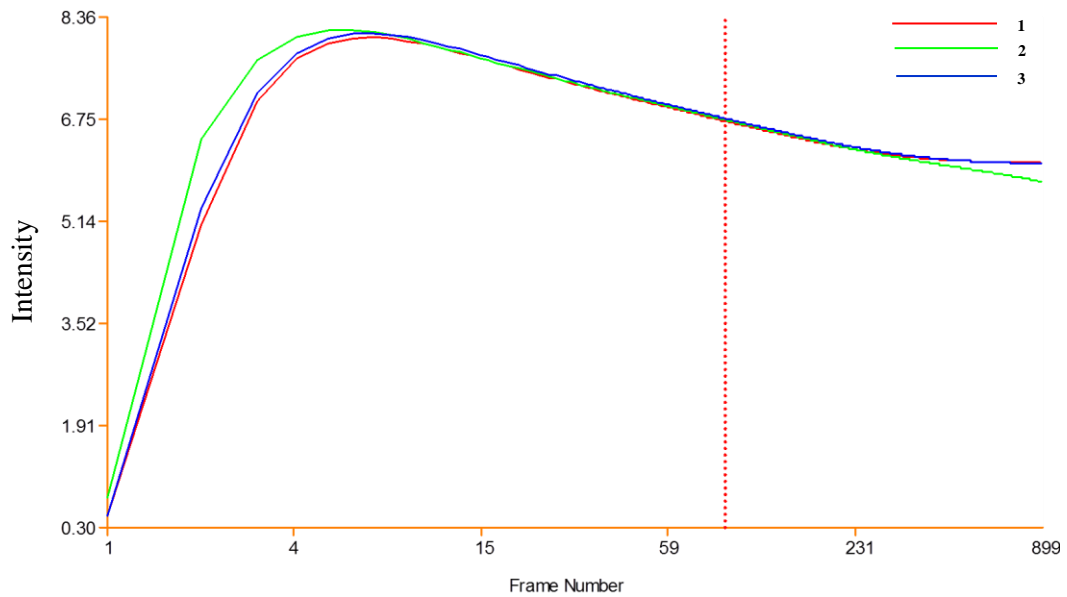


Figure 110 Pulsed thermography result; Sample: 3QI20d12JC2; RAW Thermal plot;
1&3 – sound area, 2 – damage area

It can be seen from the digital image and the microscopy image that the damage is an indentation on the surface. A careful visual surface inspection did not yield any severe damage such as delamination or crush damage either on the front or the back surface. The sample was completely intact and no surface breaking damage was found, for all trials. When subjected to pulsed thermography, for a t^* of 3.975s, neither the RAW thermal nor the 2D image yielded strong contrast confirming the presence of damage. This is because of the fact that the impact event ended up in the form of an intact dent and did not create a severe delamination and or surface breaking damage, indicating that the thermal diffusion in that area is quite similar to that of the non-damage area. Though the transient thermography captured the flexing of fibres due to the initial impact shock wave, it has not caused major damage.

But even with this barely visible impact damage, pulsed thermography does show some indication of damage presence does not however validate the damage created. This can also be seen with the high noise level in the thermogram. It should be noted that in the real world, this type of damage could be missed without knowing the exact location of the damage. This is primarily due to the high level of noise due to the structure of the laminate itself.

Further the RAW thermal logarithmic time temperature plot as seen in the image above shows that the damage is barely noticeable. The damage does not show

a high contrast as indicated in the field samples (Section 4.1) and parametric insert samples (Section 4.2).

Stress analysis results:

The thermoelastic stress method was applied to the impacted sample 3QI20d12JC2. The excitation frequency was set to 10Hz and the camera acquisition setting was set to 50Hz. See figure below for full details.

The TSA experimental setup is as described in section 4.3.2. The following is the result obtained from the thermoelastic stress analysis method.

Camera	
Camera	Jade
Serial number	125407
Format	640 x 512 (16 bits)
Frame rate	50.0 Hz (20 ms)
Integration time	1800.00 μ s
Lens	50 mm
Aperture	F/2.0
Filter	Open
GPS location	n/a
Orion	No
Radiometric data	
Calibration	None
Emissivity	1.00
Background temp	20 °C
Transmission	100 %
Atmosphere temp	20 °C
Distance	0.30 m
FPA temperature	n/a
Housing temp	-0.0 °C n/a

Figure 111 Camera settings for the TSA analysis; Sample: 3QI20d12JC2

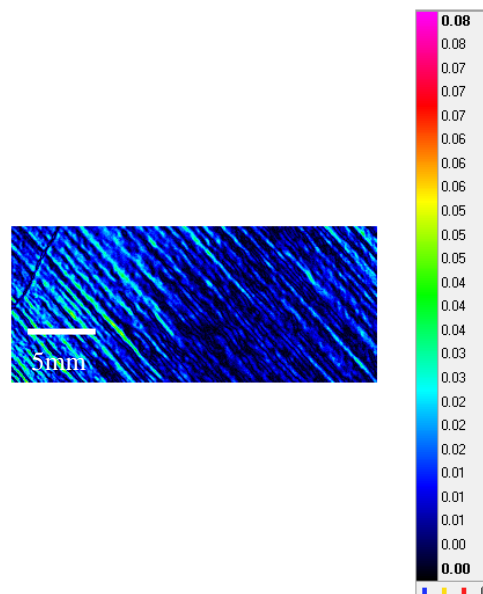


Figure 112 TSA map of Sample 3QI20d12JC2

Several trials were attempted to capture the above result. It was observed that other than a small change in the weave pattern, there was no indication of any damage. It should be noted that the intensity of the stress map was similar to the sound area thus failing to provide a clear distinction between the damage and the sound area. The tests in this case were inconclusive, suggesting that the stress build up on the damage area did not create any friction between fibres as the fibres were still intact, as suggested by the pulsed thermography results presented above.

Conclusion:

In conclusion, though the surface damage can be identified from the visual inspection, pulsed thermography data does show some indication of the damage created. The transient thermal data clearly shows the creation of the damage based on the thermal stress map in terms of change in temperature coinciding with the impact event itself. However, the TSA results do not show any strong indication of localised stress for this low speed large surface area Charpy impact that could appear due to the excitation as seen in the preliminary tests established in section 4.3.2.

Impact energy 8J; Sample: 3QI16d8JC2

The following are the results obtained for the 3mm quasi-isotropic layup laminate subjected to an 8J Charpy impact.

Microscope image:

It can be inferred from the image (Figure 113) obtained from the microscope that the damage indentation is quite similar to that of the 12 J Charpy impact as presented above. Again a similar visual dent or dislocation appears on the surface of the sample, suggesting that the sample has undergone plastic deformation as indicated by previous results confirming the damage creation methodology as established previously.



Figure 113 Microscopy image of 3QI16d8JC2 with damage dimensions

Transient thermography results:

The thermal data was captured during the Charpy impact event, similar to the 12J event described above (Acquisition: 542.1Hz; Window size: 288×156 pixels; Integration time: 1ms). The following are the results obtained from the test.

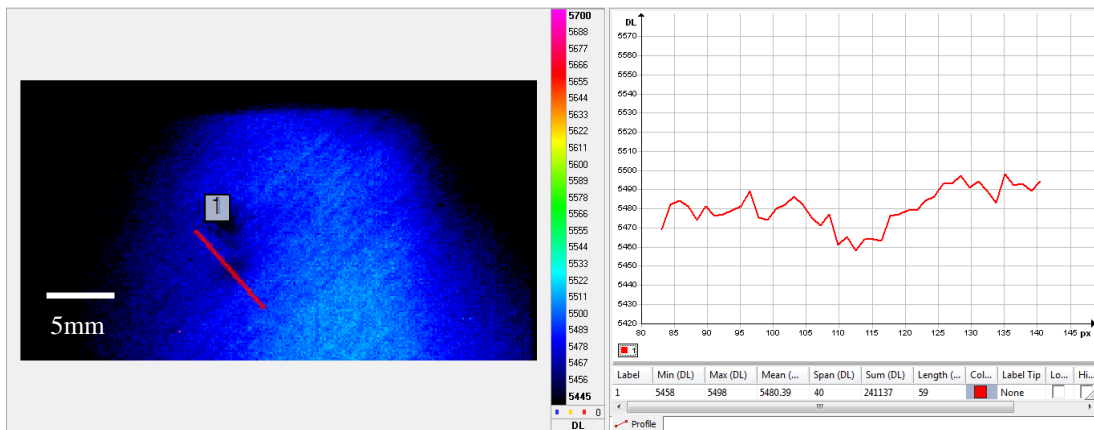


Figure 114 Sample: 3QI16d8JC2 at Frame – 0

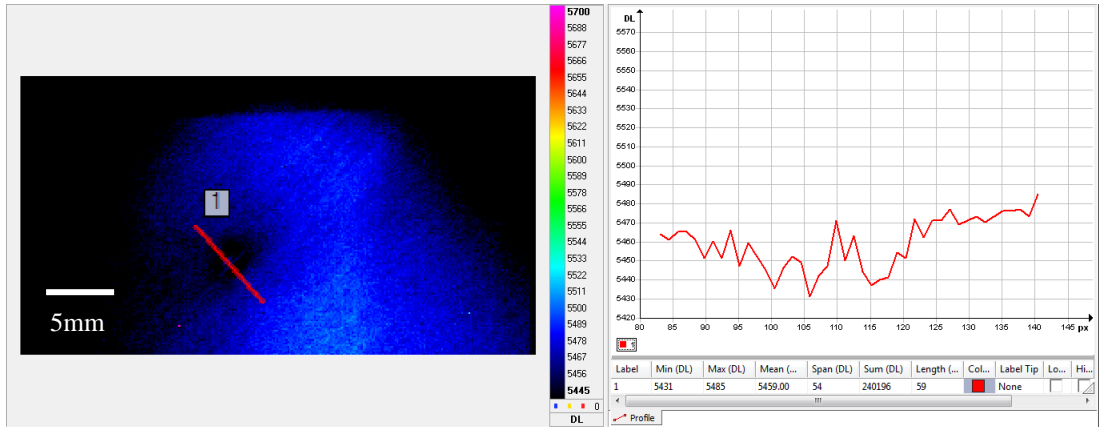


Figure 115 Sample: 3QI16d8JC2 at Frame - 1

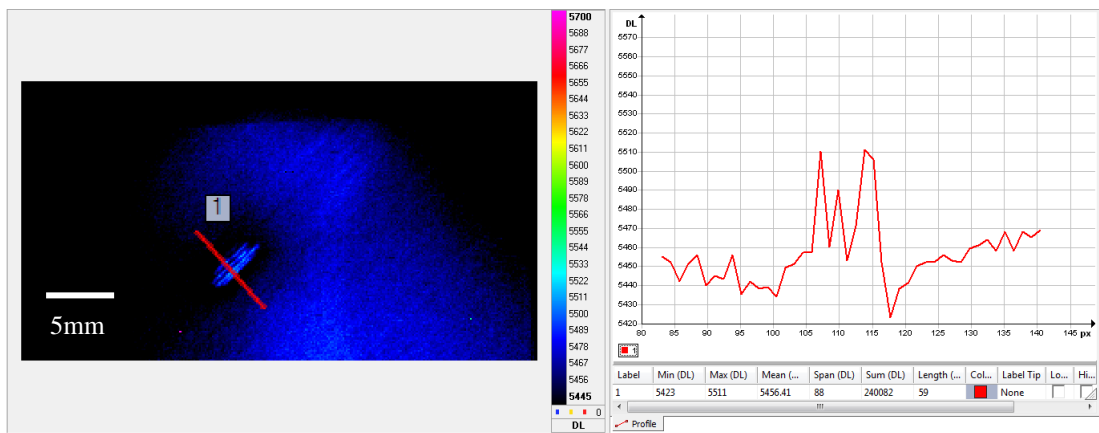


Figure 116 Sample: 3QI16d8JC2 at Frame - 2

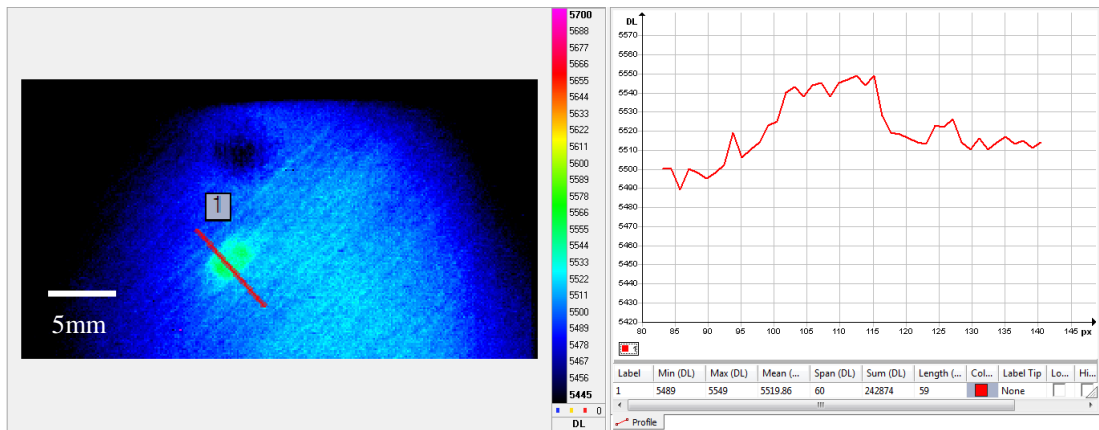


Figure 117 Sample: 3QI16d8JC2 at Frame - 3

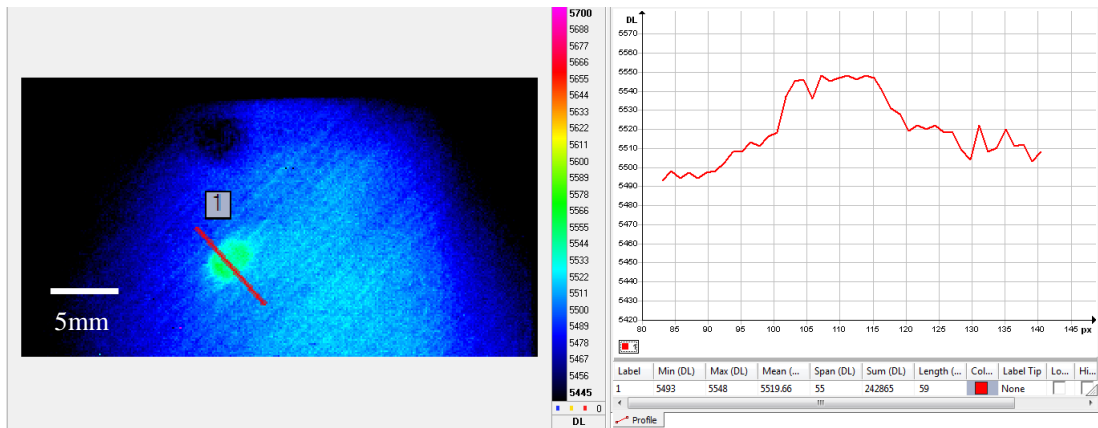


Figure 118 Sample: 3QI16d8JC2 at Frame – 8

As before, the above images (Figure 114 to Figure 118) show the thermal stress build up due to the impact event. As before, stress patterns along the fibre orientation appear and quickly disappear into a circular damage area. However, in this case, Frame 1 showed a localised drop in temperature which can be confirmed with the plot on the right indicating the pixel temperature as represented by the red line passing through the damage. This pattern was noticed in the repeat trials for the sample at 8J impact energy level indicating the difference in the impact characteristics. It was also noticed that the temperature from the fibres to the local circular area occurred much faster than the 12J impact sample.

Pulsed thermography results:

The following is the pulsed thermography result obtained from the sample 3QI16d8JC2 with the setup as established for the 12J sample.

Note: For the remainder of the 3mm Charpy results, only 2nd derivative image together with RAW thermal logarithmic time temperature plot will be used to present the results as they show better evidence of damage. The conclusion of the results was based on comparing RAW, 1D and 2D data.

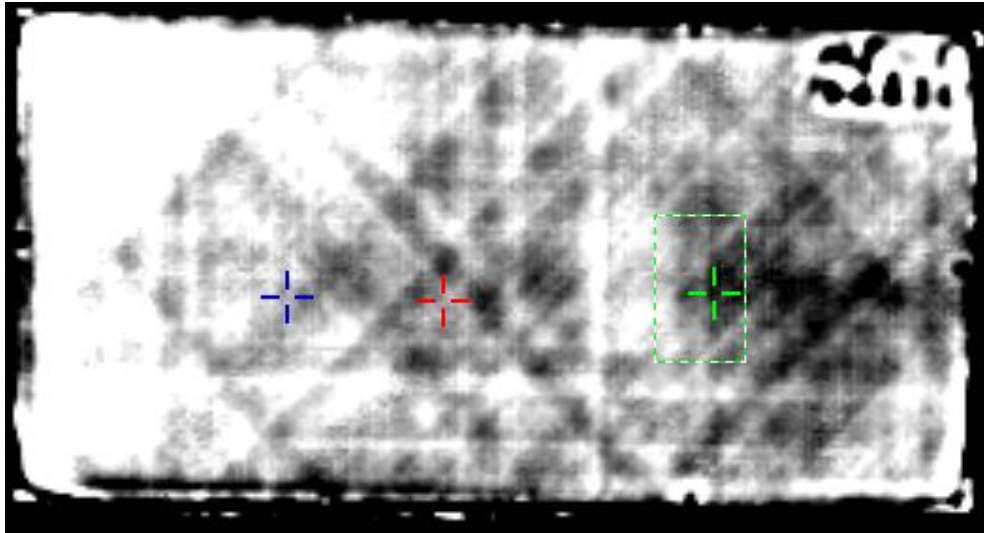


Figure 119 Pulsed thermography result; Sample: 3QI16d8JC2; Size: 200×100mm; 2D Image; Sampling: 90fms

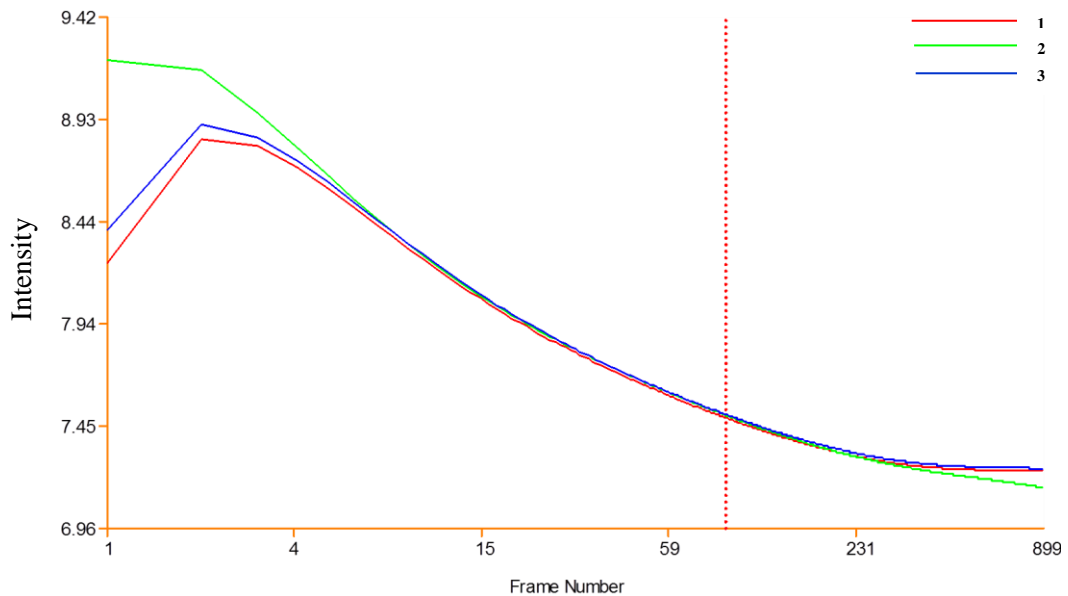


Figure 120 Pulsed thermography result; Sample: 3QI16d8JC2; RAW thermal log t-T plot; 1&3 – sound area, 2 – damage area

From the RAW thermal log t-T plot, it was observed that the data pattern is quite similar to the 12J Charpy impact sample with the t^* occurring at 3.975s. In this case, the pulsed thermal image does not clearly show the damage. The marker was placed based on an estimated damage location and hence cannot be used to deduce the results. Thus pulsed thermography results are inconclusive in this case.

Stress analysis results:

The following is the data obtained for the 8J Charpy impact 3mm quasi-isotropic sample the setting of which remained the same as the 12J sample.

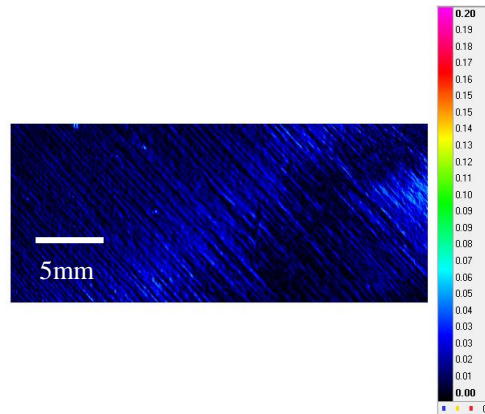


Figure 121 TSA stress map of Sample 3QI16d8JC2

The above image is the average image obtained from exciting the sample at 10Hz for an acquisition length of 2999 images. The image again fails to show any localised stress similar to the previous results (12J sample).

Conclusion:

Similar to the 12J impact sample, the 8J impact sample does show a physical deformation on the surface of the sample and corresponds to the data obtained from the transient thermal measurements indicating the creation of damage but fails to be identified by both the pulsed thermal and TSA methods.

NOTE:

Due to the nature of the damage created by the Charpy and the challenging nature of the detection using other thermal methods, only results showing damage will be presented for the remainder of the 3mm Charpy damaged laminates. Also note that each sample set will only present the results with a clear conclusion summing up the observations from the results obtained.

Impact energy 4.5J; Sample: 3QI12d4.5JC3

The following is the data obtained for the 4.5J Charpy impact on the 3mm quasi-isotropic laminate.

Microscope image:



Figure 122 Microscopy image of 3QI12d4.5JC3 showing damage site – no visible damage

In this case, the damage is barely visible both visually and through the microscope. There is no visual deformation as seen in the previous cases (12J & 8J impact) and the size of the damage is relatively small (~0.7mm).

Transient thermography results:

The following are the results obtained from the transient thermography data capturing the impact event. The acquisition settings remain the same.

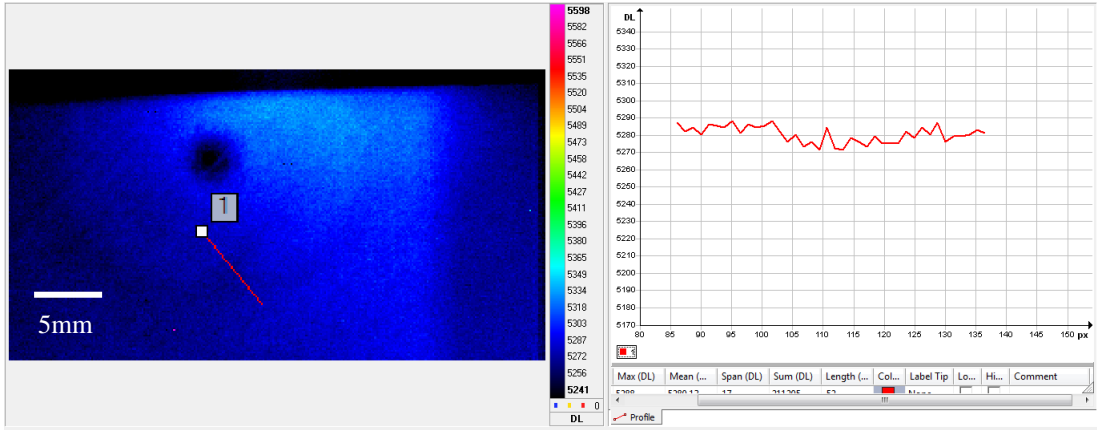


Figure 123 Sample: 3QI12d4.5JC3 at Frame - 0

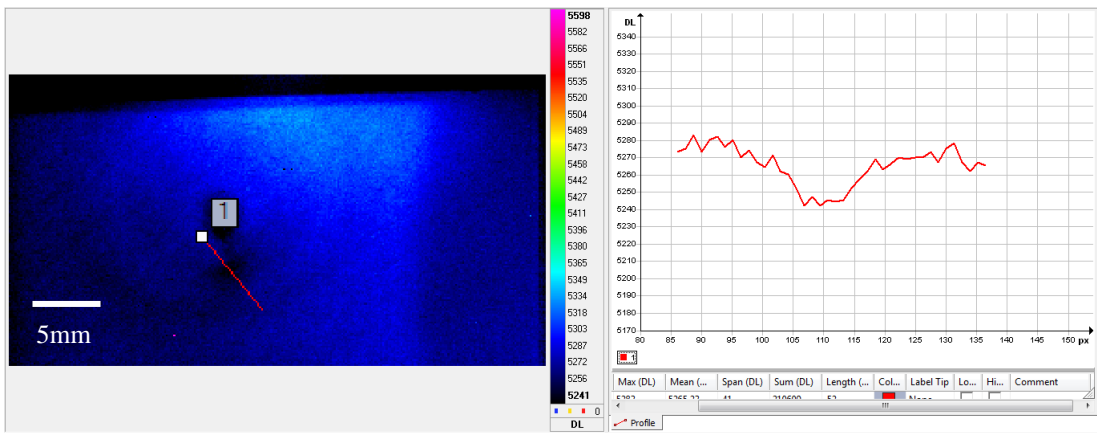


Figure 124 Sample: 3QI12d4.5JC3 at Frame - 1

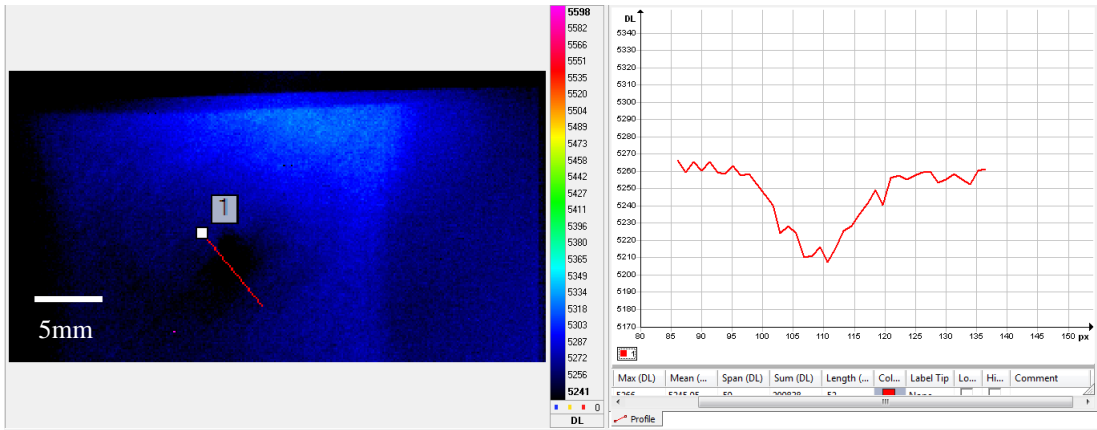


Figure 125 Sample: 3QI12d4.5JC3 at Frame - 2

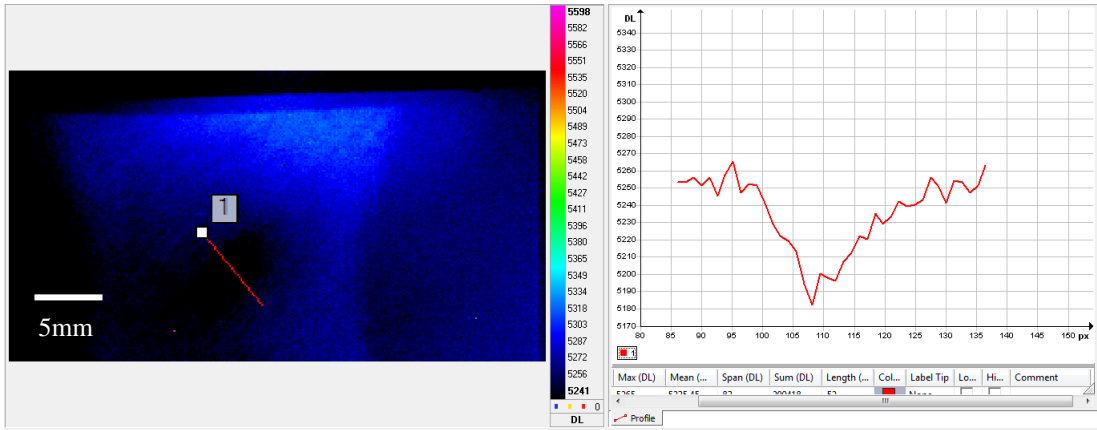


Figure 126 Sample: 3QI12d4.5JC3 at Frame – 3

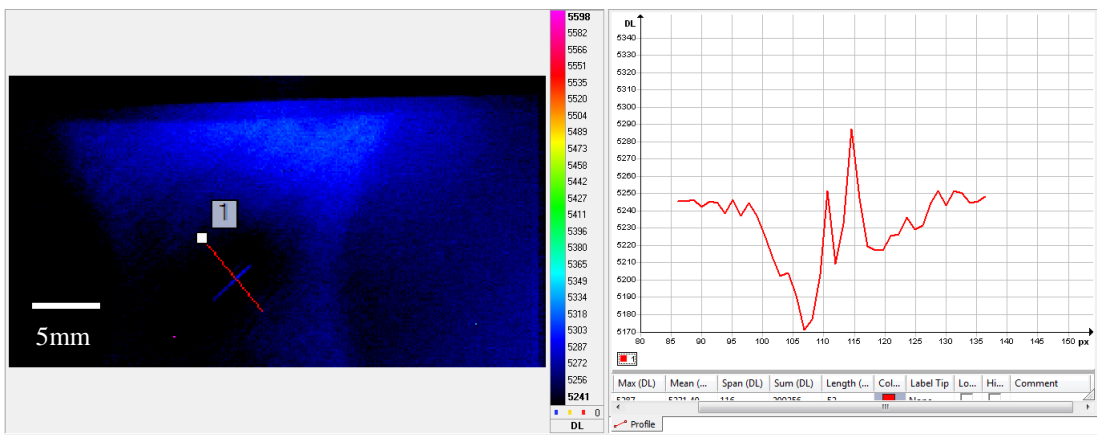


Figure 127 Sample: 3QI12d4.5JC3 at Frame – 4

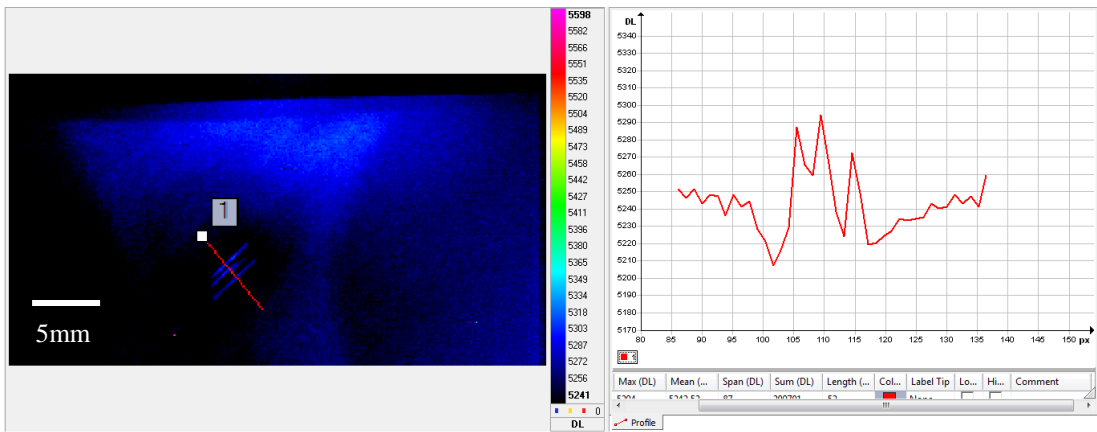


Figure 128 Sample: 3QI12d4.5JC3 at Frame – 5

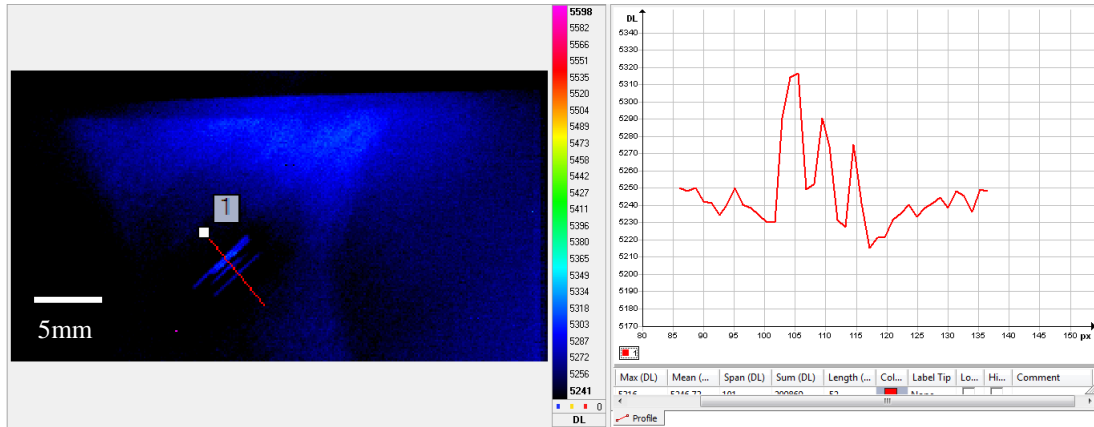


Figure 129 Sample: 3QI12d4.5JC3 at Frame – 6

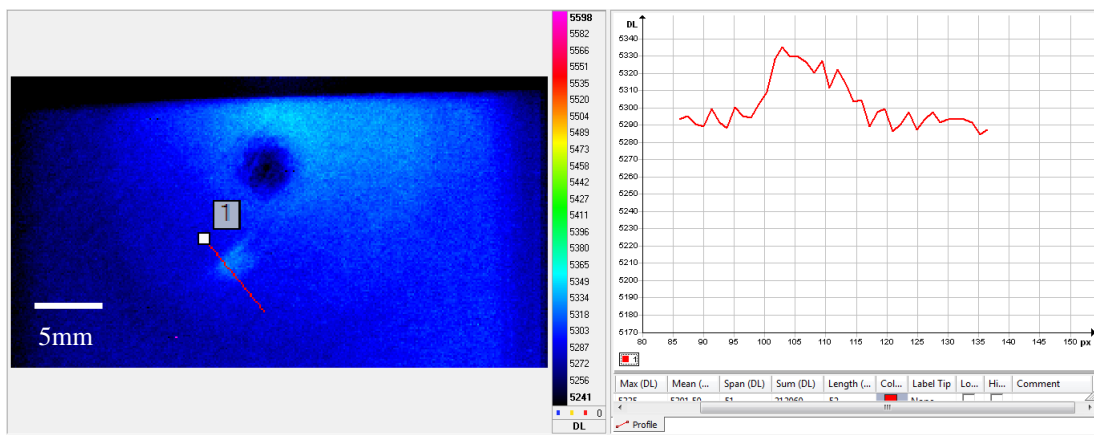


Figure 130 Sample: 3QI12d4.5JC3 at Frame – 8

From the above set of images, it was observed that at a lower energy there is first drop in temperature as observed in the 8J impact case. This temperature continues to drop until the first stress on the fibre appears in Frame 5. Further, it was seen that the lower and higher temperature areas continue to appear side by side as the damage stress, now past the thermoelastic zone continues to grow from Frame 5 – 7. At Frame 8 it changes to a faint overall temperature pattern not completely circular as seen in the previous cases. However the temperature around the damage region continued to rise which can be inferred from the temperature pixel profile plot as seen in the images above.

Conclusion:

This 4.5J impact has not produced any visible damage other than a small indication on the surface. The transient images provide more information on the impact event as a whole which can be characterised by a low temperature zone around the impact

area together with the high temperature areas progressing with the impact shock wave. The pulsed thermography and the TSA data did not detect the damage created at this low energy impact level.

4.4.1.2 3mm TWI – Charpy

The following are the set of results obtained from the second lay-up type referred to as TWI. This lay-up is different in that the majority of the fibres are oriented in the 0° and 90° direction. The detailed sequence can be found in Appendix 3 below. As before, this section reports the finding of the 3mm laminate when subjected to 12J, 8J and 4.5J Charpy impact energy levels. It should be noted that the structure of this section is similar to the previous section (4.4.1.1.).

Impact energy 12J; Sample: 3TWI20d12JC3

The following are the set of results obtained from the sample 3TWI20d12JC3 when subjected to an impact of 12J energy. As the results will follow the above pattern, all the findings will be explained in the conclusion section of this sample.

Microscope image:



Figure 131 Microscopic image of 3TWI20d12JC3 with dimension of the damage

Both the visual and microscopic images show a good level of damage that is clearly visible. It was also noticed that all trials had similar effects indicating that the damage creation is dependent on the laminate's stacking or lay-up sequence.

Transient thermography results:

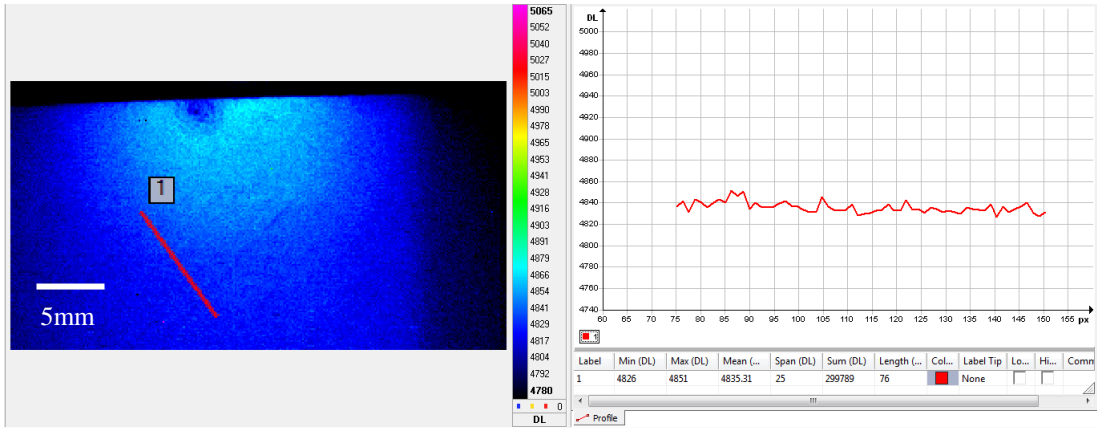


Figure 132 Sample: 3TWI20d12JC3 at Frame - 0

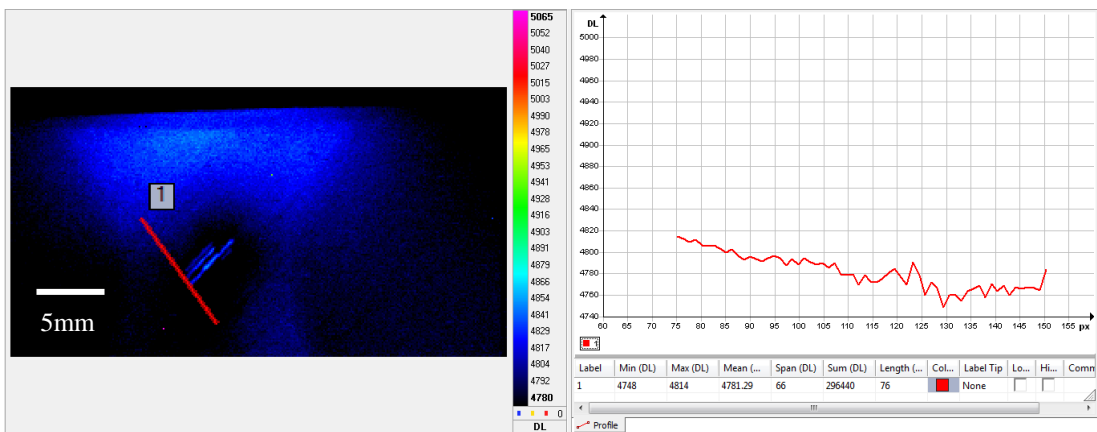


Figure 133 Sample: 3TWI20d12JC3 at Frame - 1

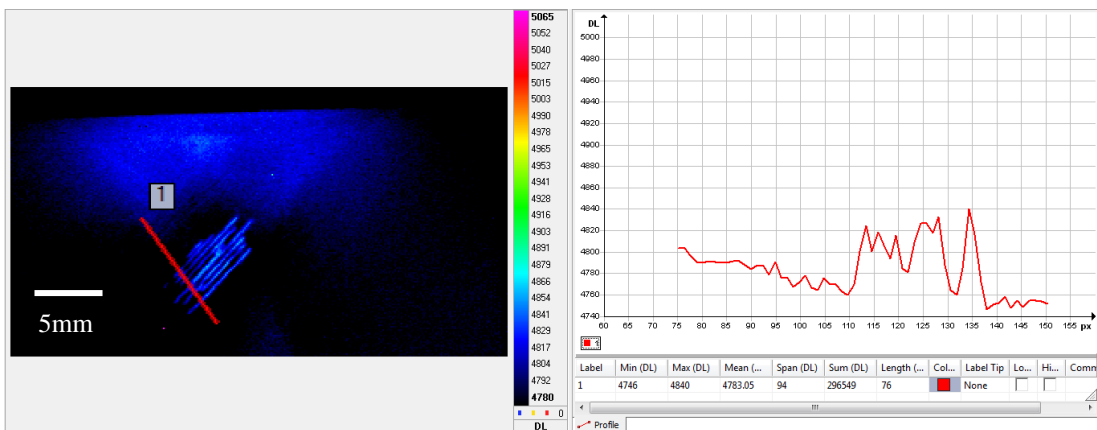


Figure 134 Sample: 3TWI20d12JC3 at Frame - 3

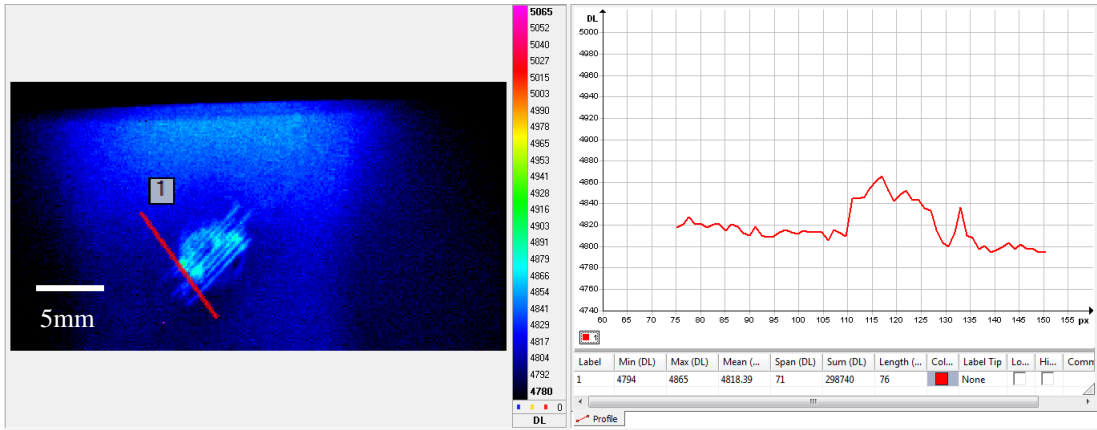


Figure 135 Sample: 3TWI20d12JC3 at Frame – 7

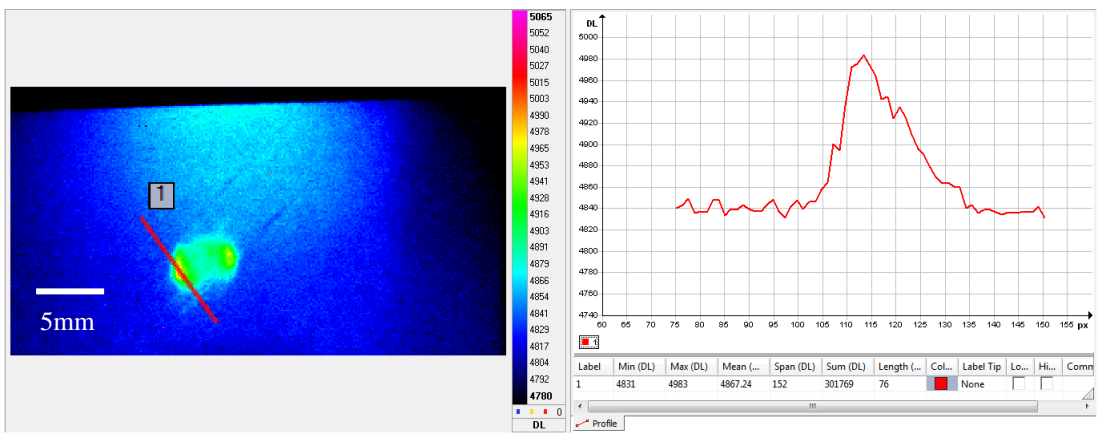


Figure 136 Sample: 3TWI20d12JC3 at Frame – 8

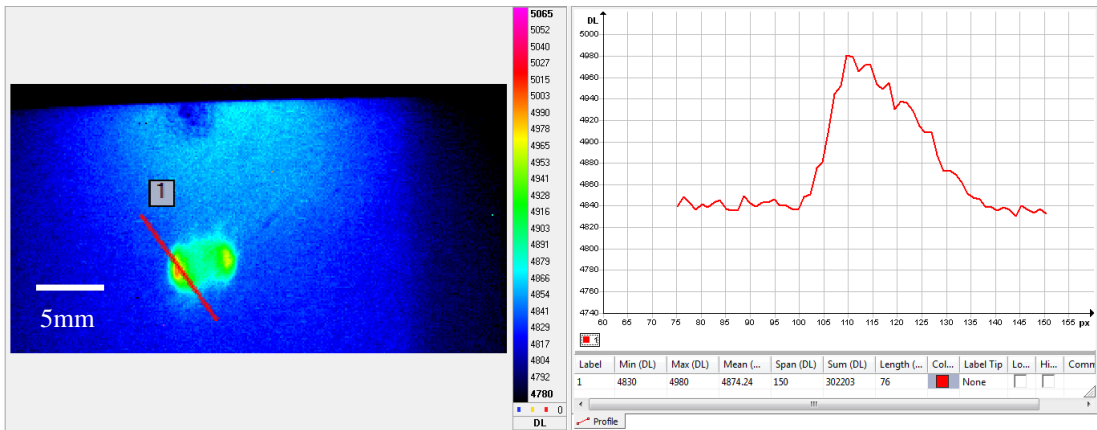


Figure 137 Sample: 3TWI20d12JC3 at Frame – 12

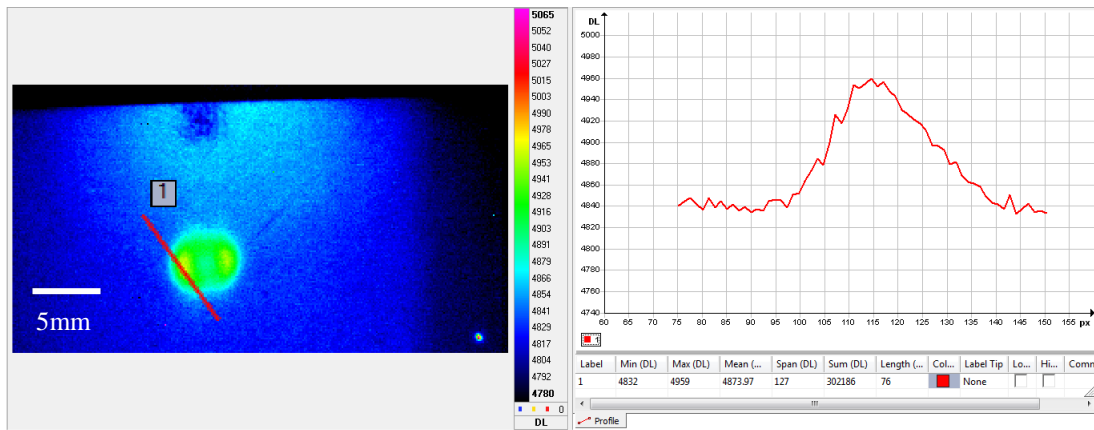


Figure 138 Sample: 3TWI20d12JC3 at Frame – 20

It can be seen from the above set of images that the temperature response time is much longer with the 12J impact. As before the individual stress concentrations along the fibre orientation is very clear until it hits Frame 8 where two localised areas of high temperature form on the thermogram. These then form into a single circular area showing a higher temperature range than the surrounding damage free area as the heat diffusion reaches the back wall (as seen in Frame 20).

Pulsed thermography results:

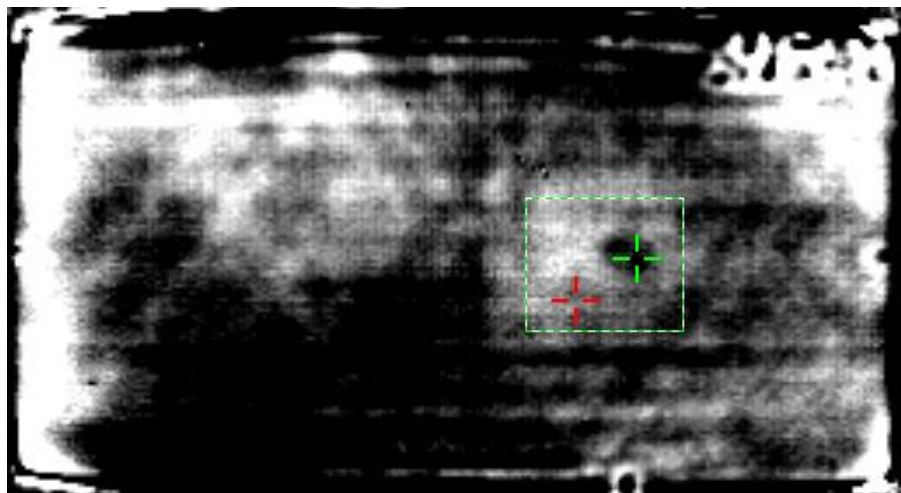


Figure 139 Pulsed thermography image; Sample: 3TWI20d12JC3; Size: 200×100mm; 2D image; Sampling: 90 frames

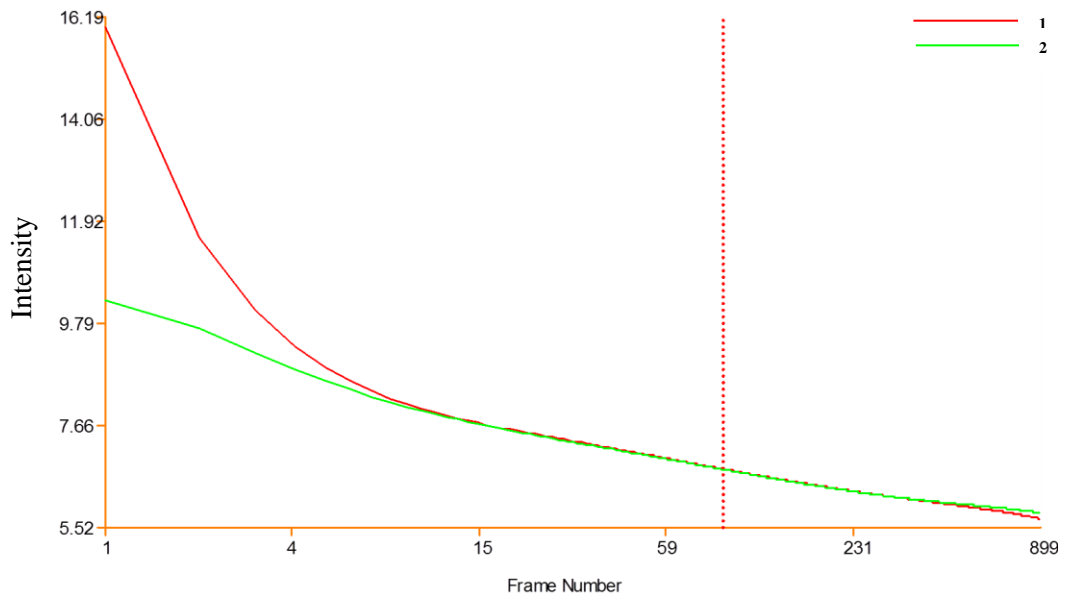


Figure 140 Pulsed thermography image; Sample: 3TWI20d12JC3; Log t-T plot;
1 – sound area, 2 – damage area

As before there is no clear distinction between the damage and the sound area of the sample as seen from the log time temperature plot above. However, with image analysis, the damage appears on the thermal image. The pattern is quite similar to that of the transient thermography results showing twin concentric areas of damage. It should be noted that the overall noise level on the thermogram and the close behaviour in terms of the time temperature curve makes it challenging to establish the feature as damage.

Conclusion:

The damage created with the TWI laminate shows a changed feature when compared with that of the QI laminate. It was also observed that the transient results different with more prominent peaks together with a secondary peak were observed in this case, confirming the hypothesis that the laminate stacking sequence governs the level and type of damage created. Though pulsed thermography results show the damage, TSA method did not yield any conclusive results.

Impact energy 8J; Sample: 3TWI16d12JC2

Microscope image:



Figure 141 Microscopic image of 3TWI16d8JC2 with dimensions of damage

The deformation formed as a result of impact is barely visible from the microscopic image above and does not show any additional indications confirming the presence of damage in the laminate.

Transient thermography results:

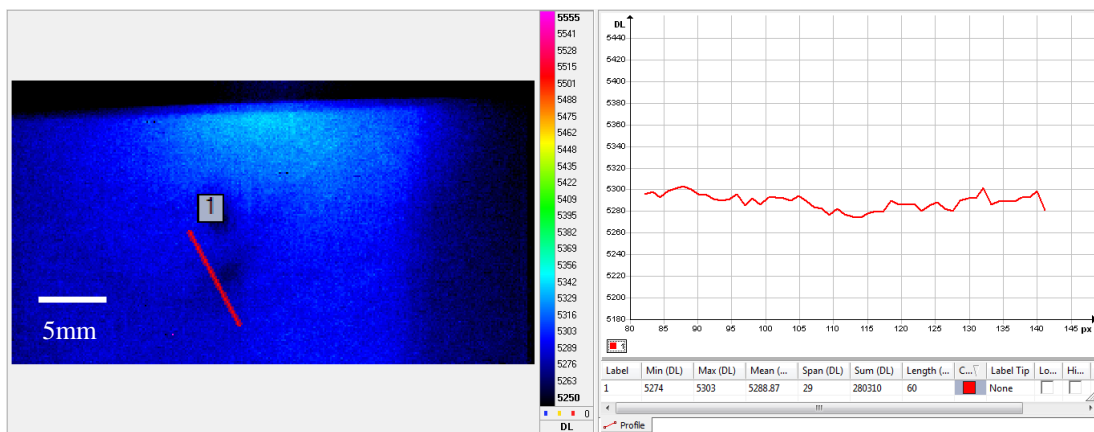


Figure 142 Sample: 3TWI16d8JC2 at Frame – 0

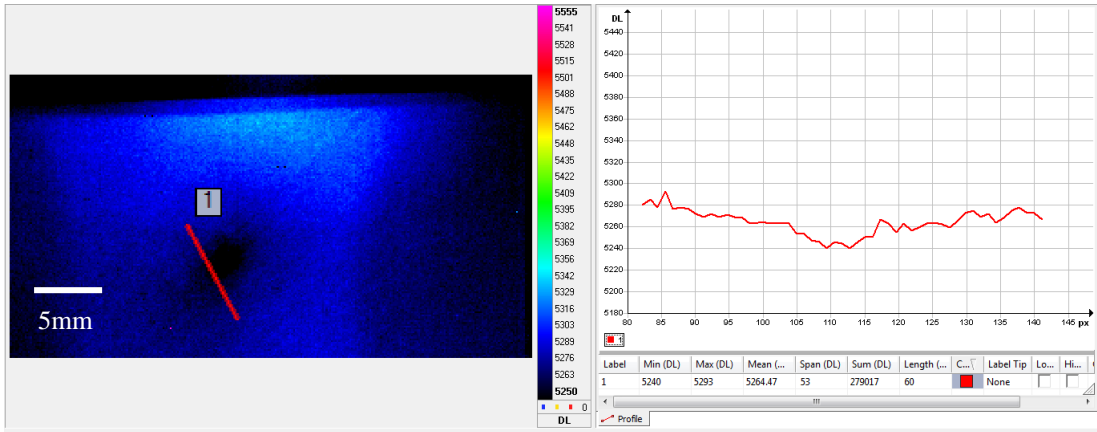


Figure 143 Sample: 3TWI16d8JC2 at Frame - 1

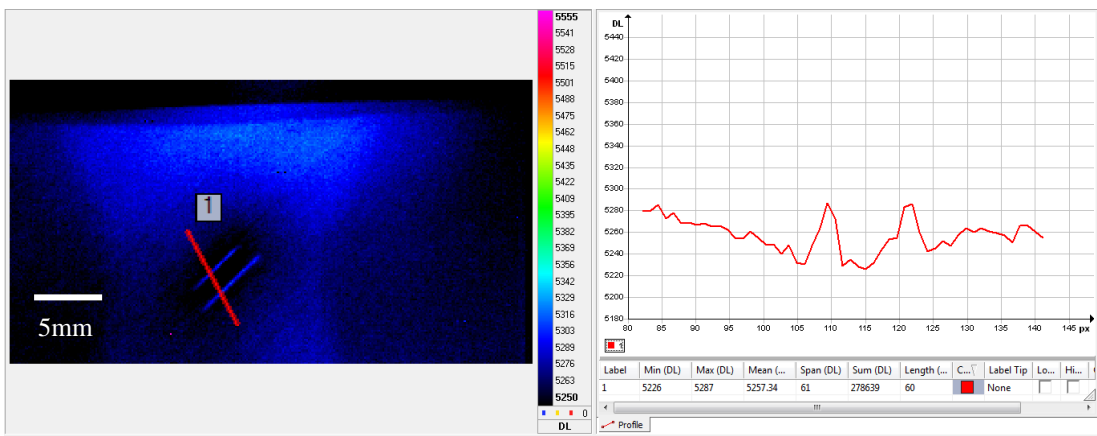


Figure 144 Sample: 3TWI16d8JC2 at Frame - 2

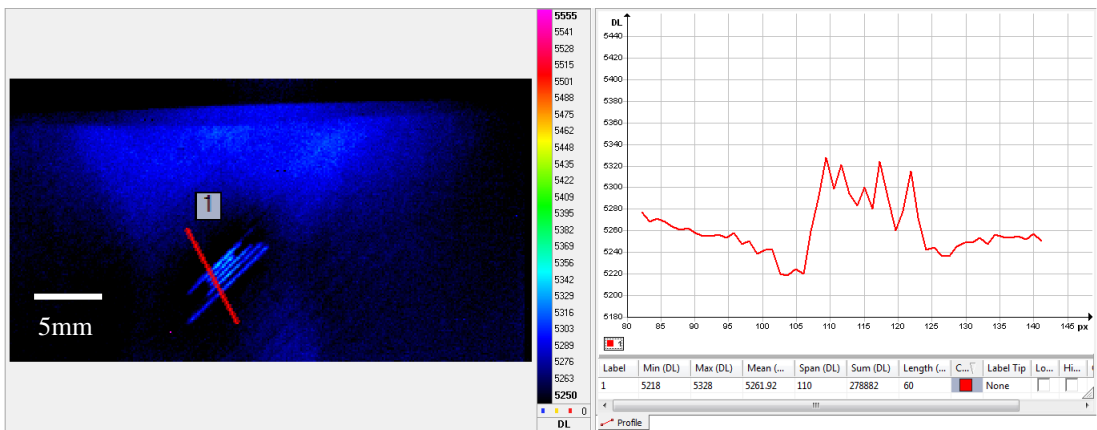


Figure 145 Sample: 3TWI16d8JC2 at Frame - 3

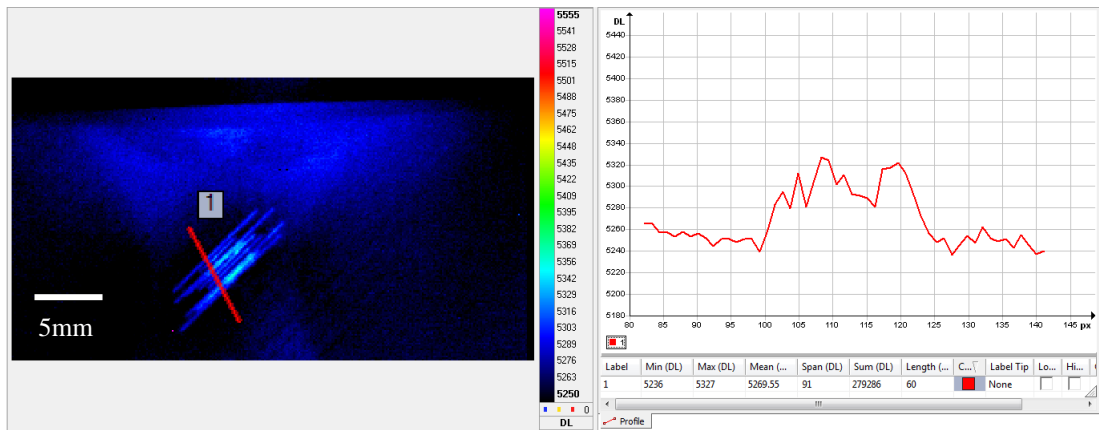


Figure 146 Sample: 3TWI16d8JC2 at Frame – 6

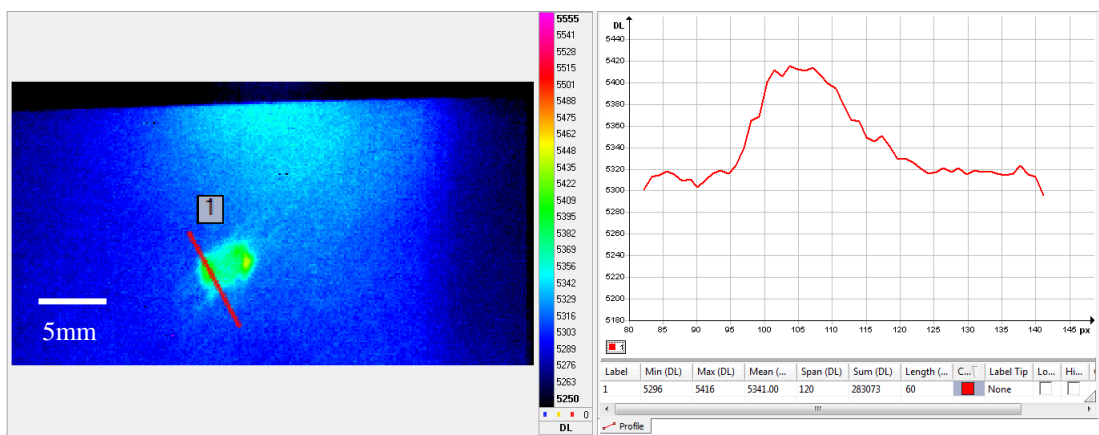


Figure 147 Sample: 3TWI16d8JC2 at Frame – 7

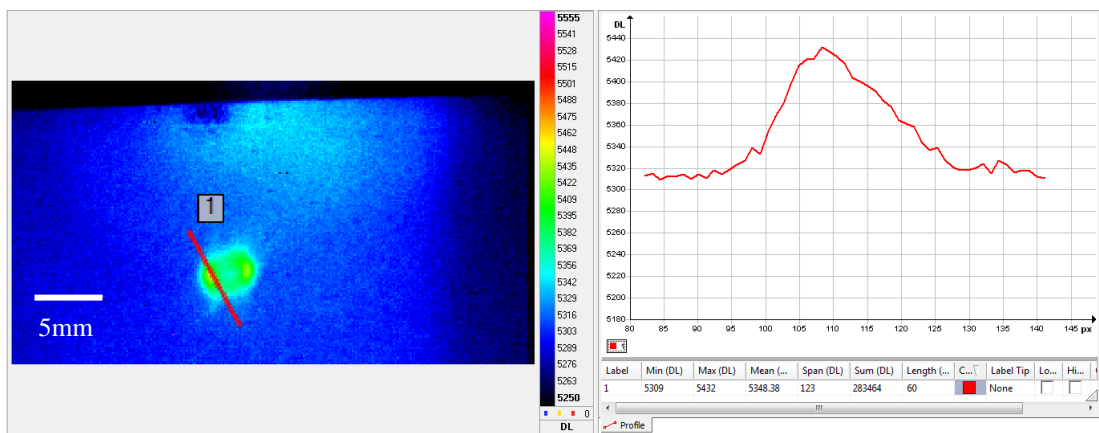


Figure 148 Sample: 3TWI16d8JC2 at Frame – 25

Conclusion:

For the 3TWI laminate with an 8J Charpy impact, the microscopic image a barely visible deformation on the laminate's surface. Though the transient thermography

results show the creation of damage, both the pulsed thermography and TSA systems were not sensitive enough to detect the damage and thus the results are inconclusive.

Impact energy 4.5J; Sample: 3TWI12d4.5JC3

Microscope image:



Figure 149 Microscopic image of 3TWI12d4.5JC3

The microscopic image does not show any indication of damage and hence the result is inconclusive.

Transient thermography results:

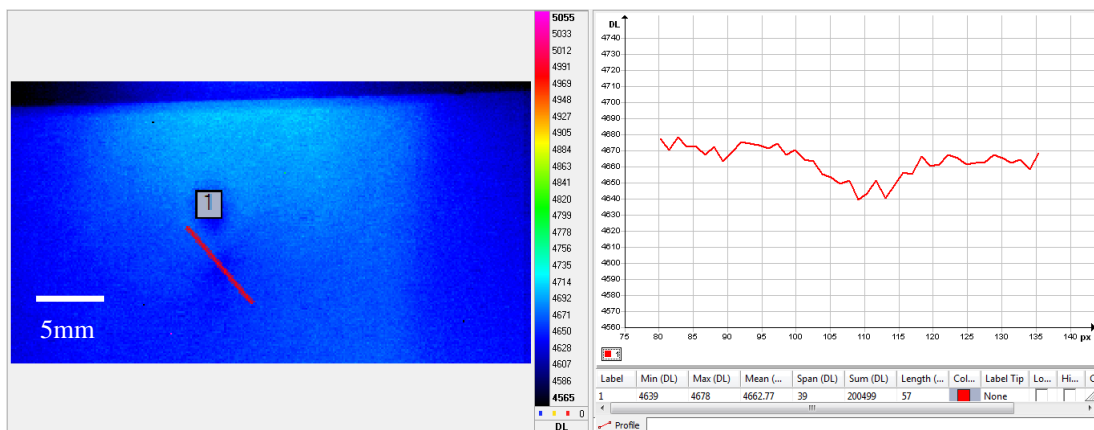


Figure 150 Sample: 3TWI12d4.5JC3 at Frame - 0

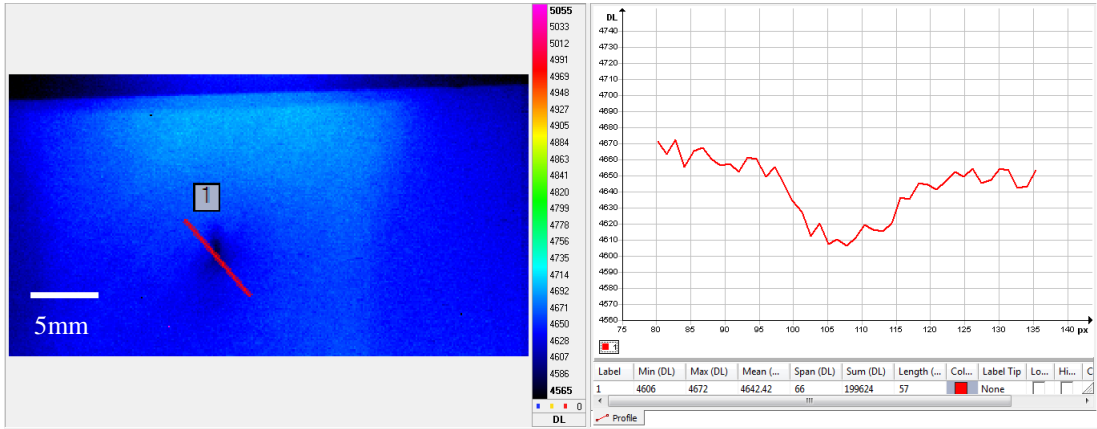


Figure 151 Sample: 3TWI12d4.5JC3 at Frame – 1

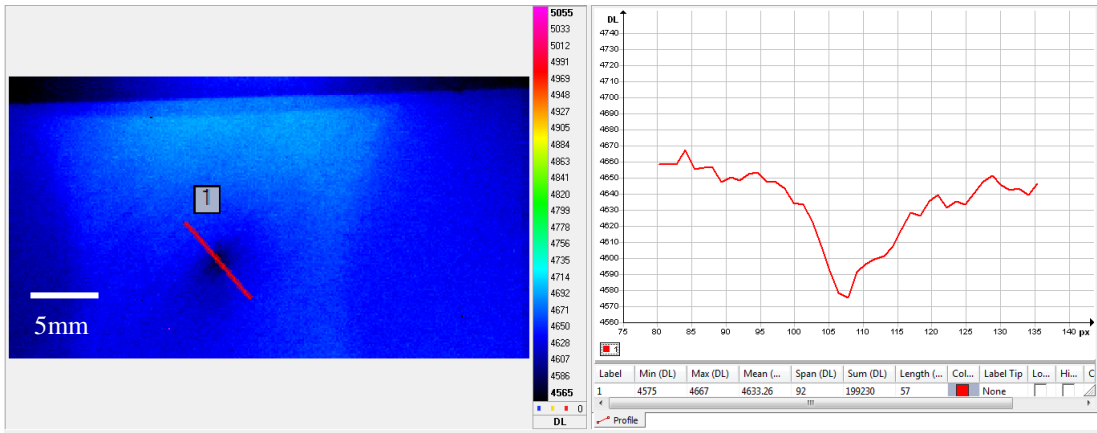


Figure 152 Sample: 3TWI12d4.5JC3 at Frame – 2

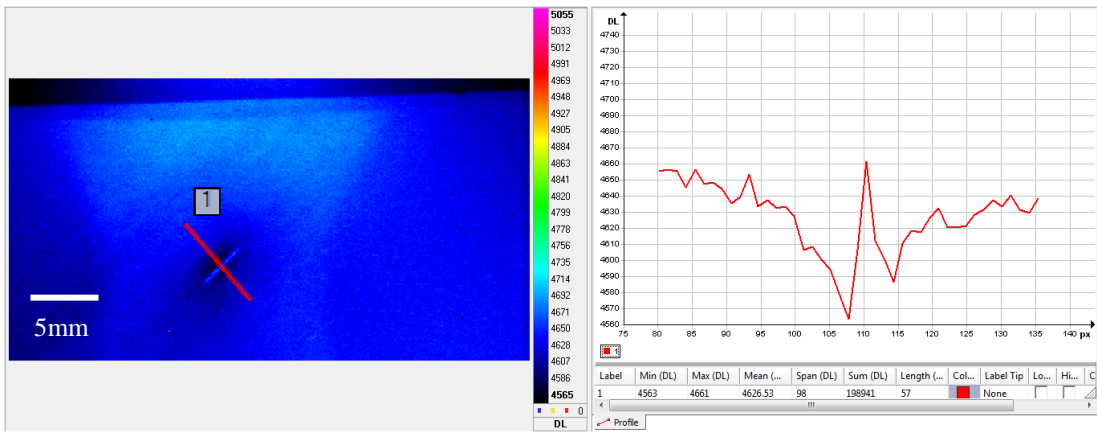


Figure 153 Sample: 3TWI12d4.5JC3 at Frame – 3

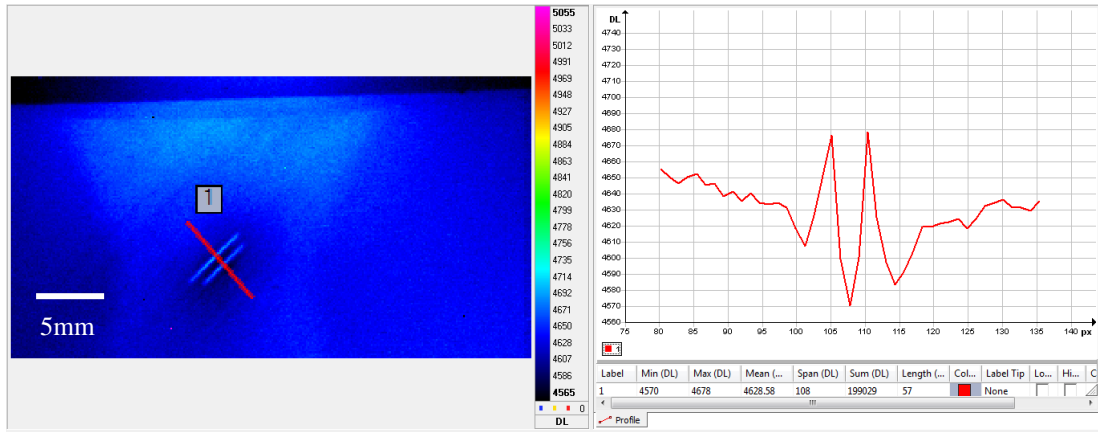


Figure 154 Sample: 3TWI12d4.5JC3 at Frame – 4

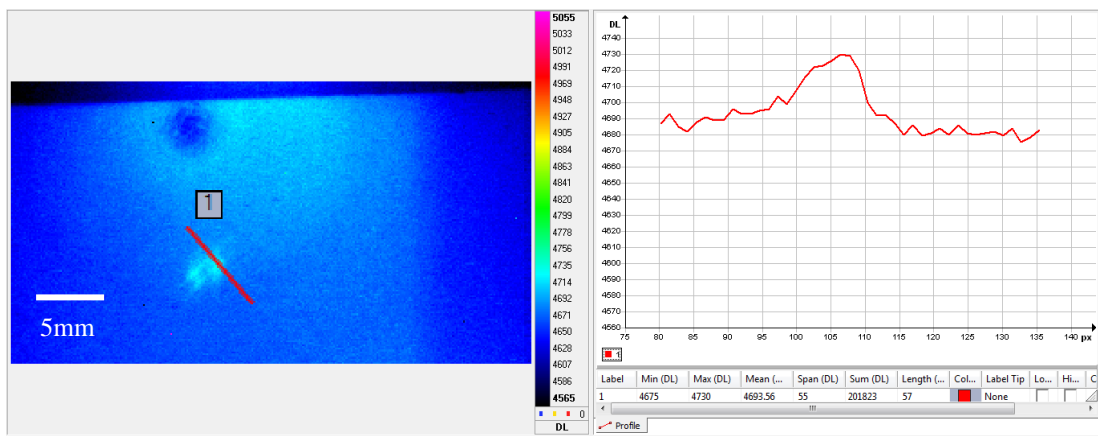


Figure 155 Sample: 3TWI12d4.5JC3 at Frame – 6

Conclusion:

For the 4.5J Charpy impact on 3mm TWI laminate, only transient thermography data shows the localised temperature rise along the fibre direction and follows the same heat diffusion pattern as observed before. All remaining inspection methods including microscopic evaluation, pulsed thermography and TSA methods do not detect the damage. This leads to a possible conclusion that the damage created is so small that it is beyond detectability threshold of the detection systems. One possible way of detecting this change could be through sample sectioning and microscopic evaluation for localised cracks. Due to the nature of the work, only selected NDT techniques have been applied for damage detection.

4.4.1.3 3mm Quasi-isotropic (QI) – Gas-gun

These experiments were intended to illustrate the ability of thermographic inspection techniques to detect damage due to high speed stone impact, the velocities and calculated energy for each impact can be found in Appendix 4. The following are the results obtained for 3mm QI layup laminates subjected to dynamic impact testing using a gas gun. The settings and result reporting style follows the previous section 4.4.1.1.

Impact energy: 12J; Sample: 3QI12JS2

Microscope image:



Figure 156 Microscopic image of 3QI12JS2

The above microscopic image shows the major damage created due to the gas gun impact testing using a stone of mass 6.7g and was set to impact at a velocity of 60m/s as described at the start of the section 4.4. The impact event created severe crush damage together with fibre breakage for an estimated area of 25.58 sq.mm as illustrated in the image above. Previously, the Charpy had a well-defined hemispherical indenter head creating a standard defined load condition as described in the literature and hence no surface breaking damages occurred and the laminates were left with surface dents. However, in case of the gas gun, stones were used to achieve the damage, and the rough surface of the stone has created localised high

stress at the impact area. There is existing evidence that the damage type created is dependent on the impactor shape (Mitrevski, Marshall et al. 2005). As the stone has sharp edges, the area of contact is a point load as opposed to a surface load, which explains why crush damage was created in this case.

Transient thermography results:

The following results were obtained during the impact event. As described in the earlier parts of section 4.4, the impact event was observed from the back surface of the laminate with the acquisition frequency of 542.1Hz and a window size of 288×156 pixels for an integration time of 1ms.

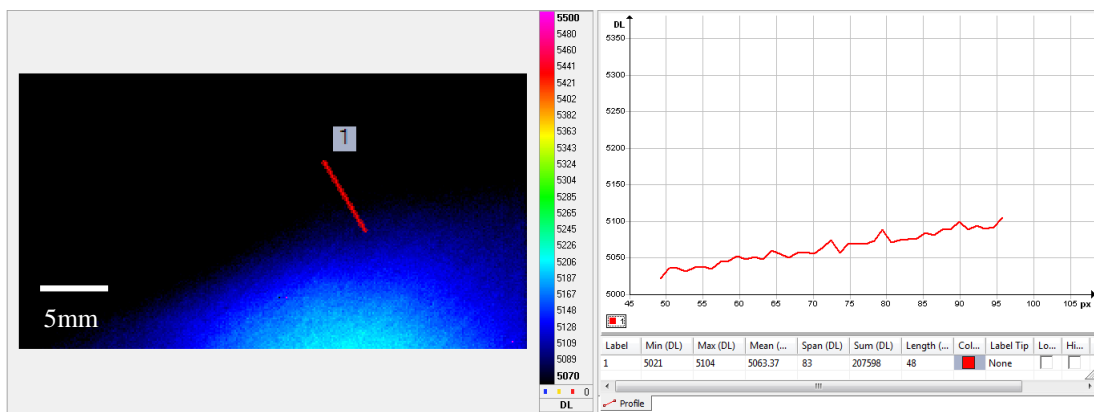


Figure 157 Sample: 3QI12JS2 at Frame - 0

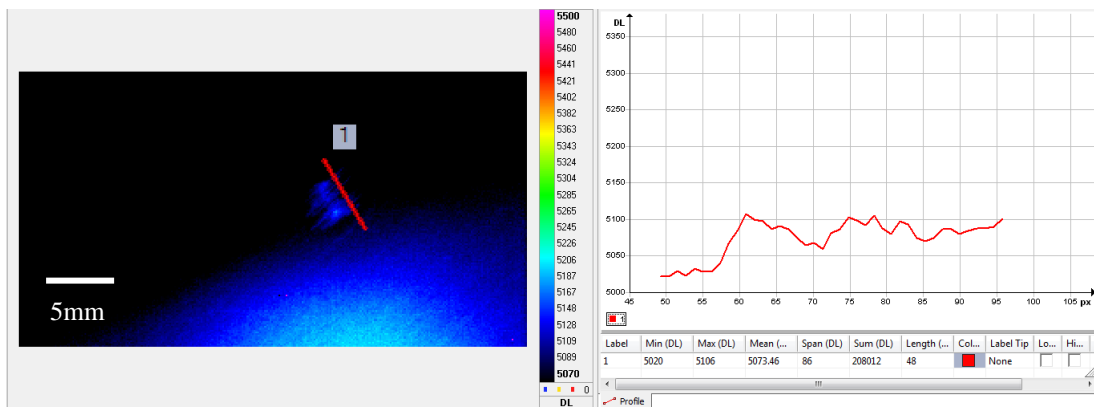


Figure 158 Sample: 3QI12JS2 at Frame - 1

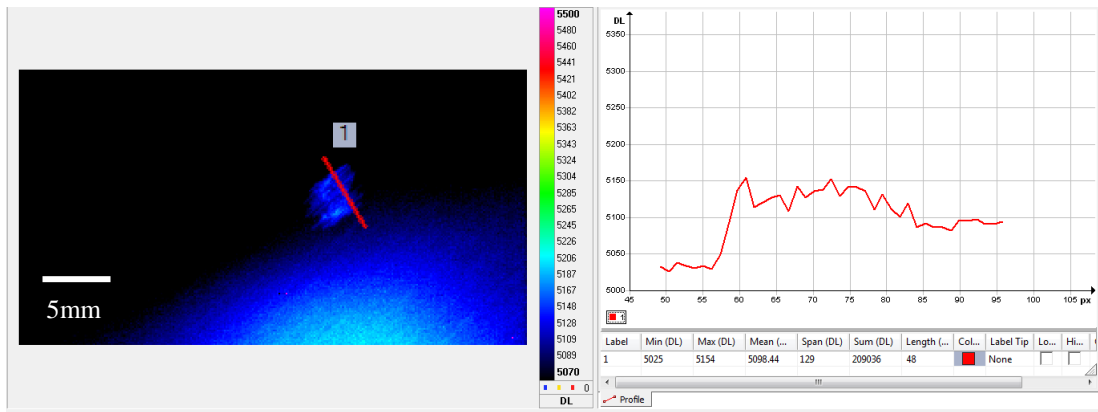


Figure 159 Sample: 3QI12JS2 at Frame - 2

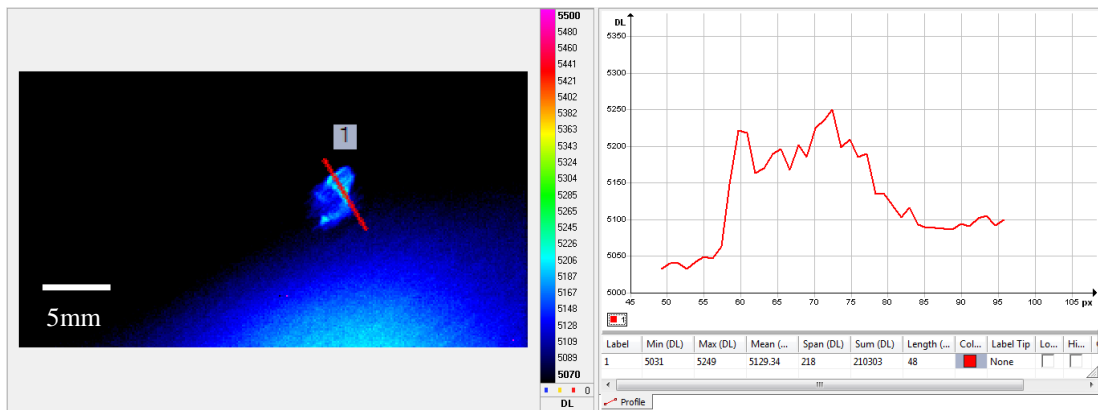


Figure 160 Sample: 3QI12JS2 at Frame - 3

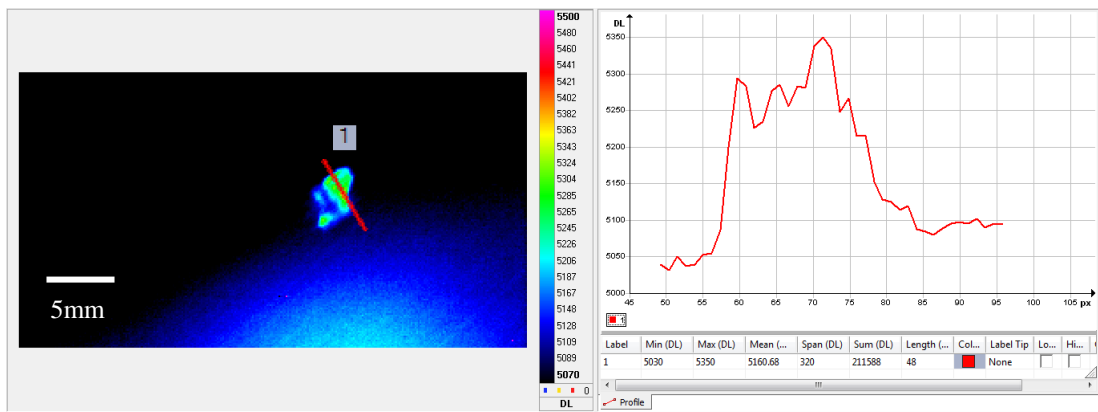


Figure 161 Sample: 3QI12JS2 at Frame - 8

The above transient thermograms for the 12J gas-gun impact test do show a similar stress pattern occurring along the fibre orientation initially as see with the Charpy samples above. However, the heat shape pattern is irregular at the heat diffusion takes place indicating that the back wall heat pattern is dependent on the impactor type and geometry. For the Charpy it was circular due to the hemispherical indenter, whereas for the gas-gun, it reflects the irregular shape of the stone. It was

also observed that the temperature at the impact area was higher in comparison with the Charpy impact.

Pulsed thermography results:

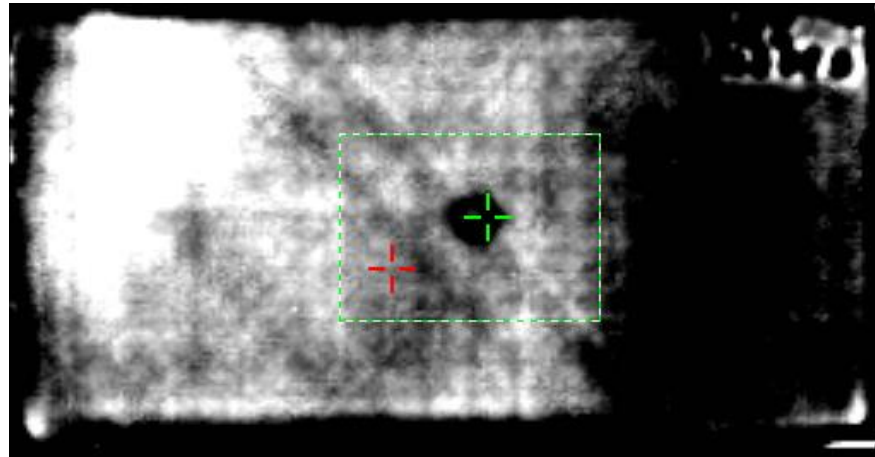


Figure 162 Pulsed thermography results: Sample: 3QI12JS2; Size: 200×100mm; 2D image; Sampling: 55fms

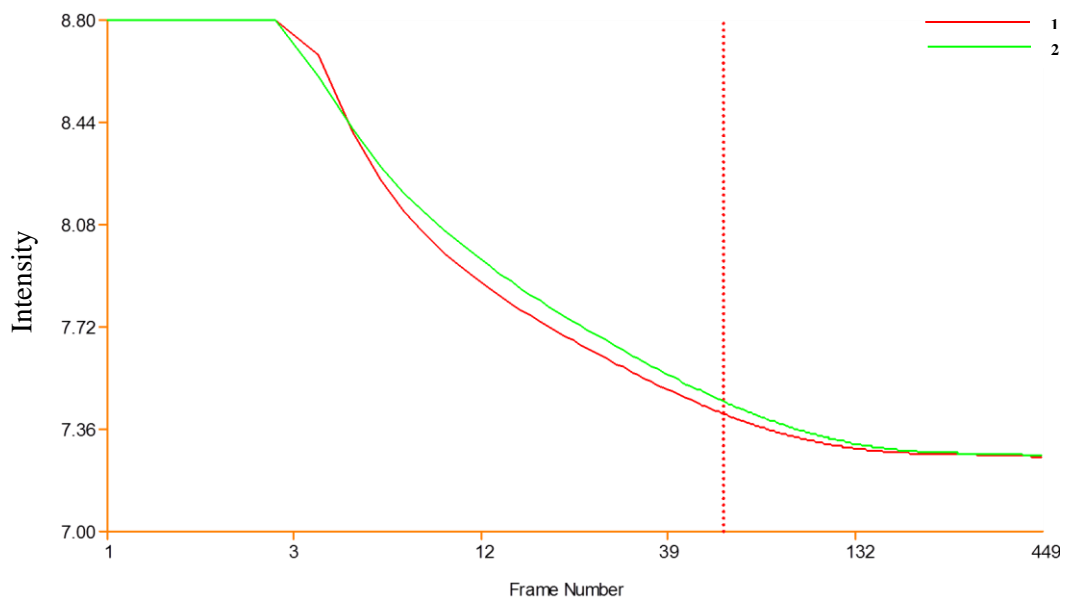


Figure 163 Pulsed thermography results: Sample: 3QI12JS2; Log t-T plot; 1 – sound area, 2 – damage area

The pulsed thermography results clearly show the damage created due to the impact event. This can also be seen in the log t-T plot above where the damage has a higher heat capacity (indicated by green curve & marker) than the sound area of the laminate (indicated by red curve & marker).

Stress analysis results:

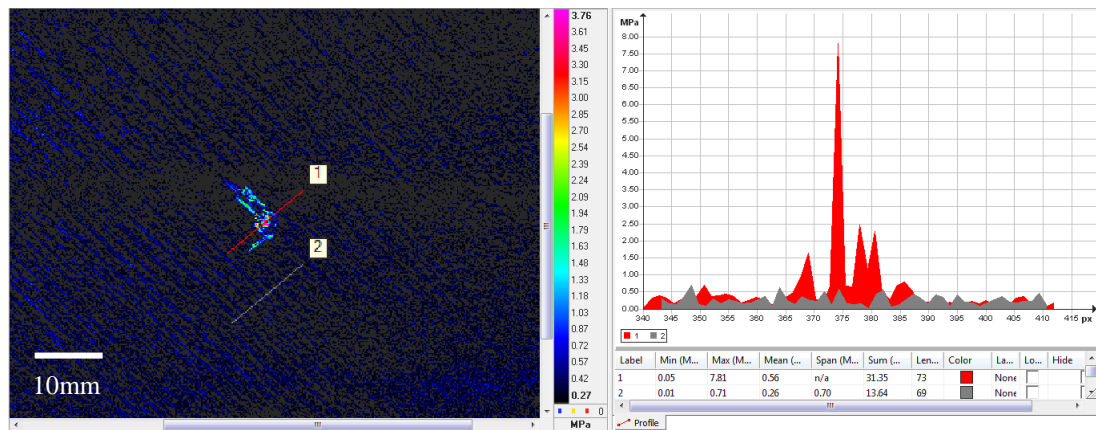


Figure 164 TSA result for 3QI12JS2

The TSA image above clearly shows the crush damage with the centre of the damage showing the highest stress value which can be inferred from the stress profile peak from the stress vs pixel plot on the right. The red area represents the stress profile marker drawn across the damage and the grey marker along the non-damage area.

Conclusion:

The above results clearly relate the damage formation indicated by the transient thermograms to both pulsed and TSA results. It was observed that the damage is a surface breaking crush damage. Previously, in the case of Charpy damage for the 12J impact energy level, there was indication of deformation on the surface; however, the material was intact and did not produce any surface breakage. This confirms the theory that the type of damage created is dependent on the impactor geometry. Further its detectability by TSA shows the techniques strength to identify this type of damage. The damage in this case is confirmed by visual – microscopic, transient, pulsed and TSA methods. It should be noted that, due to the random nature of the impact event in relation to the mass of the stone and velocity of impact, the damage creation and its characteristics were observed to be varying for the same energy of a similar impact event. The above results only present the observations of one trial only, and the damage characteristics across other trials were found to be consistent.

Impact energy: 8J; Sample: 3QI8JS1

Microscope image:



Figure 165 Microscopic image of 3QI8JS1 with dimensions of damage

As before, the stone ($m=5.9g$; $v=52.07m/s$) impact on the surface has created the crush damage with cracks occurring along the fibre orientation for the impact energy of 8J.

Transient thermography results:

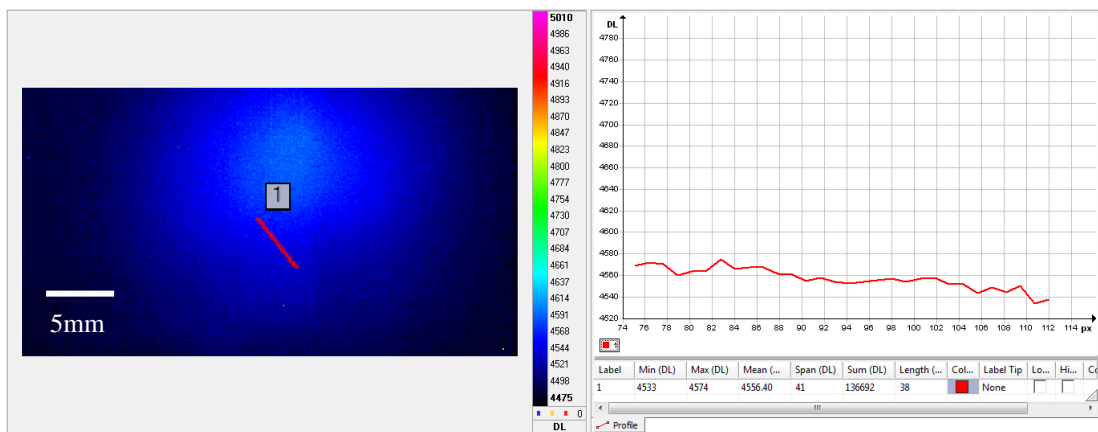


Figure 166 Sample: 3QI8JS1 at Frame - 0

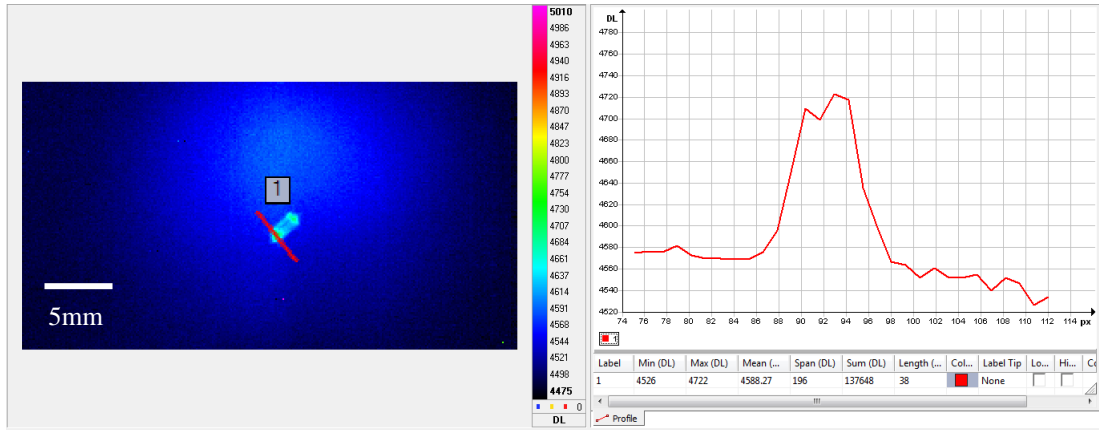


Figure 167 Sample: 3QI8JS1 at Frame – 1

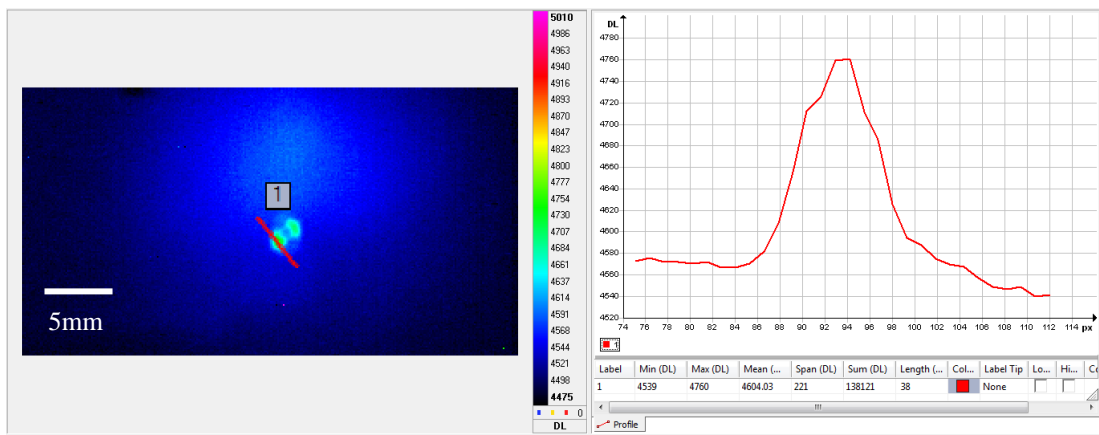


Figure 168 Sample: 3QI8JS1 at Frame – 8

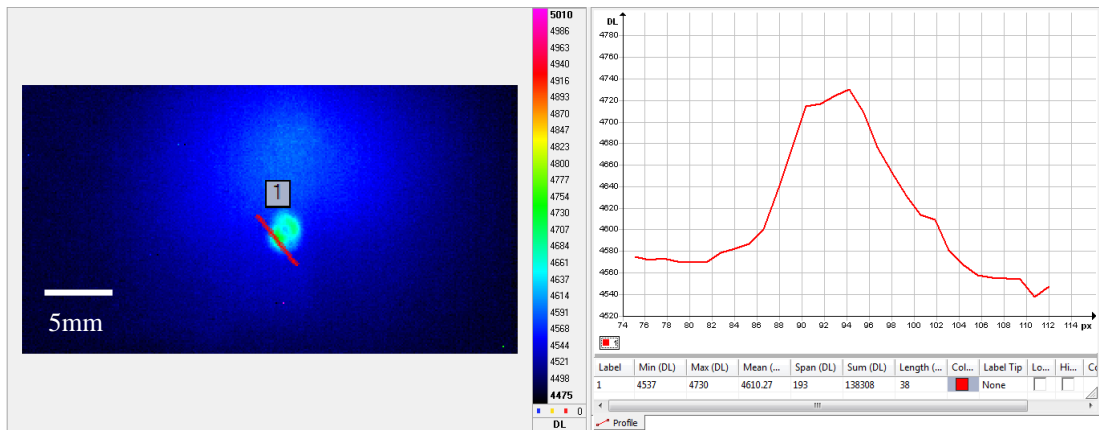


Figure 169 Sample: 3QI8JS1 at Frame – 16

As mentioned previously, the damage creation characteristics are different to the 12J gas gun impacted laminate. In this case, 2 areas of temperature stress concentration were observed.

Pulsed thermography results:

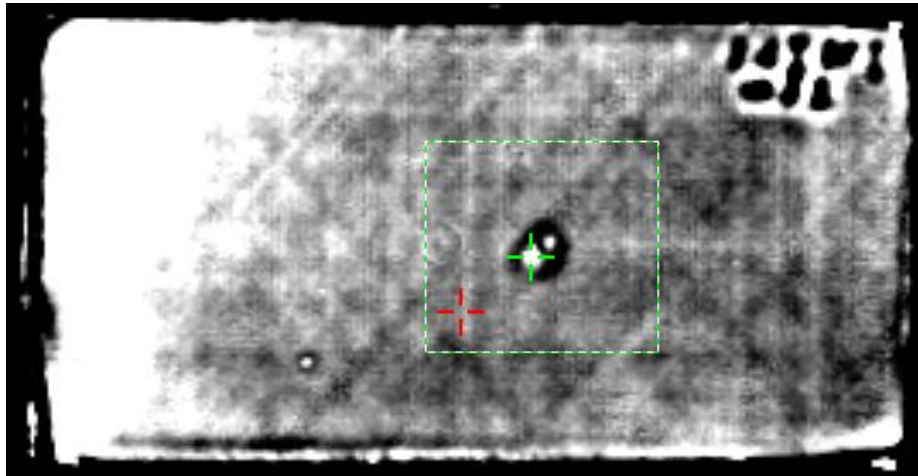


Figure 170 Pulsed thermographic image; Sample: 3QI8JS1; Size: 200×100mm; 2D image; Sampling: 55fms

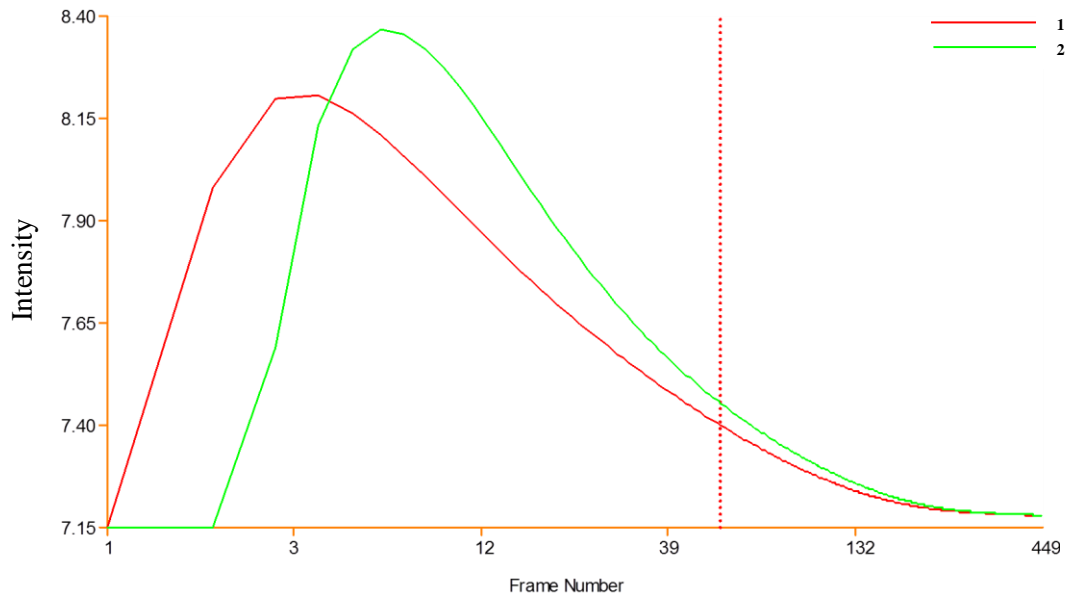


Figure 171 Pulsed thermographic image; Sample: 3QI8JS1; Log t-T plot; 1 – sound area, 2 – damage area

From the pulsed thermography data, the damage is clearly visible, also confirmed by the log t-T plot above. The image also shows two distinct hot spots and can be correlated to the transient thermography data validating the damage occurrence in the laminate. The crush damage has also caused further sub-surface damage as indicated by the thermogram above.

Stress analysis results:

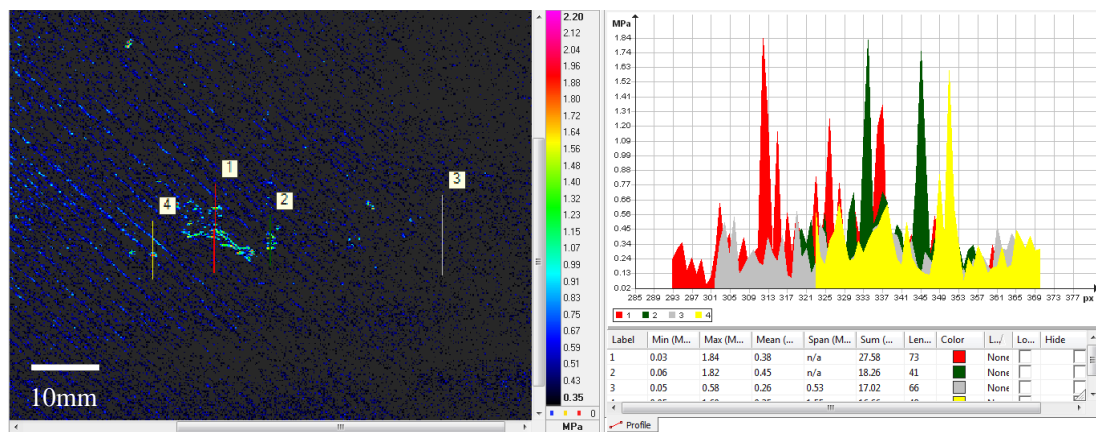


Figure 172 TSA image with stress map plot on the right showing peaks for various damage areas

The TSA stress map (Figure 172) above clearly show regions of localised stress caused due to the excitation frequency. It should be noted that the damage shape almost matched the visual – microscopic image. The primary and secondary damage indicated by the line profiles 1 & 2 (red and green peaks on the plot), there is also a third peak (label 4) with a similar stress value (indicated by yellow peak) has been observed in the data. Now this third damage is so small that it has only created a surface damage and has not been picked by either the transient or the pulsed thermal data sets. There is also a scatter of stress spots which relate to the spread of damage on the laminate’s surface due to the impact itself as observed on the visual image.

Conclusion:

The damage created at this energy level has been detected by all the methods. However, it is worth mentioning that the transient thermal data showed a noticeable difference in the laminate’s back wall temperature rise. Additional damage features were observed in the TSA data set demonstrating the strength of the technique in detecting surface breaking damage.

Impact energy: 4.5J; Sample: 3QI4.5JS1

The reminders of the results follow the previous samples and hence the observations will be presented at the end of each sub-section.

Microscope image:



Figure 173 3QI4.5JS1 laminate's microscopic image with damage measurements

Transient thermography results:

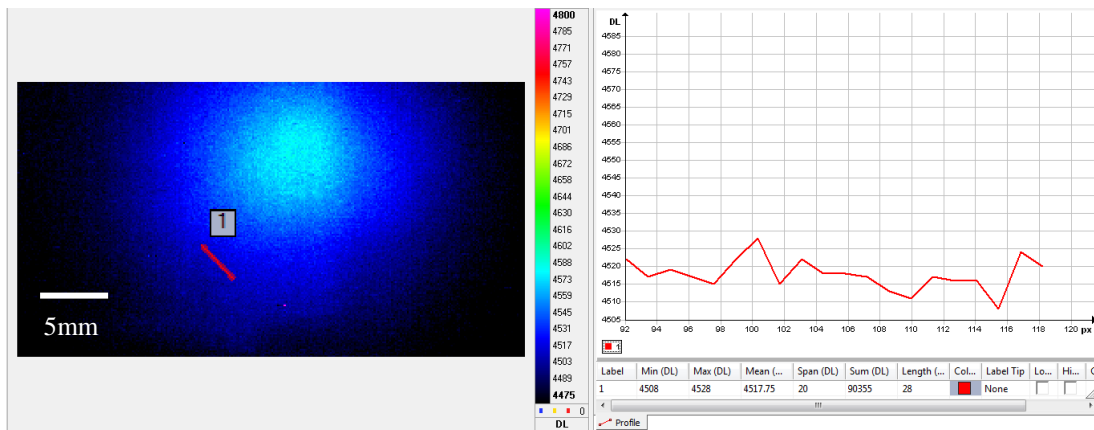


Figure 174 Sample: 3QI4.5JS1 at Frame – 0

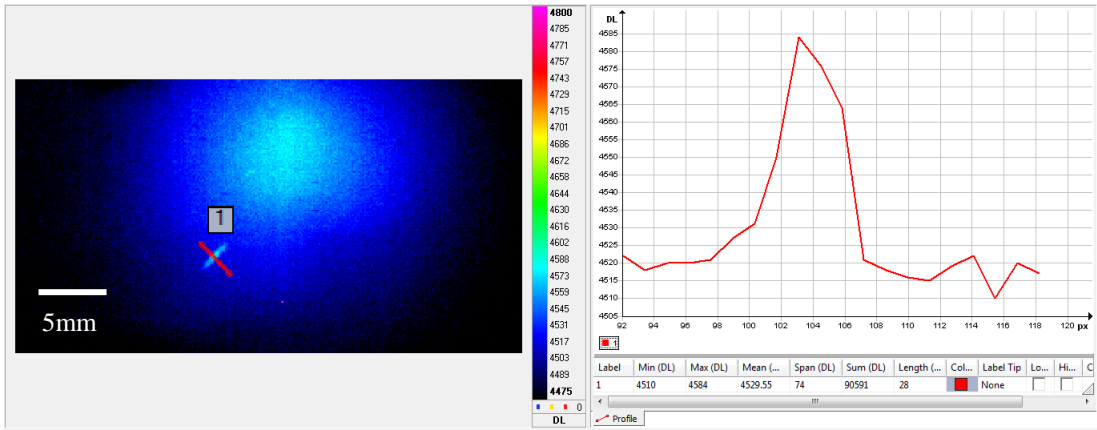


Figure 175 Sample: 3QI4.5JS1 at Frame - 1

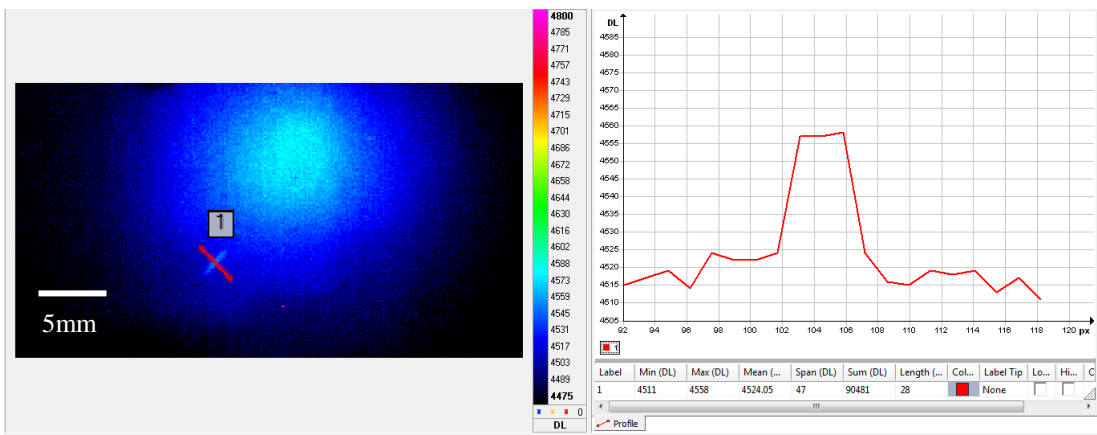


Figure 176 Sample: 3QI4.5JS1 at Frame - 8

Pulsed Thermography results:

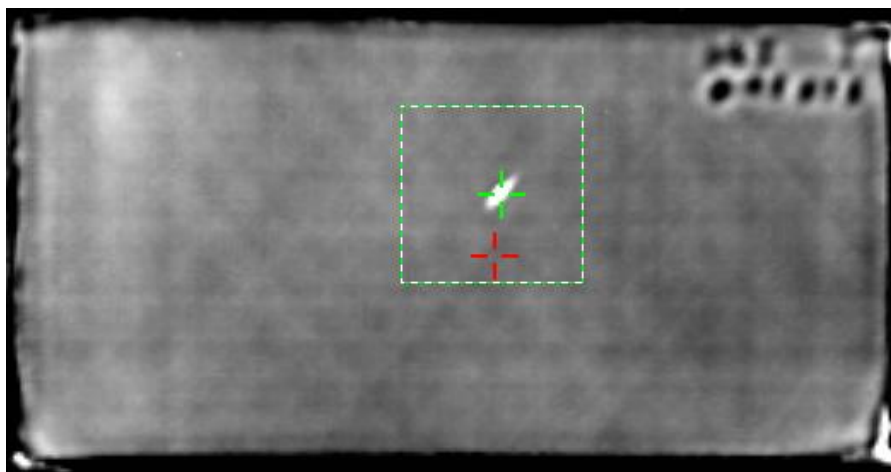


Figure 177 Pulsed thermography image; Sample: 3QI4.5JS1; Size: 200×100mm; 2D image; Sampling: 55fms

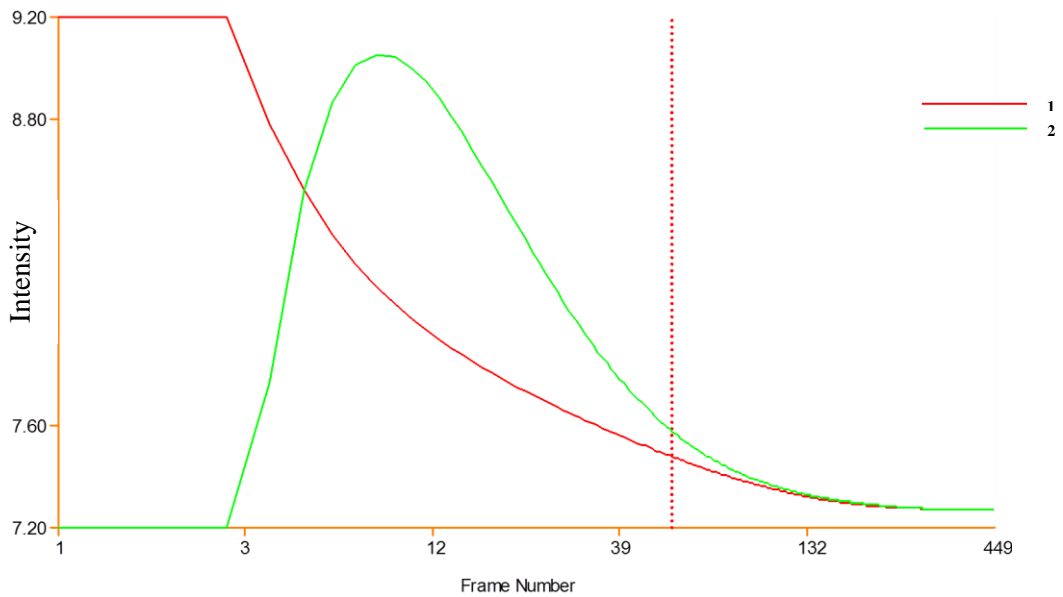


Figure 178 Pulsed thermography results; Sample: 3QI4.5JS1; Log t-T plot;
1 – sound area, 2 – damage area

Stress analysis results:

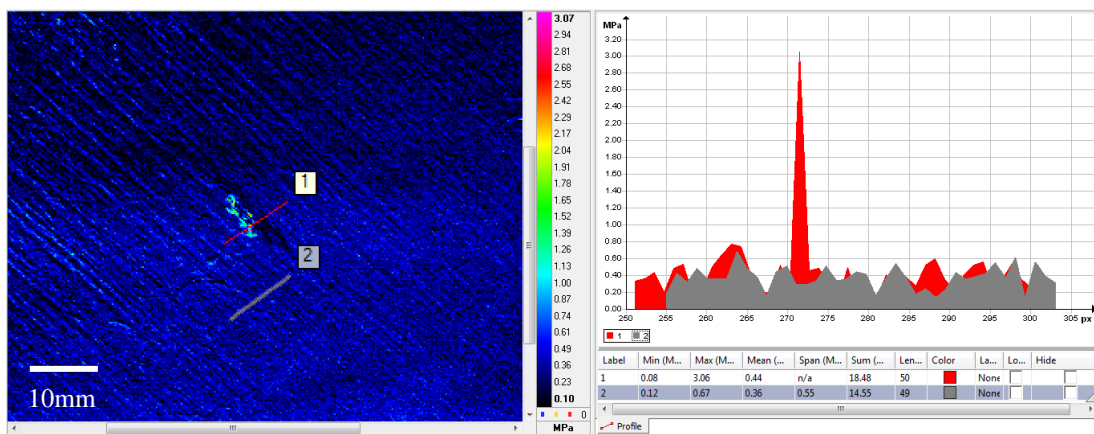


Figure 179 TSA stress map of 3QI4.5JS1 with a profile plot on the right

Conclusion:

Again, for this laminate with 4.5J gas-gun impact, the damage is clearly visible in all tests. Crush damage together with cracks and fibre breakage can be observed in the microscopic image which can be validated by both pulsed and TSA inspection methods. However, it should be highlighted that the transient thermography data showed damage and maintained a profile as observed in the microscope, pulsed and TSA images. It was also observed that, due to the low energy of impact, the heat intensity at the back wall did not show a huge distinct rise as observed previously, but still sensitive enough to show the stress associated with the damage creation.

4.4.1.4 3mm TWI – Gas-gun

This section presents the last set of results from the 3mm thick laminates subjected to ballistic impact testing at 12J, 8J and 4.5J energy level. As the results follow the same trend, only images will be presented and any additional information will be reported under the conclusion section for each of the samples.

Impact energy: 12J; Sample: 3TWI12JS3

Microscope image:

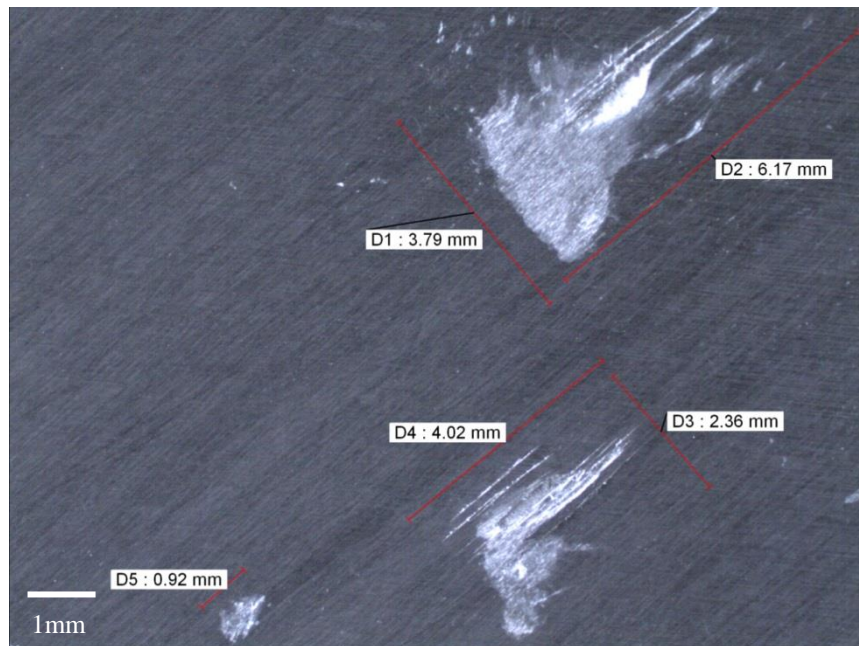


Figure 180 Microscopic image of 3TWI12JS3 laminate with damage measurements

Transient thermography results:

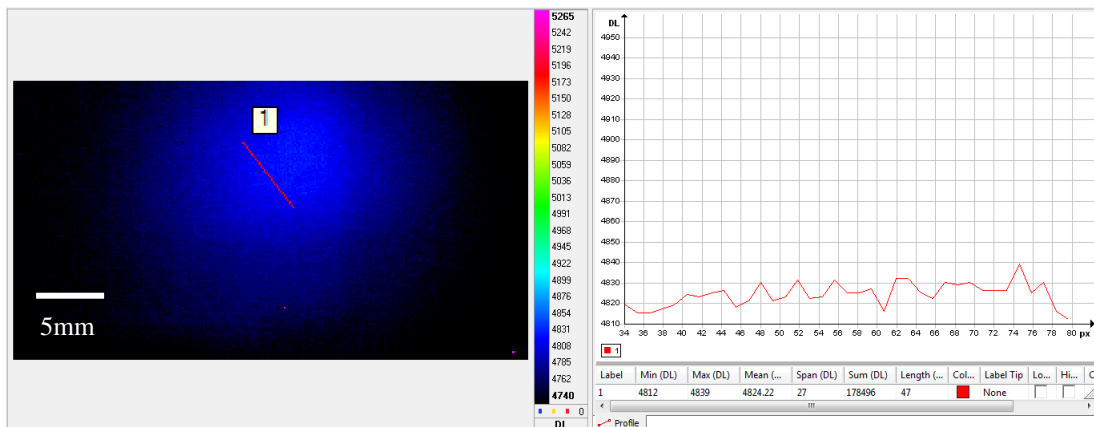


Figure 181 Sample: 3TWI12JS3 at Frame - 0

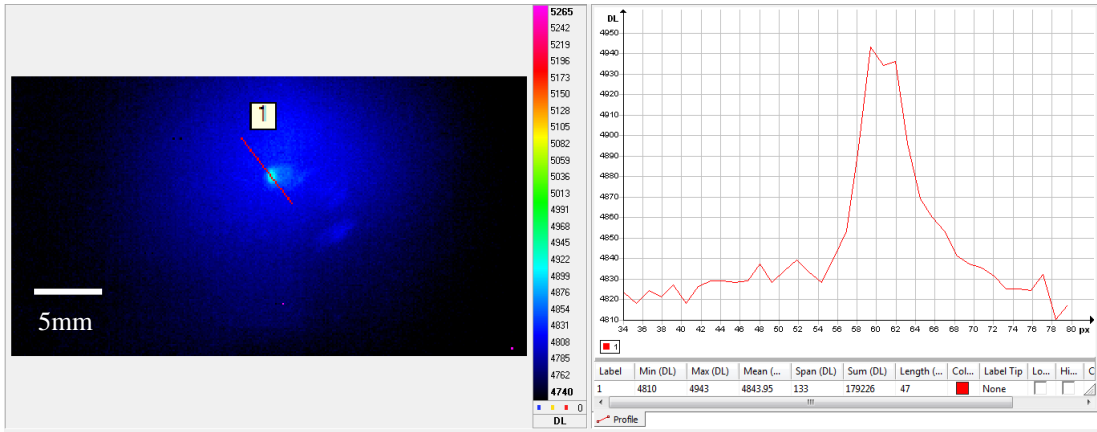


Figure 182 Sample: 3TWI12JS3 at Frame – 1

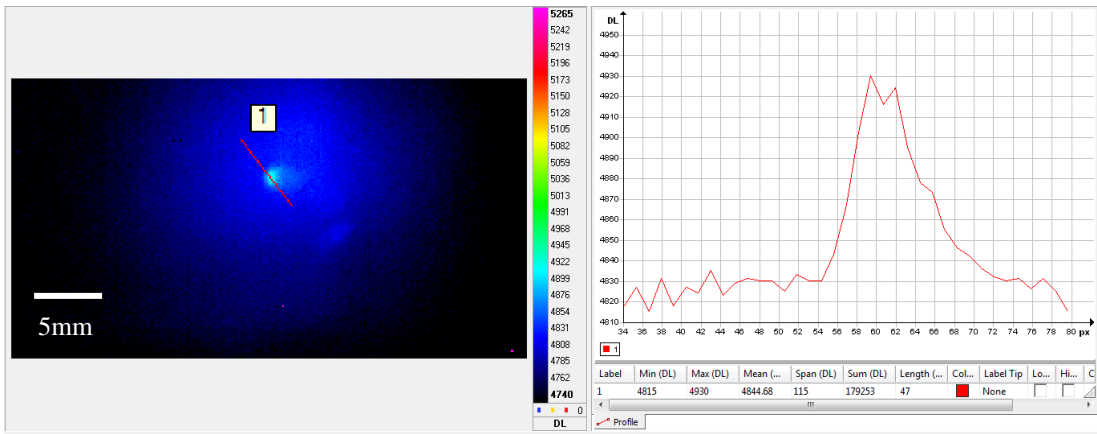


Figure 183 Sample: 3TWI12JS3 at Frame – 8

Pulsed Thermography results:

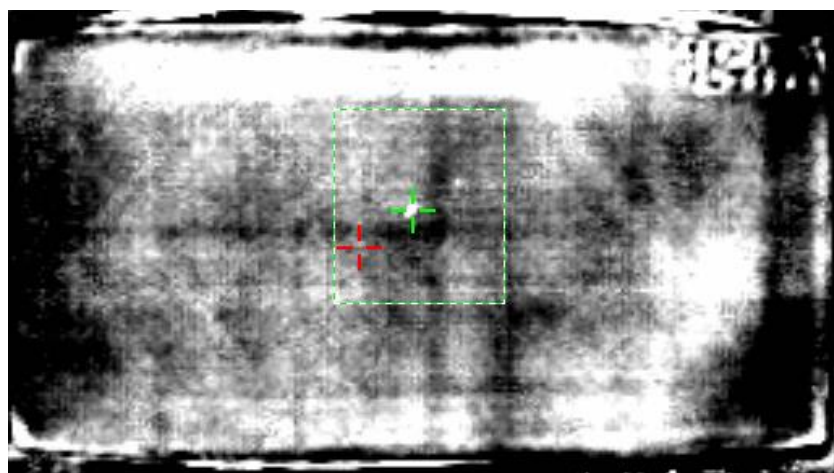


Figure 184 Pulsed thermography results; Sample: 3TWI12JS3; Size: 200×100mm; 2D image; Sampling: 23 fms

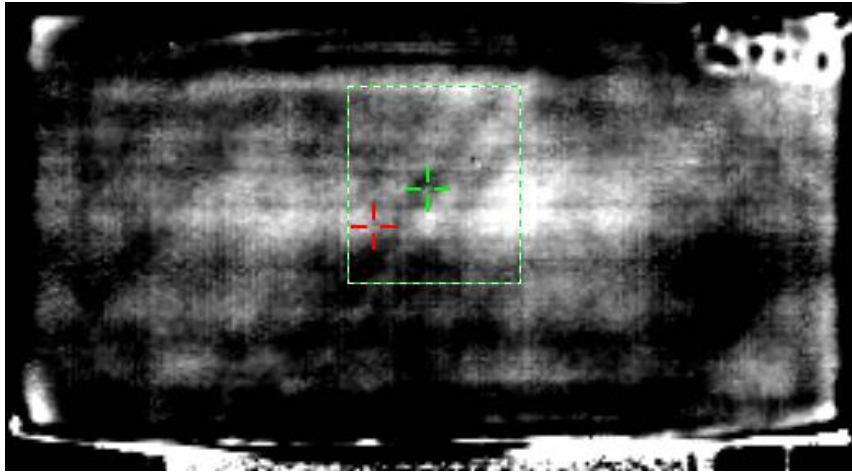


Figure 185 Pulsed thermography results; Sample: 3TWI12JS3; Size: 200×100mm; 2D image; Sampling: 55 fms

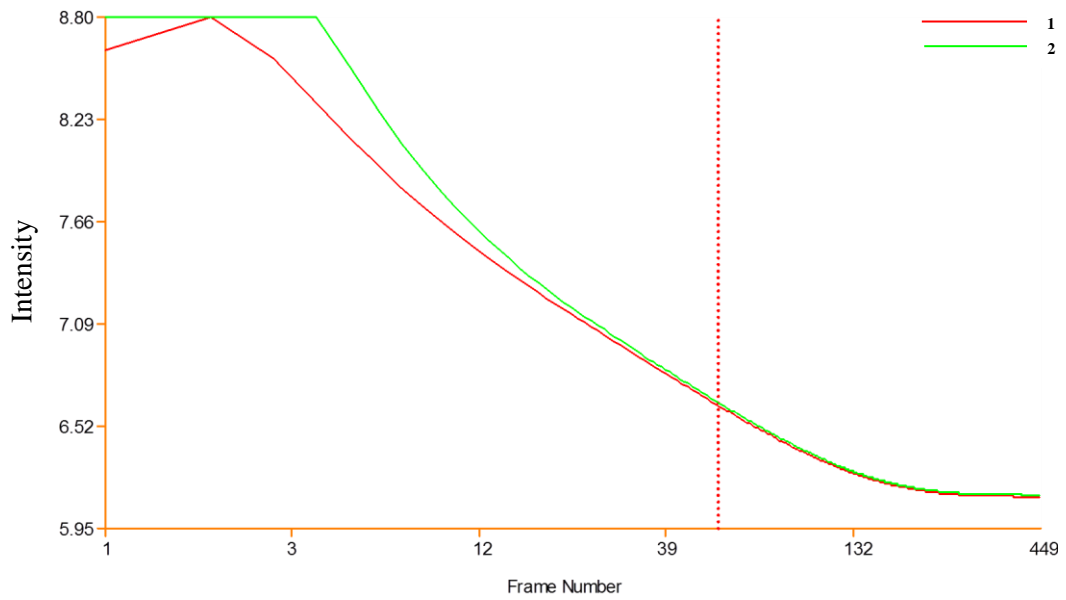


Figure 186 Pulsed thermography results; Sample: 3TWI12JS3; Log t-T plot; 1 – sound area, 2 – damage area

Stress analysis results:

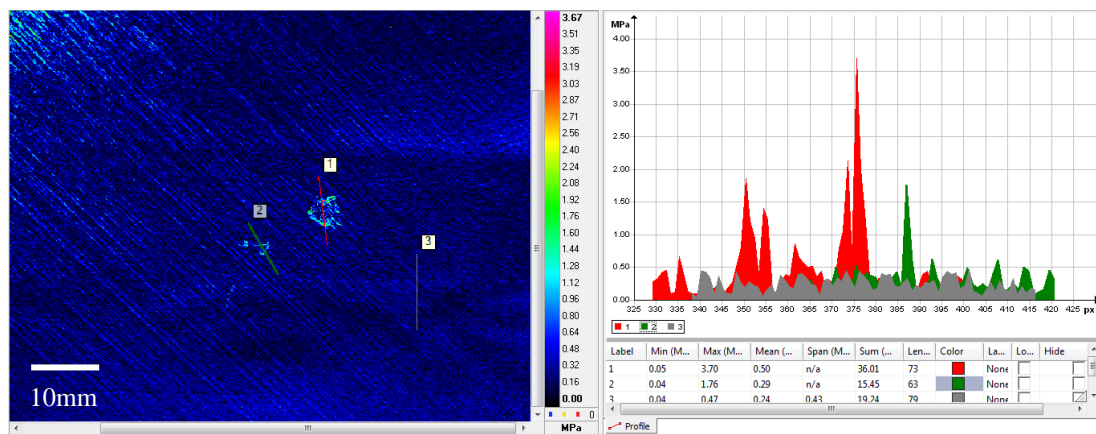


Figure 187 TSA stress map for 3TWI12JS3 with profile plot on the right

Conclusion:

The 3mm TWI laminate has shown some resistance to the 12J stone impact. Also the chip formed was much smaller when compared with that of the 3mm QI laminate. This can be evidenced by the transient thermogram results where the standard fibre stress characteristics observed in previous cases is missing. Moreover, a careful study revealed that there were secondary contact areas that appear at a low contrast in the data. The pulsed thermography system does struggle to identify the damage at the set frame indicating that the damage created was much shallower than the previous cases. This can be evidenced by looking at the 2D image at Frame 23 and Frame 55 to identify the damage created. Only the primary damage was picked up by the pulsed system, whereas the TSA system picked up the second damage (label 2) and is in line with the microscopic image.

Impact energy: 8J; Sample: 3TWI8JS3

Microscope image:



Figure 188 Microscopic image of 3TWI8JST1 laminate with damage measurements

Transient thermography results:

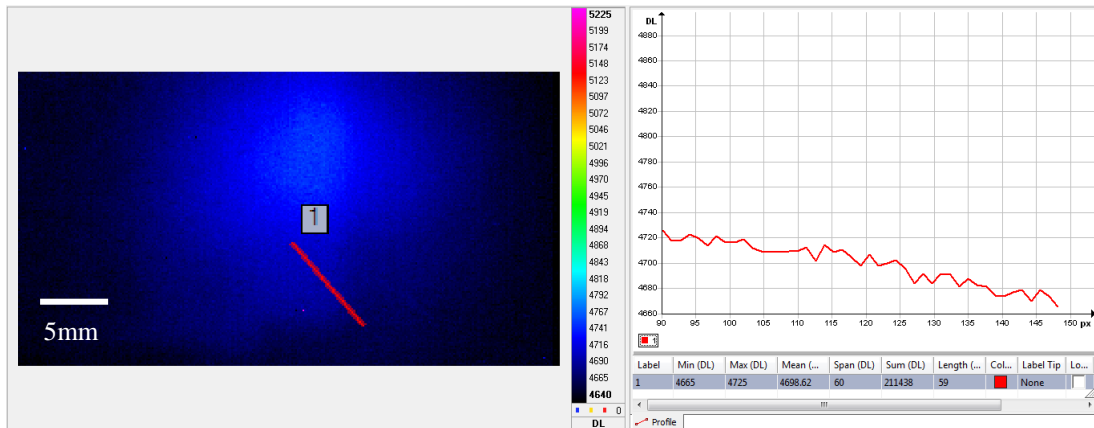


Figure 189 Sample: 3TWI8JST1 at Frame - 0

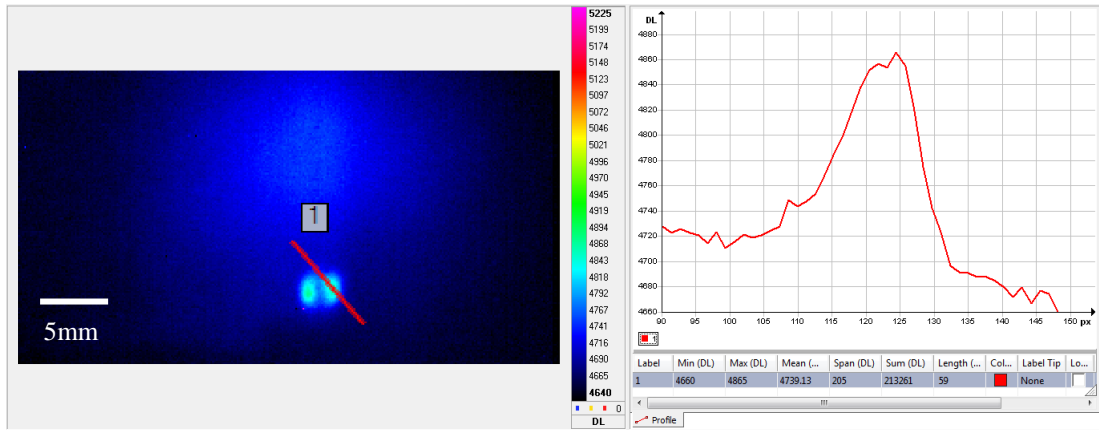


Figure 190 Sample: 3TWI8JST1 at Frame - 1

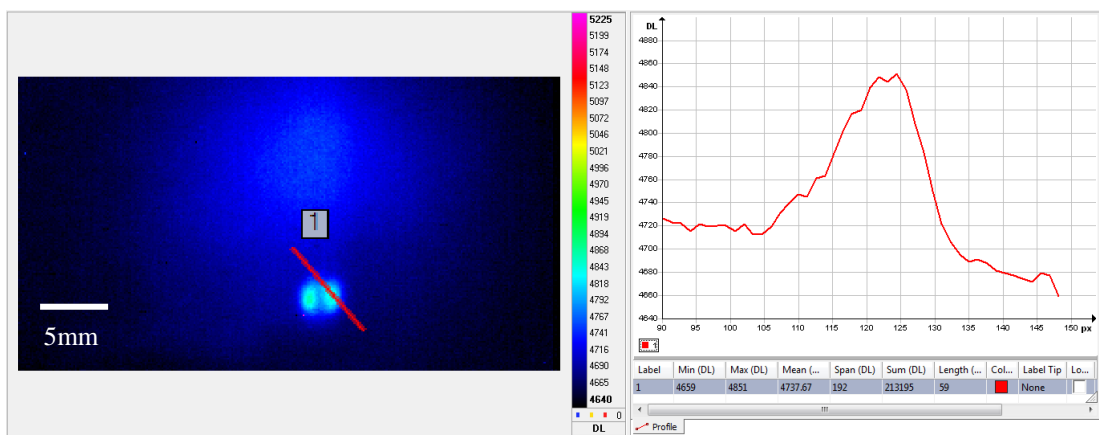


Figure 191 Sample: 3TWI8JST1 at Frame - 20

Pulsed Thermography results:

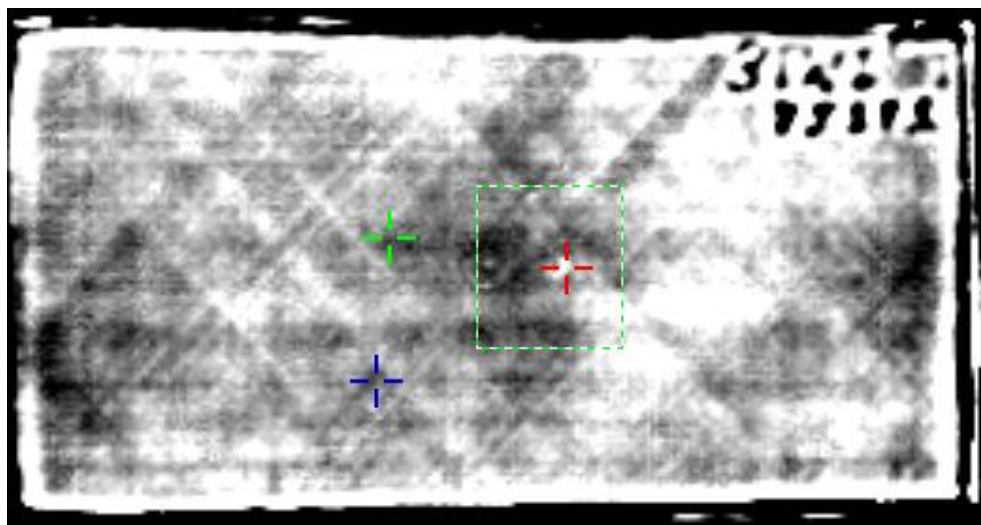


Figure 192 Pulsed thermography results; Sample: 3TWI8JST1; Size: 200×100mm; 2D image; Sampling: 39ms

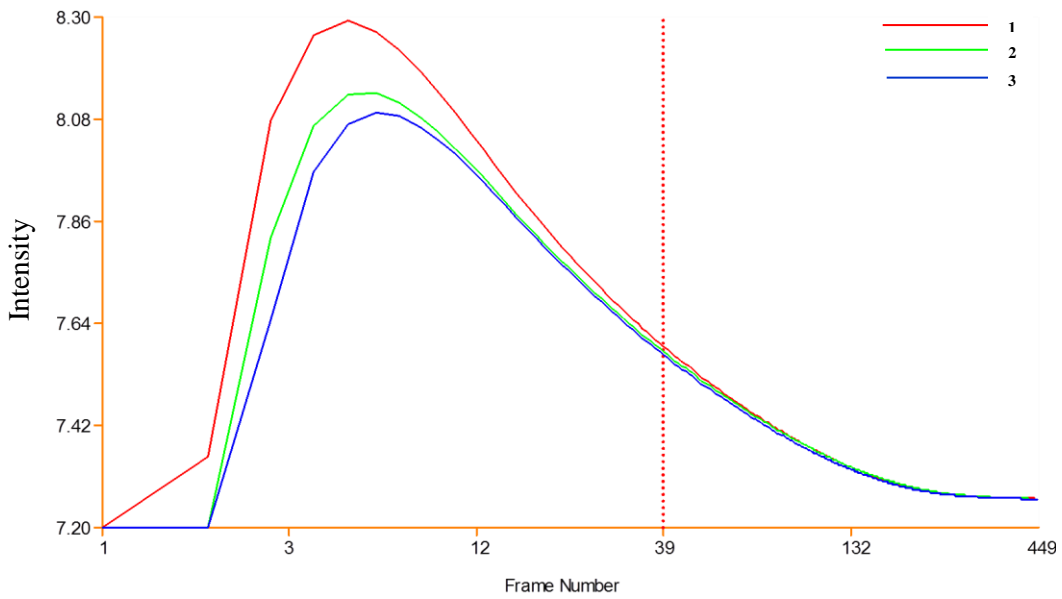


Figure 193 Pulsed thermography results; Sample: 3TWI8JST1; Log t-T plot;
1 – damage area, 2&3 – sound area

Stress analysis results:

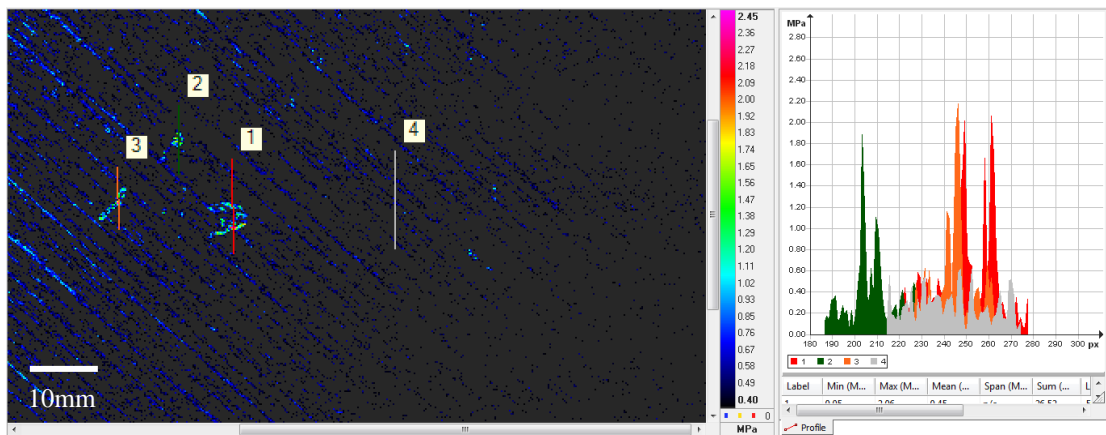


Figure 194 TSA stress map for 3TWI8JST1 with profile plot on the right

Conclusion:

From the above results, the following can be observed; the damage creation was confirmed from the transient thermography results. The pulsed data only presents the primary damage, as anticipated whereas the TSA stress map above clearly picked up indications of all damage and is in agreement with the microscopic image above.

Impact energy: 4.5J; Sample: 3TWI4.5JS3

Microscope image:



Figure 195 Microscopic image of 3TWI4.5JS3 laminate with damage measurements

Transient thermography results:

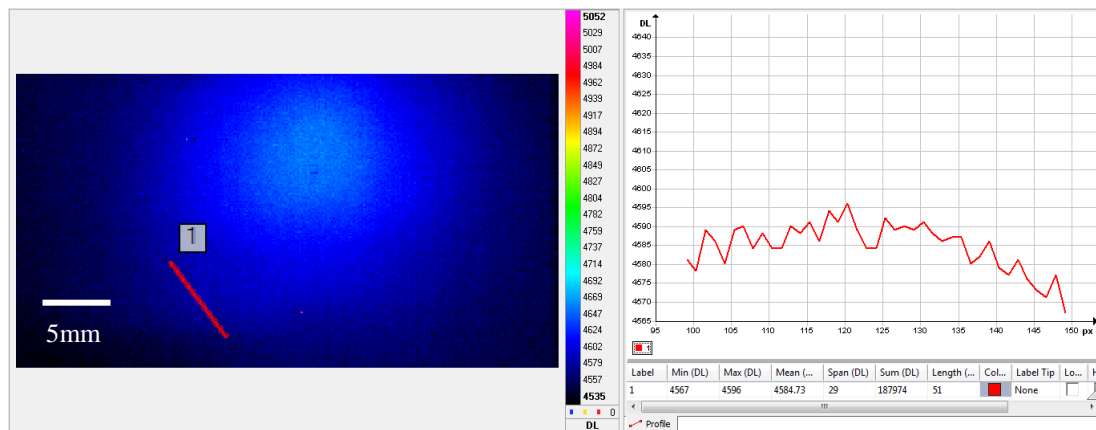


Figure 196 Sample: 3TWI4.5JS3 at Frame - 0

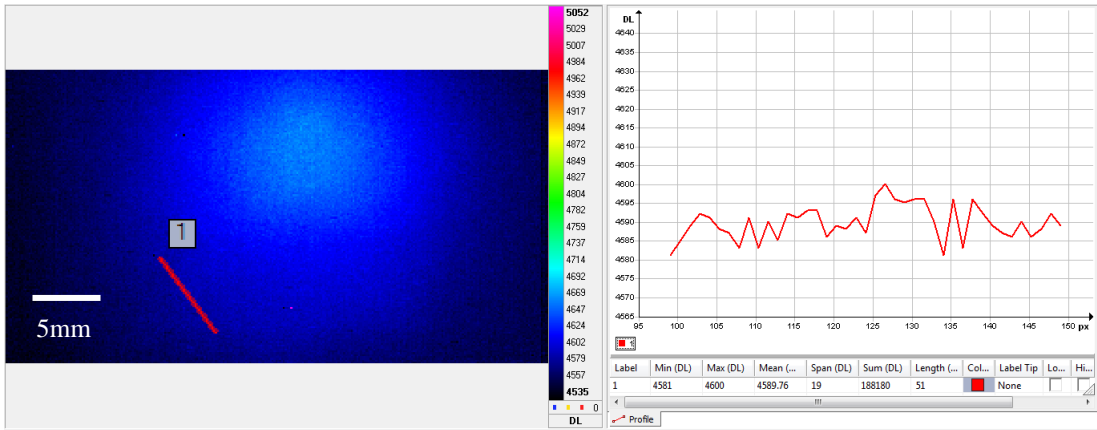


Figure 197 Sample: 3TWI4.5JS3 at Frame - 1

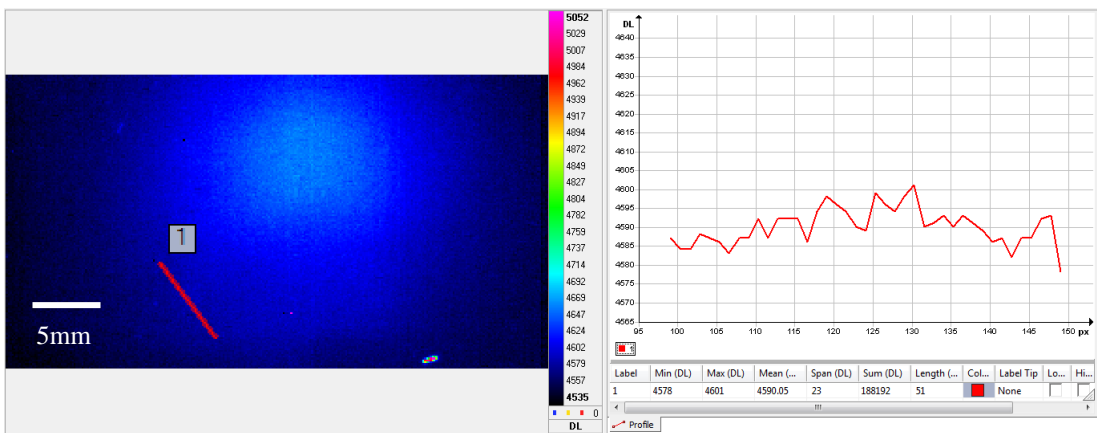


Figure 198 Sample: 3TWI4.5JS3 at Frame - 12 (Particles flying off)

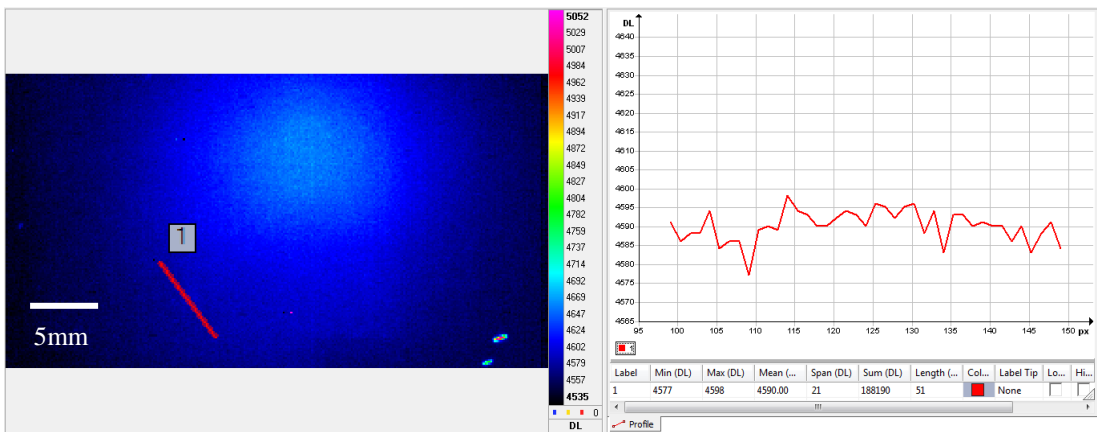


Figure 199 Sample: 3TWI4.5JS3 at Frame - 15

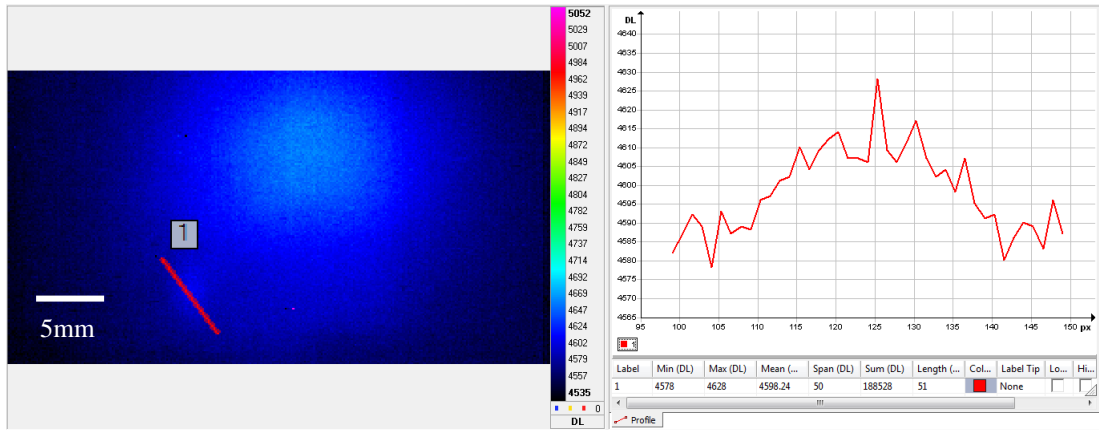


Figure 200 Sample: 3TWI4.5JS3 at Frame – 304

Pulsed Thermography results:

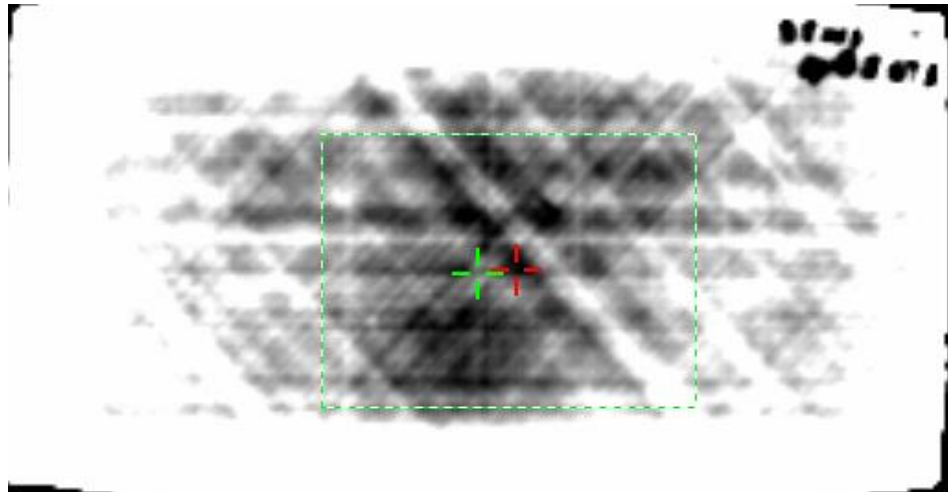


Figure 201 Pulsed thermography results; Sample: 3TWI4.5JS3; Size: 200×100mm; 2D image; Sampling: 6 fms

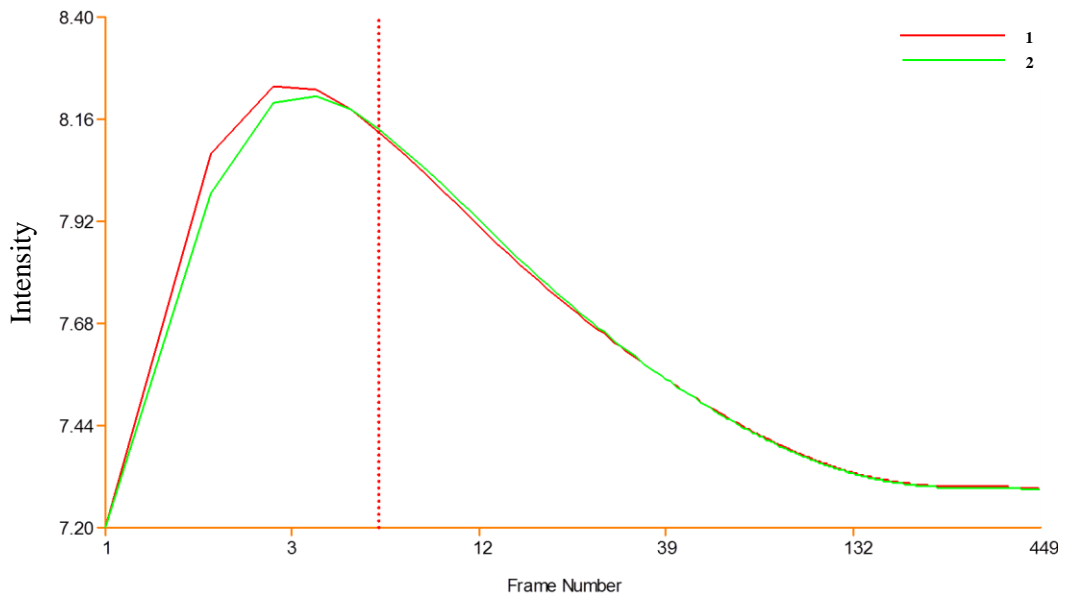


Figure 202 Pulsed thermography results; Sample: 3TWI4.5JS3; Log t-T plot;
1 – damage area, 2 – sound area

Stress analysis results:

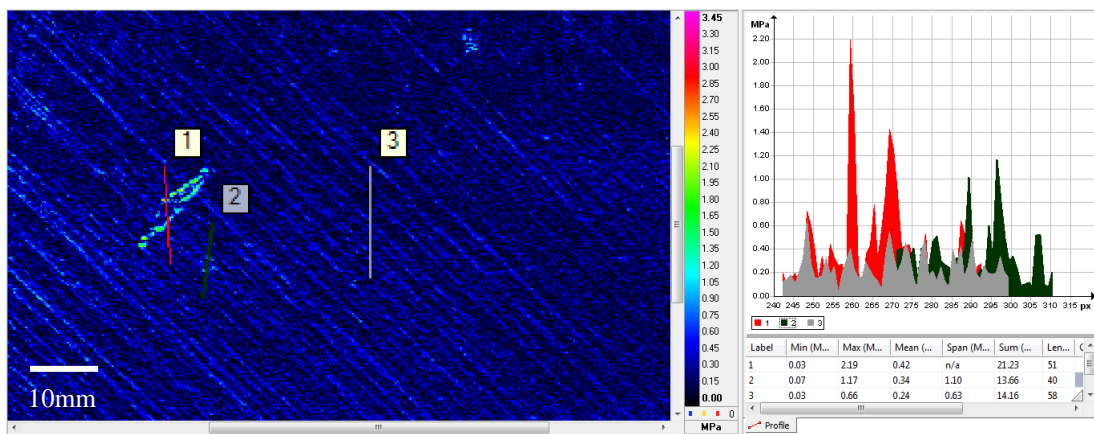


Figure 203 TSA stress map for 3TWI4.5JS3 with profile plot on the right

Conclusion:

The transient thermography results for the sample 3TWI4.5JS3 differ from the rest of the samples presented so far. The rise in temperature on the back surface is minimal and more evidence of the particles flying off from the front surface is noticed indicating the possibility that the stone used in this case disintegrated when it hit the laminate surface thus indicating that the damage created is minimal. The pulsed thermography results only indicated a low temperature rise at the damage location and hence were unable to characterise the damage. However, the TSA method acquired promising results where the damage is clearly picked up. The

improved sensitivity of the system meant, even a superficial damage that has not shown any crush or fibre breakage has now been picked up – as indicated in the image above (Figure 203).

Conclusion – 3mm laminate with impact damage:

This concludes the assessment of all 3mm thick laminates subjected to both Charpy and gas gun tests for energy levels 12J, 8J and 4.5J. A detailed analysis of the results is presented in Chapter 5 below.

4.4.1.5 6mm Quasi-isotropic – Charpy

The following are the results obtained from Charpy impact test performed on 6mm thick quasi-isotropic laid UD carbon fibre laminates. It should be noted that the transient thermography results did show any temperature rise on the back surface of the laminate as seen in the 3mm thick laminates. A detailed discussion has been presented in Chapter 5 explaining reasons as to why a back surface temperature rise was not seen in this case.

Impact energy: 12J; Sample: 6QI 20d 12J C

Microscope image:



Figure 204 Microscopic image of 6QI20d12JC3 laminate with damage measurements

Transient thermography results:

No sharp temperature rise captured from the live Charpy test.

Pulsed thermography results:

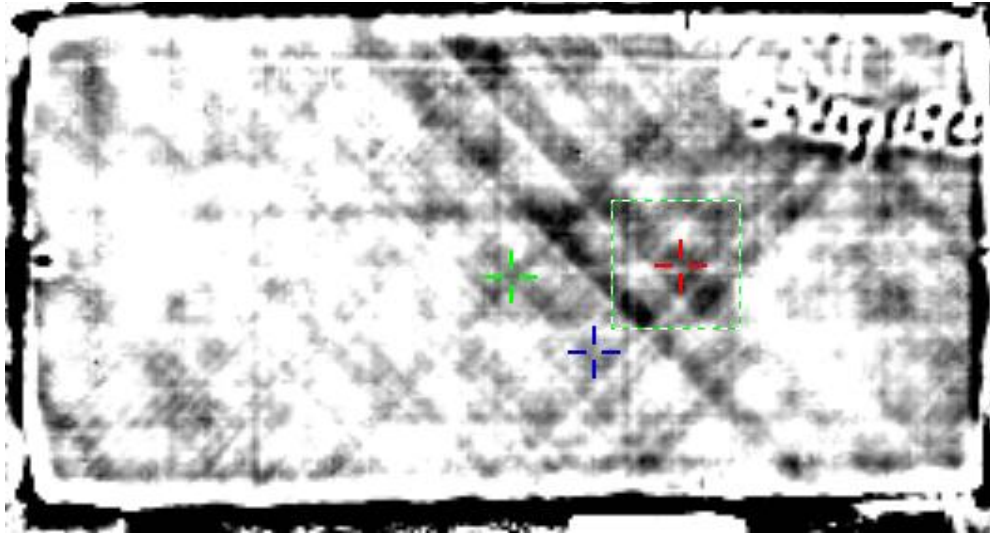


Figure 205 Pulsed thermography results; Sample: 6QI20d12JC3; Size: 200×100mm; 2D image; Sampling: 55 fms

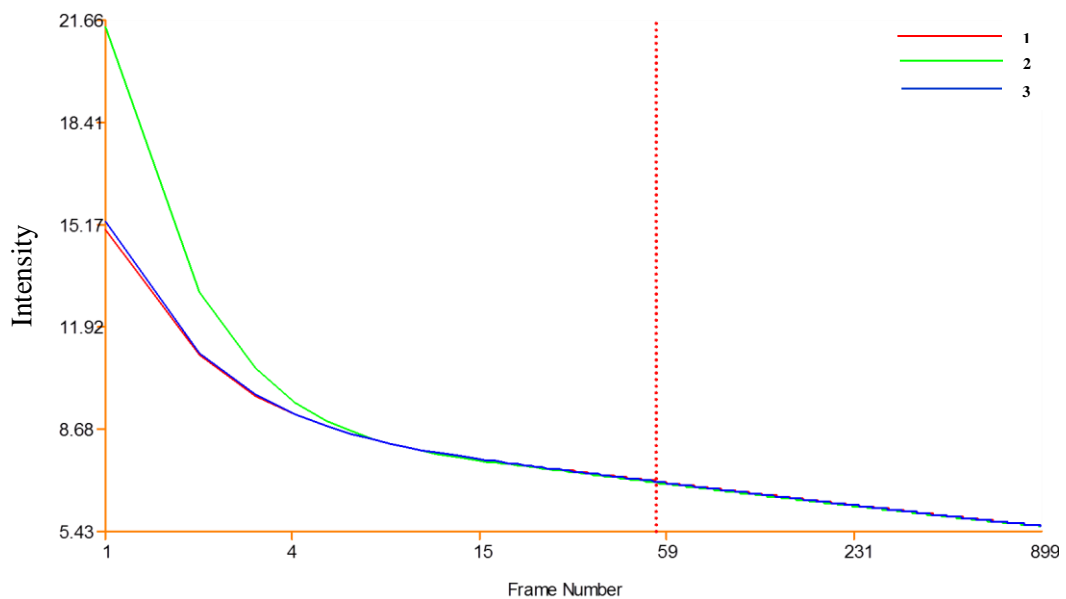


Figure 206 Pulsed thermography results; Sample: 6QI20d12JC3; Log t-T plot; 1 – damage area, 2&3 – sound area

Stress analysis results:

No indication of damage, as there was no surface breaking damage in this case.

Conclusion:

The results obtained for the sample 6QI20d12JC3 showed a low contrast indication of the damage area as seen in the microscopic image above. The transient results did not show any temperature rise in any of the 3 trials carried out on similar samples. Further, neither the pulsed nor the TSA method yielded any promising information that would characterise the damage, indicating that the impact energy was entirely absorbed by the laminate itself and thus the shock wave did not produce any noticeable damage. This is mainly due to the strength of the laminate and its impact resistance properties. The only way this could be classed as damage is by performing mechanical tests such as compression after impact or interlaminar shear tests to measure the drop in material strength.

Note:

This scenario was found consistent with laminates 6QI16d8JC, 6QI12d4.5JC, 6TWI20d12JC, 6TWI16d8JC and 6TWI12d4.5JC and hence the results for these laminates have not been presented.

4.4.1.6 6mm Quasi-isotropic – Gas gun

The following are the results obtained for 6mm quasi-isotropic layup laminates subjected to gas-gun impact. As before none of the laminates recorded a sharp rise in back wall temperature from the transient thermography mode and hence those results have not been included in this section.

Impact energy: 12J; Sample: 6QI 12J S

Microscope image:



Figure 207 Microscopic image of 6QI12JS1 laminate showing damage area 1

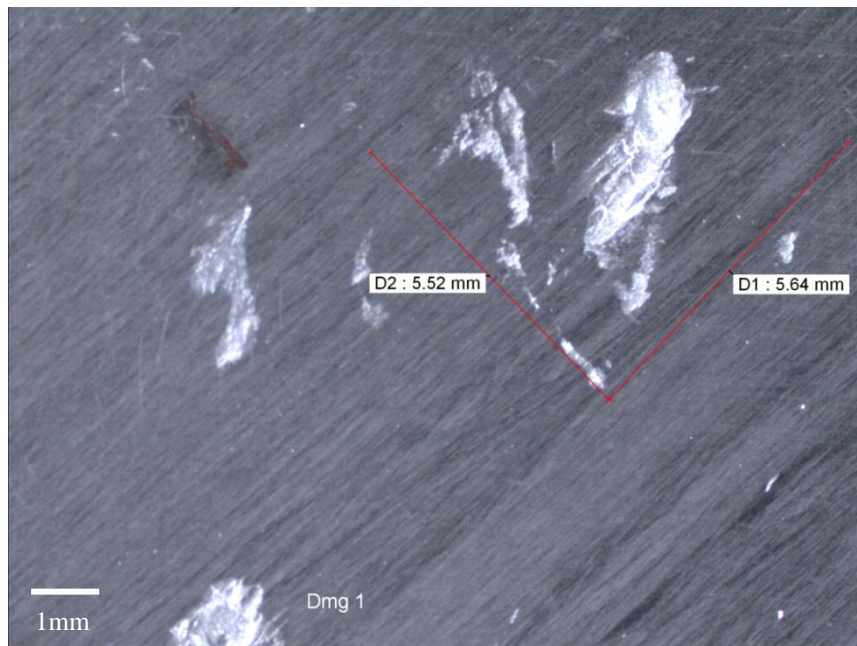


Figure 208 Microscopic image of 6QI12JS1 laminate showing damage area 2

Pulsed thermography results:

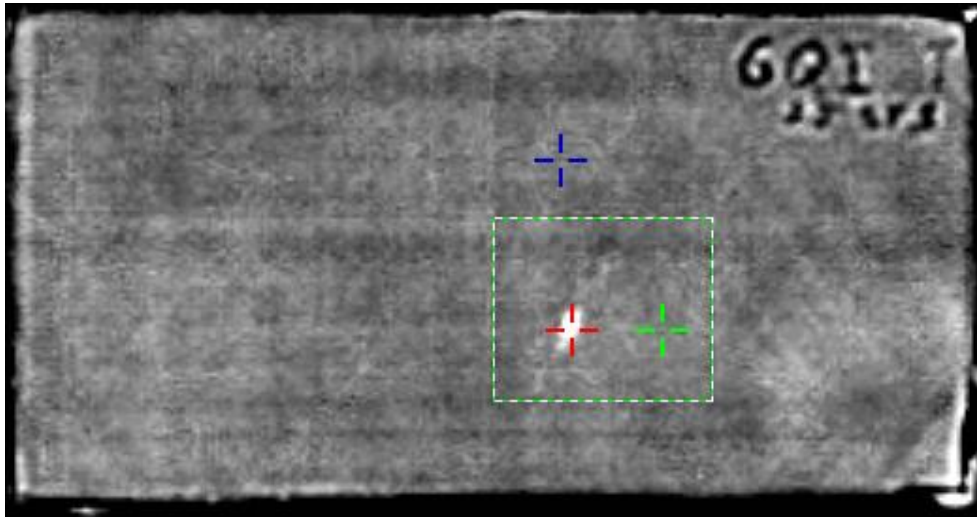


Figure 209 Pulsed thermography results; Sample: 6QI12JS1; Size: 200×100mm; 2D image; Sampling: 17 fms

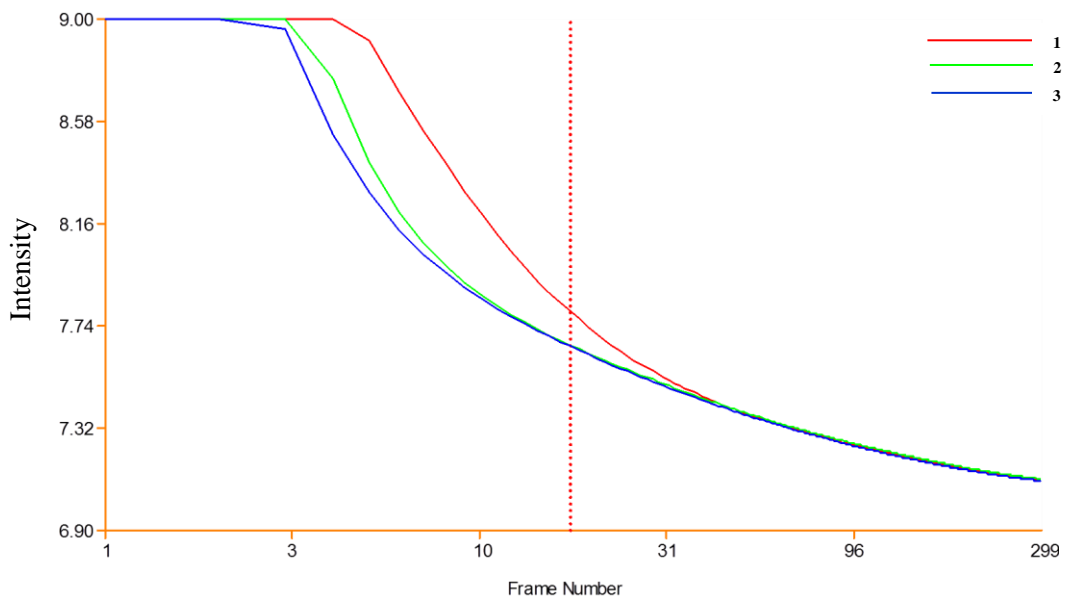


Figure 210 Pulsed thermography results; Sample: 6QI12JS1; Log t-T plot; 1 – damage area, 2&3 – sound area

Stress analysis results:

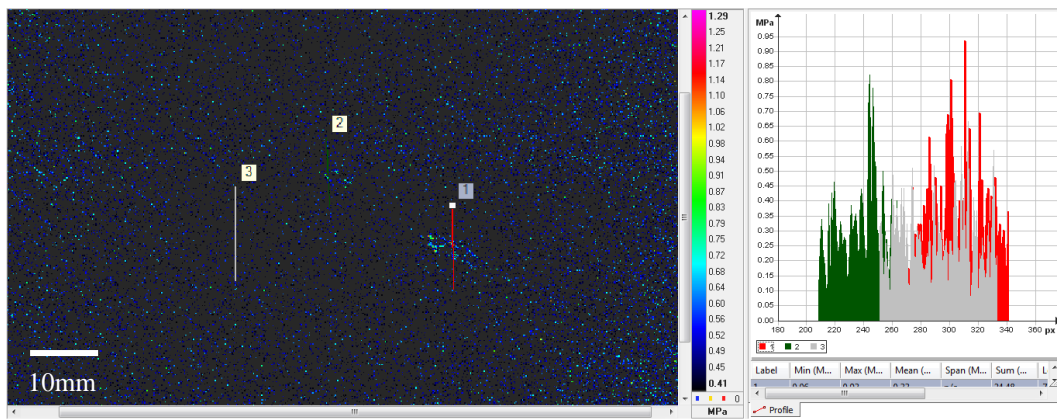


Figure 211 TSA stress map for 6QI12JS1 with profile plot on the right

Conclusion:

The ballistic impact on 6QI12JS1 laminate showed two damage areas as seen in the microscopic image above. Further the damage was picked up by both pulsed and TSA thermography methods. It was observed that the thermal stress intensity from the TSA results showed less contrast due to the low severity of the damage itself. This can be validated through the reduction in the stress values complementing the impact resistance of the laminate.

Impact energy: 8J; Sample: 6QI 8J S

Microscope image:



Figure 212 Microscope image of 6QI8JS1 with damage measurement

Pulsed thermography results:

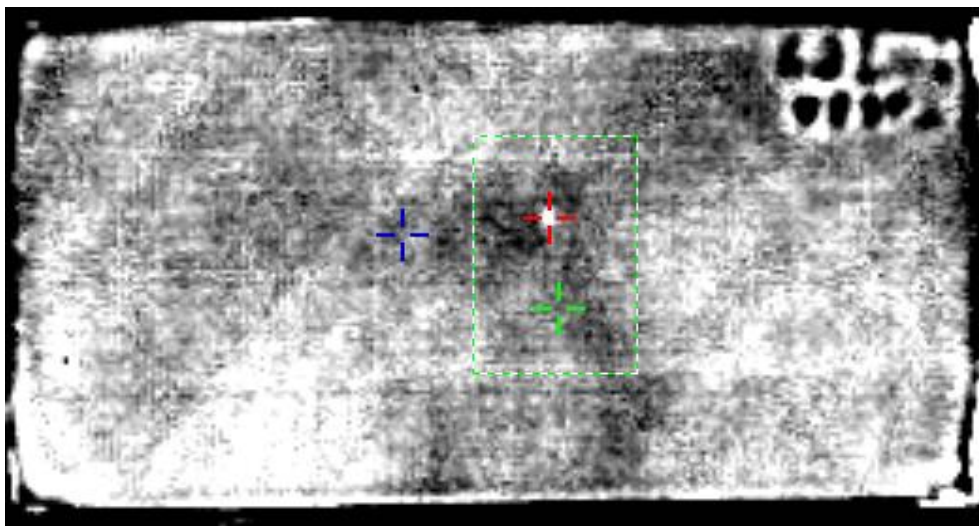


Figure 213 Pulsed thermography results; Sample: 6QI8JS1; Size: 200×100mm; 2D image; Sampling: 23 fms

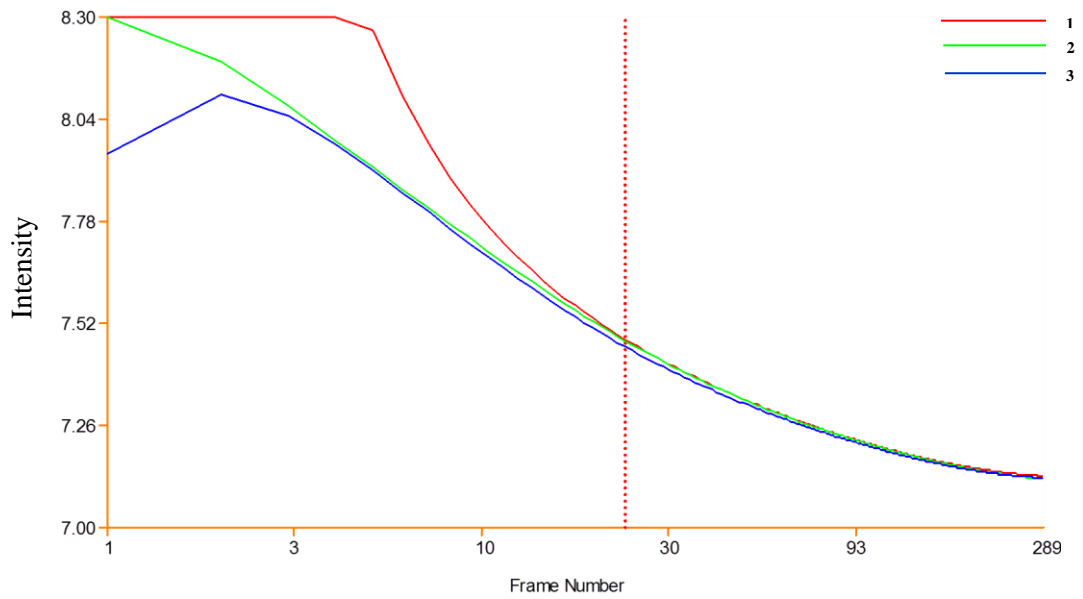


Figure 214 Pulsed thermography results; Sample: 6QI8JS1; Log t-T plot
1 – damage area, 2&3 – sound area

Stress analysis results:

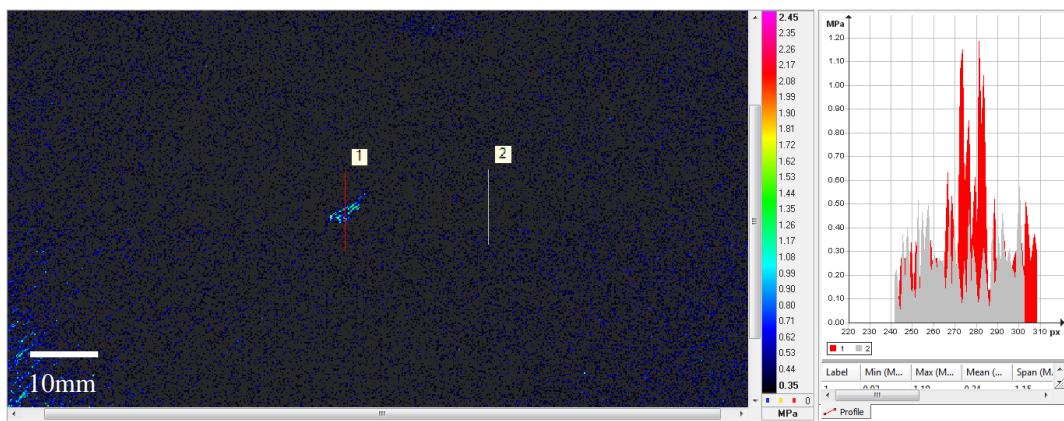


Figure 215 TSA stress map for 6QI8JS1 with profile plot on the right

Conclusion:

The above results detect the damage created on 6QI8JS1 laminate when subjected to an 8J ballistic impact test. Both pulsed thermography and TSA methods have detected the damage.

Impact energy: 4.5J; Sample: 6QI 4.5J S

Microscope image:

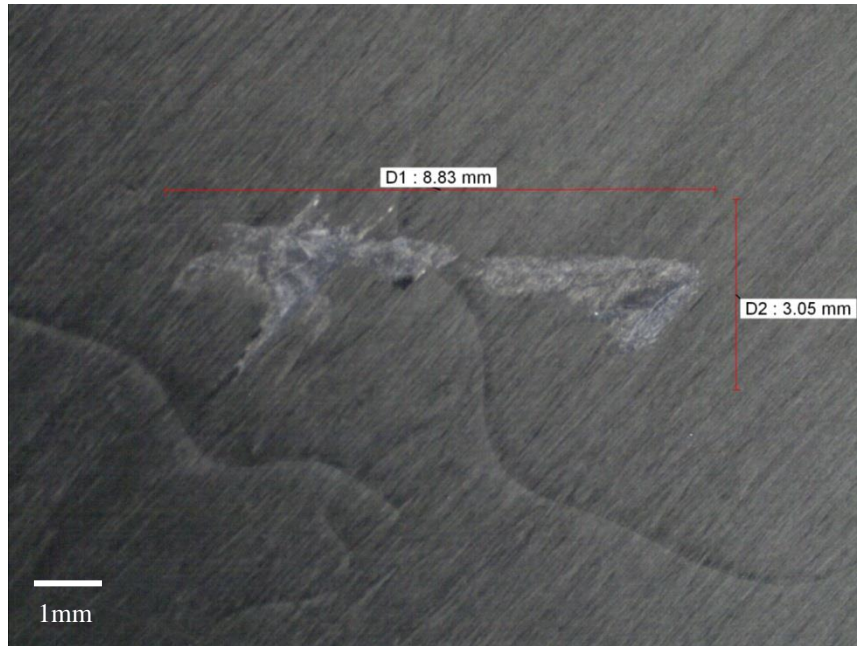


Figure 216 Microscope image of 6QI4.5JS3 with damage measurements

Stress analysis results:

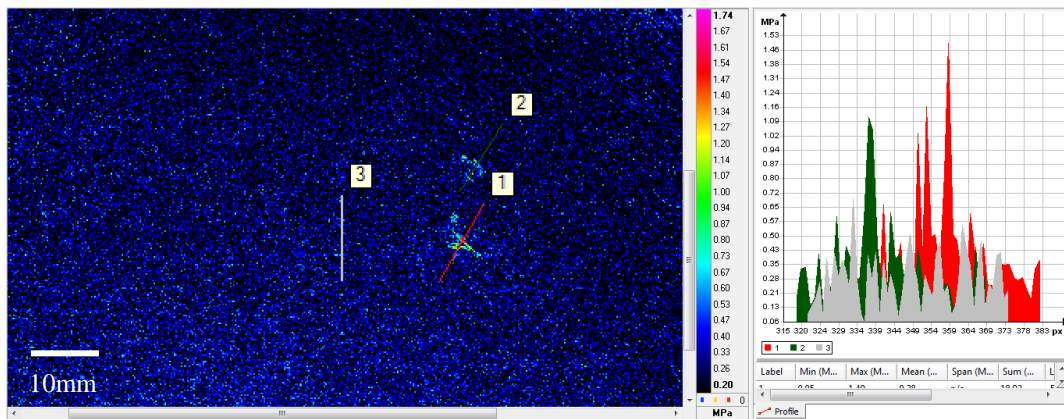


Figure 217 TSA stress map for 6QI4.5JS3 with profile plot on the right

Conclusion:

The pulsed thermography inspection did not detect the created impact damage as the damage dimension was much smaller and no serious surface damage was observed. However, the TSA method showed promising results where all near surface damage

were detected, as seen from the TSA stress map above (Figure 217). Further the results clearly showed the localised stress concentration that cracks were formed and may be classed as damage thus proving the applicability of TSA method.

4.4.1.7 6mm TWI – Gas gun

The following are the results obtained from ballistic testing carried out on 6mm laminates for energy levels 12J, 8J and 4.5J. As before, transient thermography did not produce any noticeable results and hence were not included below.

Impact energy: 12J; Sample: 6TWI 12J S

Microscope image:



Figure 218 Microscope image of 6TWI12JS1 with damage measurements

Pulsed thermography results:

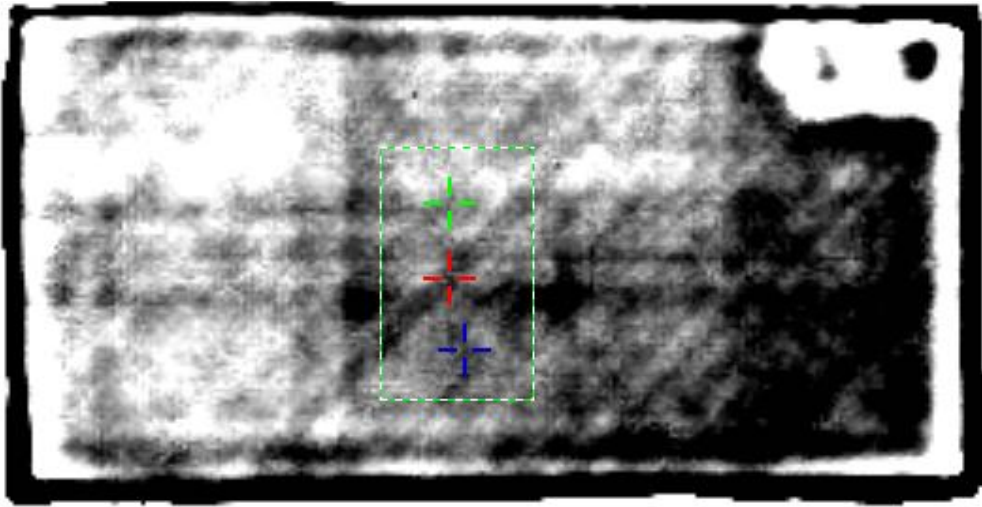


Figure 219 Pulsed thermography results; Sample: 6TWI12JS1; Size: 200×100mm; 2D image; Sampling: 44 fms

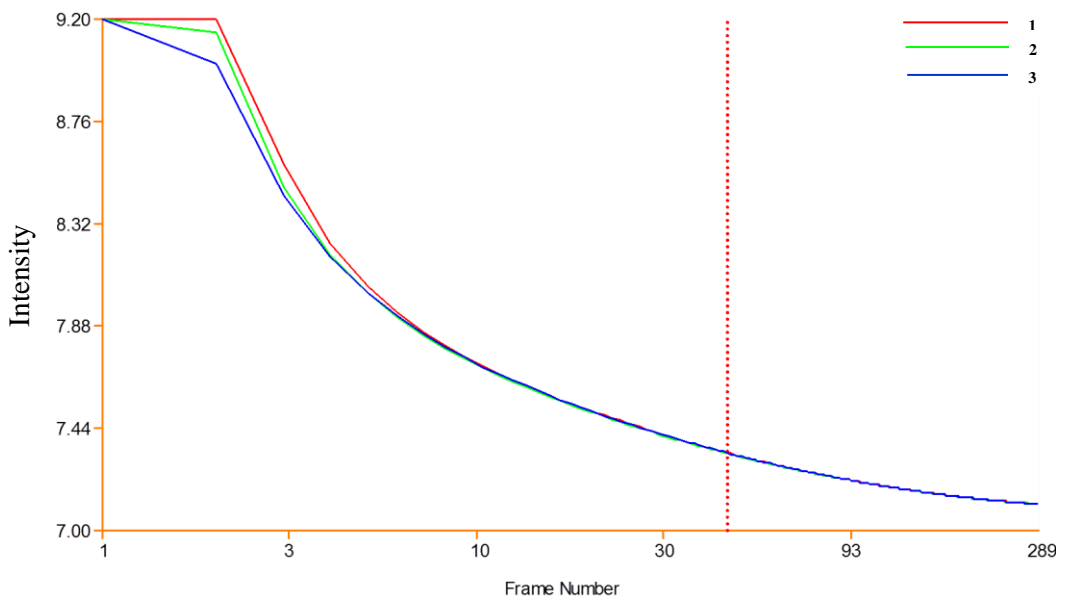


Figure 220 Pulsed thermography results; Sample: 6TWI12JS1; Log t-T plot; 1 – damage area, 2&3 – sound area

Stress analysis results:

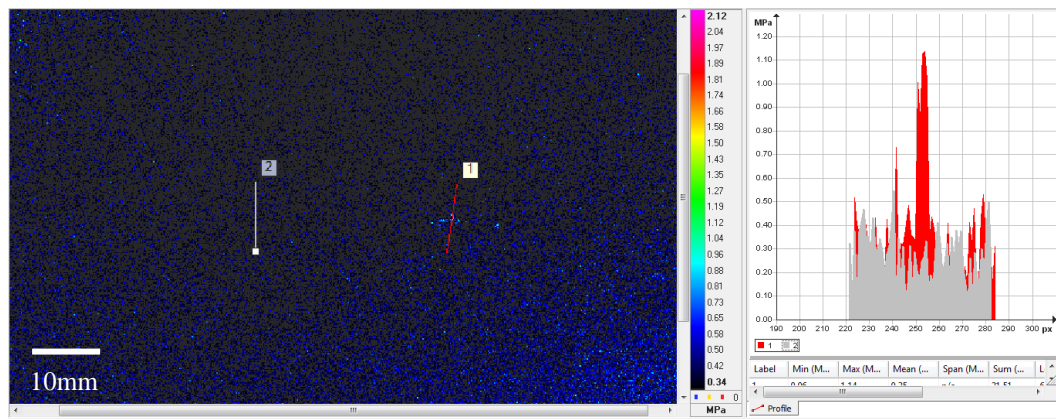


Figure 221 TSA stress map for 6TWI12JS1 with profile plot on the right

Conclusion:

As before, the 12J stone impact on the 6mm TWI laminates did not produce any temperature rise on the back wall as seen in the case of the 3mm laminates. The damage created also varied across different laminates for the same energy level. The data presented in Figure 219 and Figure 220 only picked up low contrast indication of the damage. This again concurs with the previous statements that the stone disintegrated before passing on the impact energy and that the laminate was showing better impact resistance characteristics. The TSA image picked up the damage easily.

Impact energy: 8J; Sample: 6TWI 8J ST

Microscope image:

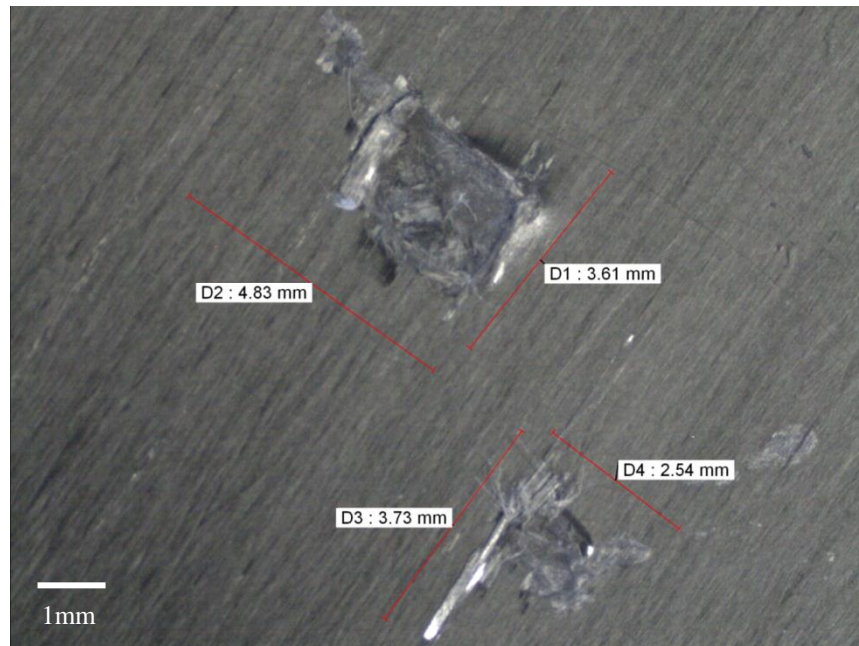


Figure 222 Microscope image of 6TWI8JS1 with damage measurements

Pulsed thermography results:

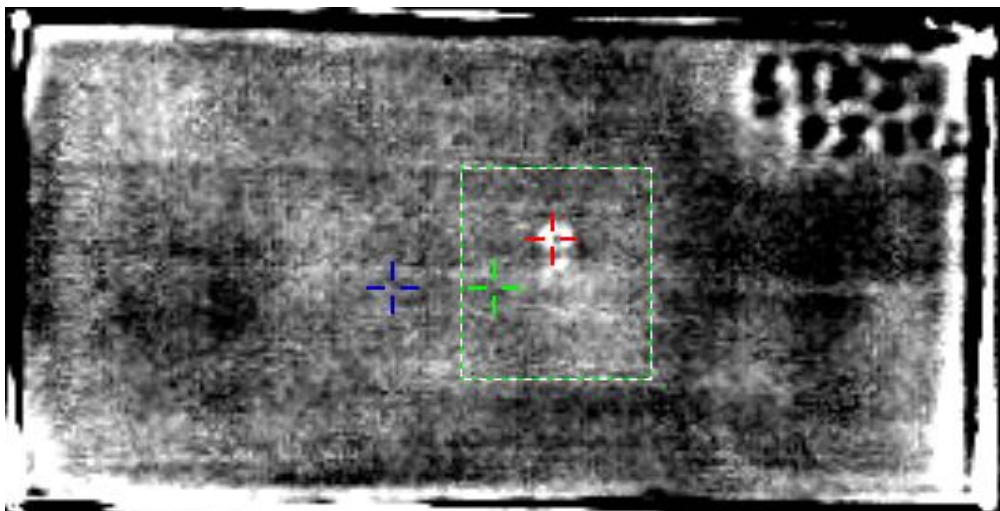


Figure 223 Pulsed thermography results; Sample: 6TWI8JS1; Size: 200×100mm; 2D image; Sampling: 24 fms

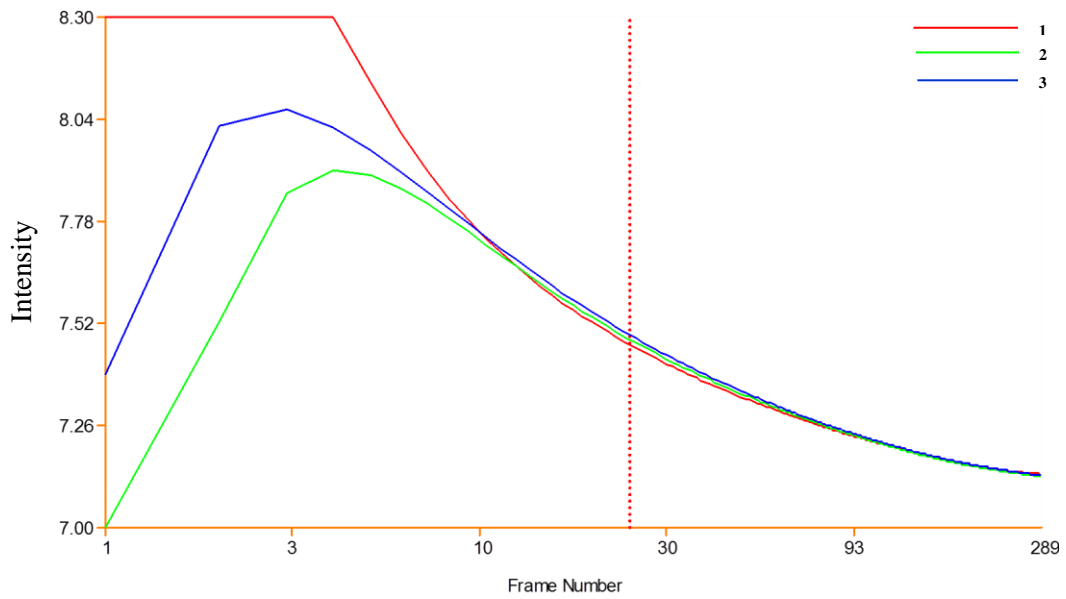


Figure 224 Pulsed thermography results; Sample: 6TWI8JS1; Log t-T plot;
1 – damage area, 2&3 – sound area

Stress analysis results:

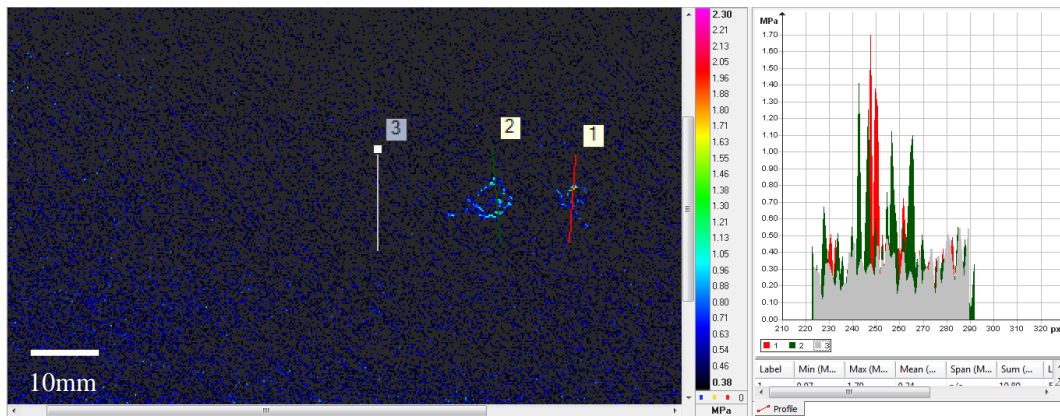


Figure 225 TSA stress map for 6TWI8JS1 with profile plot on the right

Conclusion:

In the case of the 8J impact both the pulsed and TSA thermography methods identified damage easily. The TSA image coincides with the microscopic visual image thus confirming the creation of damage due to impact.

Impact energy: 4.5J; Sample: 6TWI 4.5J S

Microscope image:



Figure 226 Microscope image of 6TWI4.5JS2 with damage measurements

Stress analysis results:

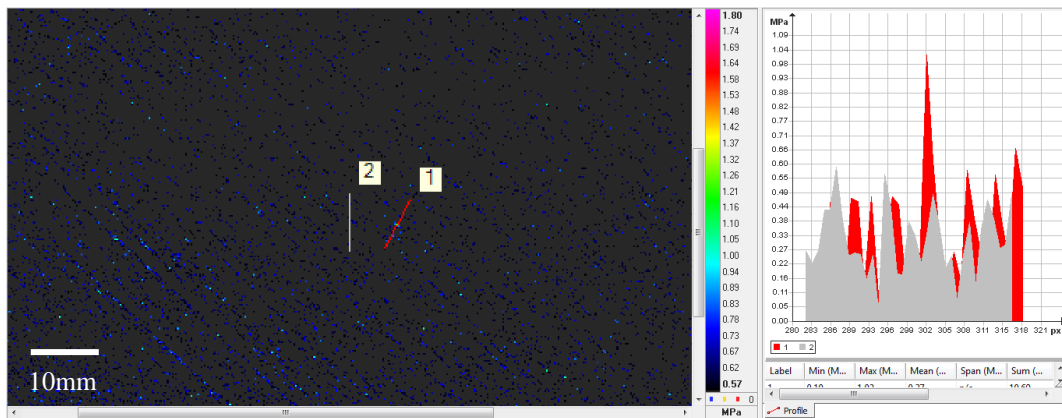


Figure 227 TSA stress map for 6TWI4.5JS2 with profile plot on the right

Conclusion:

For the 4.5J impact, the damage created was so small that the pulsed system did not pick up any damage indications. However, the TSA method picked up the damage. It should be noted that the intensity of the damage identified by the TSA method is far less sensitive than the microscopic image. The TSA data still confirms the creation of the damage.

4.4.1.8 Epilogue

This section on impact damage presented the results for 24 sets of laminates that encompasses two lay-ups, two thicknesses, two impact methods and three impact energy levels. All laminates were subjected to inspection using both pulsed thermography and TSA methods. It was observed that TSA showed better response to laminates having surface breaking damage in comparison with pulsed thermography. Even a BVID caused by a 4.5J stone impact was picked up by the TSA method establishing the strength of the technique in detecting surface breaking damage. Further transient thermography results were included in the narrative. All observations support these results were included in the narrative. Due to the elaborate and pictorial nature of the results, a detailed discussion summarising the findings of the parametric study has been presented in Chapter 5 below.

4.5 Impact Studies Comparison – vibrational analysis

In order to provide a validation that the impact has definitely changed the material characteristic by creating a damage, vibrational analysis to determine the modal frequencies of the sample were identified using a laser doppler vibrometer (LDV). Vibrational analysis is a traditional condition monitoring technique that helps determine the structural integrity of the test sample and has been adapted for this section to provide validation against the results presented in Section 4.4.

This section presents the initial results obtained from a theoretical model to identify if there is any shift in resonant frequency of the CFRP laminate due to the presence of the damage. Then a random error estimation exercise was performed to identify the error in measurement. It is the notion that, if the resonant frequencies exceed this error, this will establish the theory that this shift in frequency is in fact due to the presence of the damage.

4.5.1 Theoretical modelling – vibrational analysis

Similar to the theoretical modelling as presented in section 4.2.2, a Finite Element Method (FEM) solver was used to simulate the vibrational analysis study to determine if there is any shift in modal frequency of certain vibrational modes due to the presence of damage. The geometric model was designed in the Siemens NX-Ideas package and a mesh density of 10 elements to resolve for damage. For the model, the material properties of CFRP and air gap were used (as per Appendix 7). As before the CFRP material was assumed to be homogeneous. The samples with and without damage were designed to match a 3mm laminate and had the dimensions 200×100×3mm. The only difference between the no-damage or virgin plate and the plate with damage was a centre cut out from the sample. The dimensions of the cut-off are 20×2.5×3mm.

The following are the mesh models for the virgin plate and the plate with cut-off.

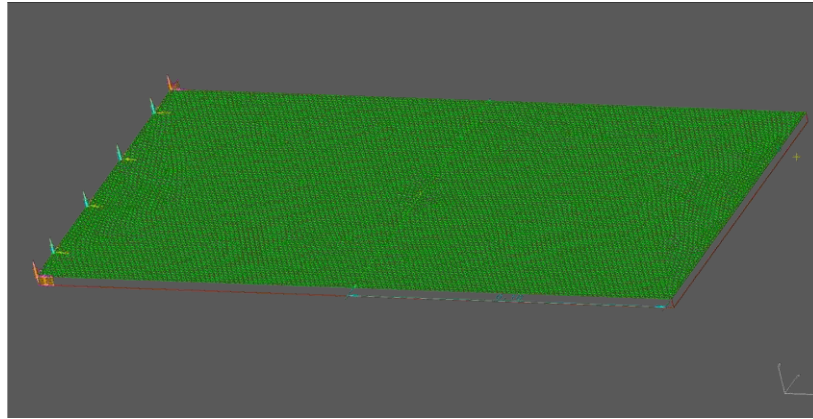


Figure 228 Mesh model of virgin CFRP laminate; Size: 200×100×3mm

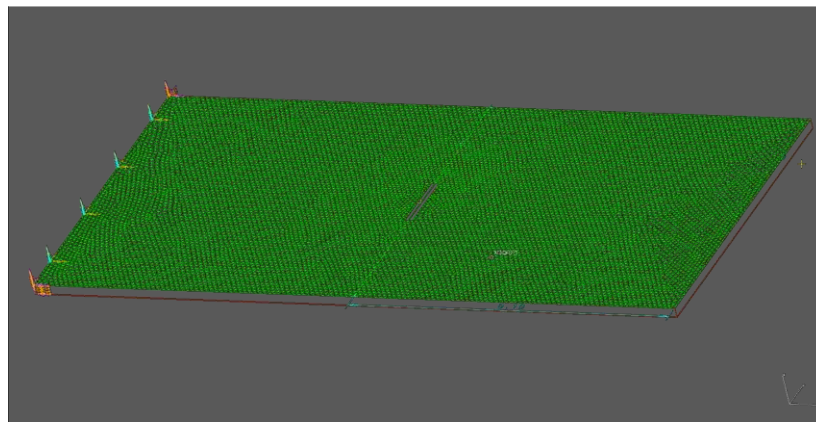


Figure 229 Mesh model of CFRP laminate with centre cut-off; Size: 200×100×3mm; Cut-off size: 20×2.5×3mm

As seen in Figure 228 and Figure 229, only one edge was restrained and normal mode dynamics analysis was used to determine the modal frequencies of both the virgin and damage plate. The following are the results obtained on solving the above model.

Table 30 Modal frequencies of virgin and damage CFRP laminate as computed from NX-Ideas

Modes	Sample - Virgin plate in Hz	Sample - With Damage in Hz
1	1.64	1.63
2	6.8	6.78
3	10.18	10.03
4	22.28	22.27
5	28.59	28.58
6	43.18	43.12
7	44.53	44.19
8	56.39	56.12
9	60.54	59.64

10	71.85	71.83
11	84.27	83.94
12	95.05	94.86
13	108.64	108.55
14	117.19	115.94
15	120.41	120.36
16	133.41	133.27
17	141.96	140.1
18	155.42	155.3
19	157.84	156.98
20	160.39	160.3
21	193.05	192.78
22	198.35	197.7
23	206.59	203.39
24	213.7	213.63
25	233.45	233.18
26	236.58	236.17
27	246.05	245.16
28	264.2	261.64
29	265.06	262.1
30	271.96	271.76
31	279.11	279.07
32	288.39	287.89
33	305.2	303.22
34	331.95	326.94
35	340.64	338.97
36	347.87	347.32
37	350.17	347.71
38	354.17	353.98
39	385.52	385.15
40	397.94	397.31
41	402.07	397.51
42	408.97	404.9
43	416.51	415.93
44	421.76	421.25
45	426.2	422.02
46	440.25	439.89
47	455.85	455.25
48	464.71	459.6
49	493.83	486.12
50	494.45	493.02

Discussion:

A close look at the computed values from Table 30 revealed that certain higher modes such as 34, 48 and 49 showed a significant shift of 5-8Hz. It should be noted that the shift in modal frequencies is entirely dependent on the geometry and location of the damage together with its vibrational frequency. The close match at lower frequencies in this case shows that the sample's resonant frequency has not changed much due to the presence of this type of damage. However, the computational model suggests that certain higher modes could indicate the presence of damage.

Conclusion:

These computations do show a slight shift in modal frequencies especially in the higher modes as evidenced from Table 30. This provides the necessary evidence to take up the vibration testing for laminates subjected to impact.

4.5.2 Random Error Estimation

As with any technique, it is necessary to understand the various errors and uncertainties associated with the inspection. To understand these aspects, the experimental setup needs to be understood to calculate the random error in measurement by the LDV system.



Figure 230 The Polytec PSV400 Laser Doppler Vibrometer

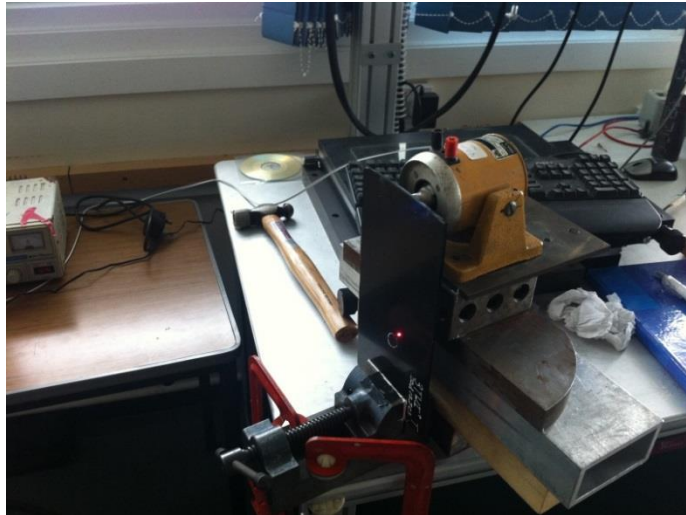


Figure 231 Test sample for the LDV measurement, clamped to a bench vice. This image also shows the laser spot on the sample together with the bench top shaker

Figure 230 and Figure 231 show the test setup used for the LDV measurement. It can be seen that the sample is clamped on the lower end using a bench vice and the bench top electro-dynamic is located on the top end of the laminate being inspected. The samples were then marked to show the vice grip area so that the sample could be re-introduced into the vice at the same level. Care was also taken to make sure the same number of turns was used to secure the sample in place. However, due to the abstract nature of the test setup, the random error that may be caused during every loading and unloading of the sample needs to be estimated to increase the accuracy of measurement.

To establish the random error a range of measurements were carried out. The test sample was introduced into the above setup and the scan was initialised based on the settings, as mentioned in Chapter 3. Three trials were performed for the sample before the sample was unclamped in order to obtain any changes in-between measurements. The sample was re-introduced into the setup for a second time, keeping the positional accuracy and the clamping force the same as the previous setup. Again, three trials were conducted, before unclamping the sample. The sample was re-introduced for a third time and same acquisition process was followed. It should be noted that for understanding the random error, the same sample was used for acquiring all trials.

To provide a rationale to the data and to calculate the random error, a sample was identified as mentioned earlier and was tested three times. It was made sure that

the sample was completely removed and re-introduced to provide a scenario where different samples could be introduced at a later stage and that the data acquired during future testing does not include the random error due to loading and unloading of the test sample.

The following are the results obtained from the LDV measurement and can be summarised below.

Table 31 shows 8 modes identified during the LDV data analysis and their respective peaks. This data represents three sample loading conditions with three trials under each loading condition

Modes	Sampling 1 in Hz				Sampling 2 in Hz				Sampling 3 in Hz			
	Trial 1	Trial 2	Trial 3	Avg 1	Trial 1	Trial 2	Trial 3	Avg 2	Trial 1	Trial 2	Trial 3	Avg 3
1	125.00	129.69	129.69	128.13	125.00	125.00	125.00	125.00	129.69	129.69	129.69	129.69
2	190.63	190.63	190.63	190.63	190.63	190.63	190.63	190.63	190.63	190.63	190.63	190.63
3	245.31	250.00	225.00	240.10	245.31	245.31	220.31	236.98	245.31	225.00	225.00	231.77
4	429.69	450.00	425.00	434.90	445.31	445.31	445.31	445.31	429.69	425.00	425.00	426.56
5	629.69	629.69	629.69	629.69						629.69	629.69	629.69
6	979.69	979.69	979.69	979.69	975.00	975.00	975.00	975.00	975.00	975.00	975.00	975.00
7	1029.69	1050.00	1025.00	1034.90	1025.00	1025.00	1025.00	1025.00	1025.00	1025.00	1025.00	1025.00
8	1425.00	1425.00	1400.00	1416.67	1420.31	1420.31	1420.31	1420.31	1420.31	1425.00	1420.31	1421.88

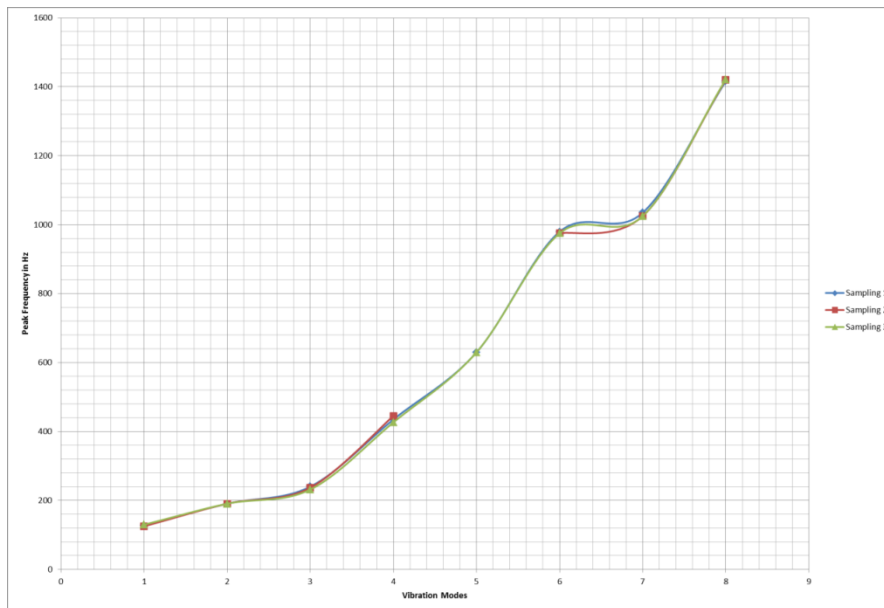


Figure 232 Graph showing the averaged trials under each loading and analysing at 8 modal frequencies

The above results were derived from looking at modal frequency images to establish the error in the LDV measurements. For this exercise, only the 1st trial from the first loading condition has been used to isolate 8 modal frequencies. The following are the 8 modes identified for this analysis.

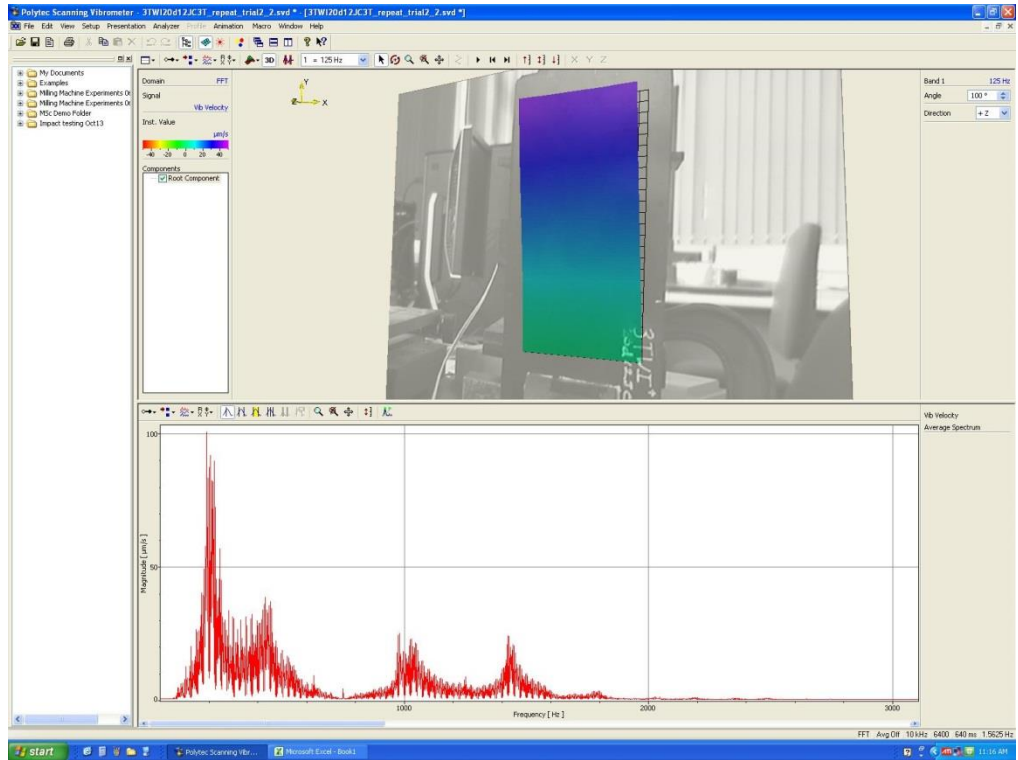


Figure 233 The modal form with full spectrum at the bottom; Sample: 3TWI20d12JC1; Mode – 1

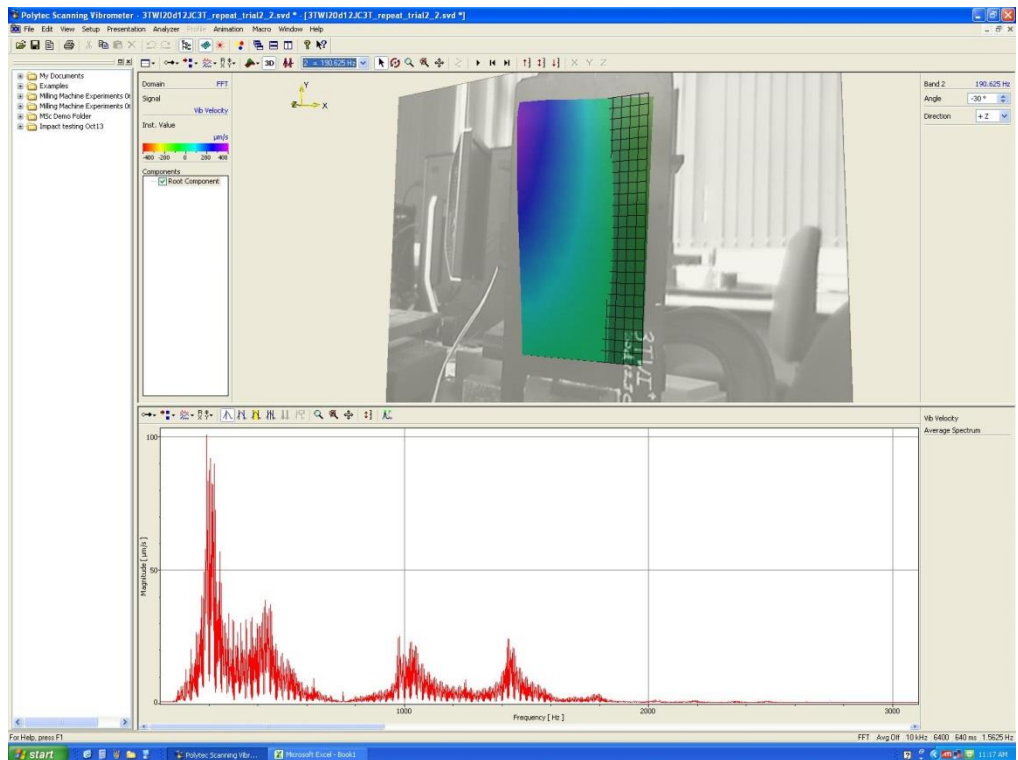


Figure 234 The modal form with full spectrum at the bottom; Sample: 3TWI20d12JC1; Mode – 2

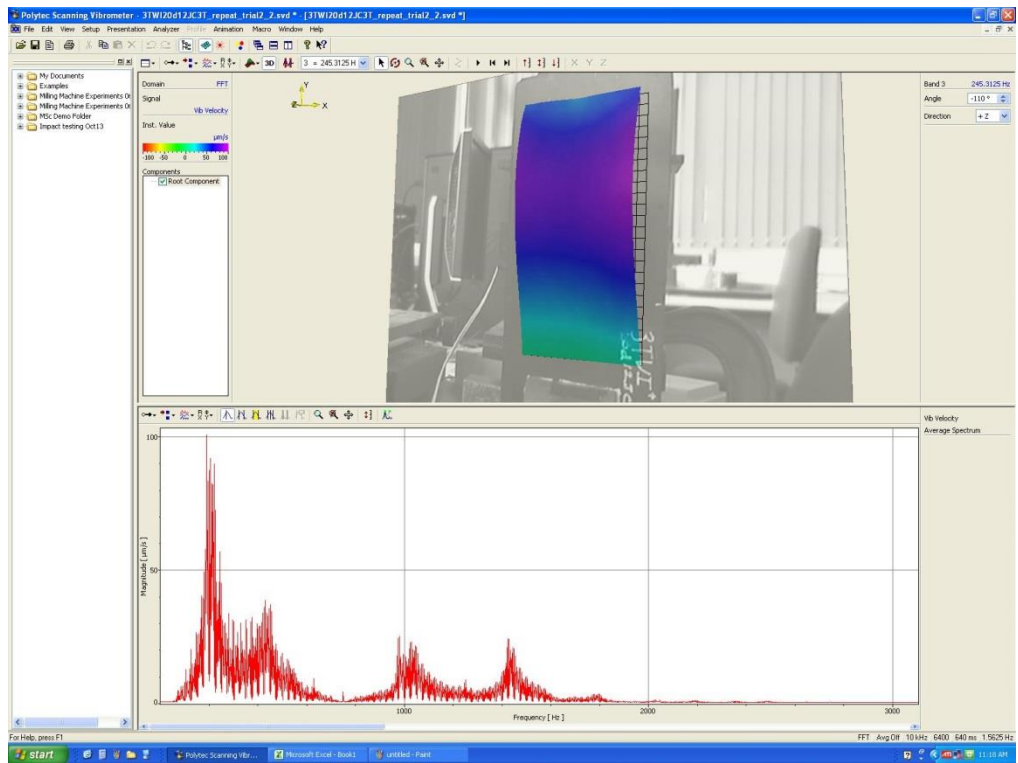


Figure 235 The modal form with full spectrum at the bottom; Sample: 3TWI20d12JC1; Mode – 3

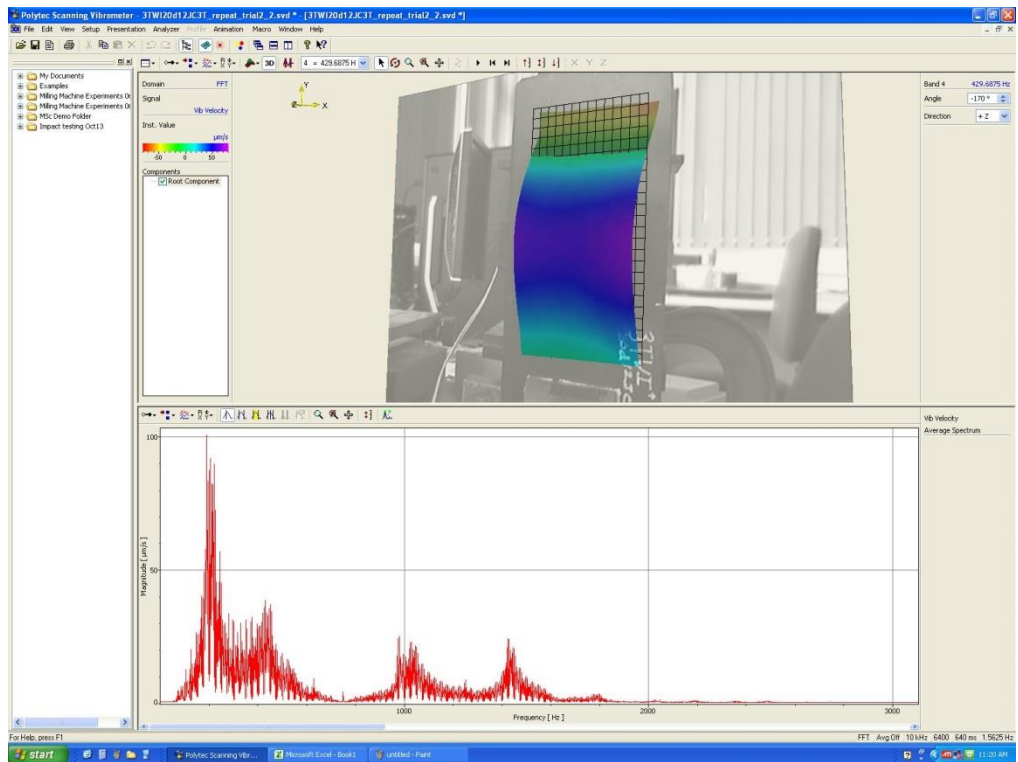


Figure 236 The modal form with full spectrum at the bottom; Sample: 3TWI20d12JC1; Mode – 4

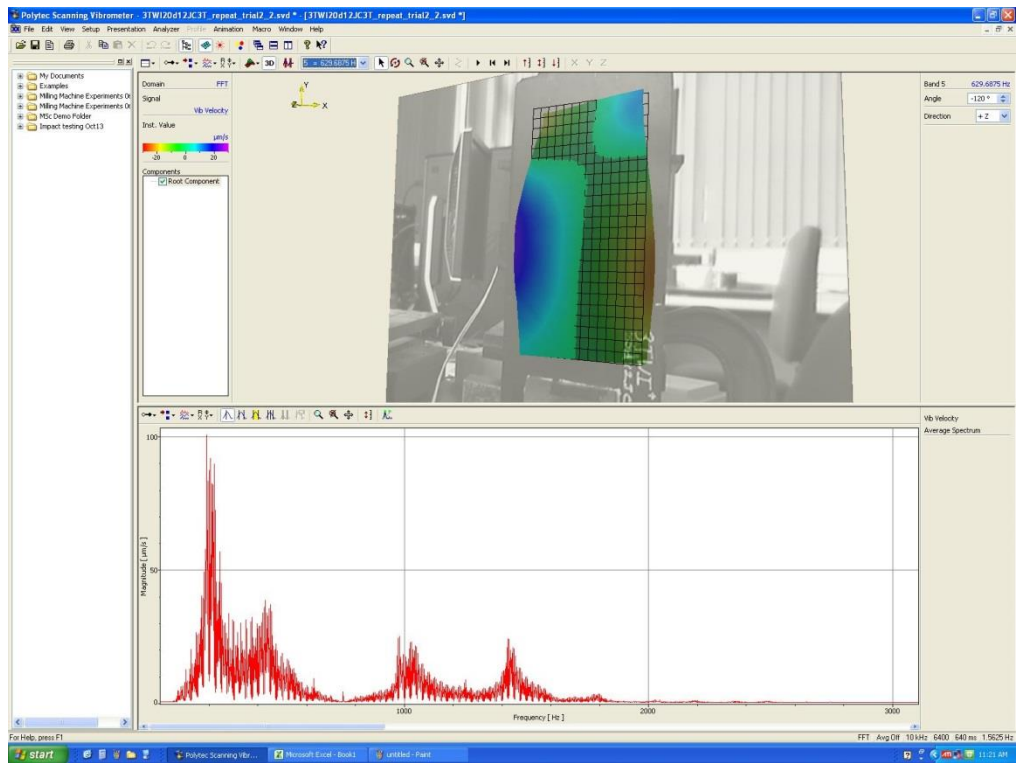


Figure 237 The modal form with full spectrum at the bottom; Sample: 3TWI20d12JC1; Mode – 5

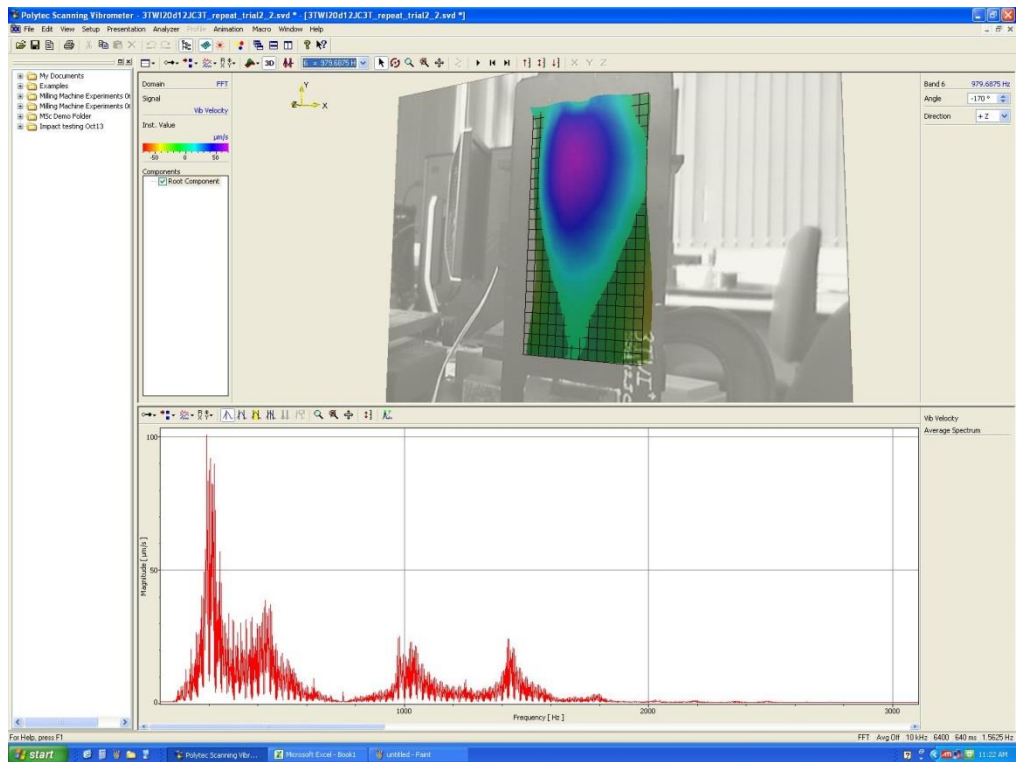


Figure 238 The modal form with full spectrum at the bottom; Sample: 3TWI20d12JC1; Mode – 6

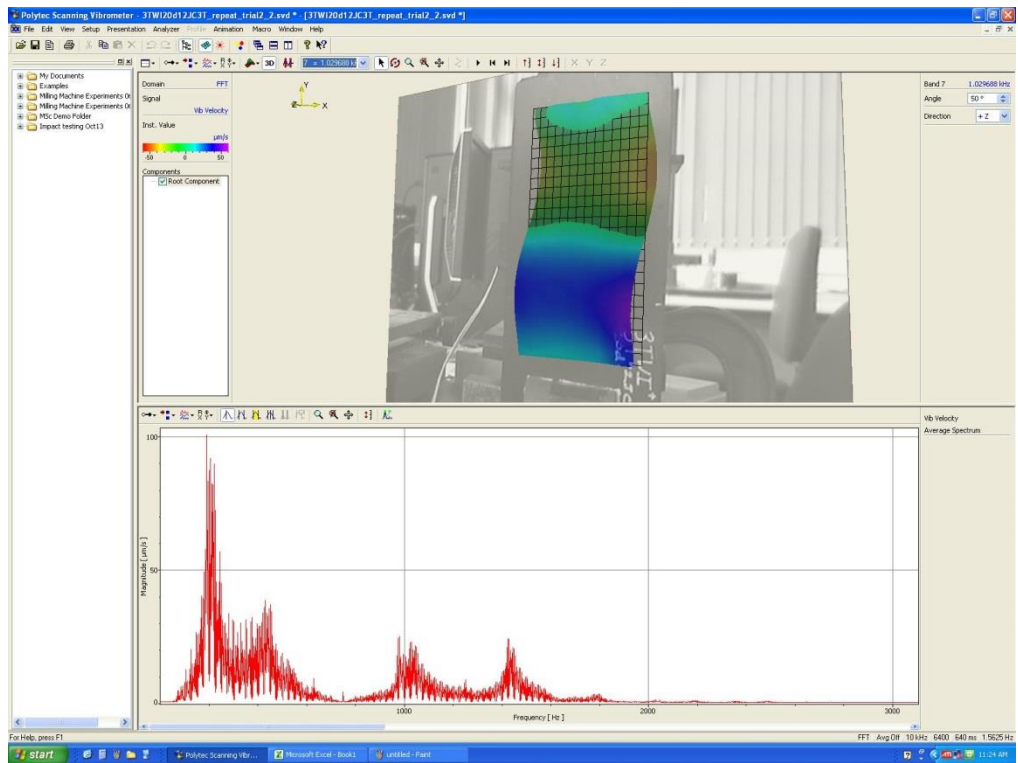


Figure 239 The modal form with full spectrum at the bottom; Sample: 3TWI20d12JC1; Mode – 7

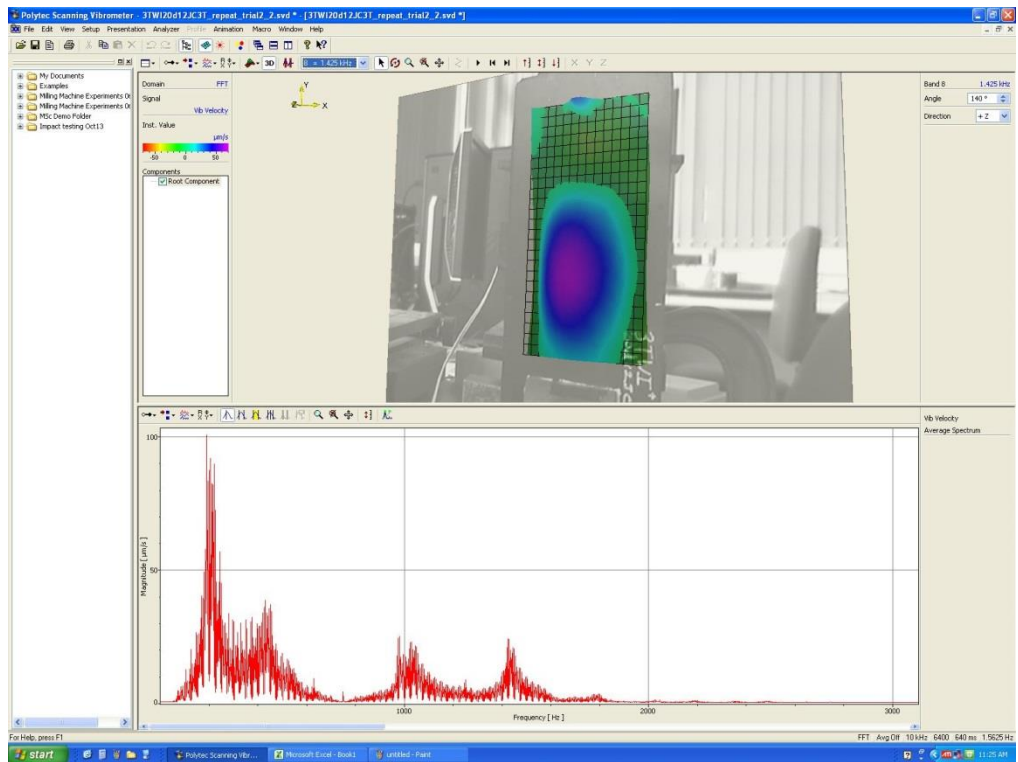


Figure 240 The modal form with full spectrum at the bottom; Sample: 3TWI20d12JC1; Mode – 8

Discussion:

In order to understand the random error created from the data, the results and the analysis of the data needs to be established. The scan setup has been discussed in Section 3 and in this section it is more to do with the analysis part of the data. When the acquired data was post processed, major modal frequency peaks were identified. Each of these frequencies represented a specific characteristic waveform of the sample, which was reconstructed in the form of modal images presented above (Modes 1- 8 represented by Figure 233 - Figure 240). It can be understood from literature that for a metallic plate the peaks are very sharp and streamlined. However, for a composite laminate, there is a lot of noise that is added to the LDV data. Hence the peaks were manually identified based on the modal frequency image.

Each of the modal frequency images (Mode 1- 8) clearly show the band frequency at which sampling was carried out. This was tabulated against the respective mode. Thus for each trial, frequencies were identified manually from the frequency map and then tabulated.

It can be seen that 5 out of 8 modal frequencies were found to be either same or within a difference of $\pm 5\text{Hz}$. It should be noted that mode 5 wasn't considered for this error identification as sampling 2 did not identify the peak modal frequency. It should be noted that the sample used here was a post Charpy impact sample 3TWI20d12JC3T.

4.5.3 Damage changes modal frequency – a hypothesis

It is well known in literature that when a metallic component develops damage such as cracks, the modal frequency of the material changes. This relates back to the old railway track testing where maintenance engineers did a tap test using a hammer to determine the soundness of the rail track (Adams and Cawley 1988; Kapadia 2013). The analogy that a damage changes the modal frequency in a test sample has now been adapted to this vibrational analysis to confirm the presence of damage. Thus, for the validation of this statement, a test was performed where a sample with no defect was first inspected using the LDV. The sample was then impacted using a

modified Charpy test, as indicated in the previous section. The impacted sample was then inspected using the LDV.

The following are the results obtained.

Table 32 Modes and modal frequency comparison between the sample 3TWI12d20JC3T before and after impact

Modes	Sample - No Damage in Hz				Sample - Impact damage in Hz			
	Trial 1	Trial 2	Trial 3	Avg.	Trial 1	Trial 2	Trial 3	Avg.
1	100	98.75	98.75	99.17	125	129.69	129.69	128.13
2	197.63	195	195	195.88	190.63	190.63	190.63	190.63
3	252.63	252.63	252.63	252.63	245.31	250	225	240.10
4	425	422.69	422.69	423.46	429.69	450	425	434.89
5	625	622.69	622.69	623.46	629.69	629.69	629.69	629.69
6	950	945.63	945.63	947.08	979.69	979.69	979.69	979.69
7	995.31	995.31	995.31	995.31	1029.69	1050	1025	1034.89
8	1395.31	1395.69	1395.69	1395.56	1425	1425	1400	1416.67

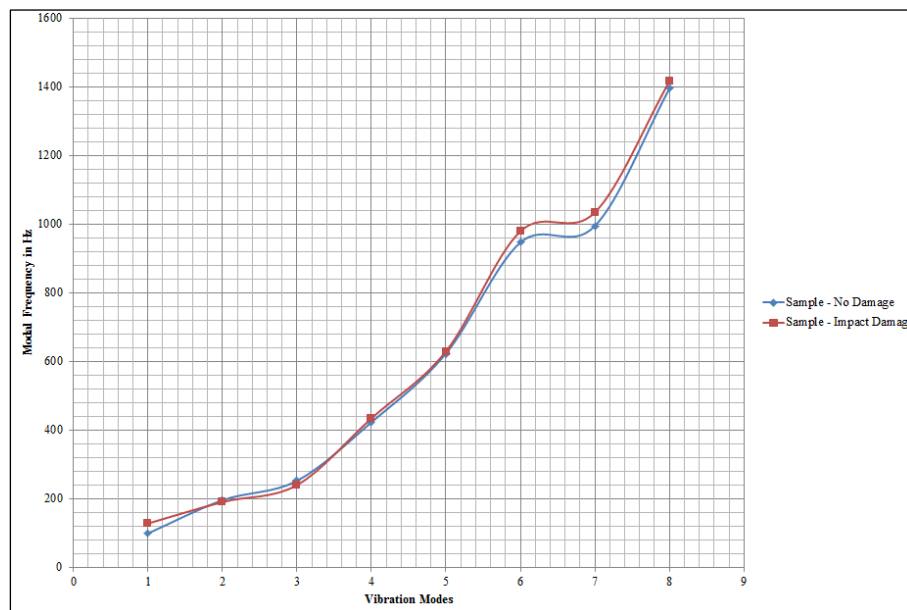


Figure 241 Vibration Modes vs modal frequencies (average values) of the laminate before and after impact

It can be observed from the table (Table 32) that modes 1, 6, 7, 8 show a change in frequencies between 20Hz and 40Hz. Though there is a small change in frequencies between modes 2, 3 and 4, they weren't considered for this analysis as they were within the margin of the random error estimation of ± 5 Hz. It is also worth

mentioning that the higher modes do show a greater difference which is mainly due to the influence of damage orientation, location and the vibration mode shape.

Conclusion:

Based on the random error in experimental data capture of $\pm 5\text{Hz}$, it can be noticed that the difference in modal frequencies is greater than 25Hz confirming the hypothesis that this modal frequencies change is due to the presence of damage and is in line with the theoretical model. It should be noted that in order to establish the damage created, the random error measurement was performed on the damaged laminate to capture the maximum variation due to the presence of the damage.

4.6 Epilogue

This chapter primarily presented results obtained from the preliminary experimental tests, the parametric study on material defect inserts and concluded with the systematic study on characterising impact damage using multiple thermography techniques. This chapter has provided not just direct results, but also presented initial experimental trials, validated test setups and a range of experimental results that help detect and characterise defects and damage occurring in CFRP laminates. Further, each set of results provided analysis and or observations that were evident from the test results. It was observed that pulsed thermography was sensitive for sub-surface defects and certain surface breaking damage. However, TSA has shown better SNR and increased sensitivity where it picked up the smallest of the damage created by 4.5J stone impact which wasn't picked up by other techniques. This chapter also presented the detection limitations of both pulsed thermography and TSA where the former could only detect certain types of defects not exceeding 4.5mm and the latter being less sensitive to non-surface breaking damage. Due to the large amount of images and plots, a comprehensive discussion of various findings of the work has been presented in Chapter 5 below.

5 REVIEW OF WORK

The primary aim of this thesis was to look at the applicability of detecting near and sub-surface artificial defects and damage occurring in CFRP laminates using pulsed thermography and TSA measurement. With the ever increasing use of these advanced composites as primary airframe structures, it is pivotal that suitable technologies are developed to perform in-field maintenance. Few of the challenges faced by the aviation industry, are looking at the applicability of these advanced techniques where accessibility and fidelity are key. Further the traditional methods have had disadvantages such as mobility, surface preparation and longer inspection lead times. Additionally, the techniques are mostly either contact based or that the non-contact methods are invasive and need highly skilled operators. The work presented in this thesis is an effort to address the needs of the industry to adapt to a rapid, non-invasive large area inspection system that could be employed in-field and provide those critical decisions in a timely fashion such that inspection downtimes are significantly reduced thereby reducing operator's burden and the associated maintenance and breakdown costs.

The literature review (Chapter 2) defined various concepts of not just the use of composites but also the presented scenarios of how damage may be created in field. Further, it also presented various NDT techniques that are now in use together with the need for the use of thermography in specific areas. Currently, thermography is perceived as a qualitative inspection tool with low fidelity. In fact, the current British Institute's NDT personnel certification and training programmes show thermography as a condition-monitoring tool as opposed to an NDT tool. Thus the current thesis is a representation of not just the detectability of defects and damage but their limitations as well.

The literature identified the gap in knowledge that exists in the area of detection limitations and a full deployment for in-field scenarios. In addition, the suitability of the TSA technique and its ability to be deployed in field has been demonstrated in this work. Thus parametric studies to detect manufacturing defects and in-field damage were proposed using the research grade infrared radiometer in multiple modes to fully characterise those anomalies.

5.1 In-field samples

To understand and explore the applicability of thermography, in-field samples with artificially introduced defects were used as a starting point of this research. The results presented in Section 4.1 show that for a tail plane wedge with defect inserts, it clearly highlighted those defects that are most likely to occur in such scenarios. The results also presented a set of capture parameters that were ideal to detect all defects. Further, the results present three distinct areas which correspond to;

1. The presence of delamination occurring in-between the fibre glass layers.
2. The presence of disbond occurring between the fibre glass skin and the honeycomb structure.
3. The presence of blocked honeycomb cells representing the scenario of water ingress.

The 2D radiograph has highlighted all defects but has failed to distinguish between the three types of defects as characterised by the pulsed thermography system. It should also be understood that performing an X-ray inspection in-field would be a very complicated process and an expensive setup when compared with the pulsed thermography system. The ability to reduce any radiation hazards, faster inspection down times directly supports the in-field applicability, suitability and robustness of the thermography system. For the purpose of this thesis, the results presented in section 4.1 were used to confirm the working principle of the pulsed thermography system.

5.2 Manufacturing defects – a parametric study

With the working principle of pulsed thermography established through ‘in-field’ samples, it was identified that it was essential to understand the limitations of the system. Multiple studies indicated the suitability of pulsed thermography to detect sub-surface damage was proposed. However, there is limited information on the limitations of the system in terms of detectability of defects occurring at controlled depth. Thus a full parametric study was identified which included both experimental work and theoretical validation of the results acquired by the system.

Based on the literature, publicly available information and practitioners' knowledge, the parametric study was designed. For this study only defects occurring at the manufacturing stage were considered. From field experts it was established that the most common types of inclusions were metallic cutters/blades, bagging films and air gaps especially in scenarios of automated cutting and lay-up. This information formed the basis of selecting the three material inserts; steel shims, Teflon and bagging film. The detection capability of the system became the main driver where the thickness of the laminates and the defect depth location was varied to arrive at the limitations of the system. The following table (Table 33) shows the detection capability and limitations of the in-house system.

Table 33 Pulsed Thermography detection capability

Sample	Defect Depth in mm	Defect Inserts		
		Steel Shims	Teflon	Bagging film
3mm Laminate	0.5	●	●	●
	1.0	●	●	●
	1.5		●	●
6mm Laminate	2.0		●	
	2.5		●	
	3.0		●	
9mm Laminate	3.5		●	
	4.0		●	
	4.5			

It has been illustrated from Table 33 that the detectability limitations of the pulsed thermography system are limited to 1.0mm in case of steel shims; 1.5mm in case of bagging film and 4.0mm in the case of Teflon. Based on the above set of results, the following conclusions can be made;

- For steel shims of 20 μ m thickness, the detectability of the pulsed thermography system is limited to 1.0mm. The main reason for this conclusion is that, this result is directly dependent on the material characteristics of the steel shim. The thickness of the metal insert is so small that by the time the heat wave arrives at the 1.5mm deep insert, the intensity is lost and hence the inability of the system to detect it. This issue of intensity affects the contrast and thus the signal response from the 1.5mm deep insert

is almost non-existent. The reason this thickness of 20 μ m was considered was to see if blade offcuts could be picked up. This also means that, thicker metal parts embedded into the laminate might be easily detected by the system.

- Similar conclusions could be made for the bagging film type inserts. Again the thickness of the material was 20 μ m. As before, both the 0.5mm and 1.0mm inserts were easily picked up in the RAW thermal image. The 1.5mm deep defect was only picked up in the 2D image indicating that the noise of the laminate was quite high masking the contrast of the defect in the first instance. This feature was found only in the case of the bagging film defect and not the steel shim insert indicating that the material conductivity was key in this image and signal improvement was achieved through the use of 2nd derivative of the RAW image as seen in the 2D image (Figure 64). In other words, the heat wave when hit the steel shim, them being conductive in nature diffused the heat much faster. However, the bagging film material being non-conductive in nature provided the necessary insulation to heat diffusion. This meant that, the SNR improved in the 2D image thereby picking up the defect. When a 6mm laminate with defects at 2.0mm, 2.5mm and 3.0mm depths was tested, none of the defects were identified even in the 2D image establishing the limitation of the pulsed thermography system to 1.5mm for bagging film inserts.
- The conclusions for the Teflon inserts differed completely. For all 3 thicknesses; 3mm, 6mm and 9mm the inserts were clearly detected to depths up to 4.0mm. It should be noted that the thickness of the Teflon off cuts was at 500 μ m. Again, due to the thick nature of the insert, the defects were easily detected up to depths of 4.0mm indicating that thick insulating materials show a sharper contrast.

This parametric study clearly established the limitations of the pulsed system with respect to the defect depth. This study also established the strength of the technique in detecting near and sub-surface defects and more appropriately their suitability to detect and characterise defects occurring in advanced composite materials.

5.3 Impact damage assessment – a parametric study

The major part of this research was focussed on the creation and detection of impact damage on composite laminates. Research by Meola and Carlomagno (2010) and (2009) provided the starting point of the impact parametric study where the authors used a modified Charpy and transient thermography to detect the rise in back wall surface temperature of GFRP and CFRP laminates when subject to impact. This study was designed based on this work and thus a parametric approach to understand the influence of laminate thickness, lay-up sequence and most importantly to understand those type of damage that are barely visible (BVID). Detecting visible damage due to impact and their characterisation using other NDT techniques exist. However, the ability to detect low energy impact damage is a challenge in itself. The necessity to characterise BVID type damage became the prime focus of this research where there is still lack of understanding as to how this damage could be detrimental to the performance of the laminate, especially in the high end application areas.

Based on the literature and practitioners knowledge, it was identified that a parametric study to investigate BVID was needed. This study also took into consideration the influence of indenter or impactor shape as indicated by Meola and Carlomagno (2010) and Mitrevski, Marshall et al. (2005). Thus the impact event was performed by using a low speed charpy impact that had a defined hemispherical impactor and a high speed ballistic gas-gun that used irregular surface stones to replicate both laboratory and real-field scenarios. The primary focus of this study was to deploy thermography in multiple ways to help detect and characterise impact damage.

As presented in Chapter 4, thermography was deployed in the transient, pulsed and TSA modes. Whilst transient mode at high frame rate acquisition was used to capture the damage created during the impact event, pulsed and TSA methods were used as post-impact NDT techniques to detect the damage created. TSA was exploited as part of this study to highlight its applicability to successfully detect surface breaking damage, even for a small crack that is barely visible on the surface of the laminate.

The following table (Table 34) summarises the detectability of transient, pulsed and TSA techniques to detect impact damage on composite laminates;

Table 34 Impact damage detectability matrix

Sample	Transient Thermography	Pulsed Thermography	TSA
Charpy			
3QI20d12JC	●	●	
3QI16d8JC	●		
3QI12d4.5JC	●		
3TWI20d12JC	●	●	
3TWI16d8JC	●		
3TWI12d4.5JC	●		
6QI20d12JC			
6QI16d8JC			
6QI12d4.5JC			
6TWI20d12JC			
6TWI16d8JC			
6TWI12d4.5JC			
Gas-gun			
3QI12JS	●	●	●
3QI8JS	●	●	●
3QI4.5JS	●	●	●
3TWI12JS	●	●	●
3TWI8JS	●	●	●
3TWI4.5JS			●
6QI12JS		●	●
6QI8JS		●	●
6QI4.5JS			●
6TWI12JS		●	●
6TWI8JS		●	●
6TWI4.5JS			●

Based on the results and the summary from Table 34, the following observations and conclusions can be made;

For low speed Charpy impact:

- Transient thermography results showed stress in individual fibres only for the 3mm laminates.
- Further pulsed thermography only identified the damage created at 12J impact energy, indicating that the plastic deformation of the laminate due to impact was identified only for the upper energy level and that all other energies went undetected. This could be because of the fact that, though the

fibres underwent stress, they haven't fully developed into a detectable damage.

- As the damage was characterised by deformation, visual detection especially for the 4.5J impact was a challenge as the laminate was found to be resistant to the impact. However, the transient thermal data does confirm the stress acting on the fibre through a resultant thermal stress value.
- As the damage was not surface breaking, the TSA did not detect any indication of the damage even for higher energy impact of 12J.
- There was no instantaneous back wall temperature rise for any of the 6mm laminates indicating that the rate of transfer of stress onto the laminate and the resulting damage formed was much less in intensity. It can be understood that this impact resistance of the laminate was contributed by the increased strength of the laminate due to added material thickness. This is quite evident with the 4.5J impact where there is no surface deformation.
- Neither the pulsed system nor the TSA system picked any damage that may have been created on the 6mm laminate due to the impact suggesting that the laminates remain undamaged.

For high speed ballistic gas-gun impact:

- Due to the thickness, material properties and strength of the laminate, only 3mm laminates showed a back wall temperature rise for the gas-gun stone impact with limitation to the 4.5J impact TWI sample. This laminate seemed to show resistance to impact and only a small damage was created, which was picked up by the TSA method.
- As the damage was surface breaking, the pulsed system picked most of the damage created due to impact except for 4.5J impact on 6mm laminates (both QI and TWI samples).
- It has been noted for this type of impact damage, TSA has been the most promising technique as it has proved that it is highly sensitive and is capable of picking up even damage created at a 4.5J impact on 6mm laminates which have not been picked by other techniques.

5.4 Epilogue

This chapter presents an overall review of the work undertaken as part of this research. The previous chapter (Chapter 4) presented results and immediate observations. Due to the length of the results chapter, it was necessary to present an overview of key findings from this research for better readability and critical reasoning. This chapter has presented the applicability of various thermography techniques and their suitability for 'in-field' 'in-situ' applications. As part of this chapter separate sections were established to provide an overview of two major types of defects and damage and together with their detectability. It was determined that pulsed thermography was more suitable for sub-surface defects and TSA was more suitable for surface breaking impact damage.

6 CONCLUSIONS & FUTURE WORK

With the increased use of CFRP laminates across industries, it has become the prime focus to understand the performance of these non-traditional materials especially in the presence of defects and damage. Though these materials are light weight and offer better corrosion and abrasion resistance, they are still susceptible to a range of degradations during service that directly affect their performance. Further, the lack of understanding of the behaviour of these materials and complex repair strategies control their applicability in complex engineering structures. This work is an attempt to deploy thermographic techniques in determining the condition of the laminate when subject to artificial introduction of defects and damage. To replicate real-life scenarios, parametric studies were undertaken to detect sub-surface artificial inserts and impact damage characterisation (creation and detection).

6.1 Conclusions

A detailed list of findings has been presented in Chapter 5. The following is the summary of the major conclusions from the research;

- Pulsed thermography is an effective technique to detect sub-surface defects.
- The detectability of the defects through pulsed thermography is dependent on the type of material, their thickness and more importantly their thermal material properties.
- Pulsed thermography limitations of detecting low energy impact damage have been limited to 8J.
- TSA is an effective technique to detect surface breaking damage especially in the case of high speed stone impact.
- TSA has shown improved SNR even for an energy as low as 4.5J which is representative of scenarios such as stone impact on aircrafts establishing this technique as a robust ‘in-field’ inspection technique.

This research also adapted techniques such as radiography, computational modelling in case of pulsed thermography and vibrational analysis case study to confirm damage caused due to impact.

Therefore the experimental work undertaken has validated the original aims and subsidiary objectives as identified in chapter 1 which are

- To establish Pulsed Thermography as an effective technique to detect sub-surface defects in advanced composite materials
- To explore and exploit the Thermoelastic Stress Analysis (TSA) technique as an alternate inspection tool to detect damage that are hard to detect using pulsed thermography especially in the case of surface and near-surface damage.

6.2 Recommendations & Future Work

The following are the list of recommendations and future work directions based on the work undertaken as part of this thesis;

- The work presented in this thesis has been extended to look at the automation of the pulsed thermography inspection, which has now been extensively developed, the findings of which have been published as Addepalli and Tinsley (2015) titled “Active thermography in through-life engineering” (See Appendix 1).
- Another direction where the work has been extended is in developing the Thermographic Signal Reconstruction (TSR) algorithms in C++ software domain to characterise impact damage and enhance damage visualisation through coefficient cluster analysis. This work has been published as Zhao, Tinsley et al. (2016) titled “A coefficient clustering analysis for damage assessment of composites based on pulsed thermographic inspection” (See Appendix 1)
- Research is being undertaken to represent damage detection ‘in-situ’ through the use of fully automated part presentation, inspection and data analysis

through the use of advanced signal and image processing techniques and super-resolution techniques.

(Submitted works:

[1] W Witwit, Y Zhao, K Jenkins, S Addepalli, “Video super-resolution using discrete wavelet transform and new edge-directed interpolation”, Submitted to IEEE transactions on Circuits and Systems for Video Technology [22 September 2016]

[2] S Addepalli, Y Zhao, L Tinsley, “Thermographic NDT for through-life inspection of high value components”, In: Through-life Engineering Services: Perspectives and Developments, Springer International. Accepted [In Press] July 2016

[3] S Addepalli, R Roy, D Axinte, J Mehnen, “‘In-situ’ inspection technologies: Trends in degradation assessment and associated technologies”, Procedia CIRP, Submitted [August 2016].)

- There is need to further analyse the data sets obtained from the transient thermography deployed to capture the impact event. Quantitative analysis of the transient thermographic results during impact has the potential to reveal plastic deformation and damage.
- A controlled environment could help reduce the interferences during data acquisition, especially the TSA analysis as reflections reduce the SNR providing weak results.
- Future work could look at phase information from pulsed thermography by looking at the frequency domain of the image using Fourier analysis which could extend the ability of the technique to potentially detect deeper defects.
- It is recommended that the impact samples be tested with mechanical tests such as compression/tension after impact and interlaminar shear tests to correlate damage created with loss in performance.
- The TSA experiments could be extended with larger excitation sources to investigate cyclic fatigue and corresponding damage growth.
- The existing experiments used a single excitation frequency to facilitate an acceptable SNR in the TSA experiments. It would be interesting to undertake further vibrational analysis using more complex excitation sources such as ‘chirp’ envelopes.

BIBLIOGRAPHY

- Adams, R. D. and P. Cawley (1988). "A review of defect types and nondestructive testing techniques for composites and bonded joints." NDT International **21**(4): 208-222.
- Addepalli, S. and L. Tinsley (2015). Active Thermography in Through-Life Engineering. Through-life Engineering Services, Theory and Practise. L. Redding and R. Roy, Springer International Publishing: 117-127.
- Avdelidis, N. P. and D. P. Almond (2004). "Through skin sensing assessment of aircraft structures using pulsed thermography." NDT & E International **37**(5): 353-359.
- Avdelidis, N. P., B. C. Hawtin, et al. (2003). "Transient thermography in the assessment of defects of aircraft composites." NDT & E International **36**(6): 433-439.
- Azouaoui, K., Z. Azari, et al. (2010). "Evaluation of impact fatigue damage in glass/epoxy composite laminate." International Journal of Fatigue **32**(2): 443-452.
- Bai, W. and B. S. Wong (2001). "Evaluation of defects in composite plates under convective environments using Lock-in thermography." Measurement Science and Technology **12**: 142-150.
- Baker, A., S. Dutton, et al. (2004). Composite Materials for Aircraft Structures. Reston, American Institute of Aeronautics and Astronautics Inc.
- Ball, R. J. and D. P. Almond (1998). "The detection and measurement of impact damage in thick carbon fibre reinforced laminates by transient thermography." NDT & E International **31**(3): 165-173.
- Barbero, E. J. (1998). Introduction to Composite Material Design. Ann Arbor, Taylor & Francis Inc.
- Blount, T. (1707). Glossographia Anglicana Nova OR A Dictionary. London.
- Brady, R. P. and M. R. Kulkarni (1996). "Determination of thermal diffusivity distribution for three types of materials by transient thermography." NDT & E International **29**(4): 205-211.
- Breitenstein, O., W. Warta, et al. (2010). Lock-in Thermography : Basics and Use of Evaluating Electronic Devices and Materials, Springer Heidelberg Dordrecht London Newyork.
- Burrows, S. E., S. Dixon, et al. (2010). Combined thermography and noncontact ultrasound inspection techniques using pulsed laser excitation, American Institute of Physics.
- Campbell, F. C. (2004). Manufacturing Processes for Advanced Composites. Oxford, Elsevier.

Carslaw, H. S. and J. C. Jaeger (1959). Conduction of Heat in Solids. London, Oxford University Press.

Chatterjee, K., S. Tuli, et al. (2011). "A comparison of the pulsed, lock-in and frequency modulated non-destructive evaluation techniques." NDT & E International **44**: 655-667.

Chawla, K. K. (2001). Composite Materials. New York, Springer-Verlag.

Choi, M., K. Kang, et al. (2008). "Quantitative determination of a subsurface defect of reference specimen by lock-in infrared thermography." NDT & E International **41**(2): 119-124.

CMH-17 (2012). Composite Materials Handbook - Polymer Matrix Composites: Guidelines for Characterization of Structural Materials, SAE International.

Composites, N. (2013). "Interactive Knowledge Base on NDE of Composites." Retrieved 30-08, 2013, from <http://www.netcomposites.com/ikb/browse/default.asp?ST=1&SC=3&T=737&P=%2E%2E%2FTopics%2FDefects%2FDefect+types+in+composites%2FDefault%2Ehtml>.

Corum, J. M., R. L. Battiste, et al. (2003). "Low-energy impact effects on candidate automotive structural composites." Composites Science and Technology **63**(6): 755-769.

Craven, R., P. Sztetek, et al. (2008). "Investigation of impact damage in multi-directional tape laminates and its effect on local tensile stiffness." Composites Science and Technology **68**(12): 2518-2525.

Dattoma, V., R. Marucuccio, et al. (2001). "Thermographic investigation of sandwich structure made of composite material." NDT & E International **34**: 515-520.

de Morais, W. A., S. N. Monteiro, et al. (2005). "Evaluation of repeated low energy impact damage in carbon–epoxy composite materials." Composite Structures **67**(3): 307-315.

Dudzik, S. (2009). "A simple method for defect area detection using active thermography." Opto-Electronics Review **17**(4): 338-344.

Duell, J. M. (2004). Impact Testing of Advanced Composites. Advanced Topics in Characterization of Composites. M. R. Kessler, Trafford Publication: 97-112.

Feuillet, V., L. Ibos, et al. (2012). "Defect detection and characterization in composite materials using square pulse thermography coupled with singular value decomposition analysis and thermal quadrupole modeling." NDT & E International **51**: 58-67.

- Garnier, C., M.-L. Pastor, et al. (2011). "The detection of aeronautical defects in situ on composite structures using Non Destructive Testing." Composite Structures **93**(5): 1328-1336.
- Genest, M., M. Martinez, et al. (2009). "Pulsed thermography for non-destructive evaluation and damage growth monitoring of bonded repairs." Composite Structures **88**(1): 112-120.
- Giorleo, G. and C. Meola (2002). "Comparison between pulsed and modulated thermography in glass-epoxy laminates." NDT & E International **35**: 287-292.
- Giorleo, G., C. Meola, et al. (2000). "Analysis of Defective Carbon-Epoxy by means of Lock-in Thermography." Research in Nondestructive Evaluation: 241-250.
- Gleiter, A., C. Spiessberger, et al. (2008). "Decay time analysis in pulse thermography." The European Physical Journal Special Topics **153**(1): 377-381.
- Grys, S. (2012). "New thermal contrast definition for defect characterization by active thermography." Measurement **45**(7): 1885-1892.
- Gunasekera, A. M. (2010). Compression after impact load prediction in graphite epoxy laminates. Material Evaluation: 880-886.
- Hexcel (2013). HexPly Prepreg Technology: 1-34.
- Hornak, J. P. (2002). Encyclopaedia of Imaging Science and Technology, John Wiley & Sons.
- Ibarra-Castanedo, C., M. Susa, et al. (2008). "Infrared thermography: principle and applications to aircraft materials." NDT.net.
- ISO18352:2009 Carbon-fibre – reinforced plastics – Determination of compression after impact properties at a specified impact energy level.
- Janna, W. S. (2000). Engineering Heat Transfer. USA, CRC Press LLC.
- Jones, R. M. (1999). Mechanics of Composite Materials. USA, Taylor & Francis Inc.
- Kapadia, A. (2013) "Non Destructive Testing of Composite Materials." Best Practice Guide, 1-48.
- Kaw, A. K. (2006). Mechanics of composite materials, CRC Press.
- Kessler, M. R. (2004). Introduction. Advanced Topics in Characterization of Composites. M. R. Kessler, Trafford Publishing: 1-9.
- Kim, H., G. DeFrancisci, et al. (2009) "Impact Damage Formation on Composite Aircraft Structures." 1-37.

- Kim, H. and K. T. Kedward (2000). "Modelling Hail Ice Impacts and Predicting Impact Damage Initiation in Composite Structures." AIAA **38**(7): 1278-1288.
- Kim, H., K. T. Kedward, et al. (2003). "Experimental Investigation of High Velocity Ice Impacts on Woven Carbon/Epoxy Composite Panels." Composites Part A **34**(1): 25-41.
- Krishnapillai, M., R. Jones, et al. (2005). "Thermography as a tool for damage assessment." Composite Structures **67**(2): 149-155.
- Krishnapillai, M., R. Jones, et al. (2006). "NDTE using pulse thermography: Numerical modeling of composite subsurface defects." Composite Structures **75**(1-4): 241-249.
- Li, C. F., N. Hu, et al. (2002). "Low-velocity impact-induced damage of continuous fiber-reinforced composite laminates. Part I. An FEM numerical model." Composites Part A **33**: 1055-1062.
- Maillet, D., A. S. Houlbert, et al. (1993). "Non-destructive thermal evaluation of delaminations in a laminate: Part I – Identification of measurement by thermal contrast." Composites Science and Technology **47**: 137-153.
- Maldague, X., F. Galmiche, et al. (2002). "Advances in pulsed phase thermography." Infrared Physics & Technology **43**: 175-181.
- Maldague, X., T. Jones, et al. (2001). Fundamentals of infrared and thermal testing. ASNT Nondestructive Testing Handbook: Infrared and Thermal Testing. X. Maldague and P. Moore, ASNT. **3**: 31-52.
- Maldague, X. P. V. (2001). Theory and Practice of Infrared Thermography for Nondestructive Testing. USA, John Wiley & Sons Inc.
- Maldague, X. P. V., J. L. Beaudoin, et al. (2001). Techniques of Infrared Thermography. ASNT Nondestructive Testing Handbook: Infrared and Thermal Testing. X. P. V. Maldague and P. O. Moore, ASNT. **3**: 307-357.
- Marty, P. N., N. Desai, et al. (2004). NDT of Kissing bonds in Aeronautical structures. WCNDT 2004.
- Matthews, F. L. and R. D. Rawlings (1999). Composite materials : Engineering and science. North America, Woodhead Publishing Ltd and CRC Press.
- Meola, C. and G. M. Carlomagno (2009). "Infrared thermography of impact-driven thermal effects." Applied Physics A **96**(3): 759-762.
- Meola, C. and G. M. Carlomagno (2010). "Impact damage in GFRP: New insights with infrared thermography." Composites Part A: Applied Science and Manufacturing **41**(12): 1839-1847.

- Meola, C., G. M. Carlomagno, et al. (2006). "Non-destructive evaluation of aerospace materials with lock-in thermography." Engineering Failure Analysis **13**(3): 380-388.
- Miracle, D. B. and S. L. Donaldson. (2011). "Introduction to composites." Retrieved 22 July, 2011, from http://www.compositecarbonfiberprop.com/carbon_fiber.pdf.
- Mitrevski, T., I. H. Marshall, et al. (2005). "The effect of impactor shape on the impact response of composite laminates." Composite Structures **67**(2): 139-148.
- Montanini, R. (2010). "Quantitative determination of subsurface defects in a reference specimen made of Plexiglas by means of lock-in and pulse phase infrared thermography." Infrared Physics & Technology **53**(5): 363-371.
- Morgan, P. (2005). Carbon Fibers and Their Composites. USA, Taylor & Francis Inc.
- Nino, G. F., T. J. Ahmed, et al. (2009). "Thermal NDI of resistance welded composite structures." Composites Part B: Engineering **40**(3): 237-248.
- Omar, M. A. and Y. Zhou (2008). "A quantitative review of three flash thermography processing routines." Infrared Physics & Technology **51**(4): 300-306.
- Pavier, M. J. and M. P. Clarke (1995). "Experimental techniques for the investigation of the effects of impact damage on carbon-fibre composites." Composites Science and Technology **55**: 157-169.
- Pickering, S. and D. Almond (2008). "Matched excitation energy comparison of the pulse and lock-in thermography NDE techniques." NDT & E International **41**(7): 501-509.
- Pratt, W. R. (2013). "The Science is settled?" Retrieved 07/09, 2013, from http://www.spinonthat.com/co2_files/o2_n2_ir_absorption.html.
- Ring, E. F. J. (2000). "The discovery of infrared radiation in 1800." The Imaging Science Journal **48**(1): 1-8.
- Sakagami, T. and S. Kubo (2002). "Applications of pulse heating thermography and lock-in thermography to quantitative nondestructive evaluations." Infrared Physics & Technology **43**: 211-218.
- Schmutzler, H., M. Alder, et al. (2014). "Degradation monitoring of impact damaged carbon fibre reinforced polymers under fatigue loading with pulse phase thermography." Composites Part B: Engineering **59**: 221-229.
- Schroeder, J. A., T. Ahmed, et al. (2002). "Non-destructive testing of structural composites and adhesively bonded composite joints : pulsed thermography." Composites Part A: Applied Science and Manufacturing **33**: 1511-1517.

- Schubel, P. M., J.-J. Luo, et al. (2007). "Impact and post impact behavior of composite sandwich panels." Composites Part A: Applied Science and Manufacturing **38**(3): 1051-1057.
- Shepard, S. (2007). Flash Thermography of Aerospace Composites. IV Conferencia Panamericana de END, Buenos Aires.
- Shepard, S. M. (2007). Flash thermography of aerospace composites. IV Conferencia Panamericana de END. Buenos Aires.
- Shyr, T.-W. and Y.-H. Pan (2003). "Impact resistance and damage characteristics of composite laminates." Composite Structures **62**(2): 193-203.
- Sohn, M. S., X. Z. Hu, et al. (2000). "Impact damage characterisation of carbon fibre/epoxy composites with multi-layer reinforcement." Composites Part B: Engineering **31**: 681-691.
- Toubal, L., M. Karama, et al. (2006). "Damage evolution and infrared thermography in woven composite laminates under fatigue loading." International Journal of Fatigue **28**(12): 1867-1872.
- University, C. "Materials Selection Chart : An overview of physicists." Retrieved 21 October, 2011, from <http://www-materials.eng.cam.ac.uk/mpsite/physics/overview/default.html>.
- Vinson, J. R. and R. L. Sierakowski (2008). The Behaviour of Structures Composed of Composite Materials. The Netherlands, Springer.
- Vollmer, M. and K.-P. Möllmann (2010). Infrared Thermal Imaging : Fundamenatls, Research and Applications. Weinheim, Germany, WILEY-VCH Verlag GmbH & Co.
- Yan, D., B. W. Drinkwater, et al. (2009). "Measurement of the ultrasonic nonlinearity of kissing bonds in adhesive joints." NDT & E International **42**(5): 459-466.
- Zhao, Y., L. Tinsley, et al. (2016). "A coefficient clustering analysis for damage assessment of composites based on pulsed thermographic inspection." NDT & E International **83**: 59-67.

Appendix 1

The following book chapter is published as Addepalli and Tinsley 2015.

Chapter 8 Active Thermography in Through-Life Engineering

Sri Addepalli and Lawrence Tinsley

Abstract With the increased use of high-value components in aerospace industries, there is huge emphasis on reliability as their failure in service could lead to catastrophic failure of the system. Thus, there continues to be increasing dependency of such high-value components to undergo critical maintenance routines in order to reduce the probability of failure. The prediction of Remaining Useful Life (RUL) is a critical factor in estimating the service cost. It has direct impact upon product and service pricing. With increasing maintenance costs, manufacturers have adopted a range of techniques such as non-destructive testing (NDT) to help assess the serviceability of these high-value components, where a component is inspected for quality without causing damage to the part. This allows for inspection of entire batches, instead of sample subsets. In service-focussed business models such as the aerospace sector, high-value components are required to perform for an optimum life cycle, balanced between maximising operation hours and a confidence in its safety. NDT has become a key process in determining the current state of degradation during the component's use, allowing estimation of remaining life and determination of repairs required. Detection of defects and anomalies is still a major challenge in the development of NDT practices in advanced manufacturing processes even more so with the introduction of new materials for higher reliability and performance. This research looks at expanding the NDT practices in maintenance by identifying the emerging challenges and suggesting areas of research for a robust development of NDT techniques and improved component degradation analysis. Active thermographic NDT is a recent technique that has become more widely included in NDT processes over recent years. However, due to its shallow depth and lower resolution limitations, it has not been exploited to its full potential in maintenance routines. Current challenges involve the further development of thermography as a quantitative technique as opposed to its traditionally qualitative implementations. This chapter focusses on the detection of damages caused due to component degradation using the pulsed active thermography technique. It also presents a novel approach on

S. Addepalli (✉) · L. Tinsley
EPSRC Centre for Through-Life Engineering Services, Cranfield University,
Cranfield, Bedfordshire MK43 0AL, UK
e-mail: p.n.addepalli@cranfield.ac.uk

© Springer International Publishing Switzerland 2015
L. Redding and R. Roy (eds.), *Through-life Engineering Services*,
Decision Engineering, DOI 10.1007/978-3-319-12111-6_8

117



Contents lists available at ScienceDirect

NDT&E International

journal homepage: www.elsevier.com/locate/ndteint



A coefficient clustering analysis for damage assessment of composites based on pulsed thermographic inspection



Yifan Zhao*, Lawrence Tinsley, Sri Addepalli, Jörn Mehnen, Rajkumar Roy

Through-life Engineering Services Institute, Cranfield Manufacturing, Cranfield University, Cranfield MK43 0AL, UK

ARTICLE INFO

Article history:
Received 29 February 2016
Received in revised form
27 April 2016
Accepted 9 June 2016
Available online 11 June 2016

Keywords:
NDT
Thermography
Impact damage assessment
Delamination

ABSTRACT

This paper introduces a coefficient clustering analysis method to detect and quantitatively measure damage occurring in composite materials using pulsed thermographic inspection. This method is based on fitting a low order polynomial model for temperature decay curves, which (a) provides an enhanced visual confirmation and size measurement of the damage, (b) provides the reference point for sound material for further damage depth measurement, (c) and reduces the burden in computational time. The performance of the proposed method is evaluated through a practical case study with carbon fibre reinforced polymer (CFRP) laminates which were subjected to a drop impact test with varying energy levels. A novel method for reducing an entire thermogram sequence into a single image is introduced, which provides an enhanced visualisation of the damage area.

© 2016 Elsevier Ltd. All rights reserved.

1. Introduction

Composite materials are well known for their high strength-to-weight ratios, low density and corrosion resistant properties in comparison with traditional metallic components. As such, they are applied in a wide variety of contexts, increasingly in automotive and aerospace sectors; where there is a huge requirement to improve system performance through weight reduction. With the rising price of aviation fuel and attitude towards environmental issues, modern aircraft manufacturers are looking out for innovative solutions that can offer better performance without compromising the structural integrity and safety features of the aircraft. Thus the current generation of aircrafts are seeing large introduction of composite components that constitute to about 50% by weight of the aircraft in parts such as engine casings, wing sections, tail plane, control structures and fuselage [1]. However, composites are also well known for their vulnerability to impact damage and their difficulty to repair compared to metal based components. An impact or strike on the surface may cause structural damage that may be exhibited with only a small surface visual profile – this is known as barely visible impact damage (BVID) [2]. Even though the damage is “barely visible” on the surface, the damage to the structure could severely affect its properties and performance, which may not be apparent from the surface profile of the impact.

A variety of impact sources exist, such as stones, hail, bird strike

and even accidental drop of workmen tools during maintenance that can cause impact damage. Literature suggests that bird strikes account for up to 80% of service damage to composites in the aerospace sector [3]. While the surface may appear sound, there may be significant damage hidden in the internal structure, and may not be appreciated on the surface because of a difficult relationship between appearance of surface features and structural integrity of the part [4,5]. When the composite structure is subjected to a minor impact damage that is barely visible on the surface, the damage even at the micro scale can progress to significant structural damage that affects the strength, durability and stability of the composite laminates [6].

In the aviation industry, multiple non-destructive testing or NDT methods are employed, ranging from direct visual inspection, dye-penetrant, magnetic particle, eddy current, radiography to advanced methods such as 3D computed tomography, ultrasound and thermography to capture the health and structural integrity of the component without creating or intensifying any further damage to the component that is being inspected. This diversity of inspection methods requires a range of skills and expertise, providing results with differing margins of error between them.

Thermography has been attracting increasing attention over recent decades as the method involves a rapid, robust, non-contact, non-invasive inspection. Thermography can be divided into two modes: passive and active. The passive mode applies where deviations from normal operation exhibit a change in thermal contrast to be observed by an infrared imager, while active thermography involves the input of an external heat that generates a measurable thermal contrast. This particularly applies where an inspected part is not in use and is in thermal equilibrium with its

* Corresponding author.
E-mail address: yifan.zhao@cranfield.ac.uk (Y. Zhao).

Appendix 2

UD Carbon prepreg material database.

CONFIDENTIAL

ADVANCED COMPOSITES GROUP MATERIALS
DATABASE

VTM 260 Product Range for Marine Applications

J3446/J8560



High Strength Carbon Fibre UD Material : Nominal 56% Vf (35% RW)					
1) 300 gsm VTM264/T700 (24k)					
Material					
T700					
Oven Vacuum Bag Cure Cycle					
5 hrs @ 80°C					
Test Conditions					
Property	Test Method	Units	20°C dry		
0° Tensile Modulus	D 3039	GPa	131		
0° Compressive Modulus	D695 (MOD)	GPa	118		
90° Trans. Tensile Modulus	D 3039	GPa	9.1		
90° Trans. Comp. Modulus	D695 (MOD)	GPa			
0° Tensile Strength	D 3039	MPa	2575		
0° Compressive Strength	D695 (MOD)	MPa	1235		
90° Trans. Tensile Strength	D 3039	MPa	40		
90° Trans. Comp. Strength	D695 (MOD)	MPa	181.7		
0° Tensile Strain to Failure	D 3039	%	2.11		
0° Comp. Strain to Failure	D695 (MOD)	%	0.96		
90° Trans. Tensile Strain	D 3039	%			
90° Trans. Comp. Strain	D695 (MOD)	%	1.71		
In-Plane Shear Modulus	D 3518	GPa	3.94		
In-Plane Shear Strength	D 3518	MPa	85.7		
Maj. Tensile Poisson's Ratio	D 3039	-	0.32		
Maj. Comp. Poisson's Ratio	D695 (MOD)	-	0.33		
Min. Tensile Poisson's Ratio	D 3039	-			
Min. Comp Poisson's Ratio	D695 (MOD)	-	0.02		
Flexural Modulus	CRAG 200	GPa	128.4		
Flexural Strength	CRAG 200	MPa	1833		
ILSS	D 2344	MPa	88.6		
All UD data normalised to 56% fibre volume fraction (except for ILSS and In-Plane Shear).					

Checked by: Mike Davies

Date: 8th November 2011

All statements, technical information and recommendations contained in this data sheet are given in good faith and are based on tests believed to be reliable, but their accuracy and completeness are not guaranteed. They do not constitute an offer to any person and shall not be deemed to form the basis of any subsequent contract, nor to constitute any warranty or representation as to quality, merchantability or fitness for purpose. All products are sold subject to seller's Standard Terms and Conditions of Sale. Accordingly, the user shall determine the suitability of the products for their intended use prior to purchase and shall assume all risk and liability in connection therewith. It is the responsibility of those wishing to sell items made from or embodying the products to inform the user of the properties of the products and the purposes for which they may be suitable, together with all precautionary measures required in handling those products. The information contained herein is under constant review and liable to be modified from time to time.

© Copyright 2004 - The Advanced Composites Group. All rights reserved.

Appendix 3

3mm thick laminate - Stacking sequence to make up for a 3mm thick laminate assuming a post-cure thickness of 0.125mm per ply

Table 35 A 3mm laminate stacking sequence

Ply no	Quasi isotropic layup	TWI layup
1	45	45
2	135	135
3	0	0
4	90	0
Defect	-	-
5	45	0
6	135	90
7	0	0
8	90	0
Defect	-	-
9	45	45
10	135	135
11	0	0
12	90	0
Defect	-	-
13	90	0
14	0	0
15	135	135
16	45	45
17	90	0
18	0	0
19	135	90
20	45	0
21	90	0
22	0	0
23	135	135
24	45	45

% of 0 degree	25	58.33333333
% of +/- 45 degree	50	33.33333333
% of 90 degree	25	8.33333333

6mm thick laminate:

Table 36 A 6mm laminate stacking sequence

Ply no	Quasi isotropic layup	TWI layup
1	45	45
2	135	135
3	0	0
4	90	0
5	45	45
6	135	135
7	0	0
8	90	0
9	45	90
10	135	0
11	0	0
12	90	45
13	45	135
14	135	0
15	0	0
16	90	90
Defect	-	-
17	45	0
18	135	0
19	0	135
20	90	45
Defect	-	-
21	45	0
22	135	0
23	0	135
24	90	45
Defect	-	-
25	90	45
26	0	135
27	135	0
28	45	0
29	90	45
30	0	135
31	135	0
32	45	0
33	90	90
34	0	0
35	135	0

36	45	135
37	90	45
38	0	0
39	135	0
40	45	90
41	90	0
42	0	0
43	135	135
44	45	45
45	90	0
46	0	0
47	135	135
48	45	45

% of 0 degree	25	50
% of +/- 45 degree	50	41.66666667
% of 90 degree	25	8.333333333

9mm thick laminate:

Table 37 A 9mm laminate stacking sequence

Ply no	Quasi isotropic layup	TWI layup
1	45	45
2	135	135
3	0	0
4	90	0
5	45	90
6	135	0
7	0	0
8	90	45
9	45	135
10	135	0
11	0	0
12	90	90
13	45	0
14	135	0
15	0	135
16	90	45
17	45	0
18	135	0
19	0	0

20	90	0
21	45	45
22	135	135
23	0	0
24	90	0
25	45	90
26	135	0
27	0	0
28	90	135
Defect	-	-
29	45	45
30	135	0
31	0	0
32	90	90
Defect	-	-
33	45	0
34	135	0
35	0	135
36	90	45
Defect	-	-
37	90	45
38	0	135
39	135	0
40	45	0
41	90	90
42	0	0
43	135	0
44	45	45
45	90	135
46	0	0
47	135	0
48	45	90
49	90	0
50	0	0
51	135	135
52	45	45
53	90	0
54	0	0
55	135	0
56	45	0
57	90	45
58	0	135

59	135	0
60	45	0
61	90	90
62	0	0
63	135	0
64	45	135
65	90	45
66	0	0
67	135	0
68	45	90
69	90	0
70	0	0
71	135	135
72	45	45

% of 0 degree	25	55.55555556
% of +/- 45 degree	50	33.33333333
% of 90 degree	25	11.11111111

Appendix 4

The following are the Charpy test settings:

Table 38 Charpy impact test parameters

Sample Name	Impact Angle	Actual Impact Energy in Joules
3QI20d12JC1	19.5	12.82
3QI20d12JC2	19.5	12.82
3QI20d12JC3	19.0	11.50
3TWI20d12JC1	19.0	11.50
3TWI20d12JC2	19.0	11.50
3TWI20d12JC3	19.0	11.50
6QI20d12JC1	19.0	11.50
6QI20d12JC2	19.0	11.50
6QI20d12JC3	19.0	11.50
6TWI20d12JC1	19.0	11.50
6TWI20d12JC2	19.5	12.82
6TWI20d12JC3	19.0	11.50
3QI16d8JC1	16.0	8.25
3QI16d8JC2	16.0	8.25
3QI16d8JC3	16.0	8.25
3TWI16d8JC1	16.0	8.25
3TWI16d8JC2	16.0	8.25
3TWI16d8JC3	16.0	8.25
6QI16d8JC1	16.0	8.25
6QI16d8JC2	16.0	8.25
6QI16d8JC3	16.0	8.25
6TWI16d8JC1	16.0	8.25
6TWI16d8JC2	16.0	8.25
6TWI16d8JC3	16.0	8.25
3QI12d4.5JC1	12.0	4.65
3QI12d4.5JC2	12.0	4.65
3QI12d4.5JC3	12.0	4.65
3TWI12d4.5JC1	12.0	4.65
3TWI12d4.5JC2	12.0	4.65
3TWI12d4.5JC3	12.0	4.65
6QI12d4.5JC1	12.0	4.65
6QI12d4.5JC2	12.0	4.65
6QI12d4.5JC3	12.0	4.65
6TWI12d4.5JC1	12.0	4.65
6TWI12d4.5JC2	12.0	4.65
6TWI12d4.5JC3	12.0	4.65

The following are the test settings for the ballistic gas-gun impact experiment

Table 39 Gas-gun experimental settings

Sample Name	Mass of stone in gms	Velocity of gun in m/s	Actual Impact Energy in Joules
3QI12JS1	5.7	65.00	12.04
3QI12JS2	6.7	60.00	12.06
3QI12JS3	8.7	52.50	11.99
3TWI12JS1	7.5	57.00	12.18
3TWI12JS2	8.1	55.00	12.25
3TWI12JS3	6.7	57.85	11.21
6QI12JS1	6.7	57.85	11.21
6QI12JS2	6.7	57.85	11.21
6QI12JS3	7.2	58.00	12.11
6TWI12JS1	5.7	65.00	12.04
6TWI12JS2	6.0	63.00	11.91
6TWI12JS3	8.4	53.50	12.02
3QI8JS1	5.9	52.07	8.00
3QI8JS2	4.9	57.14	8.00
3QI8JS3	4.8	57.74	8.00
3TWI8JS1	4.4	60.30	8.00
3TWI8JS2	4.2	61.72	8.00
3TWI8JS3	4.5	59.63	8.00
6QI8JS1	4.9	57.14	8.00
6QI8JS2	5.1	56.01	8.00
6QI8JS3	4.8	57.74	8.00
6TWI8JS1	4.6	58.98	8.00
6TWI8JS2	4.1	62.47	8.00
6TWI8JS3	5.1	56.01	8.00
3QI4.5JS1	3.8	48.67	4.50
3QI4.5JS2	4.0	47.43	4.50
3QI4.5JS3	3.6	50.00	4.50
3TWI4.5JS1	3.2	53.03	4.50
3TWI4.5JS2	3.1	53.88	4.50
3TWI4.5JS3	3.4	51.45	4.50
6QI4.5JS1	3.6	50.00	4.50
6QI4.5JS2	3.6	50.00	4.50
6QI4.5JS3	3.2	53.03	4.50
6TWI4.5JS1	3.4	51.45	4.50
6TWI4.5JS2	3.4	51.45	4.50
6TWI4.5JS3	3.4	51.45	4.50

Appendix 5

EchoTherm® System Specification

Input Power: 120 / 240 VAC, 50/60Hz, 20A (worldwide compatibility)

Variable Flash Power Output: 10KJ (nominal max.) adjustable in 8 steps.

Precise Flash Control: min. 2.0ms duration (adjustable in 0.1ms increments - requires optional Precision Flash Controller).

Nominal Shot Size: 12" x 9". Nominal Capture Duration: 5 sec. per shot.

Integrated Illumination Head: 2 xenon flash lamps in optimized reflectors for uniform heating, access door for on-the-spot part mark-up, universal camera mounting bracket, LCD image display – 26" x 14" x 11".

Data Acquisition & Analysis System: Integrated rackmount design or portable, ruggedized lunchbox design. Dual core processor implementation, 2GB RAM, 250GB HDD, DVD±R/ RW, Gigabit Ethernet, USB 2.0, IEEE1394, Windows XP Pro.

High-Speed Digital Data Capture: up to 16 bits @ 60Hz and > 1KHz (RS-422, LVDS, IEEE1394, Camera Link, etc.).

Integrated Intelligent System Control: multiple trigger I/O capability (TTL, OC), synchronized capture, filtered and protected power distribution for all connected components (UL)

Plug-n-Play compatibility: with IR cameras supplied by major manufacturers – FLIR Systems (Indigo, Inframetrics, Agema), CEDIP, Raytheon

Multi-Format / Wavelength FPA Support: 640x512, 320x256, 160 x 128; InSb, MCT, QWIP, Microbolometer, PtSi, etc.

Integrated TSR® Processing: for advanced data analysis and evaluation capability - MOSAIQ® and EchoTherm® software.

Quantitative Measurement: depth/size of feature, coating/material thickness, thermal properties, Temperature vs. Time profiling, etc.

Active X Automation Interface: for customizable user front end applications, and automated report generation.

Smart Configuration: Stand-alone; Portable; Fully Automated (optimized for rapid, wide-area inspection).

Umbilical Length: 10m standard (max. 15m).

Open Architecture Design: for simple, low-cost upgradeability

Appendix 6

NUC Procedure for CEDIP Titanium Camera – Two-point correction method using a black body

1. Turn ON the camera and the laptop. Make sure that the data transfer card is in position and the camlink cable is connected to the camera and the laptop.
2. Allow the camera to settle down before opening the Altair software.
3. Open the Altair software and choose the working directory.
4. Click the LIVE camera icon (A) in the Altair window for the laptop to communicate with the camera and open a Live image window.

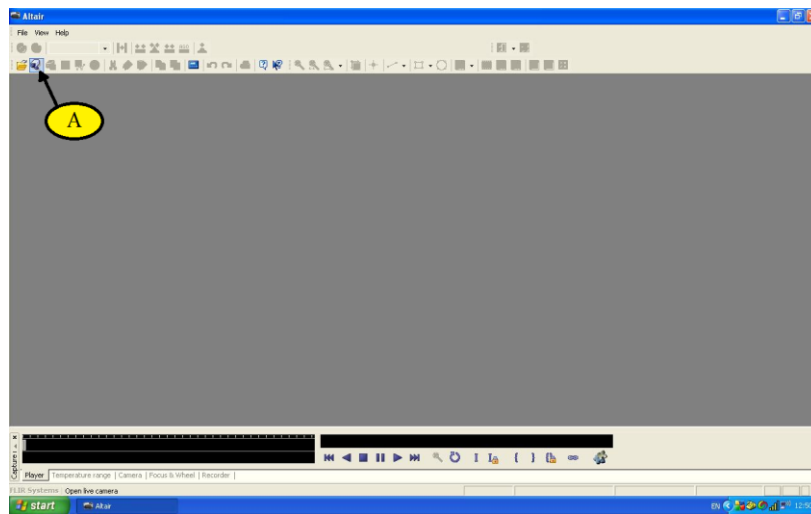


Figure 242 Altair software interface

5. At the bottom of the software window, make sure to check the Temperature tab (B) and click on an existing NUC table (C)

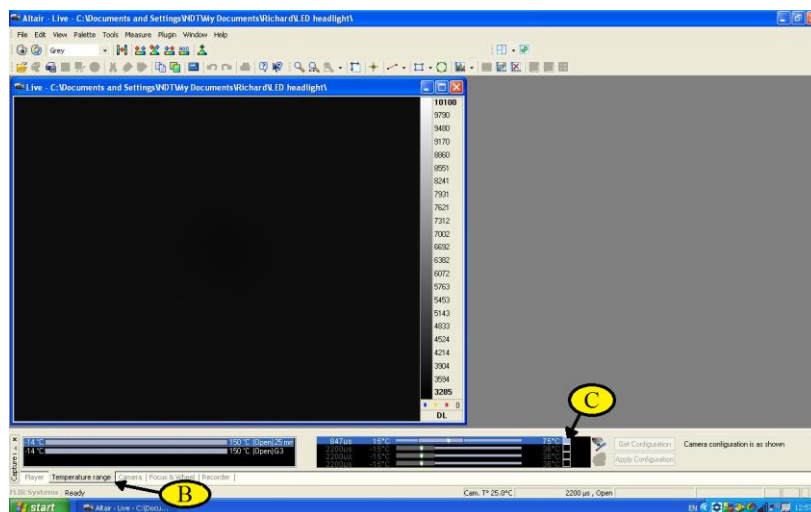


Figure 243 Altair software with camera live feed

6. Use the Temperature tab and select the appropriate temperature range.
7. To set the overall temperature range of the camera, move the slider in the NUC selection to match the operating environment's temperature. Make sure to note the Integration time.
8. Now set the temperature on the "Live" window of the camera to the operating (Working environment) temperature and make a note of the digital temperature reading. The temperature scale can be changed between digital and Celsius degree scale by clicking on the DL tab just below the temperature scale.
9. Use the windowing tab in the bottom tool bar to window down the pixel size of the image. Define the size of the window for custom settings.
10. Minimize the Altair software window and start the CIRRUS software.
11. Now click the tab marked " $\Sigma\sigma$ "(1) to show the digital level – DL for the camera.

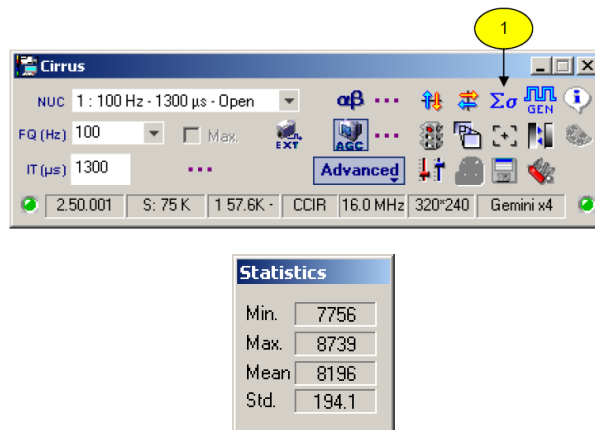


Figure 244 Cirrus Control interface with digital temperature level window

12. The main screen now shows the current NUC applied to the camera (2)

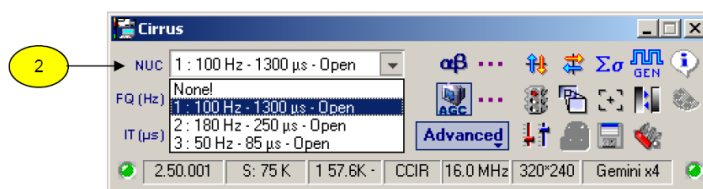


Figure 245 Cirrus control window

Note:

- i. The current setting for the camera in this case is
 - a. Frequency – 100Hz

- b. Integration time - 1300 μ s
 - c. Filter – No filter
- ii. Depending on the camera there will be 3 – 6 NUC values. “None” indicates no correction is applied and “Open” mean that there is no filter applied to the camera.

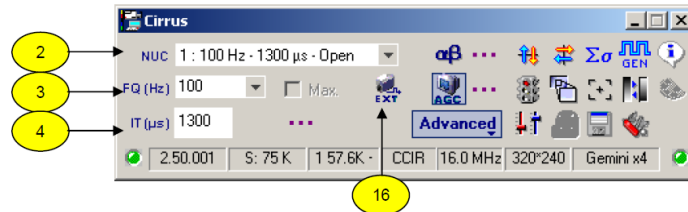


Figure 246 Cirrus control window with annotations

13. Now carry out the following steps to input settings to the CIRRUS software.
- a. Select the NUC to replace from the available list (2)
 - b. Select an appropriate frequency. (3) This should be noted even when it does not affect the main work area
 - c. Specify the integration time (IT) (4) which was noted previously from the Altair software
 - d. Leave the Filter Wheel window option as Open as there are no filters applied in this case.
 - e. Click “ $\alpha\beta$ ” to update NUC & BPR (Bad Pixel Replacement) settings (5)

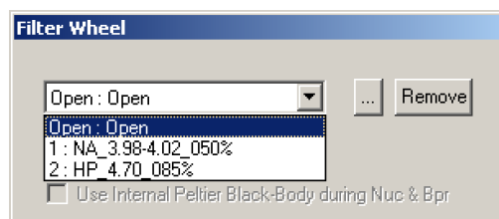


Figure 247 Filter window to select for any filters

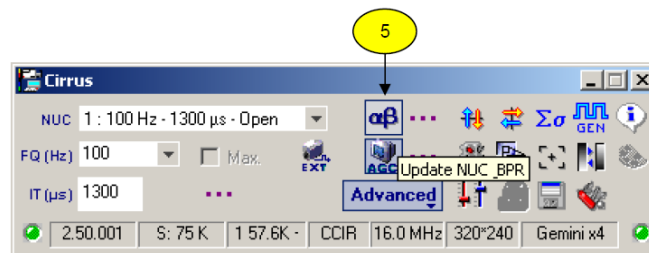


Figure 248 Cirrus control window

14. The following window will open,

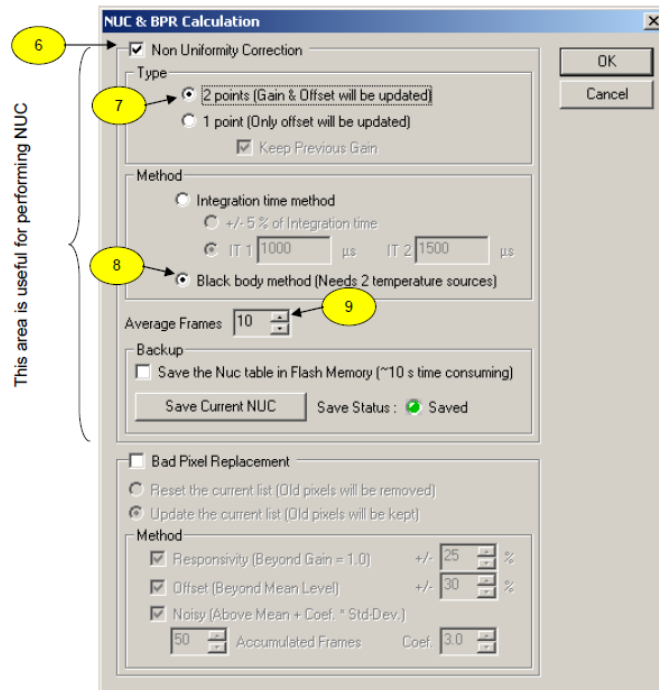


Figure 249 NUC Control window

Now do the following settings

- a. Tick the “Non Uniformity Correction” box (6)
- b. Choose the Type as “2 points” (7)
- c. Choose the Method as “Black body method” (8)
- d. Finally choose the average frames as 10 (9). This will make sure that the result retained for each point is the average from the image measurements.
- e. And make sure not to tick the Bad Pixel Replacement option
- f. Now click “Ok” to start the NUC process.

15. A new window will now open prompting you to expose the camera to the low temperature reference in front of the lens. For this case, use the lens cap and over the lens. Make sure it is not influenced by external temperatures.

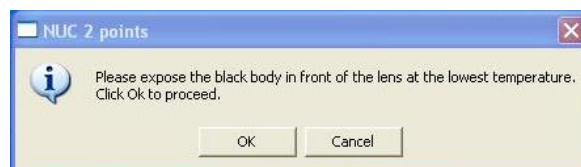


Figure 250 NUC confirmation window for low temperature exposure

- a. Now click Ok. The following window will open prompting you to expose the camera to the high temperature reference (Blackbody).

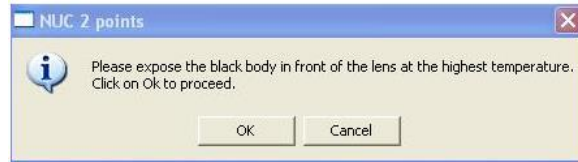


Figure 251 NUC confirmation window for high temperature exposure

- b. Click Ok. Now the camera will perform the NUC and will now update the NUC.

Note:

- c. Make sure the lower and upper temperature references are 30% and 70% of the over temperature range (working environment) of the camera.
- d. The NUC performed has not been saved. Once you verify the NUC results, save the setting using the option “Save Current NUC”

Saving a NUC

There are two ways of saving the NUC.

1. Saving the NUC to flash memory – Can be done by clicking the option “Save Current NUC” from the NUC & BPR option.
2. By saving NUC from camera to the PC – this can be done from the following steps
 - a. Select the NUC to be saved from the drop down list (2)
 - b. Click the NUC BPR preferences button (12)
 - c. In the “NUC” file box access the file path and save the NUC with a file name. (with .coe extension) (13)
 - d. Click “Get” to transfer the NUC from the camera to the PC (14)
 - e. In case you wanted to load an existing NUC from the PC to the camera then click “Put” and will transfer an existing NUC from the PC to the camera (15)

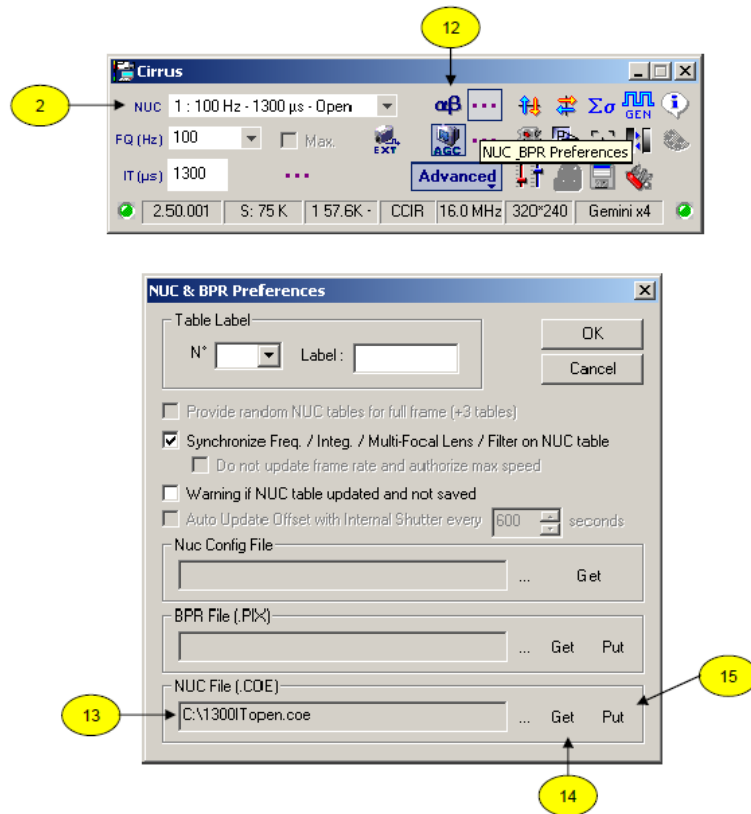


Figure 252 Cirrus control window with NUC & BPR preferences control window

Appendix 7

The following are the snapshot of the modelling process together with boundary conditions used for running the Ideas solver.

Mesh generation for PTFE and air gap:

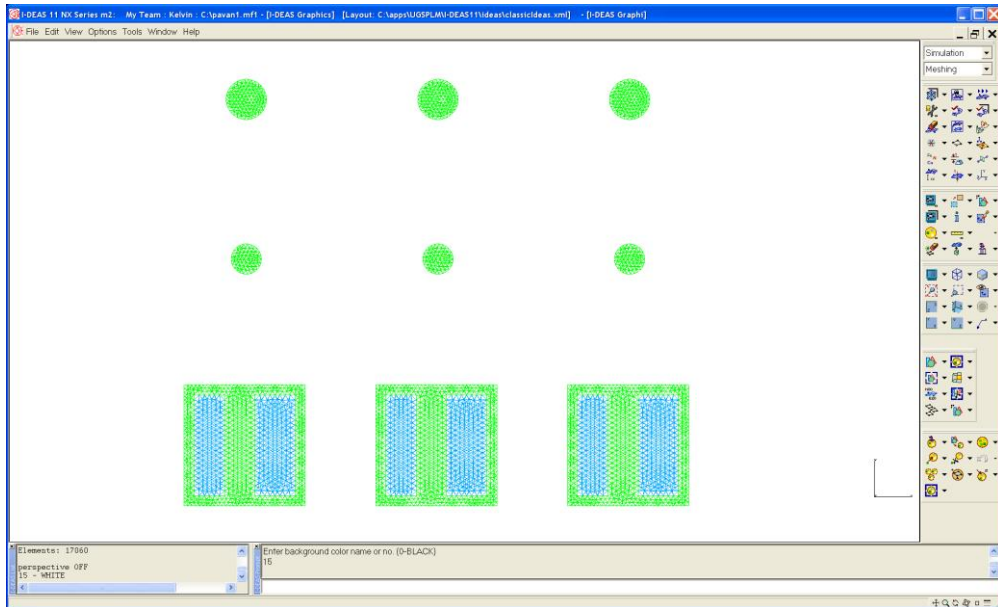


Figure 253 Defect materials meshed separately; Green - PTFE; Blue - Air gap

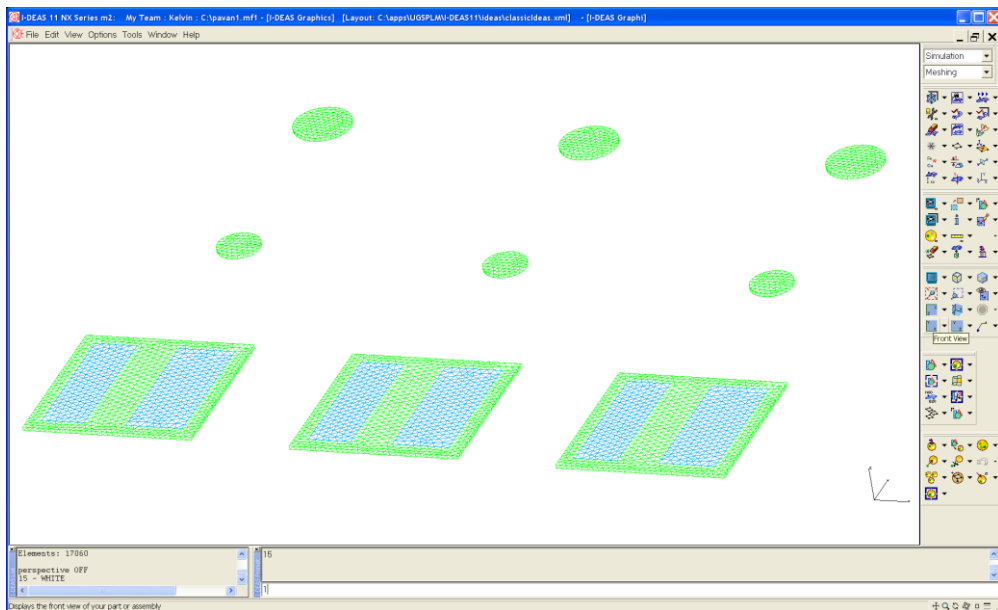


Figure 254 Model showing defect materials with mesh; orthogonal view

Material properties for CFRP:

Examine Material

Name: Number:

Description:

Material Type: Show Properties:

Material

Entity	Version	Variability	Value	Meter (N)
Properties (Required)				
THERMAL CONDUCTIVITY	1*	Constant	0.546601	J/M/K/SEC
THERMAL CONDUCTIVITY	2	Constant	0.461518	J/M/K/SEC
THERMAL CONDUCTIVITY	3	Constant	0.692259	J/M/K/SEC
THERMAL CONDUCTIVITY	4	Null	Null	J/M/K/SEC
Properties (Optional)				
MASS DENSITY	1*	Constant	1273.27	KILOGRAM/
MASS DENSITY	2	Constant	1190.24	KILOGRAM/
MASS DENSITY	3	Constant	1411.67	KILOGRAM/METER^3
MASS DENSITY	4	Null	Null	KILOGRAM/
COEFFICIENT OF THERMAL E	1*	Constant	2.16e-005	1/CELSIUS
COEFFICIENT OF THERMAL E	2	Constant	1.08e-005	1/CELSIUS
COEFFICIENT OF THERMAL E	3	Constant	2.7e-005	1/CELSIUS
COEFFICIENT OF THERMAL E	4	Null	Null	1/CELSIUS
SPECIFIC HEAT	1*	Constant	2093.4	J/KG/K
SPECIFIC HEAT	2	Constant	2093.4	J/KG/K
SPECIFIC HEAT	3	Constant	2093.4	J/KG/K
SPECIFIC HEAT	4	Null	Null	J/KG/K
EMISSIVITY	1*	Null	Null	UNITLESS
ABSORPTIVITY	1*	Null	Null	UNITLESS

Version Contro

Show Current Version Only Sort Alphabetically

Material properties for Air gap:

Examine Material

Name: AIR_CORRECTED Number: 25

Description:

Material Type: Simulation Show Properties: TMG

Isotropic: Steady state: Use Default Values:

Material

Entity	Version	Variability	Value	Meter (N)
Properties (Required)				
THERMAL CONDUCTIVITY	1*	Constant	0.0257	J/M/K/SEC
Properties (Optional)				
MASS DENSITY	1*	Constant	1.205	KILOGRAM/
COEFFICIENT OF THERMAL EXPANSION	1*	Constant	1.17e-005	1/CELSIUS
SPECIFIC HEAT	1*	Constant	1005	J/KG/K
EMISSIVITY	1*	Constant	1	UNITLESS
ABSORPTIVITY	1*	Constant	1	UNITLESS
SPECIFIC HEAT ABOVE PHASE CHANGE	1*	Null	Null	J/KG/K
SOLAR TRANSMISSIVITY	1*	Null	Null	UNITLESS
SOLAR SPECULAR REFLECTIVITY	1*	Null	Null	UNITLESS
SOLAR ABSORPTIVITY	1*	Null	Null	UNITLESS
PHASE CHANGE TEMPERATURE	1*	Null	Null	C
LATENT HEAT PER UNIT MASS	1*	Null	Null	J/KG
REVERSE SIDE EMISSIVITY	1*	Null	Null	UNITLESS
REVERSE SIDE SOLAR ABSORPTIVITY	1*	Null	Null	UNITLESS
REVERSE SIDE SOLAR SPECULAR REFLECTIVITY	1*	Null	Null	UNITLESS
IR SPECULAR REFLECTIVITY	1*	Null	Null	UNITLESS
IR TRANSMISSIVITY	1*	Null	Null	UNITLESS
REVERSE SIDE IR SPECULAR REFLECTIVITY	1*	Null	Null	UNITLESS

Version Control

Show Current Version Only
 Sort Alphabetically

Material properties for PTFE:

Examine Material

Name: Number: Locked

Description:

Material Type: Show Properties:

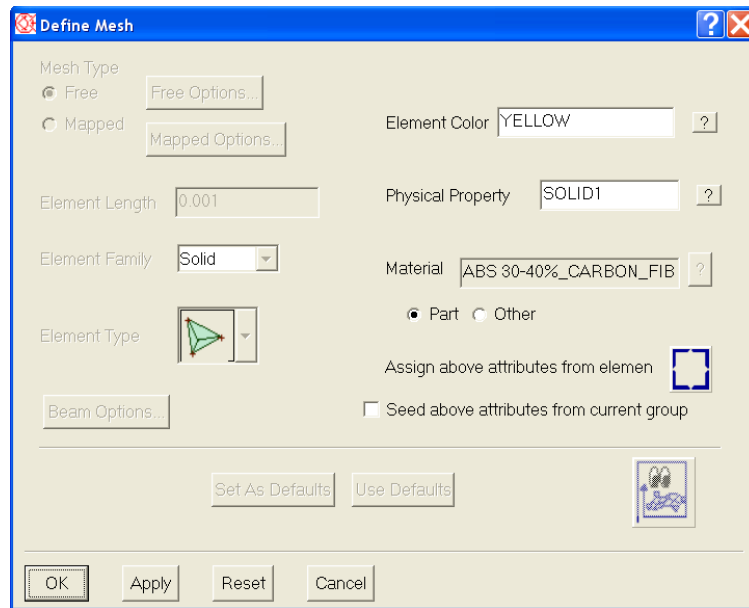
Material

Entity	Version	Variability	Value	Meter (N)
Properties (Required)				
THERMAL CONDUCTIVITY	1*	Constant	0.470171	J/M/K/SEC
THERMAL CONDUCTIVITY	2	Constant	0.213451	J/M/K/SEC
THERMAL CONDUCTIVITY	3	Constant	1.21146	J/M/K/SEC
THERMAL CONDUCTIVITY	4	Null	Null	J/M/K/SEC
Properties (Optional)				
MASS DENSITY	1*	Constant	2325.08	KILOGRAM/
MASS DENSITY	2	Constant	941.116	KILOGRAM/
MASS DENSITY	3	Constant	3958.16	KILOGRAM/
MASS DENSITY	4	Null	Null	KILOGRAM/
COEFFICIENT OF THERMAL E	1*	Constant	0.00010638	1/CELSIUS
COEFFICIENT OF THERMAL E	2	Constant	2.52e-005	1/CELSIUS
COEFFICIENT OF THERMAL E	3	Constant	0.00044208	1/CELSIUS
COEFFICIENT OF THERMAL E	4	Null	Null	1/CELSIUS
SPECIFIC HEAT	1*	Constant	1004.83	J/KG/K
SPECIFIC HEAT	2	Constant	962.964	J/KG/K
SPECIFIC HEAT	3	Constant	1004.83	J/KG/K
SPECIFIC HEAT	4	Null	Null	J/KG/K
EMISSIVITY	1*	Null	Null	UNITLESS
ABSORPTIVITY	1*	Null	Null	UNITLESS

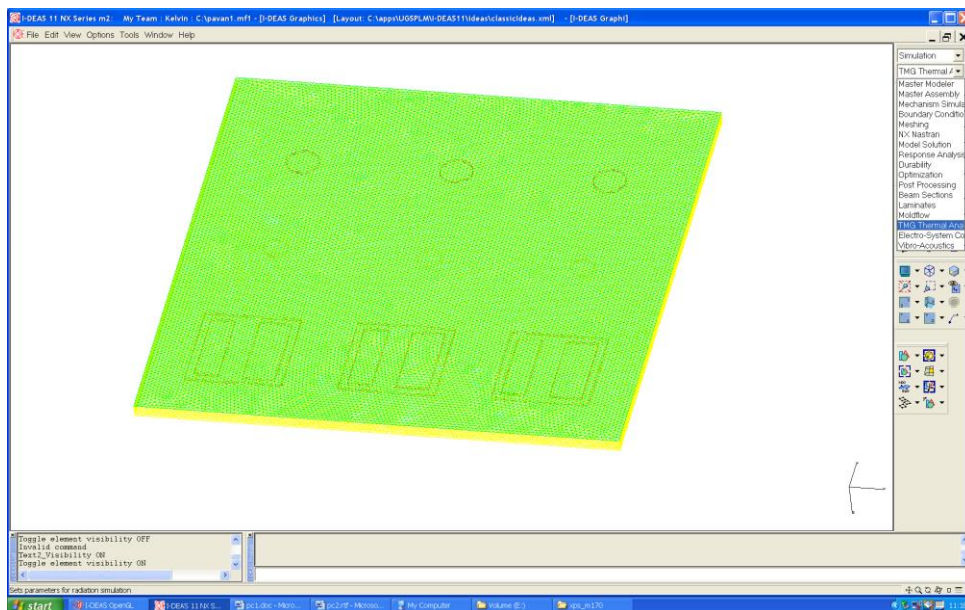
Version Control

Show Current Version Only Sort Alphabetically

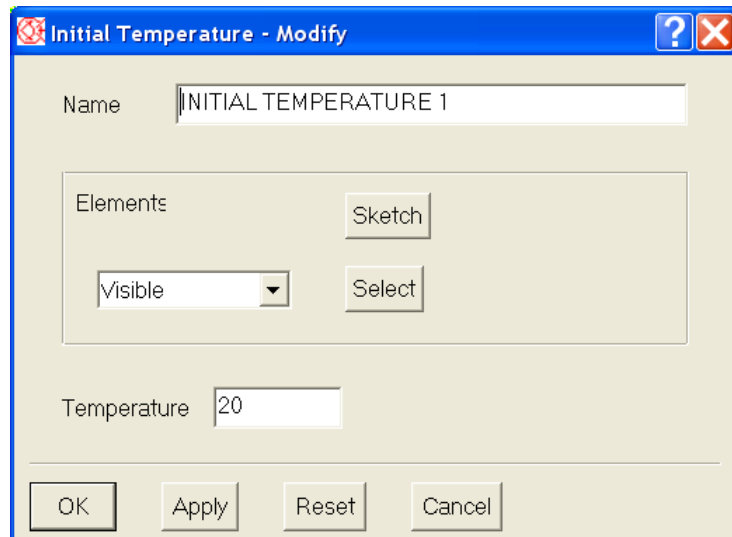
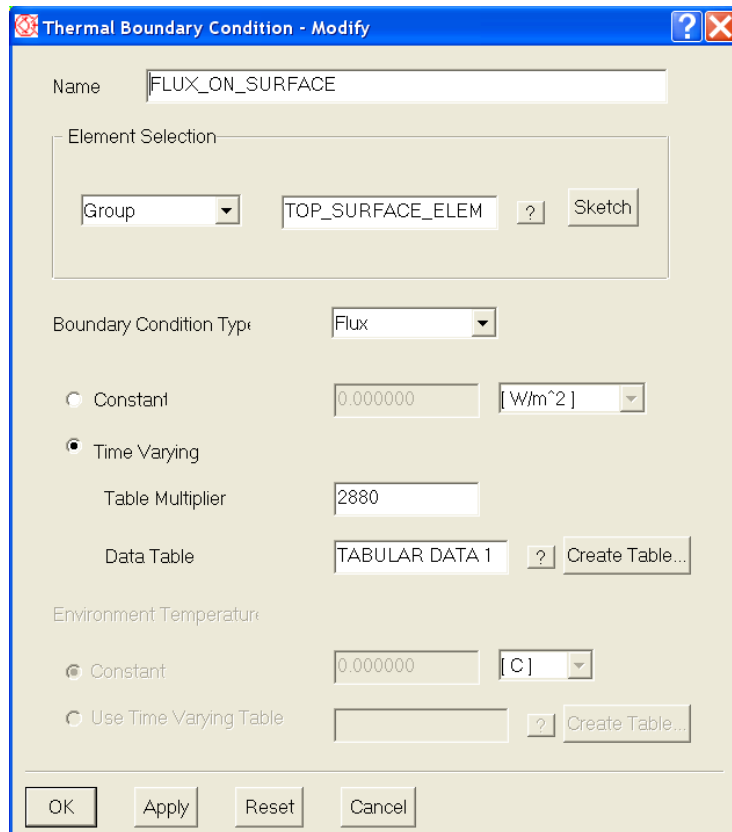
Mesh parameters:



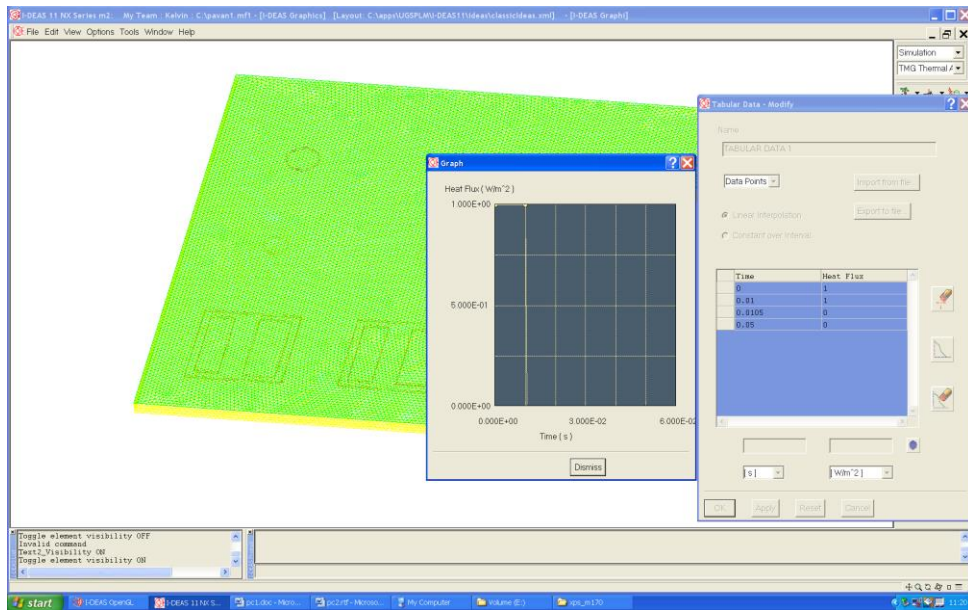
Generated mesh:



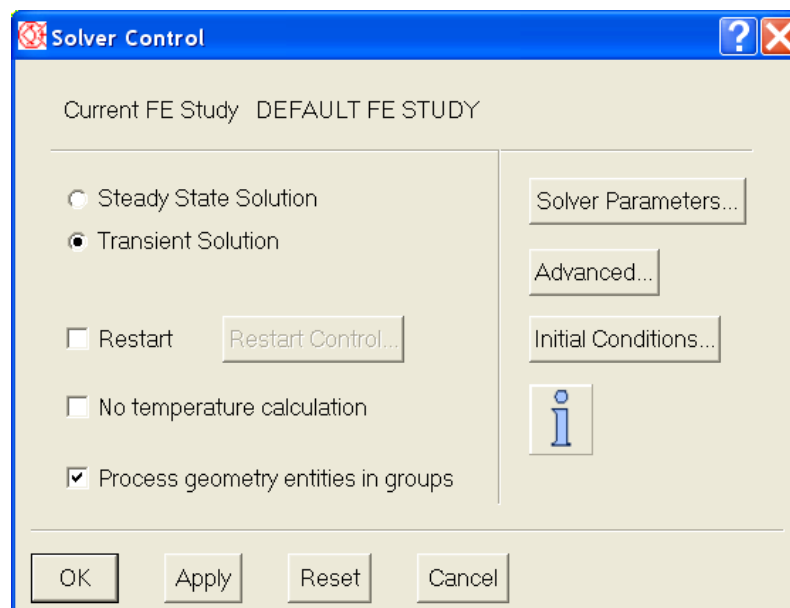
Applied thermal boundary conditions:



Boundary conditions confirmation:



Solver control parameters:



Transient Analysis Parameters [?] [X]

Start Time sec End Time sec

Integration Control

Method

Time Step

Time Table [?]

Convergence Control

Iteration Limit

Relaxation Factor

Update Radiative Conductances when $\Delta T >$

Convergence when Temperature Difference $<$

Results Output

At Constant Time Interval

At Specified Times